Searching for Strangelets and Macro-SQM Candidates from Neutron Stars, Binary Mergers, and Gamma-Ray Bursts

Multimessenger Constraints and Direct-Detection Prospects

C.R. Das

The Bogoliubov Laboratory of Theoretical Physics (BLTP)
International Intergovernmental Scientific Research Organization — Joint Institute for Nuclear Research (JINR)
6 Joliot-Curie St, Dubna, Moscow Region, Russia, 141980

Next Frontiers in Magnetic Monopole Searches
Institute of High Energy Physics, Chinese Academy of Sciences, Beijing, China
Monday 14 September 2026, 09:30 A.M.

Outline of the Talk

1. **Motivation.**
   Why strange quark matter (SQM) is a compelling idea for the true ground state of dense QCD.
2. **Theoretical framework.**
   The 2SC $\rightarrow$ CFL phase transition, strangelet production, and the relevant cross-sections.
3. **Observational strategy.**
   Monochromatic γ-ray lines from strangelet–anti-strangelet annihilation.
4. **Three case studies.**
   - HESS J1731-347 — a strange quark star (SQS) candidate.
   - GW170817 — the first binary neutron-star merger.
   - GRB 250702B — an ultra-long gamma-ray burst.
5. **Direct searches for macro-scale SQM.**
   Nuclearites, Q-balls, and current/future limits.
6. **Summary and outlook.**

Notation I — Strangelet Properties

Strangelet properties

A	Baryon number (mass number): one third of total quark number.
Z	Net electric charge in units of e.
Z_V	Valence charge of a uniformly charged sphere.
$R_{\rm ch}$	Coulomb radius of a uniformly charged sphere.
R_S	Strangelet radius, $R_S \propto A^{1/3}$.
m_S	Strangelet mass, $m_S \approx A\, m_N$; therefore the annihilation line energy is $E_\gamma = m_S \approx 0.94\, A$ GeV.
m_N	Nucleon mass, $m_N \approx 0.94$ GeV$/c^2$.
m_q	Constituent quark mass.
E_γ	Annihilation line energy, $E_\gamma = m_S$.
$E_\gamma^{\rm obs}$	Observed line energy, $E_\gamma^{\rm obs} = E_\gamma/(1+z)$.

Strangelet properties (cont.)

Y_Q	Charge fraction. $Y_Q \equiv Z/A$; the symbols Y_Q and Z/A denote the *same* physical quantity and are used interchangeably.
δ	Two-photon deviation angle from 180° in $S\bar{S} \to \gamma\gamma$ (see the two-photon angular-correlation frame).
$v_{\rm rel}$	Relative velocity of the $S\bar{S}$ pair in the source frame; drives the angular spread $\delta \sim \frac{1}{2}(v_{\rm rel}/c)$.
$\delta_{\rm dec}$	Declination of a source.
$M_\odot$	Solar mass.
u, d, s	Up, down, and strange quarks.
$\bar{u}, \bar{d}, \bar{s}$	Anti-quarks.

Notation II — Electron Cloud and Neutralisation

Electron cloud

N_e Number of electrons bound in the neutralising cloud of a positively charged strangelet; $N_e \simeq Z$ for electric neutrality at large distance.

λ_{Debye} Debye screening length of the electron cloud, $\lambda_{\mathrm{Debye}} = \sqrt{k_B T_e/(4\pi e^2 n_e)}$, with T_e the electron temperature and n_e the electron number density.

T_e Electron-cloud temperature (distinct from the quark-matter temperature T).

Why this matters

$\mathcal{R}$ Rigidity of the *bare* strangelet, $\mathcal{R} = p/(Ze)$; the electron cloud is stripped in the first few μm of a detector, so direct detection sees the bare Z, not the neutralised total charge.

R_{ch} Coulomb radius of the electron cloud; used in $E_{\mathrm{coul}} = \frac{3}{5}\alpha Z_V^2/R_{\mathrm{ch}}$.

Z_V Valence charge.

Warning N_e is a *bound-electron count*, not to be confused with N_{evt} (expected direct-detection events) or N_H (hydrogen column density).

Notation III — Strangelet Kinematics

Strangelet kinematics

- R Compact-object radius (in km).
- $\mathcal{R}$ Rigidity, $\mathcal{R} = p/(Ze)$.
- p Momentum.
- E Particle energy.
- v Particle velocity; $\beta_{\mathrm{vel}} = v/c$. The symbol v denotes the physical velocity ($\mathrm{cm\,s^{-1}}$), while β_{vel} is its dimensionless ratio v/c.
- β_{vel} Velocity in units of c (subscript "vel" distinguishes it from β_{frag}).
- γ_L Lorentz factor, $\gamma_L = (1 - \beta_{\mathrm{vel}}^2)^{-1/2}$.
- $\hbar c$ Natural-units conversion constant, $\hbar c \simeq 0.197$ GeV·fm; used to translate between energy, length, and cross-section units.

Strangelet kinematics (cont.)

- G Gravitational constant.
- g Magnetic charge of a monopole (used only in the strangelet–monopole comparison frame). Not to be confused with the NJL coupling ratio g_V/G_D or with the metric determinant g.
- M_{nuc} Nuclearite (macro-SQM) mass.
- c Speed of light.
- k_B Boltzmann constant.
- e Elementary charge.
- α Fine-structure constant, $\alpha \approx 1/137$.
- θ_W Weinberg (weak-mixing) angle. Distinct from the scattering angle ϑ.

Notation IV — QCD Phases

Gaps and couplings

Δ	Generic pairing gap / order parameter.
$\Delta_{2\mathrm{SC}}$	Two-flavour colour-superconducting gap.
Δ_{CFL}	Colour-flavour-locked gap.
Δ_0	Zero-temperature BCS gap.
m_s	Strange-quark mass.
G_D	Scalar diquark coupling.
G_V, G_S	Vector and scalar couplings.
B_{bag}	Bag constant (energy density).
B_{eff}	Effective bag constant; in the simplest case $B_{\mathrm{eff}} = B_{\mathrm{bag}}$.
$B_{\mathrm{bag}}^{1/4}$	Bag-constant scale (MeV).

Gaps and couplings (cont.)

$B_{\mathrm{eff}}^{1/4}$	Effective bag-constant scale (MeV). By definition $B_{\mathrm{eff}}^{1/4} = (B_{\mathrm{eff}})^{1/4}$; the two notations are numerically related by the fourth root and are not independent quantities.
γ_5	Chirality matrix.
γ^μ	Dirac matrices.
$q, \bar{q}$	Light quark and anti-quark.
ψ	Quark field (spinor).
C	Charge-conjugation matrix, $C = i\gamma_2\gamma_0$.
τ_2	Second Pauli matrix (flavour space).
λ_2	Second Gell-Mann matrix (colour space).

Notation V — QCD Thermodynamics

Thermodynamics

T	Temperature.
T_c^{QCD}	QCD critical temperature, $T_c^{\mathrm{QCD}} \approx 156$ MeV; abbreviated as $T_c \equiv T_c^{\mathrm{QCD}}$.
μ	Quark chemical potential.
μ_B	Baryon chemical potential.
μ_I	Isospin chemical potential.
μ_u, μ_d, μ_s	Up/down/strange-quark chemical potentials.
μ_i	Chemical potential of quark species i.
μ_e	Electron chemical potential.
μ_{K^-}	Charged-kaon chemical potential.

Thermodynamics (cont.)

$\delta\mu$	$\delta\mu = (\mu_d - \mu_u)/2$.
P	Pressure.
ϵ	Energy density (MeV/fm^3). Distinct from the matrix $\mathcal{E}$ appearing in the matrix kinetic equation.
ϵ_B	Energy per baryon (MeV).
n_A	Baryon density.
n_0	Nuclear saturation density, $n_0 \approx 0.16$ fm^{-3}.
n_B	Net baryon density (often plotted as n_B/n_0).
V	Volume (distinct from vector current V^μ).

Notation VI — QCD Scales and Thermodynamic Potentials

QCD scales

Λ_{QCD}	QCD scale, ~ 200 MeV.
Λ_{NJL}	NJL cutoff.
N_c	Number of colours, $N_c = 3$.
N_f	Number of quark flavours.
L_0	Symmetry-energy slope parameter. Distinct from the null-hypothesis likelihood $\mathcal{L}_0$.
m_0	Chiral invariant mass.
$\sqrt{s_{NN}}$	Centre-of-mass energy per nucleon pair.

Energy and thermodynamic potentials

E_A	Total strangelet energy.
E_{coul}	Coulomb energy of a uniformly charged sphere.
Ω_{th}	Grand potential (thermodynamic), $\Omega_{\mathrm{th}} = \sum_i \Omega_i$.
Ω_i	Thermodynamic potential of quark species i (per-flavour contribution).
$\Omega_{2\mathrm{SC}}$	Grand potential in the 2SC phase.
Ω_{CFL}	Grand potential in the CFL phase.
N_i	Quark number of species i.
ϵ_p	Free-quark dispersion: $\epsilon_p = \sqrt{p^2 + m_q^2}$.
E_p	Bogoliubov quasiparticle energy: $E_p = \sqrt{(\epsilon_p - \mu)^2 + \Delta^2}$.
ΔP	Pressure difference, $\Delta P = -(\Omega_{\mathrm{CFL}} - \Omega_{2\mathrm{SC}})$.
σ_{ST}	Surface tension of the interface.
R_*	Critical bubble radius.

Notation VII — Production and Accumulation (I)

Production

$\Gamma_{\rm trans}$	2SC $\to$ CFL transition rate per unit volume and time.
$\dot{N}(A)$	Strangelet production rate (dot notation for rate; consistent throughout this talk).
$\dot{N}_{\rm peak}$	Peak production rate.
$A_{\rm peak}$	Baryon number at peak production.
$N_{\rm acc}$	Accumulated strangelet number, $N_{\rm acc} = \dot{N}(A)\,\tau_{\rm acc}$.
δE	Activation energy barrier.
$V_{\rm core}$	Quark-core volume.
$V_{\rm source}$	Accumulation volume.
$R_{\rm core}$	Quark-core radius.
$\tau_{\rm acc}$	Accumulation time. For HESS J1731-347 we adopt $\tau_{\rm acc} = 10^6$ yr $\simeq 3.16 \times 10^{13}$ s as a benchmark accumulation timescale; this is a model parameter representing the effective duration over which strangelet accumulation is integrated, and is not necessarily equal to the SNR age.
η	Escape/conversion efficiency factor (dimensionless). This is the scenario efficiency $\eta \sim 10^{-22}$–10^{-18}, the exponential barrier factor $\exp(-\delta E/T)$ is absorbed into it. *Distinct* from $\eta_{\rm budget}$ (below) and $\eta_{\rm form}$.

Notation VIII — Production and Accumulation (II)

Production (cont.)

η_{budget} Mass-budget normalisation factor (integrated over all A): the scale factor applied to a raw peak rate $\dot{N}_{\mathrm{peak}}$ so that the total accumulated mass satisfies $\int A\, m_N\, \dot{N}(A)\, \tau_{\mathrm{acc}}\, dA \leq f_{\mathrm{max}} M_\star$.
At the Baseline benchmark, $\eta_{\mathrm{budget}} \simeq 3.4 \times 10^{-18}$. *Not* the same as the per-A convention ($f_{\mathrm{ret}} \lesssim 7 \times 10^{-5}$ at $A = 100$) used by the line-flux figures.

$g_{\mathrm{geom}}(A)$ Geometric growth factor of the production law, $g_{\mathrm{geom}}(A) = (A/A_{\mathrm{peak}})^{2/3}$; reflects the cross-sectional area $\propto A^{2/3}$ of a strangelet of radius $R_S \propto A^{1/3}$.

$g_{\mathrm{supp}}(A)$ Exponential suppression factor, $g_{\mathrm{supp}}(A) = \exp\left[\frac{2}{3}(1 - A/A_{\mathrm{peak}})\right]$; encodes combined multifragmentation and coalescence suppression.
The product $g_{\mathrm{geom}}\, g_{\mathrm{supp}}$ has a unique maximum at $A = A_{\mathrm{peak}}$.

τ_{form} Formation (nucleation) timescale; set by the critical-bubble growth rate, $\tau_{\mathrm{form}} \sim R_*/v_{\mathrm{growth}}$ with R_* the critical radius.

τ_{esc} Escape timescale of a strangelet from the quark core against the surrounding hadronic envelope.

τ_{surv} Survival timescale against fragmentation in the ejecta; sets the large-A behaviour of $S_{\mathrm{surv}}(A)$.

t Time variable.

Notation IX — Stability and Retention

Stability and retention

$f_{\rm ret}^{\rm min}$	Minimum detectable retention proxy.
$f_{\rm ret}^{\rm max}$	Retention allowed by the per-A mass budget, evaluated at $A = 100$ (where the CTA line search is most sensitive): $f_{\rm ret} \lesssim 7 \times 10^{-5}$ for the Baseline benchmark.
$f_{\rm ret}^{\rm global}$	Retention allowed by the integrated mass budget across all A: $f_{\rm ret} \lesssim 3.4 \times 10^{-18}$ for the Baseline benchmark.
$f_{\rm ret}^{\rm CTA}$	Retention required to reach the CTA threshold. With the *digitized* CTA narrow-line limit at $E_\gamma = 94$ GeV ($A = 100$) this quantity evaluates to $\simeq 0.22$, i.e. it is *physically allowed* (< 1) but $\sim 3200\times$ above the mass-budget ceiling $f_{\rm ret} \lesssim 7 \times 10^{-5}$.
$S_{\rm form}$	Formation probability.
$A_{\rm min}$	Minimum stable baryon number, $A_{\rm min} \sim 50$–200.
$f_{\rm ret}$	Retention factor, $f_{\rm ret} = S_{\rm form} S_{\rm esc} S_{\rm surv}$.
$S_{\rm esc}$	Escape probability from the quark core.
$S_{\rm surv}$	Survival probability against fragmentation.
$a_{\rm surf}$	Surface energy coefficient (MeV).
$a_{\rm curv}$	Curvature energy coefficient (MeV).
$A_{\rm frag}$	Fragmentation scale.
$A_{\rm esc}$	Escape threshold baryon number.
n_S	Strangelet number density (source frame).
$n_{\bar{S}}$	Anti-strangelet number density.
$\tau_{\rm ann}$	Annihilation timescale, $\tau_{\rm ann} = 1/(n_S \langle\sigma v\rangle)$; the typical time between two strangelet–anti-strangelet encounters in the source frame.

Notation X — Annihilation

Annihilation

$\langle \sigma v \rangle$	Velocity-averaged annihilation cross-section ($\mathrm{cm}^3\,\mathrm{s}^{-1}$ unless stated otherwise).
K	Annihilation kernel, $K \equiv B_{\gamma\gamma}\langle \sigma v \rangle$.
R_{ann}	Total annihilation rate.
a, b	s-wave and p-wave coefficients (dimensionless in natural units with $c = 1$).
E_{act}	Activation energy (formerly E_a).
σ_{max}	Maximum s-wave cross-section, $\sigma_{\mathrm{max}} = 4\pi/k^2$ (partial-wave unitarity bound; k is the wavenumber). The benchmark normalisation π/m_S^2 used in the annihilation kernel is *inspired by*, but not derived from, this bound.

Notation XI — Line Flux

Line flux and geometry

Φ_γ Line-photon flux at Earth, with the overall factor $2B_{\gamma\gamma}$ arising from two photons per annihilation, each carrying $E_\gamma = m_S$.

$\Phi_\gamma^{\lim}(E_\gamma)$ Line-flux sensitivity limit as a function of photon energy. Two reference values used throughout this talk:

- CTA ($E_\gamma = 94$ GeV)$\simeq 1.2 \times 10^{-14}$ ph cm^{-2} s^{-1} — digitized CTAO South Alpha differential sensitivity $\times \Delta E = 0.1E$,at the benchmark line energy for $A = 100$.
- HGPS ($E_\gamma = 1$ TeV)$\simeq 2.3 \times 10^{-13}$ ph cm^{-2} s^{-1} — HGPS 1%-Crab narrow-line limit, reference energy for the line-flux thresholds shown in figures and in the retention plots.

$\Phi_\gamma^{\mathrm{base}}$ Baseline line flux (evaluated at the benchmark inputs with $f_{\mathrm{ret}} = 1$); used in the tornado plot as the reference.

$B_{\gamma\gamma}$ Branching fraction to $\gamma\gamma$ (line yield per annihilation).
Treated as a benchmark input, not a QCD-derived quantity; realistic values are $\ll 1$.

D Distance to source.

D_L Luminosity distance.

z Redshift.

$r_{S\bar{S}}$ Anti-strangelet asymmetry ratio, $r_{S\bar{S}} \equiv n_{\bar{S}}/n_S$.
The benchmark assumes $r_{S\bar{S}} = 1$; the line flux scales linearly with $r_{S\bar{S}}$ at fixed n_S, since $R_{\mathrm{ann}} = n_S n_{\bar{S}} \langle\sigma v\rangle V_{\mathrm{source}}$.

Notation XII — Cross-Sections

Strangelet–nucleon cross-section

σ_S	Strangelet–nucleon cross-section (total, unless stated otherwise).
σ_0	Reference cross-section, $\sigma_0 \sim 1$ mb.
ϑ	Scattering angle. Distinct from the Weinberg angle θ_W.
$f(\vartheta)$	Angular distribution, normalised as $\int f(\vartheta)\, d\Omega/(4\pi) = 1$.
dE/dx	Energy loss per unit path length.
ρ_{targ}	Target density (nuclearite energy loss).

Notation XIII — Direct Detection (I)

Direct-detection observables

$F_{\rm dir}$	Total direct-detection flux at Earth ($\mathrm{cm}^{-2}\,\mathrm{s}^{-1}$).
$\Phi_{\rm dir}$	Direct-detection flux per unit solid angle ($\mathrm{cm}^{-2}\,\mathrm{s}^{-1}\,\mathrm{sr}^{-1}$), $\Phi_{\rm dir} = F_{\rm dir}/(4\pi)$.
$N_{\rm evt}$	Number of expected events.
$A_{\rm eff}$	Effective detector area.
$T_{\rm live}$	Live time.
$\Delta\Omega$	Angular acceptance (sr).
$L_{\rm path}$	Path length in a detector.
N_H	Hydrogen column density.
$n_S^{\rm local}$	Local strangelet number density (detector frame, distinct from source-frame n_S).
n_H	Interstellar hydrogen *number* density (cm^{-3}). Distinct from the column density N_H (cm^{-2}) used in the absorption analysis.

Notation XIV — Direct Detection (II)

Direct-detection observables (cont.)

$\lambda_{\rm ISM}(A)$ ISM mean free path of a strangelet, $\lambda_{\rm ISM}(A) = 1/[n_H\,\sigma_S(A)]$, with $\sigma_S(A) \sim \sigma_0\,(A/100)^{2/3}$ and $\sigma_0 \sim 1$ mb. At $n_H \sim 1$ cm^{-3}:

$$\lambda_{\rm ISM}(A) \;\sim\; \frac{3.2\times 10^5\ \text{kpc}}{(A/100)^{2/3}}.$$

For $A \sim 10^2$, $\lambda_{\rm ISM} \sim 3.2\times 10^5$ kpc ≈ 0.3 Gpc (essentially unattenuated over galactic or even extragalactic scales); for $A \sim 10^8$, $\lambda_{\rm ISM} \sim 30$ kpc (comparable to the size of the Galactic disk); for $A \gtrsim 10^{11}$, $\lambda_{\rm ISM} \lesssim 0.3$ kpc and the strangelet is efficiently absorbed before reaching the observer.

Direct-detection observables (cont.)

$L_{\rm ISM}$ Propagation path length through the interstellar medium (kpc or cm).

$S_{\rm prop}(A)$ Propagation survival factor, $S_{\rm prop}(A) = \exp[-L_{\rm ISM}/\lambda_{\rm ISM}(A)]$. Not included in the benchmark line-flux or direct-flux formulas; a separate systematic that depends strongly on A.

Notation XV — Neutrino Physics

Neutrino quantities and transport

$\sigma_{\nu S}$	Neutrino–strangelet cross-section.
E_ν	Neutrino energy.
λ_ν	Neutrino mean free path.
L_ν	Neutrino luminosity.
$\langle E_\nu \rangle$	Mean neutrino energy.
Y_L	Lepton fraction (electron + neutrino).
Y_{L_e}	Electron lepton fraction.
T_c^{pair}	BCS critical temperature, $\Delta_0 \approx 1.76\, k_B\, T_c^{\mathrm{pair}}$ (distinct from the QCD critical temperature $T_c \equiv T_c^{\mathrm{QCD}}$).
ν	Neutrino.
$\bar{\nu}$	Anti-neutrino.
ℓ^-	Charged lepton (e^- or μ^-).

Notation XVI — Weak-interaction (I)

Weak-interaction formalism

$\mathcal{L}_W$	Weak Lagrangian.
G_F	Fermi coupling constant. The prefactor $G_F/(2\sqrt{2})$ used here is a convention; some references absorb the factor 2 differently.
$\mathcal{J}^\mu$	Weak hadronic current.
ℓ^μ	Neutrino current, $\ell^\mu = \bar{\nu}\gamma^\mu(1-\gamma^5)\nu$.
V^μ	Vector current, $V^\mu = \bar{q}\gamma^\mu q$.
A^μ	Axial-vector current, $A^\mu = \bar{q}\gamma^\mu\gamma^5 q$.
c_V, c_A	Single-quark vector/axial couplings.
c_V^u, c_V^d	Up/down single-quark vector couplings.
c_A^u, c_A^d	Up/down single-quark axial couplings.
C_V, C_A	Effective vector/axial couplings for the strangelet (coherent sum over quarks).
N_{coh}	Number of coherently scattering quarks, $N_{\mathrm{coh}} \sim A$. The actual value may be suppressed by the finite coherence length of the strangelet and by form-factor effects at large Q^2; the $N_{\mathrm{coh}} \sim A$ scaling is a benchmark upper limit.

Notation XVII — Weak-interaction (II)

Weak-interaction formalism (cont.)

Q^μ	Neutrino pair 4-momentum, $Q^\mu = (\omega, \mathbf{q})$.
ω	Energy transfer.
$\mathbf{q}$	Momentum transfer (bold; distinct from quark q).
Q^2	Invariant momentum transfer, $Q^2 = \omega^2 - \lvert\mathbf{q}\rvert^2$.
$\Pi^{\mu\nu}$	Polarization tensor.
$\ell^{\mu\nu}$	Lepton tensor, $\ell^{\mu\nu} = Q^\mu Q^\nu - Q^2 g^{\mu\nu}$.
$F(Q^2)$	Form factor, normalised as $F(0) = 1$.
$S_{\mathrm{pair}}(T)$	Pairing suppression factor, $S_{\mathrm{pair}}(T) = \Delta(T)^2/\Delta_0^2$.
$\mathcal{N}_k$	Bogoliubov–de Gennes (BdG) matrix, $\mathcal{N}_k = \begin{pmatrix} n_k & F_k \\ F_k^\dagger & 1 - n_k \end{pmatrix}$.
I_{coll}	Collision integral in the matrix kinetic equation.
$\mathcal{E}$	Matrix entering the commutator $[\mathcal{N}, \mathcal{E}]$ in the matrix kinetic equation (distinct from scalar energy density ϵ).

Notation XVIII — Statistics and Likelihood

Statistics and likelihood

$\mathcal{L}$	Likelihood.
$\mathcal{L}_0$	Null-hypothesis likelihood, $\mathcal{L}_0 = \mathcal{L}(\hat{\boldsymbol{\Theta}}_0)$. Distinct from the symmetry-energy slope L_0.
$\mathcal{L}_{\max}$	Maximum likelihood, $\mathcal{L}_{\max} = \mathcal{L}(\hat{\boldsymbol{\Theta}})$.
$\boldsymbol{\Theta}$	Parameter vector.
$\pi(\boldsymbol{\Theta}\|\mathcal{M})$	Prior density for the parameters $\boldsymbol{\Theta}$ under model class $\mathcal{M}$.
$\mathcal{Z}$	Bayesian evidence (marginal likelihood), $\mathcal{Z} = \int d\boldsymbol{\Theta}\, \mathcal{L}(D\|\boldsymbol{\Theta})\, \pi(\boldsymbol{\Theta}\|\mathcal{M})$.
$\mathcal{B}$	Bayes factor / evidence ratio.
$\mathcal{B}^{\mathcal{M}_1}_{\mathcal{M}_2}$	Bayes factor between model classes $\mathcal{M}_1$ and $\mathcal{M}_2$, $\mathcal{B}^{\mathcal{M}_1}_{\mathcal{M}_2} = \mathcal{Z}_{\mathcal{M}_1}/\mathcal{Z}_{\mathcal{M}_2}$. Distinct from the bag constant $B_{\rm bag}$ and from $B_{\rm eff}$.

Statistics and likelihood (cont.)

$\mathcal{M}$	Model class.
$p(D\|\boldsymbol{\Theta},\mathcal{M})$	Likelihood of data D.
$\Delta\mathrm{TS}$	Test-statistic difference.
$N_{\rm bins}$	Number of bins.
n_i	Observed counts in bin i.
λ_i	Predicted counts in bin i.
N_0	Flux normalisation of the continuum power law.
$\Gamma_{\rm spec}$	Power-law spectral index.
$\mathcal{S}_{\rm det}$	Detection significance expressed in units of σ; e.g. $\mathcal{S}_{\rm det} = 5$ means a 5σ detection.
M_0	Dimensionless normalised line-yield proxy.
$M_0^{\rm lit}$	Alternative normalisation, $M_0^{\rm lit} = M_{\rm abs}/M_\star$.
$N_{\rm eff}$	Effective line-weighted yield proxy, $N_{\rm eff} = \dot{N}(A)\, B_{\gamma\gamma}$.

Notation XIX — Astrophysics and Source Parameters

Source and compact-object parameters

$M_{\rm SQM}$ Accumulated SQM mass at $f_{\rm ret} = 1$ (literal benchmark). Context-dependent: the *per-A* mass $M_{\rm SQM}(A) = A\, m_N \dot{N}(A) \tau_{\rm acc}$; the *integrated* mass $M_{\rm SQM}^{\rm tot} = \int A\, m_N \dot{N}(A) \tau_{\rm acc}\, dA$.
For the Baseline benchmark: $M_{\rm SQM}(A = 100) \approx 1.1 \times 10^3 M_\odot$, $M_{\rm SQM}^{\rm tot} \approx 2 \times 10^{16} M_\odot$.

$M_\star$ Source mass. For HESS J1731-347, $M_\star = 0.77\, M_\odot$, mass budget $f_{\rm max} M_\star = 0.1 \times 0.77\, M_\odot = 0.077\, M_\odot$.

$M_{\rm acc}$ Accumulated mass (subject to budget).

$M_{\rm abs}$ Absolute mass limit (upper bound on the accumulated SQM mass, used in the alternative normalisation $M_0^{\rm lit} = M_{\rm abs}/M_\star$; for H.E.S.S.-related limits, $M_{\rm abs} < 10^{-17}\, M_\odot$).

M Compact-object mass.

M_1, M_2 Binary component masses.

$E_{\rm iso}$ Isotropic equivalent energy.

$\Delta t_{\rm obs}$ Observed duration.

$\Delta t_{\rm rest}$ Rest-frame duration.

$\bar{d}_{\rm def}$ Effective deformation parameter entering the EOS posterior; parametrises how strongly the mass–radius posterior is deformed away from a purely hadronic reference EOS.

T_s Surface temperature.

$t_\star$ Stellar age.

Notation XX — Gravitational-Wave and Tidal Observables

Tidal deformability

Λ	Dimensionless tidal deformability; used in the Bayesian likelihood as $p(D_{\rm GW}\|\Lambda, \mathbf{\Theta})$.
$\tilde{\Lambda}$	Effective (mass-weighted) tidal deformability.
$\Lambda_{1.4}$	Tidal deformability of a $1.4\,M_\odot$ star.
$\Lambda(m)$	Tidal deformability as a function of mass.
k_2	Second tidal Love number.

Radius and post-merger observables

$R_{1.4}$	Radius of a $1.4\,M_\odot$ star.
$R_{2.0}$	Radius of a $2.0\,M_\odot$ star.
$R_{\rm eq}$	Equatorial radius of a rotating compact object (e.g. PSR J0740+6620).
$f_{\rm postmerger}$	Dominant post-merger GW frequency.
$M_{\rm TOV}$	Tolman-Oppenheimer-Volkoff maximum mass.
$M_{\rm TOV}^{\rm QS}$	Quark-star maximum mass.
$M_{\rm max}^{\rm EOS}$	Maximum mass of the EOS (distinct from the mass-budget fraction $f_{\rm max}$).

Notation XXI — EOS Parameters and Phase Transition

EOS parameters

a_4	QCD correction parameter (phase-dependent).
c_s^2	Speed of sound squared.
$\Delta\epsilon$	Latent energy-density jump at the transition.
n_{tr}	Transition density.

Notation XXII — Cosmological Density Parameters

Cosmological densities

ρ_c Critical density of the Universe.

$\rho_{\rm DM}$ Dark-matter energy density.

$\Omega_{\rm DM}$ Dark-matter density parameter.

$\Omega_{\rm DM}h^2$ Scaled dark-matter density parameter (≈ 0.12).

$\Omega_S h^2$ Scaled strangelet relic density parameter.

h Reduced Hubble parameter, $h = H_0/(100\ \mathrm{km\,s^{-1}\,Mpc^{-1}})$; enters the scaling ρ_c/h^2 in $\Omega_S h^2$.

$K_{\rm corr}$ Cosmological K-correction, entering the observed line flux as

$$\Phi_\gamma^{\rm obs} \propto \frac{1}{D_L^2(1+z)^{2-\alpha_{\rm src}}};$$

for a narrow line ($\alpha_{\rm src} = 0$) this reduces to $\Phi_\gamma^{\rm obs} \propto 1/[D_L^2(1+z)^2]$.

Not the annihilation kernel $K \equiv B_{\gamma\gamma}\langle\sigma v\rangle$.

Cosmological production

$\eta_{\rm form}$ Formation efficiency of strangelets.

$n_S^{\rm relic}$ Relic strangelet number density.

$n_{S,\rm eq}$ Equilibrium strangelet number density, entering the Boltzmann equation $\dot{n}_S + 3Hn_S = -\langle\sigma v\rangle(n_S^2 - n_{S,\rm eq}^2)$.

$n_{\rm QCD}$ QCD-phase number density, $\sim T_c^3$, with $T_c \equiv T_c^{\rm QCD} \approx 156$ MeV.

T_f Freeze-out temperature.

H Hubble rate.

x_f Freeze-out parameter, $x_f = m_S/T_f$.

g_* Effective relativistic degrees of freedom.

$M_{\rm Pl}$ Planck mass ($M_{\rm Pl} = 1.22 \times 10^{19}$ GeV/c^2).

Notation XXIII — Additional Astrophysical and Neutrino Symbols

Additional astrophysical, neutrino, and likelihood symbols

$F_{\bar{\nu}_e}$	$\bar{\nu}_e$ flux limit ($\mathrm{cm}^{-2}\,\mathrm{s}^{-1}$).
$F_{\nu_\mu}, F_{\bar{\nu}_\mu}$	$\nu_\mu, \bar{\nu}_\mu$ flux limits ($\mathrm{cm}^{-2}\,\mathrm{s}^{-1}$).
v_1, v_2, v_3	Directed, elliptic, triangular flow harmonics of a heavy-ion collision.
dN/dy	Charged-particle rapidity density.
$\langle p_T \rangle$	Mean transverse momentum.

Notation XXIV — Additional Pairing Symbols

Additional QCD & pairing symbols

H_{NJL}	NJL scalar (chiral) coupling. Not to be confused with the Hubble rate H.
G_D	Diquark coupling; the ratio H_{NJL}/G_D is used in the parity-doublet frame.
g_V/G_D	NJL vector-coupling ratio entering the parity-doublet equation of state. Not to be confused with the metric determinant g or with G the gravitational constant, or with the magnetic charge g of a monopole.
k	Wavenumber (relative momentum) in the s-wave unitarity bound, $\sigma_{\max} = 4\pi/k^2$. The benchmark normalisation π/m_S^2 used in the annihilation kernel is *inspired by*, but not derived from, this bound.
ϵ_k	Free-quasiparticle dispersion in state k, $\epsilon_k = \sqrt{k^2 + m_q^2}$.
E_k	Bogoliubov quasiparticle energy in state k, $E_k = \sqrt{\xi_k^2 + \Delta_k^2}$.
ξ_k	Normal-state energy, $\xi_k = \epsilon_k - \mu$.
$j_1(x)$	Spherical Bessel function, $j_1(x) = (\sin x - x\cos x)/x^2$.

Notation XXV — Global Symbols (I)

These symbols appear in multiple frames; they are collected here for convenience.

$\beta_{\rm frag}$	Fragmentation power-law index, $\beta_{\rm frag} \sim 1$–2.
$q_{\rm bin}$	Binary mass ratio, $q_{\rm bin} = M_1/M_2 \leq 1$.
$\mathcal{H}(x)$	Heaviside step function, $\mathcal{H}(x) = 0$ for $x < 0$, $\mathcal{H}(x) = 1$ for $x \geq 0$.
$f_{\rm max}$	Dimensionless maximum mass-fraction in the mass budget, $f_{\rm max} = 0.1$.
$S_{\rm sup}$	Suppression ratio, $S_{\rm sup} = P_{\rm brem}/P_{\rm fusion}$.
$P_{\rm brem}$	Bremsstrahlung power.
$P_{\rm fusion}$	Fusion power.

Notation XXVI — Global Symbols (II)

Overloaded symbols: same glyph, different objects

- Λ: QCD scale Λ_{QCD} vs. tidal deformability Λ.
- Δ: generic pairing gap vs. latent energy jump $\Delta\epsilon$.
- $\mathcal{L}$: likelihood vs. weak Lagrangian $\mathcal{L}_W$.
- $\mathcal{M}$: model class vs. mass M.
- $\mathcal{B}$: Bayes factor vs. bag constant B_{bag}.
- ℓ: neutrino current ℓ^μ vs. charged lepton ℓ^- vs. lepton tensor $\ell^{\mu\nu}$.
- σ: strangelet–nucleon cross-section σ_S vs. reference cross-section σ_0 vs. surface tension σ_{ST} vs. maximum s-wave cross-section σ_{max}.
- g: magnetic charge vs. g_V/G_D: NJL vector-coupling ratio vs. metric determinant g.
- δ: source declination δ_{dec} vs. quark chemical-potential asymmetry $\delta\mu = (\mu_d - \mu_u)/2$ vs. activation barrier δE vs. two-photon deviation angle δ vs. Dirac delta $\delta(x)$.
- $\mathcal{S}$: detection significance $\mathcal{S}_{\mathrm{det}}$ vs. survival factors $S_{\mathrm{form}}, S_{\mathrm{esc}}, S_{\mathrm{surv}}$.
- $\mathcal{N}$: BdG matrix $\mathcal{N}_k$ vs. quark/event numbers $N_i, N_{\mathrm{evt}}, \ldots$.
- $\mathcal{H}$: Heaviside $\mathcal{H}(x)$ vs. Hubble H, H_{NJL}.
- $\mathcal{E}$: kinetic-equation matrix vs. energy density ϵ.
- $\mathcal{R}$: rigidity vs. radius R.
- T_c: QCD critical temperature $T_c \equiv T_c^{\mathrm{QCD}}$ vs. BCS critical temperature T_c^{pair}.
- L_0: symmetry-energy slope parameter vs. $\mathcal{L}_0$: null-hypothesis likelihood. The calligraphic font distinguishes them, but they are easily confused in OCR.
- T: temperature T vs. live time T_{live} vs. surface temperature T_s vs. freeze-out temperature T_f vs. critical temperatures T_c^{QCD}, T_c^{pair}.

Notation XXVII — Global Symbols (III)

Overloaded symbols: same glyph, different objects (cont.)

- A: baryon number A vs. axial-vector current A^{μ} vs. effective area A_{eff} vs. peak A_{peak} vs. fragmentation scale A_{frag} vs. escape threshold A_{esc}.
- B: bag constant B_{bag} vs. branching fraction $B_{\gamma\gamma}$ vs. Bayes factor $\mathcal{B}$.
- F: form factor $F(Q^2)$ vs. direct flux F_{dir} vs. neutrino flux limits $F_{\bar{\nu}_e}, F_{\nu_\mu}, F_{\bar{\nu}_\mu}$.
- K: annihilation kernel $K \equiv B_{\gamma\gamma}\langle\sigma v\rangle$ vs. cosmological K-correction K_{corr} vs. Boltzmann constant k_B vs. wavenumber k vs. second tidal Love number k_2.
- v: physical velocity v vs. flow harmonics v_1, v_2, v_3.
- V: volume V vs. vector current V^{μ} vs. volume factors V_{core}, V_{source}.
- Y: charge fraction Y_Q vs. lepton fractions Y_L, Y_{L_e} vs. rapidity density dN/dy.
- z, Z: net electric charge Z vs. redshift z vs. valence charge Z_V.
- θ: scattering angle ϑ vs. Weinberg angle θ_W vs. polar angle in spherical coordinates.
- Q: net electric charge Z vs. 4-momentum transfer Q^{μ} vs. charge fraction Y_Q vs. binary mass ratio q_{bin} vs. quark field q.
- P: pressure P vs. Bremsstrahlung power P_{brem} vs. fusion power P_{fusion}.
- f: mass-budget fraction f_{max} vs. retention factor f_{ret} vs. angular distribution $f(\vartheta)$ vs. post-merger frequency $f_{\mathrm{postmerger}}$.

Notation XXVIII — Global Symbols (IV)

Additional overloaded symbols (cont.)

- π: mathematical constant π vs. prior density $\pi(\boldsymbol{\Theta}|\mathcal{M})$.
- ϵ: scalar energy density ϵ vs. energy per baryon ϵ_B vs. free-quark dispersion ϵ_p vs. free-quasiparticle dispersion ϵ_k vs. latent energy jump $\Delta\epsilon$ vs. kinetic-equation matrix $\mathcal{E}$ (distinct glyph).
- E-family: particle energy E; Bogoliubov quasiparticle energy E_p or E_k; total strangelet energy E_A; Coulomb energy E_{coul}; activation energy E_{act}; isotropic-equivalent energy E_{iso}; line energy E_γ; neutrino energy E_ν. Distinguished by the subscripts, not by different glyphs.
- λ: wavelength / mean free path λ_ν vs. λ_{ISM}: ISM mean free path vs. λ_{Debye}: Debye length.
- n_H: interstellar hydrogen *number* density vs. N_H: hydrogen *column* density (cm^{-2}). The subscript case and the H are easily confused in OCR.
- τ: accumulation time τ_{acc} vs. formation/escape/survival/annihilation timescales $\tau_{\mathrm{form}}, \tau_{\mathrm{esc}}, \tau_{\mathrm{surv}}, \tau_{\mathrm{ann}}$.
- g: metric determinant / magnetic monopole charge / NJL coupling ratio g_V/G_D vs. $g_{\mathrm{geom}}, g_{\mathrm{supp}}$: production-law factors (subscripts distinguish them).
- N: quark/event numbers N_i, N_{evt} vs. N_e: bound electrons in the cloud vs. N_H: hydrogen column density (cm^{-2}) vs. N_{acc}: accumulated strangelet number.

Acronyms (I)

Acronyms used in this talk

χEFT	Chiral effective field theory.
pQCD	Perturbative QCD.
RGOPT	Renormalisation group optimised perturbation theory.
NJL	Nambu–Jona-Lasinio model.
MIT bag	Massachusetts Institute of Technology bag model.
CFL	Colour-flavour-locked phase.
2SC	Two-flavour colour-superconducting phase.
BCS	Bardeen–Cooper–Schrieffer (theory of Cooper pairing).
ISM	Interstellar Medium.
CTA / CTAO	Cherenkov Telescope Array / Cherenkov Telescope Array Observatory.

Acronyms used in this talk (cont.)

SNR	Supernova remnant.
EOS	Equation of state.
GW	Gravitational wave.
BNS	Binary neutron star.
GRB	Gamma-ray burst.
VHE	Very high energy.
IRF	Instrument response function.
CL	Confidence level.
SQS	Strange quark star.
SQM	Strange quark matter.
Urca	Neutrino cooling processes (direct/modified Urca) in dense nuclear or quark matter.

Acronyms (II)

Acronyms used in this talk (cont.)

FRB	Fast Radio Burst.
GRB	Gamma-Ray Burst.
GW	Gravitational Wave.
AT	Astronomical Transient.
PSR	Pulsar / Pulsating Radio Source.
Her	Hercules Constellation.
AXP	Anomalous X-ray Pulsar.
4U	Fourth Uhuru catalogue.
XTE	Rossi X-ray Timing Explorer.
Cyg	Cygnus Constellation.
GRO	Compton Gamma Ray Observatory.
SGR	Soft Gamma Repeater.
NS	Neutron Star.

Acronyms used in this talk (cont.)

RX	ROSAT X-ray source.
Cen	Centaurus Constellation.
EXO	EXOSAT X-ray source.
LMC	Large Magellanic Cloud.
SMC	Small Magellanic Cloud.
LSPM	Lépine–Shara Proper Motion catalogue.
LP	Luyten Palomar survey.
BD	Bonner Durchmusterung.
WD	White Dwarf.
SDSS	Sloan Digital Sky Survey.
2MASS	Two Micron All-Sky Survey.
GP Com	Coma Berenices.

Units and Practical Conversions (I)

Natural units used in this talk

$$\hbar = c = k_B = 1.$$

Quantity	Conversion	Value
$\hbar c$	1 GeV·fm	0.197
1 GeV^{-2}	$\mathrm{cm}^3\,\mathrm{s}^{-1}$	1.17×10^{-17}
1 $\mathrm{cm}^3\,\mathrm{s}^{-1}$	GeV^{-2}	8.55×10^{16}
1 fm	cm	10^{-13}
1 MeV	eV	10^{6}
1 GeV	eV	10^{9}

Astrophysical conversions

Quantity	Conversion	Value
1 $M_\odot$	g	1.989×10^{33}
1 $M_\odot c^2$	erg	1.79×10^{54}
1 kpc	cm	3.086×10^{21}
1 Mpc	cm	3.086×10^{24}
1 yr	s	3.156×10^{7}
1 Gpc	cm	3.086×10^{27}

Worked example: converting $\langle \sigma v \rangle$

A benchmark value $\langle \sigma v \rangle = 10^{-25}\ \mathrm{cm}^3\,\mathrm{s}^{-1}$ becomes

$$10^{-25} \times 8.55 \times 10^{16} \;\approx\; 8.55 \times 10^{-9}\ \mathrm{GeV}^{-2}.$$

Units and Practical Conversions (II)

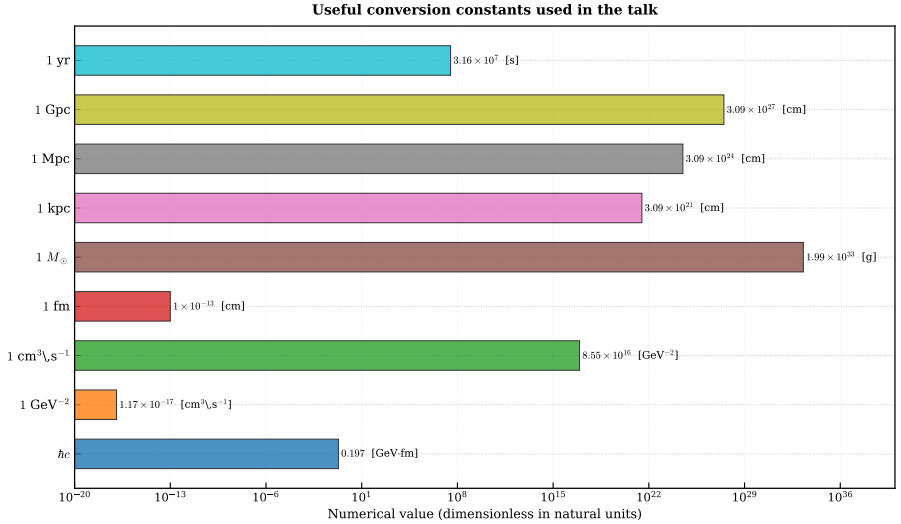

Natural units: $\hbar = c = k_B = 1$. Values shown with three significant figures.

What Is New in This Framework

Compared with earlier strangelet searches

Previous work has typically focused on one of the following:

- production rates from first-principles fragmentation models,
- propagation of strangelets in the interstellar medium,
- direct detection limits in cosmic rays, or
- gamma-ray line searches in a fixed source.

This work links all four in a single end-to-end phenomenological framework.

The four novel elements

1. A benchmark production law that reconciles geometric growth with exponential suppression and has a unique maximum at A_{peak}.
2. Explicit retention and mass-budget conditions that any physical strangelet population must satisfy.
3. Application to three complementary source classes (steady, merger-driven, burst-driven).
4. A compilation of direct-search constraints (PAMELA, MACRO, SLIM, ANTARES, IceCube) shown as distinct, experiment-specific regimes.

Honest framing

The production spectrum, annihilation kernel, and line branching fraction are treated as *benchmark inputs*, not QCD-derived quantities. The plots are *benchmark sensitivity maps*, not 95% CL exclusions.

Motivation: Why Strange Quark Matter?

The Bodmer–Witten–Terazawa hypothesis

Ordinary hadronic matter (nuclei, neutron stars) may *not* be the true ground state of QCD.
If strange quark matter (SQM) — a phase with roughly equal numbers of up, down, and strange quarks — has a lower energy per baryon, then:

- neutron stars could convert to strange quark stars (SQSs);
- stable clusters called strangelets could be produced in dense QCD phase transitions;
- the released energy ($\sim 10^{53}$ erg) would be comparable to a supernova.

Observational consequences

- Monochromatic γ-ray lines from strangelet–anti-strangelet annihilation are a direct signature, *if* an appreciable $\gamma\gamma$ branching fraction is realised.
- Anomalous compact objects such as HESS J1731-347 may be SQSs.
- Direct detection of macroscopic SQM objects (nuclearites, Q-balls) would be complementary.

No strangelets have yet been detected. Multimessenger observations with next-generation instruments may change this.

What Is a Strangelet?

A strangelet is a hypothetical stable cluster of strange quark matter (SQM), a phase consisting of roughly equal numbers of up, down, and strange quarks.

- Mass number A (also called baryon number) $\rightarrow$ one third of the total quark number.
- Charge number $Z \rightarrow$ net electric charge in units of the elementary charge e.
- Predicted mass-to-charge ratios: the MIT-bag band 30–60 GeV/c^2 corresponds to $A \sim 10^3$ in the CFL scaling used here.

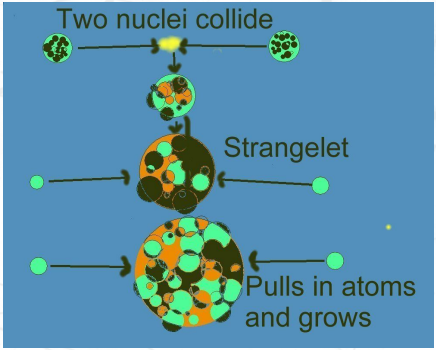

Why A and Z matter for the signal

- A controls the annihilation line energy $E_\gamma = m_S \approx 0.94\,A$ GeV.
- Z/A controls the rigidity of the strangelet in cosmic rays and hence its direct-detection signature.
- A strangelet of $A = 10^6$ annihilates to a ~ 940 TeV photon — visible to LHAASO, but above CTA's nominal range and far above Fermi-LAT's.

Stable Macroscopic Quark Matter

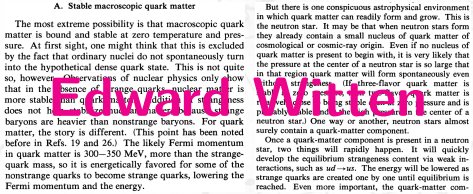

A. Stable macroscopic quark matter

The most extreme possibility is that macroscopic quark matter is bound and stable at zero temperature and pressure. At first sight, one might think that this is excluded by the fact that ordinary nuclei do not spontaneously turn into the hypothetical dense quark state. This is not quite so, however. Observations of nuclear physics only show that in the absence of strange quarks, nuclear matter is more stable than quark matter. Addition of strangeness does not help much, as multiple strange baryons are heavier than nonstrange baryons. For quark matter, the story is different. (This point has been noted before in Refs. 19 and 26.) The likely Fermi momentum in quark matter is 300–350 MeV, more than the strange-quark mass, so it is energetically favored for some of the nonstrange quarks to become strange quarks, lowering the Fermi momentum and the energy.

But there is one conspicuous astrophysical environment in which quark matter can readily form and grow. This is the neutron star. It may be that when neutron stars form they already contain a small nucleus of quark matter of cosmological or cosmic-ray origin. Even if no nucleus of quark matter is present to begin with, it is very likely that the pressure at the center of a neutron star is so large that in that region quark matter will form spontaneously even with strange masses. If three-flavor quark matter is stable at zero pressure, then three-flavor quark matter is probably the ground state of matter at the center of a neutron star.) One way or another, neutron stars almost surely contain a quark-matter component.

Once a quark-matter component is present in a neutron star, two things will rapidly happen. It will quickly develop the equilibrium strangeness content via weak interactions, such as $sd \to uu$. The energy will be lowered as strange quarks are created one by one until equilibrium is reached. Even more important, the quark-matter com-

Strange matter, stable in bulk, may also come in small chunks for which surface effects are important and which are too small to support an electron gas within. We call these chunks of strange matter "strangelets." These systems with baryon numbers lower than (very roughly) 10^7 are studied in Sec. III. However, we leave $A \lesssim 10^2$ to Sec. IV. We discuss the origin and effect of a surface tension and find that strange matter stable in bulk may be unbound for small enough baryon number. We also discuss the charge that develops on strangelets and finally how these charged systems neutralize themselves like ordinary nuclei, by accumulating electron (or perhaps positron) clouds.

Edward Witten

Edward Farhi

and

R. L. Jaffe

Stable bulk quark matter

- Macroscopic quark matter may be bound and stable at zero temperature and pressure.
- Ordinary nuclei do not spontaneously convert because nonstrange nuclear matter is more stable than quark matter when strange baryons are heavier.
- In quark matter, the Fermi momentum is 300–350 MeV, larger than m_s. It is therefore energetically favoured for some nonstrange quarks to become strange, lowering the Fermi momentum and the energy.

Neutron stars as quark-matter factories

- A neutron star may already contain a small quark-matter seed of cosmological or cosmic-ray origin.
- Even without a seed, the central pressure is likely large enough to form quark matter spontaneously.
- Once present, weak interactions develop the equilibrium strangeness content, lowering the energy until equilibrium is reached.

From bulk matter to strangelets

Stable bulk strange matter can also appear in small chunks where surface effects matter and which are too small to support an electron gas. These are strangelets, with baryon number roughly below 10^7. They acquire charge and neutralise by accumulating electron (or positron) clouds, like ordinary nuclei.

Why Strangelets Can Exist: Finite-Size Stability (I)

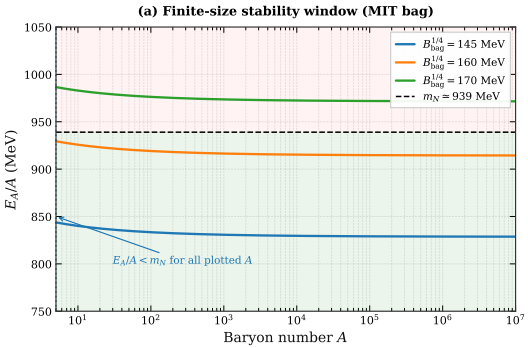

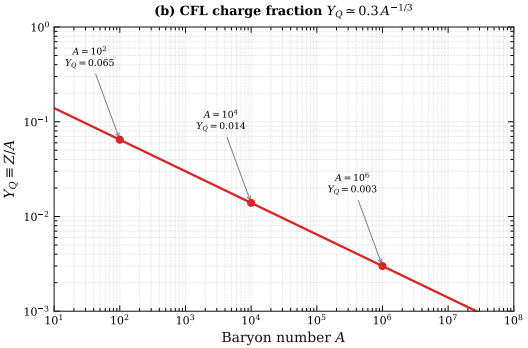

Computation

The bulk term is evaluated from the MIT bag free energy for massless quarks: at the strange-star surface ($P = 0$), the baryon number density is $n_B = \mu_q^3/\pi^2$ with $\mu_q^4 = 4\pi^2 B/3$ ($N_c = N_f = 3$). Surface and curvature coefficients $a_{\rm surf} = 20$ MeV, $a_{\rm curv} = 10$ MeV. Coulomb correction $E_{\rm coul} = \frac{3}{5}\alpha Z_V^2/R_{\rm ch}$ uses the CFL charge scaling $Z_V = 0.3\,A^{2/3}$.

Why Strangelets Can Exist: Finite-Size Stability (II)

MIT-bag energy of a finite strangelet

$$E_A = \sum_i (\Omega_i + N_i \mu_i) + B_{\rm bag} V + E_{\rm coul} + a_{\rm surf} A^{2/3} + a_{\rm curv} A^{1/3},$$

with $E_{\rm coul} = \frac{3}{5}\,\alpha Z_V^2 / R_{\rm ch}$.

Stability criterion

A strangelet is stable if

$$\frac{E_A}{A} < m_N \simeq 939\ \mathrm{MeV}.$$

The surface ($\propto A^{2/3}$) and curvature ($\propto A^{1/3}$) penalties dominate at small A, so a minimum stable baryon number $A_{\rm min} \sim 50$–200 exists.

What the plot shows

E_A/A vs. A for three values of $B_{\rm bag}^{1/4}$ (145, 160, 170 MeV) at fixed $a_{\rm surf}$, $a_{\rm curv}$. The horizontal dashed line is m_N. The window $A \gtrsim A_{\rm min}$ where $E_A/A < m_N$ is the finite-size stability window. For $B_{\rm bag}^{1/4} \gtrsim 170$ MeV the window closes: no stable strangelets exist.

Anatomy of the Production Law (I)

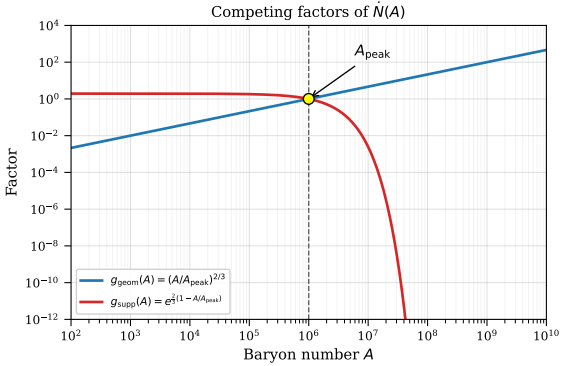

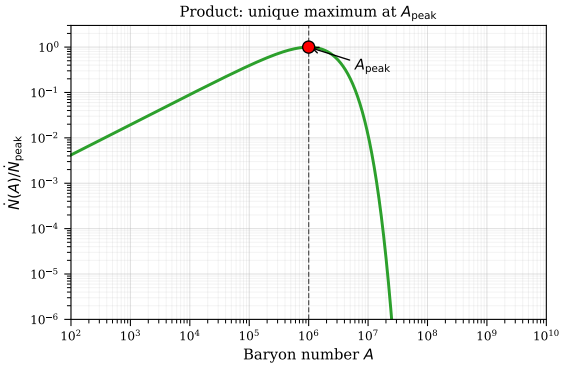

Left: competing factors $g_{\mathrm{geom}}(A) = (A/A_{\mathrm{peak}})^{2/3}$ (blue, geometric growth) and $g_{\mathrm{supp}}(A) = \exp[\frac{2}{3}(1 - A/A_{\mathrm{peak}})]$ (red, multifragmentation/coalescence suppression).
Right: their product, normalised to its peak, showing a unique maximum at $A = A_{\mathrm{peak}}$.
This is the benchmark production law $\dot{N}(A) = \dot{N}_{\mathrm{peak}}(A/A_{\mathrm{peak}})^{2/3} \exp[\frac{2}{3}(1 - A/A_{\mathrm{peak}})]$, with $A_{\mathrm{peak}} = 10^6$ in the displayed case. The maximum follows from $\mathrm{d} \ln \dot{N}/\mathrm{d}A = 0$, i.e. $A = A_{\mathrm{peak}}$.

Anatomy of the Production Law (II)

Two competing factors

$$\dot{N}(A) \;=\; \dot{N}_{\mathrm{peak}} \underbrace{\left(\frac{A}{A_{\mathrm{peak}}}\right)^{2/3}}_{g_{\mathrm{geom}}(A)} \underbrace{\exp\left[\frac{2}{3}\left(1-\frac{A}{A_{\mathrm{peak}}}\right)\right]}_{g_{\mathrm{supp}}(A)}.$$

Interpretation

- $g_{\mathrm{geom}}(A)$: geometric growth. A strangelet of radius $R_S \propto A^{1/3}$ has cross-sectional area $\propto A^{2/3}$; more surface means more coalescence.
- $g_{\mathrm{supp}}(A)$: combined multifragmentation and coalescence suppression. Falls exponentially for $A > A_{\mathrm{peak}}$.

Why the maximum is unique

$\mathrm{d}\ln\dot{N}/\mathrm{d}A = 0$ gives $\frac{2}{3A} - \frac{2}{3A_{\mathrm{peak}}} = 0$, i.e. a single maximum at $A = A_{\mathrm{peak}}$.

The curvature at the peak is $\mathcal{O}(1/A_{\mathrm{peak}}^2)$. A factor-of-two change in A_{peak} shifts $\dot{N}_{\mathrm{peak}}$ by several orders of magnitude through g_{supp}.

The Original Stability Arguments

The Bodmer–Witten–Terazawa hypothesis proposes that SQM is the true ground state of quantum chromodynamics (QCD) at high baryon density. Foundational and recent references:

- A. R. Bodmer, *Collapsed nuclei*, Phys. Rev. D **4**, 1601 (1971).
- E. Witten, *Cosmic separation of phases*, Phys. Rev. D **30**, 272 (1984).
- E. Farhi and R. L. Jaffe, *Strange matter*, Phys. Rev. D **30**, 2379 (1984).
- C. Alcock and E. Farhi, *Evaporation of strange matter in the early universe*, Phys. Rev. D **32**, 1273 (1985).
- J. Madsen, H. Heiselberg and K. Riisager, *Does strange matter evaporate in the early universe?*, Phys. Rev. D **34**, 2947 (1986).
- F. Weber, *Strange quark matter and compact stars*, Prog. Part. Nucl. Phys. **54**, 193 (2005).
- H.-S. You et al., *Strangelets at finite temperature: Nucleon emission rates, interface, and shell effects*, Phys. Rev. D **109**, 034003 (2024).
- F. Di Clemente, A. Drago and G. Pagliara, *Strange Dwarfs: A review on the (in)stability*, Universe **10**, 322 (2024).
- F. Di Clemente et al., *Strange quark matter as dark matter: 40 yr later, a reappraisal*, MNRAS **537**, 1056 (2025).
- G. Cao, *Extended Nambu–Jona-Lasinio model for quark and nuclear matters*, Phys. Lett. B **860**, 139140 (2025).
- F. Köpp et al., *Repulsive vector couplings and massive strange stars*, Astron. Nachr. **346**, e20240119 (2025).

Low-A, Negatively Charged Strangelets as a Danger

Hypothetically, a negatively charged strangelet could catalyse the conversion of ordinary matter into SQM. Foundational and recent references:

- C. Greiner, P. Koch and H. Stöcker, *Separation of strangeness from anti-strangeness in the phase transition from quark to hadron matter: Possible formation of strange quark matter in heavy-ion collisions*, Phys. Rev. Lett. **58**, 1825 (1987).
- A. Kent, *A critical look at catastrophe risk assessments*, Risk Anal. **24**, 157 (2004).
- R. L. Jaffe et al., *Review of speculative "disaster scenarios" at RHIC*, Rev. Mod. Phys. **72**, 1125 (2000).
- J. Madsen, *Intermediate mass strangelets are positively charged*, Phys. Rev. Lett. **85**, 4687 (2000).
- J. Madsen, *Strangelet propagation and cosmic ray flux*, Phys. Rev. D **71**, 014026 (2005).
- J. Madsen, *Universal charge-radius relation for subatomic and astrophysical compact objects*, Phys. Rev. Lett. **100**, 151102 (2008).
- S. Biswas et al., *Multifragmentation model for astrophysical strangelets*, Phys. Lett. B **715**, 30 (2012).
- M. Guerrini et al., *Role of thermal fluctuations in nucleation of three-flavor quark matter*, Universe **11**, 258 (2025).
- C. R. Das, *Finding strangelets in cosmic rays from HESS J1731-347*, Phys. Atom. Nuclei **88**, 1142 (2025); arXiv:2507.12817.

Existing Experimental Constraints

If stable and negatively charged strangelets existed, they would be observable in cosmic rays and at colliders.
None have been discovered. Key references:

- A. Chodos et al., *A new extended model of hadrons*, Phys. Rev. D **9**, 3471 (1974).
- S. Ahlen et al., *Search for nuclearites using the MACRO detector*, Phys. Rev. Lett. **69**, 1860 (1992).
- K. Borer et al., *Strangelet search in S-W collisions at 200A GeV/c*, Phys. Rev. Lett. **72**, 1415 (1994).
- G. Appelquist et al., *Strangelet Search in Pb-Pb Interactions at 158 GeV/c per Nucleon*, Phys. Rev. Lett. **76**, 3907 (1996).
- A. L. S. Angelis and A. D. Panagiotou, *CASTOR: A dedicated detector for the detection of centauros and strangelets at the LHC*, J. Phys. G: Nucl. Part. Phys. **23**, 2069 (1997).
- A. Kent, *A critical look at catastrophe risk assessments*, Risk Anal. **24**, 157 (2004).
- J. Madsen, *Colour–flavour locked strangelets and their detection*, J. Phys. G: Nucl. Part. Phys. **28**, 1737 (2002).
- A. H. Tang (STAR Collaboration), *Strangelet search at RHIC*, J. Phys. G: Nucl. Part. Phys. **31**, S1187 (2005).
- J. Madsen, *Strangelets, nuclearites, Q-balls — a brief overview*, arXiv:astro-ph/0612740.
- S. Cecchini et al., *Results of the search for strange quark matter and Q-balls with the SLIM experiment*, Eur. Phys. J. C **57**, 525 (2008).
- J. Ellis et al., *Review of the safety of LHC collisions*, J. Phys. G: Nucl. Part. Phys. **35**, 115004 (2008).
- O. Adriani et al. (PAMELA Collaboration), Phys. Rev. Lett. **115**, 111101 (2015).
- S. Kasuya, M. Kawasaki and T. T. Yanagida, *IceCube potential for detecting Q-ball dark matter in gauge mediation*, Prog. Theor. Exp. Phys. **2015**(5), 053B02 (2015).
- A. Albert et al. (The ANTARES Collaboration), JCAP **2023**, 012 (2023).
- M. Bianchi et al., *Search for strange quark matter and nuclearites on board the International Space Station (SQM-ISS): A future detector to search for massive, non-relativistic objects in space*, Sensors **24**, 5090 (2024).

Instruments Referenced in This Talk

Table: Ground-based and space-based instruments used to constrain strangelet signatures.

Acronym	Full name	Role
H.E.S.S.	High Energy Stereoscopic System	Ground-based Cherenkov array in Namibia; observed HESS J1731-347.
Fermi-LAT	Fermi Large Area Telescope	Space-based γ-ray telescope; GeV constraints.
Fermi-GBM	Fermi Gamma-ray Burst Monitor	Space-based all-sky monitor of GRBs.
MAGIC-II	Major Atmospheric Gamma Imaging Cherenkov telescopes	Ground-based Cherenkov array on La Palma.
VERITAS	Very Energetic Radiation Imaging Telescope Array System	Ground-based Cherenkov array in Arizona.
CTA / CTAO	Cherenkov Telescope Array / Observatory	Next-generation Cherenkov array; tenfold improvement over H.E.S.S.
LHAASO	Large High Altitude Air Shower Observatory	Ground-based EAS array in Tibet.

Summary of Key Constraints

1. **Experimental limits.**
   - No strangelets detected in accelerators (NA52, fixed-target) or cosmic rays.
   - PAMELA covers $A \sim 10$–1.2×10^5.
   - MACRO's nuclearite search covers the mass range $10^{-10} < M_{\mathrm{nuc}} < 0.1$ g, which corresponds to $A \sim 6 \times 10^{13}$–6×10^{22} (i.e. $A \sim 10^{14}$–10^{23} for $m_N \approx 0.94$ GeV$/c^2$).
2. **Astronomical limits.**
   - No evidence of strange matter in neutron stars. Strangelet–anti-strangelet annihilation may produce γ rays.
   - No confirmed strangelet impact events on Earth or Solar System bodies.
3. **Theoretical stability.**
   - Minimum stable baryon number $A_{\mathrm{min}} \sim 50$–200, depending on $B_{\mathrm{bag}}^{1/4}$ and n_A.
   - NJL model: shallow, metastable bound states with $\sim 40\%$ strange-quark content for $G_V/G_S \approx 0.5$–1.0.
   - Both MIT bag and NJL predict $m_S/|Z| \sim 30$–60 GeV$/c^2$ for $A \sim 10^3$.

Strange Quark Matter (SQM) in Cosmic Rays

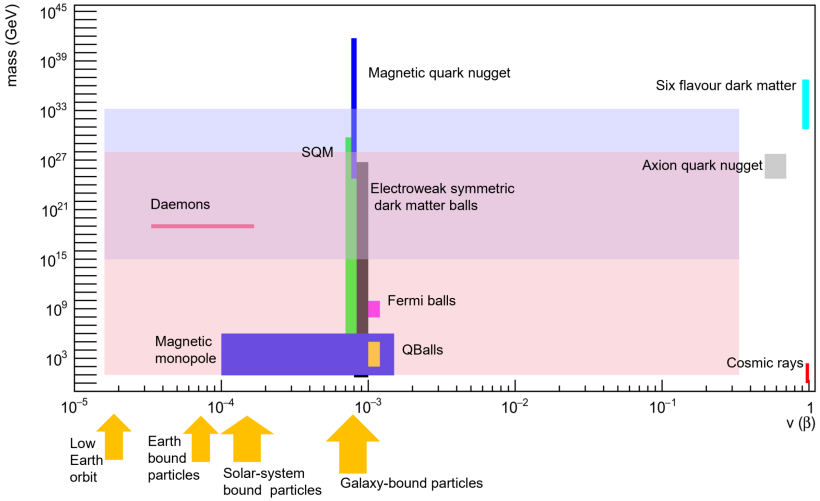

Velocity–mass parameter space for hypothetical slow-moving, heavy particles. The horizontal axis is velocity $\beta_{\mathrm{vel}} = v/c$; the vertical axis is mass in GeV/c^2. Shaded regions indicate representative candidates: magnetic monopoles, Q-balls, nuclearites (SQM nuggets), and other exotic objects. The arrows at the bottom indicate typical velocities for particles bound to different gravitational systems (low Earth orbit, Earth, Solar System, Galaxy). "Slow-moving" means non-relativistic or sub-relativistic; "heavy" means masses far exceeding nuclear masses. This plot motivates direct searches for macroscopic SQM composites such as nuclearites and Q-balls, which would traverse detectors as slow, highly ionising tracks.

Current Upper Bounds on SQM in Cosmic Rays

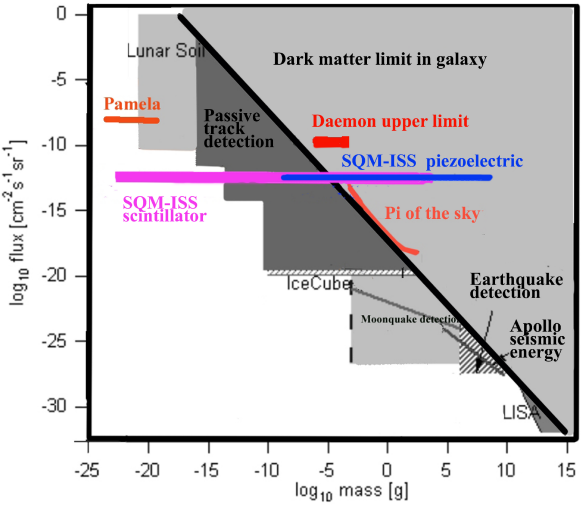

Current upper bounds on the flux of massive SQM candidates (nuclearites, Q-balls, and strangelets) as a function of presumed mass. The different curves correspond to distinct experimental techniques and energy/mass regimes: nuclear track detectors (e.g. MACRO, SLIM), neutrino telescopes (e.g. ANTARES, IceCube), and cosmic-ray spectrometers (e.g. PAMELA). The horizontal axis spans microscopic to macroscopic masses; the vertical axis is the flux upper limit. No single experiment covers the entire mass range, and the limits are model-dependent: they assume a particular velocity distribution, charge state, and interaction cross-section. The plot is therefore a benchmark compilation, not a model-independent exclusion.

Strangelet Formation Mechanisms

Several mechanisms can produce strangelets during the 2SC $\rightarrow$ CFL phase transition:

- Diquark condensates (Cooper pairs of quarks) coagulate and fuse when strange quarks become involved in pairing.
- Fragmentation related to altering the Fermi surfaces during the transition.
- Surface emission of quark clusters from neutron-star cores under appropriate pressure and density.

Strangelet–anti-strangelet annihilation ($S\bar{S} \rightarrow$ hadrons $\rightarrow \gamma\gamma$) could result in two monochromatic γ rays.

Detecting γ-ray fingerprints from HESS J1731-347 (neutron star), GW170817 (merger), or GRB 250702B would prove the existence of strangelets.

The Greiner Mechanism — Strangeness Separation

The problem

In a hot quark-gluon plasma, strange quarks and anti-strange quarks are produced in pairs:

$$\text{gluon} + \text{gluon} \to s + \bar{s}, \qquad q + \bar{q} \to s + \bar{s}.$$

If the system cools adiabatically, the s and $\bar{s}$ would normally annihilate back. How do strangelets survive?

The Greiner mechanism (1987)

- During the quark-hadron phase transition, strange quarks are trapped in the quark phase while anti-strange quarks are emitted into the hadron phase.
- This creates a strangeness excess in the quark phase.
- The quark phase cools into strange quark matter droplets (strangelets).

Why this matters for the framework

- This is the microphysical origin of the strangeness-enrichment process invoked in the production-rate ansatz.
- It provides a natural mechanism for producing both strangelets *and* anti-strangelets (from the $\bar{s}$ excess in the hadron phase).
- The efficiency of the mechanism depends on the phase-transition dynamics and the cooling rate.

Open question

A first-principles calculation of the strangeness separation efficiency in astrophysical environments (neutron stars, mergers, GRBs) is still lacking. This is a key uncertainty in the framework.

Strange Stars

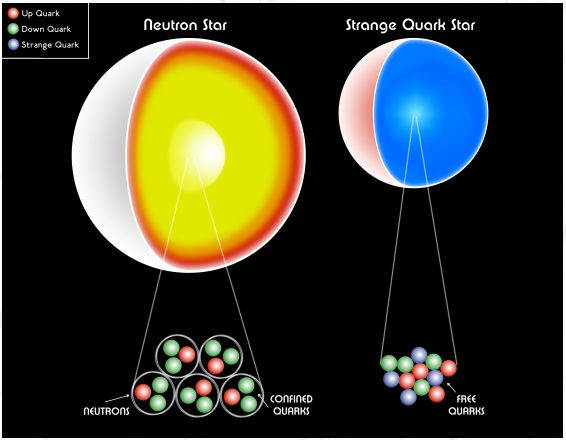

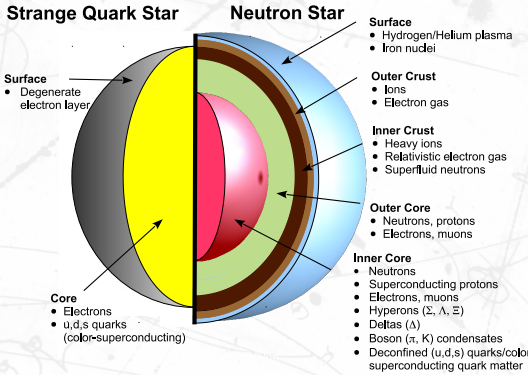

Left: Schematic comparison of a conventional neutron star and a strange quark star. A neutron star has a hadronic crust and a neutron-rich interior, while a strange quark star is composed almost entirely of strange quark matter (SQM).
Right: Cross-sectional view of a strange quark star (left half) and a neutron star (right half). The strange quark star consists of a degenerate electron layer and a core of u, d, s quarks in a colour-superconducting state. The neutron star shows the standard onion-like structure: outer crust (ions, electron gas), inner crust (heavy ions, superfluid neutrons), and outer/inner core (neutrons, protons, electrons, muons, hyperons, and possibly deconfined quarks).

The transition from hadronic matter to SQM is the central hypothesis motivating strangelet searches.

Strange Star & Quark Star Candidate Audit (I)

Candidates with modern (post-2015) multimessenger data — gravitational-wave events and the strongest electromagnetic anomaly.

Object	Key observable	Physics behind candidacy	Status
HESS J1731-347 (XMMU J173203.3-344518)	$M = 0.77^{+0.20}_{-0.17}\ M_\odot$, $R = 10.4^{+0.86}_{-0.78}$ km	Low M lies below the minimum for iron-core-collapse NSs ($\sim 1.17\ M_\odot$). Self-bound matter follows $M \propto R^3$ at low mass, naturally allowing a compact low-mass branch. CFL pairing with small $\Delta_{\rm CFL}$ reproduces slow cooling.	Strongest EM candidate; not confirmed.
GW190814 secondary	$M_2 = 2.585^{+0.09}_{-0.08}\ M_\odot$, no R measured	Mass lies in the mass gap. Requires $M_{\rm TOV} \gtrsim 2.6\ M_\odot$ if NS. udQM reaches $M_{\rm TOV} \simeq 2.87\ M_\odot$; CFL requires large $\Delta_{\rm CFL} \gtrsim 200$ MeV and $B_{\rm eff}^{1/4} \simeq 170$–$192$ MeV.	Strong GW proposal; low-mass BH also viable.
GW170817 / AT2017gfo	$M_1 \simeq 1.46\ M_\odot$, $M_2 \simeq 1.27\ M_\odot$, $R_{1.4} = 12.2 \pm 0.5$ km, $120 \lesssim \tilde{\Lambda} \lesssim 1110$	Kilonova light curve depends on ejecta mass, Y_e, velocity, opacity, which depend indirectly on EOS and tidal interaction. Self-bound strange stars change Λ, crust mass, contact/merger dynamics, ejecta composition, remnant stability, and post-merger collapse time. Quark-star interpretation favors $M_{\rm TOV} \lesssim 2.35\ M_\odot$.	Constrains SQM; does *not* exclude it.
GW190425	$M_{\rm total} \simeq 2.4$–$2.7\ M_\odot$	Second BNS merger. Possible long-lived strange quark star remnant proposed. Tidal constraints weaker than GW170817 due to lower SNR.	Speculative; EOS constraint.
GW230529	$M_{\rm heavier} = 2.5$–$4.5\ M_\odot$, paired with NS	First GW detection of a mass-gap object in a binary with a NS. Requires $M_{\rm TOV} \gtrsim 2.5\ M_\odot$ if quark star.	Emerging candidate.

Strange Star & Quark Star Candidate Audit (II)

NICER mass–radius constraints and high-mass pulsars. These objects primarily constrain the dense-matter EOS rather than positively identifying quark matter.

Object	Key observable	Physics behind candidacy	Status
PSR J0740+6620	$M = 2.073 \pm 0.069\, M_\odot$, $R = 12.49^{+1.28}_{-0.88}$ km	Requires $M_{\rm TOV} \gtrsim 2\, M_\odot$ with moderate R. Minimal MIT bag fails; vMIT with $G_V \simeq 0.3$–1.0 fm^2 or CFL with large $\Delta_{\rm CFL}$ can satisfy both.	EOS constraint; not a positive identification.
PSR J0030+0451	$M = 1.43^{+0.20}_{-0.17}\, M_\odot$, $R_{\rm eq} = 12.68^{+1.31}_{-1.04}$ km (Kini et al. 2026, 6-yr NICER)	NICER pulse-profile inference. Self-bound sequences can pass, but ordinary nucleonic EOSs also fit; no composition-specific signature.	EOS constraint; not unique.
PSR J0437-4715	$M = 1.418 \pm 0.037\, M_\odot$, $R = 11.36^{+0.95}_{-0.63}$ km	Favors softer EOSs at $1.4\, M_\odot$. Mildly disfavors stiffest CFL configurations and largest $\Delta_{\rm CFL}$; still compatible with vMIT SQM.	EOS constraint.
PSR J0614-3329	$M = 1.44^{+0.06}_{-0.07}\, M_\odot$, $R = 10.29^{+1.01}_{-0.86}$ km	2025 NICER analysis: Bayesian model comparison favors the SQS hypothesis over standard NS models within the adopted priors and EOS parameterisation.	Emerging strong candidate.

Reading the NICER numbers

The PSR J0030+0451 radius depends on the assumed hotspot geometry (two- vs. three-spot solutions), and the PSR J0740+6620 radius is sensitive to the joint NICER+XMM treatment. The quoted error bars are statistical; the dominant uncertainty is the model of the X-ray emitting region, not the equation of state. NICER's pulse-profile modelling also assumes a specified instrument response, a background model, and a prior on the hydrogen column density; these choices move the credible region by an amount comparable to the statistical error. The PSR J0437-4715 analysis additionally depends on the radio-timing parallax and on the treatment of the non-thermal pulsed component. None of these effects is captured by the symmetric 1σ bars shown in the table.

Strange Star & Quark Star Candidate Audit (III)

NICER mass–radius constraints and high-mass pulsars. These objects primarily constrain the dense-matter EOS rather than positively identifying quark matter.

Object	Key observable	Physics behind candidacy	Status
PSR J1614-2230	$M \simeq 1.97\,M_\odot$ (Shapiro delay)	High mass challenges soft quark EOSs; accommodated by NJL or modified MIT bag with vector interactions.	EOS constraint.
PSR J0952-0607	$M \simeq 2.35 \pm 0.17\,M_\odot$	One of the most massive pulsars. Optical companion modelling; model/systematic dependent.	EOS constraint; plausible SQS.
PSR J2215+5135	$M = 1.98 \pm 0.08\,M_\odot$ (Sullivan & Romani 2024)	Best-fit optical-atmosphere model. Broader systematic span ~ 1.85–$2.3\,M_\odot$ depending on heating/atmosphere assumptions; older $2.27^{+0.17}_{-0.15}\,M_\odot$ used a different model.	Speculative; EOS constraint.
PSR J1231-1411	NICER M–R posterior (prior-dependent)	Restricted radius prior gives $M \simeq 1.04^{+0.05}_{-0.03}\,M_\odot$, $R \simeq 12.6 \pm 0.3$ km; broader prior gives $R \simeq 13.5^{+0.3}_{-0.5}$ km.	EOS constraint; prior-sensitive.

Not a homogeneous error budget

The Shapiro-delay mass of PSR J1614-2230 is essentially model-independent (it assumes only GR), whereas the optical masses of PSR J0952-0607 and PSR J2215+5135 depend on the companion's heating and atmosphere; the PSR J1231-1411 radius is explicitly prior-dependent. The quoted uncertainties should not be combined as if they were statistically equivalent. For the black-widow and redback systems, the mass inference additionally assumes isotropic pulsar-wind irradiation, a unity Roche-lobe filling factor, and a radial-velocity curve uncontaminated by the heated face; relaxing any of these shifts the mass by several hundredths of a solar mass. In contrast, the Shapiro-delay measurement for PSR J1614-2230 rests only on the Keplerian orbit and the post-Keplerian range parameter, and is therefore the cleanest single mass in the table. A useful cross-check would be a system in which both a Shapiro delay and a clean optical radial-velocity curve are measurable; such overlap is currently rare, but it would provide an internal estimate of the optical-model systematics.

Strange Star & Quark Star Candidate Audit (IV)

Historical electromagnetic candidates from the Weber (2005) and Maxim tables, plus the Magnificent Seven class. Spectroscopic and radius anomalies. None is presently a confirmed strange star.

Object	Key observable	Physics behind candidacy	Status
RX J1856.5-3754	Featureless X-ray blackbody; early $R_\infty \sim 5$ km	Absence of atomic lines motivated a bare quark surface. No spectral lines detected by Chandra LETGS (Drake et al. 2002). Later distance/atmosphere modelling allows a condensed-surface NS.	Historical; weakened.
1E 1207.4-5209	Three absorption lines: $E_1 = 0.7$ keV, $E_2 = 1.4$ keV, $E_3 = 2.1$ keV (tentative)	Phase-dependent absorption features (Sanwal et al. 2002, ApJ 574, L61; Mori et al. 2006, ApJ 648, 1139). Features modelled as hydro-cyclotron oscillations on a bare strange-star surface. 2026 radio detection supports CCO/pulsar interpretation instead.	Historical; weakened.
SAX J1808.4-3658	Broad Fe Kα line at $E = 6.4$ keV (Papitto et al. 2009)	Relativistically broadened Fe Kα reflection line from accretion disc, not a strange-star signature. Early timing/luminosity analysis favored a self-bound sequence; model-dependent accretion assumptions.	Historical; model-dependent.
4U 1728-34 (MXB 1728-34)	Burst spectra; kHz QPOs	Atmosphere fits gave $M \sim 0.4$–$0.6\,M_\odot$, $R \sim 5$ km, interpreted as strange matter. Later work finds substantial spectral-model complications.	Historical; model-dependent.

A selection-effect caveat

The historical candidates were often selected because their inferred radii were anomalously small. Since radius inference depends on the assumed atmosphere, magnetic field, and distance, a consistent reanalysis tends to remove most of the anomalies. The absence of a modern confirmation is therefore informative, not merely a lack of data. A blind reanalysis of the archival spectra, with the radius kept free, would be the cleanest test of whether any anomaly survives.

Strange Star & Quark Star Candidate Audit (V)

Historical electromagnetic candidates from the Weber (2005) and Maxim tables, plus the Magnificent Seven class. Spectroscopic and radius anomalies. None is presently a confirmed strange star.

Object	Key observable	Physics behind candidacy	Status
4U 1746-37	X-ray burst M–R	Weber-table candidate; small inferred radius. Not confirmed.	Historical.
4U 1700-24	Claimed redshift + broad bands	Interpreted as strange-star oscillations with $M \sim 1.2\,M_\odot$, $R \sim 7$ km. Highly speculative.	Highly speculative.
4U 1702-429	Modern X-ray M–R inference	Useful modern target for quark-EOS testing; not a positive detection.	EOS test.
2S 0921-630	X-ray burst spectral fitting	$M \simeq 1.9$–$2.9\,M_\odot$, $R \simeq 9$–15 km. High mass and compact radius may favor SQM in some models.	Moderate; model-dependent.

Accreting sources: where the systematics live

Most entries here are accreting X-ray binaries. Their mass and radius inferences are limited by distance, interstellar absorption, and the accretion geometry (disc, boundary layer, corona) rather than by the EOS. Independent dynamical masses from optical spectroscopy are available for some systems (e.g. 2S 0921-630) and should be used to break the degeneracy. For the burst sources (4U 1746-37, 4U 1702-429), the radius inference assumes that the burst atmosphere is in local thermodynamic equilibrium, that the colour-correction factor f_c is known a priori, and that the photospheric radius expansion is modelled correctly; a variation of f_c by 10% shifts the inferred radius by ~ 1 km. For 4U 1700-24 the claimed redshift and broad-band features have not been reproduced by independent analyses. In all cases, the X-ray data alone cannot distinguish a compact strange star from a moderately compact neutron star without an external prior on the distance and on the interstellar column. This is the reason these entries are flagged as historical or model-dependent rather than as quark-matter evidence. A modern reanalysis would require simultaneous broadband spectroscopy and timing, with the distance and column treated as free nuisance parameters, and would then have to demonstrate that the residual compactness is inconsistent with a purely nucleonic interior. Accretion variability further complicates this: the source state changes on timescales shorter than a typical observation, so the spectral and timing data used to infer the compactness are not strictly simultaneous.

Strange Star & Quark Star Candidate Audit (VI)

Historical electromagnetic candidates from the Weber (2005) and Maxim tables, plus the Magnificent Seven class. Spectroscopic and radius anomalies. Burst, timing, and compact-binary candidates. None is presently a confirmed strange star.

Object	Key observable	Physics behind candidacy	Status
Her X-1	X-ray pulse/spectral M–R	Compact M–R solution sometimes fits bag-model EOSs. No unique quark signature.	Historical.
4U 1820-30	Ultra-compact binary; frequent burster	High orbital frequency matches strange-star dimensions in some models. Not observationally confirmed.	Historical.
PSR B0943+10	"Microstorms"; peculiar timing	Proposed as a bare strange star in early literature. Not confirmed.	Historical.
PSR B1516+02B (M5)	High mass ($\sim 2\,M_\odot$)	Exceptionally high mass potentially favors strange-star or exotic NS interpretation. Further measurements needed.	Speculative.
Neutron Star in Corona Australis	Small diameter $\sim$ 11 km; no atmosphere; no pulsations	Roughly half the size expected for a typical NS; absence of pulsations weakens hot-spot interpretation. Alternative explanations exist.	Speculative.
XTE J1739-285	Sub-millisecond spin candidate (616/1122 Hz)	High density requirement; rapid rotation could favor exotic composition.	Speculative.
Cyg X-2	Atoll source; M–R	Mass $\sim 1.7\,M_\odot$, $R \sim$ 10–12 km; consistent with NS but overlaps compact SQS models.	Speculative.
4U 1636-53	kHz QPOs; continuum hardness	Can be accommodated by strange-star EOSs; not primarily a spectral diagnostic.	Speculative.

Strange Star & Quark Star Candidate Audit (VII)

Historical electromagnetic candidates from the Weber (2005) and Maxim tables, plus the Magnificent Seven class. Spectroscopic and radius anomalies. The Magnificent Seven and modified-gravity interpretations. None is presently a confirmed strange star.

Object	Key observable	Physics behind candidacy	Status
Magnificent Seven (RX J0720.4-3125, RX J0806.4-4123, RX J1308.6+2127, RX J1605.3+3249)	Soft thermal continua + optical/UV excess	Strangeon-star atmosphere models can reproduce continua, optical excess, and broad absorption features. One source (RX J0806) yields a particularly small radiation radius.	Speculative.
RX J0806	Particularly small radiation radius	Consistent with a low-mass strange star in strangeon-star atmosphere models.	Speculative.
PSR J1416-2230 (also PSR J1416-2230)	Modified-gravity M–R fits	Interpreted as a strange star under specific gravitational parameters in Rastall, $f(Q)$, or massive gravity.	Speculative.
Vela X-1	Maxim-table M–R	Phenomenological fit within bag-model / modified-gravity tables.	Speculative.
4U 1608-52	Maxim-table M–R	Same as above.	Speculative.
PSR J1903+327	Maxim-table M–R	Same as above.	Speculative.
Cen X-3	Maxim-table M–R	Same as above.	Speculative.

Strange Star & Quark Star Candidate Audit (VIII)

Historical electromagnetic candidates from the Weber (2005) and Maxim tables, plus the Magnificent Seven class. Spectroscopic and radius anomalies. Remaining Maxim-table entries and the SGR/AXP class. None is presently a confirmed strange star.

Object	Key observable	Physics behind candidacy	Status
EXO 1785-248	Maxim-table M–R	Phenomenological fit within bag-model / modified-gravity tables.	Speculative.
LMC X-4	Maxim-table M–R	Same as above.	Speculative.
SMC X-1	Maxim-table M–R	Same as above.	Speculative.
GRO J1744-28	Weber-table; X-ray burst features	Historical candidate.	Historical.
SGR 0526-66	Weber-table; burst features	Historical candidate.	Historical.
SGR 1900+14	Weber-table; burst features	Historical candidate.	Historical.
SGR 1806-20	Weber-table; burst features	Historical candidate.	Historical.
AXPs/SGRs (class)	Extreme magnetic fields; emission mechanisms	Theorized to potentially harbor strange quark matter cores or be composed of strange matter with crusts. No specific AXP confirmed as a strange star.	Theoretical proposal.

Why this is not yet a detection

The entries are *historical*, *speculative*, or *theoretical*. Maxim/Weber-table mass–radius fits are model-dependent (bag model, modified gravity, composition), while burst and AXP/SGR observables mainly constrain magnetic-field and emission physics. None provides a unique quark-matter signature; a composition-specific observable (surface spectrum, tidal response, cooling/neutrino signal, or direct strangelet signature) is still required. None is presently a confirmed strange star.

Strange Star & Quark Star Candidate Audit (IX)

Compact objects whose thermal evolution is difficult to reconcile with standard neutron-star cooling. The enhanced neutrino emission required by these sources can be provided by quark direct Urca ($d \to u + e^- + \bar{\nu}_e$), but hadronic direct Urca, meson condensates, and pairing transitions can also explain it. None is a unique quark-matter signature.

Object	Key observable	Physics behind candidacy	Status
3C 58 / PSR J0205+6449	T_s too low for age	Requires enhanced neutrino emission. Quark direct Urca ($d \to u + e^- + \bar{\nu}_e$) can provide this, but hadronic direct Urca, meson condensates, and pairing transitions can also explain it.	Cooling candidate; not unique.
Cassiopeia A	Rapid cooling rate	Faster than standard modified-Urca models. A quark-matter core with enhanced ν emission is one of several explanations (ranked 4th–5th by Drake). Superfluidity in hybrid stars could also slow the rate.	Cooling candidate; not unique.
Young, Cold Isolated NSs	T_s 10–100$\times$ lower than peers	Disqualifies $\sim$ 75% of NS EOS models; points to a fast-cooling mechanism characteristic of SQS interiors with colour-superconducting phases. Color superconductivity can suppress rapid cooling, but the overall framework of enhanced neutrino emission in quark matter is consistent with these data.	Suggestive indirect evidence.

Why this is not yet a detection

Enhanced cooling is a *necessary* but not *sufficient* condition for quark matter. The degeneracy with hadronic channels (hyperons, kaon condensates, nucleon pairing) means that a composition-specific observable (surface spectrum, tidal response, or a direct strangelet signature) is still required.

Strange Star & Quark Star Candidate Audit (X)

If strange quark matter is the true ground state, stable sequences of low-mass self-bound objects may exist, distinct from neutron stars because they lack a nuclear crust and follow a different M–R relation. None has been observationally confirmed. Recall the self-bound scaling $M \propto R^3$ at low mass, in contrast to the gravitationally bound NS sequence.

Object	Key observable	Physics behind candidacy	Status
Strange quark planets (PSR J1719-1438 b; XTE J1807-294 b; XTE J1751-305 b; PSR J0636 b; PSR J1807-2459A b; PSR J2051-0827 b)	Planetary mass; $P_{\rm orb} < 6100$ s	Self-bound SQM objects survive tidal disruption at very short orbital periods, unlike ordinary planets. Conventional interpretation: stripped carbon-rich stellar remnant. No composition measurement.	Highly speculative.
Strange dwarfs (LSPM J0815+1633; LP 240-30; BD+20 5125B; WD J1257+5428; LP 462-12; 2MASS J13453297+4200437; SDSS J085557.46+053524.5)	$M \simeq 0.02$–$0.12\,M_\odot$, $R \simeq 9000$–15000 km	Proposed as white dwarfs with SQM cores, which would make them smaller and denser than ordinary WDs. No confirmed detection.	Highly speculative.
White-dwarf planets (GP Com b; V396 Hya b; J1433 b; WD 0137-349 b; SDSS J1411+2009 b)	Short-period companions of WDs	Same tidal-survival criterion as pulsar planets. Possible SQM objects if self-bound matter permits substellar configurations.	Highly speculative.

Future discriminant

A genuine strange-quark planet would have an anomalously high density for its mass, detectable through microlensing or through gravitational-wave emission from strange-star–strange-planet mergers. Both channels are long-term observational targets.

Strange Star & Quark Star Candidate Audit (XI)

High-energy transients that have been interpreted as signatures of the birth or transformation of a strange quark star ("quark nova"). The conversion of a neutron star into an SQS releases $\sim 10^{53}$ erg; repeated crust collapse on a strange star could power periodic FRBs and GRBs. None of these associations is confirmed.

Object	Key observable	Physics behind candidacy	Status
SN 2006gy	Super-luminous supernova	Proposed as a signature of the birth of a strange quark star (quark nova). The released energy is comparable to a supernova.	Speculative.
ASASSN-15lh	Luminous supernova event	Proposed as a signature of SQS birth or transformation from a NS via quark deconfinement.	Speculative.
GRB 240529A	Long-duration burst	Interpreted as a model involving magnetar-to-SQS transition followed by cooling.	Speculative.
Short GRBs (class)	$\sim 10^{53}$ erg release	The conversion of a NS into an SQS via a phase transition is believed to release a colossal amount of energy, which could power short gamma-ray bursts. No individual GRB has been confirmed as a quark-nova.	Speculative.
FRBs (class)	Periodic repeating bursts	Collapse of the normal-matter crust covering a strange star is a proposed mechanism that could generate FRBs and other electromagnetic bursts. Geng et al. (2021) found that crust collapse on an SQS can occur repeatedly.	Speculative.

Key point

These associations are currently theoretical. They provide motivation for multi-messenger searches, not evidence for strange matter. A confirmed detection of a quark-nova signature would require a coincident γ-ray, neutrino, and gravitational-wave signal consistent with a single self-bound EOS.

Strange Star & Quark Star Candidate Audit (XII)

Theoretical constructs that predict or accommodate strange-star-like compact objects. These are model classes, not individual candidates; they provide the theoretical scaffolding for the observational searches described in the previous frames.

Framework	Key prediction	Physics	Status
Ultra-compact sub-stellar strangelets	$M \sim 10^{-6}$–$10^{-2}\ M_{\odot}$, $R \sim 10^{2}$–10^{3} km	2026 prediction: self-gravitating SQM objects confined to the substellar regime. Distinct from brown dwarfs and exoplanets. Occupies a density gap; targets for microlensing surveys and high-cadence photometry.	Theoretical.
Twin stars	Two stable branches at the same M with different R	A first-order phase transition to quark matter creates a third family of compact stars. No specific object identified; mass–radius data from NICER and the GW170817 tidal constraint are actively used to search for signatures. The slope of $\Lambda(M)$ is the structural discriminant.	Theoretical.
Dark matter admixed quark stars	Modified M–R curves	SQM core with dark matter admixture can reproduce HESS J1731-347 and other constraints, including one-fluid and two-fluid configurations. Provides an additional theoretical branch but does not by itself identify any specific object.	Theoretical.

Common structural feature

All three frameworks predict a distinct $\Lambda(M)$ slope from the purely hadronic or pure-SQM sequences. A future joint Bayesian analysis must compare these hypotheses quantitatively. Because the frameworks differ in their number of free parameters, any evidence comparison must include the Occam penalty.

Strange Star & Quark Star Candidate Audit (XIII)

Theoretical constructs that predict or accommodate strange-star-like compact objects (continued). These are model classes, not individual candidates.

Framework	Key prediction	Physics	Status
Hybrid stars (class)	Hadronic mantle + quark core	Can mimic the HESS J1731-347 M–R point and support high masses through a strong transition. The M–R curve develops a kink at the transition, and $\Lambda(M)$ is modified. Often naturally compatible with NICER.	Theoretical framework.
Quark-cluster phase stars	Chromatically confined surface	Quarks condense into clusters at 2–10 n_0. Could explain non-atomic thermal spectra and absorption features via hydro-cyclotron oscillations of an electron sea. Proposed as a resolution of the high binding energies needed for pulsar vacuum gaps and baryon contamination in GRBs.	Theoretical.
Strangeon stars	Clustered quark matter; very stiff self-bound EOS	Alternative to conventional SQM; produces a stiff EOS that can support high masses (including the GW190814 mass gap). Microphysical description is phenomenological rather than derived from the QCD Lagrangian.	Theoretical.

Why these frameworks matter

Each framework predicts a distinct $\Lambda(M)$ slope and cooling behaviour. A future joint Bayesian analysis comparing {hadronic, hyperonic, K-condensed, hybrid(2SC/CFL), pure strange, strangeon, dark-matter-admixed} matter is needed to determine which, if any, is realized in nature. Several of these frameworks are not nested, so a simple likelihood-ratio test does not apply; a full evidence calculation with consistent prior ranges is required. A decisive test would need an observable in a regime where the frameworks differ qualitatively, not merely in the slope of a fitted curve.

The Colour-Flavour-Locked (CFL) Phase (I)

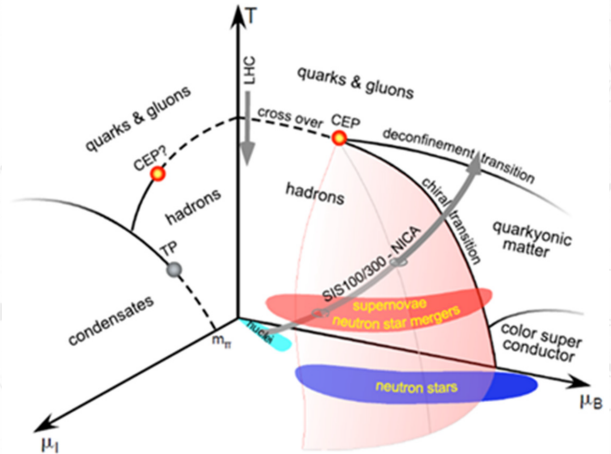

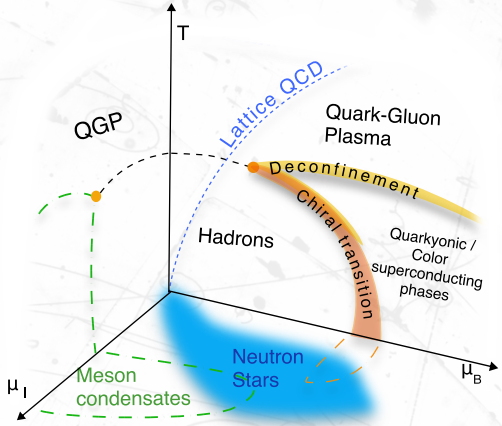

Left panel: Schematic QCD phase diagram in the temperature–baryon-chemical-potential (T–μ_B) plane. At low μ_B and high T, the transition from the quark–gluon plasma to hadrons is a crossover; at larger μ_B, a critical endpoint may terminate a first-order deconfinement transition. The regions labelled "quarks & gluons", "hadrons", "quarkyonic matter", and "colour superconductor" indicate candidate phases. The neutron-star trajectory probes the high-μ_B, low-T regime, where colour-superconducting phases such as 2SC and CFL are expected. **Right panel:** QCD phase diagram extended to include the isospin-chemical potential μ_I, relevant for neutron-rich matter in compact stars. It shows the hadronic phase, the quark–gluon plasma, and possible meson-condensate phases, with trajectories for neutron stars. Together, the two panels illustrate the T–μ_B–μ_I space in which the 2SC → CFL transition is expected to occur, providing the microphysical setting for strangelet nucleation in the cores of neutron stars or strange quark stars.

The Colour-Flavour-Locked (CFL) Phase (II)

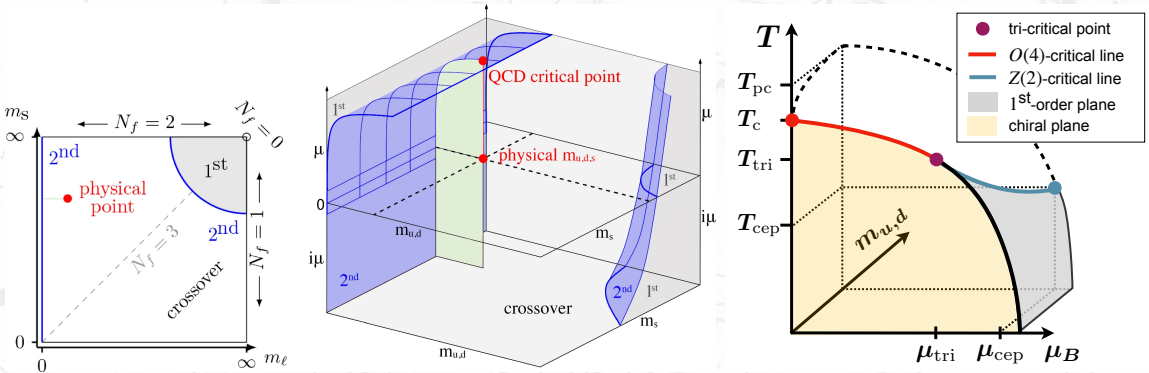

Lattice constraint 2025: Recent lattice-QCD simulations exclude, at the 2σ level, the existence of a critical point at $\mu_B < 450$ MeV. Padé-resummation estimates locate the CEP at $T^{\mathrm{CEP}} = 102^{+11}_{-23}$ MeV, $\mu_B^{\mathrm{CEP}} = 428^{+162}_{-74}$ MeV.

This is consistent with the schematic phase boundaries shown before.

The CFL Phase: Matter Composition

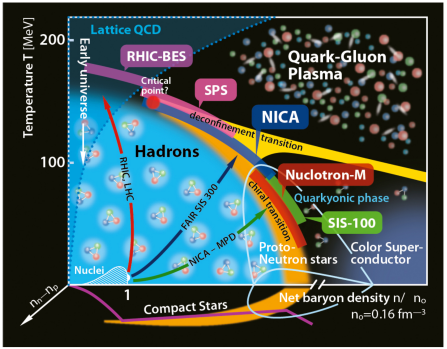

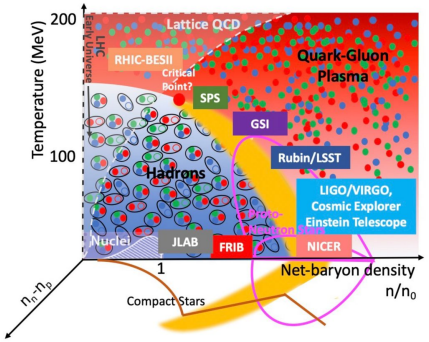

Present probes of the QCD phase diagram

- RHIC Beam Energy Scan (BES-I & II) — Au+Au collisions at $\sqrt{s_{NN}} = 7.7$–200 GeV. Searches for the QCD critical point and the onset of deconfinement at finite μ_B.
- SPS (NA61/SHINE) — fixed-target p+p, p+A, and A+A at $\sqrt{s_{NN}} \lesssim 17$ GeV.
  Systematic scan of the phase diagram at $\mu_B \sim 200$ MeV.
- Nuclotron-M (JINR) — operational superconducting synchrotron; provides extracted heavy-ion beams for the BM@N fixed-target experiment and serves as the injector chain for NICA.

Future facilities

- NICA (JINR) — collider Au+Au at $\sqrt{s_{NN}} = 4$–11 GeV.
  Ideal for the baryon-rich regime and the critical endpoint.
- SIS-100 (FAIR, GSI) — fixed-target Au+Au at $\sqrt{s_{NN}} = 2.7$–4.9 GeV.
  Highest net-baryon densities ($\mu_B \sim 520$–785 MeV).
- J-PARC-HI (J-PARC) — planned heavy-ion injector for the existing J-PARC complex. Will provide high-intensity beams at $\sqrt{s_{NN}} \simeq 2$–6 GeV and explore the highest-baryon-density regime of the QCD phase diagram.

The CFL Phase in Cosmology

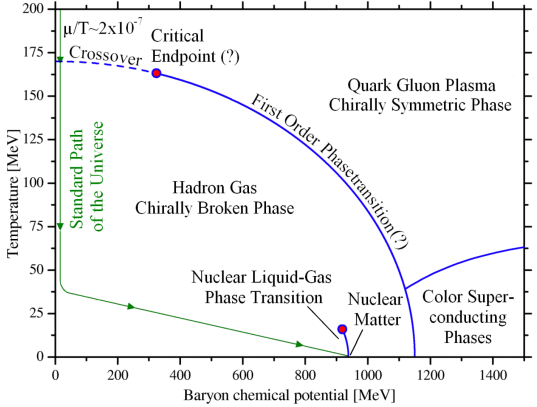

(a)

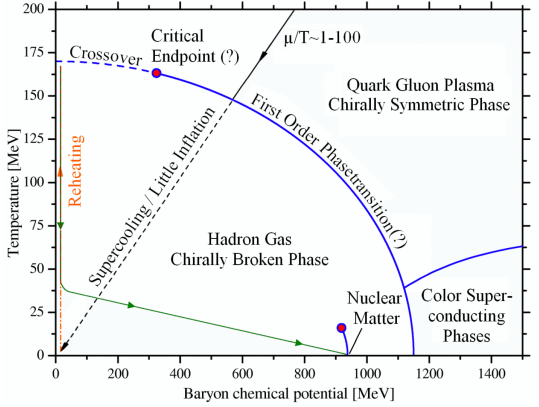

(b)

Schematic QCD phase diagram in the temperature–baryon-chemical-potential plane, showing two possible cosmological trajectories. **(a) Conventional evolution:** the early Universe follows the crossover from the quark–gluon plasma to hadrons, so no stable strange quark matter is produced. **(b) Cosmic phase separation:** if the QCD transition proceeds through a non-equilibrium or first-order-like path, dense quark-matter regions can separate and cool into the CFL phase. This provides a cosmological route to strangelet/SQM relics: if the CFL phase is the true ground state, it could be populated during this separation and survive until late times.

Quark-Gluon Plasma Temperatures: A More Detailed Picture of the Big Bang

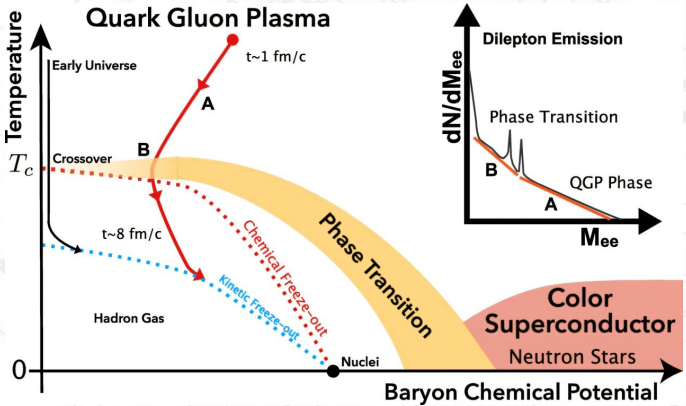

Temperature evolution of the early Universe and the quark–gluon plasma (QGP) phase.
The QGP existed for the first few microseconds after the Big Bang.

What is the quark–gluon plasma?

- A state of matter at extremely high temperature and/or density in which quarks and gluons are deconfined rather than bound into hadrons.
- Occurs when $T \gtrsim T_c^{\mathrm{QCD}}$ with $T_c^{\mathrm{QCD}} \approx 156$ MeV $\approx 1.8 \times 10^{12}$ K at $\mu_B \approx 0$.
- The inverse of confinement: a phase in which the QCD vacuum is screened and quarks move freely over length scales larger than $1/\Lambda_{\mathrm{QCD}}$.

QGP in the early Universe

- The Universe passed through the QGP phase during the first $\sim 10^{-6}$ s after the Big Bang, when $T \sim 10^{12}$–10^{13} K.
- The hadronisation transition (QGP $\rightarrow$ hadrons) occurred at $t \approx 10^{-6}$ s and $T \approx 170$ MeV.
- Studying the QGP in the laboratory therefore probes the primordial state of matter at the earliest observable epoch.

Heavy-ion collisions at RHIC, LHC, and the future NICA, FAIR, and J-PARC-HI facilities recreate the QGP in the laboratory and scan the QCD phase diagram in the (T, μ_B) plane. This provides a direct experimental window onto the physics of the early Universe.

Heavy-Ion Collision Constraints on the Dense-Matter EOS

Density/temperature distinction is essential

High-energy LHC and RHIC collisions create approximately deconfined QCD matter, but typically at relatively small μ_B. The cold cores of neutron stars instead lie at much higher μ_B and lower temperature.
RHIC Beam Energy Scan is therefore more directly relevant to the neutron-star EOS than top-energy LHC data.

RHIC Beam Energy Scan (BES)

- STAR 3 GeV K^0_S, Λ production probes the baryon-rich medium.
- BES-II fixed-target extends to $\sqrt{s_{NN}} = 3.2$–4.5 GeV.
- Key observables: v_1, v_2, v_3, dN/dy, $\langle p_T \rangle$, net-proton cumulants.
- Only v_1/v_2 and related collective observables have a relatively direct connection to pressure gradients and the EOS.
- No clear critical-point signatures down to $\sqrt{s_{NN}} \approx 7.7$ GeV.

FAIR/CBM and NICA/MPD

- CBM (FAIR): designed for $\mu_B \gtrsim 500$ MeV and densities of several times n_0. First beam projected around 2028.
- MPD (NICA): 4–11 GeV, anisotropic-flow measurements of identified particles.
- Current assessment: STAR BES is the mature experimental EOS input; FAIR/CBM and NICA/MPD are next-generation inputs.

MUSES review

The 2024 MUSES review provides the most systematic bridge among laboratory constraints and neutron-star observations.

The 2SC and CFL Phases in Dense QCD

In extremely dense quark matter, quarks can form Cooper pairs, leading to colour superconductivity. Two key phases:

1. 2SC (Two-Flavour Colour-Superconducting): pairing of up and down quarks only. Order parameter
$$\Delta_{2\mathrm{SC}} \propto \langle \psi^T(x)\, C\gamma_5\tau_2\lambda_2\, \psi(x)\rangle \neq 0,$$
with ψ the quark field, $C = i\gamma_2\gamma_0$ the charge conjugation matrix, τ_2 the second Pauli matrix in flavour space, and λ_2 the second Gell-Mann matrix in colour space. Occurs when $\delta\mu = (\mu_d - \mu_u)/2 < \Delta_{2\mathrm{SC}}/2$.
2. CFL (Colour-Flavour-Locked): pairing of all three flavours; colour and flavour indices are "locked". Order parameter
$$\Delta_{\mathrm{CFL}} \propto \langle \psi^T_{i\alpha}(x)\, C\gamma_5\, \epsilon^{\alpha\beta A}\, \epsilon_{ijB}\, \psi_{j\beta}(x)\rangle \neq 0, \qquad \phi^A{}_B = \delta^A{}_B,$$
where i, j are flavour indices, α, β are colour indices, and $\epsilon^{\alpha\beta A}$, ϵ_{ijB} are the Levi-Civita tensors in colour and flavour space. Characterised by the gap Δ_{CFL}, typically larger than $\Delta_{2\mathrm{SC}}$.

These two phases coexist in a strange quark star: an inner CFL core and an outer 2SC shell. The 2SC→CFL interface is where strangelet nucleation is expected to occur.

How NICER Constrains 2SC and CFL Phases

NICER measures (M, R), not the quark pairing order parameter

$$(M, R) \implies P(\epsilon) \implies \{n_{\rm tr}, \Delta\epsilon, c_s^2, \Delta_{\rm 2SC}, \Delta_{\rm CFL}, G_V, \dots\}.$$

Key NICER results (2024–2026)

- PSR J0740+6620 ($2.073\,M_\odot$): $R_{\rm eq} = 12.49^{+1.28}_{-0.88}$ km.
- PSR J0437−4715 ($1.418\,M_\odot$): $R = 11.36^{+0.95}_{-0.63}$ km.
- PSR J0030+0451 ($M = 1.43^{+0.20}_{-0.17}\,M_\odot$): $R_{\rm eq} = 12.68^{+1.31}_{-1.04}$ km. The previous value ($M = 1.34\,M_\odot$, $R = 12.71$ km) has been superseded.
- PSR J0614-3329 ($M = 1.44^{+0.06}_{-0.07}\,M_\odot$): $R_{\rm eq} = 10.29^{+1.01}_{-0.86}$ km.
- Combined χEFT + GW: $R_{1.4} = 12.28^{+0.50}_{-0.76}$ km; $R_{2.0} = 12.33^{+0.70}_{-1.34}$ km.

Implications for 2SC/CFL models

- A 2SC transition at low density softens the EOS; if too strong, it becomes difficult to reach $2\,M_\odot$.
- A subsequent 2SC→CFL transition can stiffen the quark EOS again, particularly with large G_V.
- NICER therefore constrains the combination of $n_{\rm tr}$, $\Delta\epsilon$, G_V, and Δ, rather than $\Delta_{\rm CFL}$ or $\Delta_{\rm 2SC}$ individually.
- The inclusion of PSR J0614-3329 (low radius, 10.29 km) slightly softens the EOS inference, shifting the allowed mass–radius region toward lower radii by ~ 300 m.

Observational statement

NICER does *not* exclude CFL cores and does *not* establish 2SC cores; it restricts the range of microscopic parameters that can produce an acceptable mass–radius relation.



Reflection in an astronaut's visor during an Extravehicular Activity (EVA), showing the NICER X-ray timing instrument installed on the ISS alongside the astronaut capturing the selfie.

GW170817 Tidal Deformability and Quark-Matter Constraints

The tidal deformability is a radius-sensitive observable

$$\Lambda = \frac{2}{3} k_2 \left(\frac{c^2 R}{GM} \right)^5 ,$$

so even modest changes in radius lead to large changes in Λ.

Implications for quark matter

- GW170817 restricts the stiffness and compactness of CFL/2SC EOSs, *not* the existence of CFL pairing itself.
- There is no model-independent upper or lower limit on $B_{\rm eff}$ or $B_{\rm eff}^{1/4}$ from GW170817 alone.
- Representative model-dependent windows from *different* analyses, expressed in *different parameterisations*:
  – $B_{\rm eff}^{1/4} \sim 114$–$185$ MeV
  (broad QCD-informed fits, quoted as a fourth-root scale);
  – $B_{\rm eff} \sim 47$–55 MeV fm^{-3}
  (specific Bayesian priors, quoted as an energy density).
  These two windows refer to different quantities in different units and should not be converted into one another.

Key quantitative bounds

- GW170817 GW-only 90% CL interval: $\Lambda_{1.4} = 70$–580.
- Model-dependent refined constraint $\Lambda_{1.4} = 222.89^{+420.33}_{-98.85}$.
  This is one of several published analyses; the archive does not contain the corresponding samples.
- Combined GW + X-ray multimessenger: $\Lambda_{1.4} = 265.18^{+237.88}_{-104.38}$ (EOS-agnostic).
- Quark-star upper bound on the maximum mass: $M_{\rm TOV}^{\rm QS} \lesssim 2.35^{+0.07}_{-0.17}\, M_\odot$.
- GW170817 combined tidal deformability (low-spin prior): $\tilde{\Lambda} = 300^{+420}_{-230}$ at 90% CL.

Why CFL Pairing Is Difficult to Identify from EOS Data

Several fundamental degeneracies

Degeneracy	Physical origin
Pairing gap vs. vector repulsion	Increasing G_V can stiffen quark matter in a way that mimics part of the effect of pairing.
Pairing vs. bag pressure	The pairing contribution can partially compensate B_{eff}.
2SC vs. CFL transition location	The observable star may contain only a CFL core even if the microscopic model has a 2SC region at higher volume fraction elsewhere.
Transition strength vs. post-transition sound speed	A strong first-order transition followed by a stiff quark phase can produce almost the same M–R–Λ curve as a smooth crossover.
Finite-temperature merger effects	Inspiral observations constrain essentially cold matter, while merger neutrinos and post-merger GWs probe $T \sim 10$–100 MeV, making the thermodynamic EOS different.

Bottom line

A unique identification of CFL from an inspiral tidal-deformability measurement is presently unrealistic.

Hybrid vs. pure strange-star mass–radius

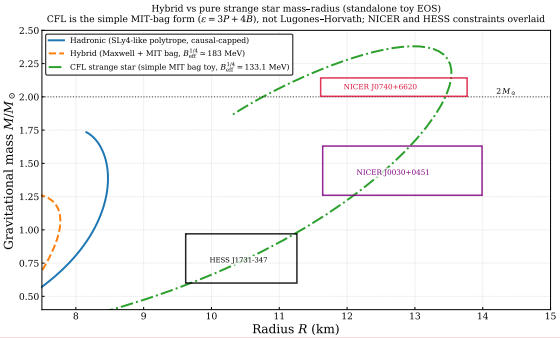

The three structural hypotheses

- Pure strange (MIT bag): self-bound quark matter reaches the surface; the low-mass branch follows $M \propto R^3$ and yields small, light objects.
- Hybrid: hadronic mantle plus a deconfined quark core; the M–R curve develops a kink at the transition.
- Hadronic: no deconfinement; purely nucleonic sequence.
- Dark-matter-admixed: an SQM (or hybrid) core with a fermionic or bosonic dark-matter admixture shifts the M–R curve.

The central structural degeneracy and the model-dependent nature of the curves

The EOS families shown are toy models (piecewise polytrope, Maxwell construction + MIT bag, massless MIT bag). They are not validated equations of state and have not been checked for thermodynamic consistency, causality, or phase-jump matching. All three families can pass through the NICER 1.4–2.1 $M_\odot$ error boxes and remain compatible with the 2 $M_\odot$ lower bound. The M–R diagram alone therefore cannot distinguish hybrid from strange. The low-mass, low-radius object HESS J1731-347 ($M = 0.77^{+0.20}_{-0.17}\,M_\odot$, $R = 10.4^{+0.86}_{-0.78}$ km) lies on the self-bound branch, and the slope of $\Lambda(M)$ is an additional discriminant. NICER values: PSR J0740+6620 $R = 12.49$ km; PSR J0030+0451 $M = 1.43^{+0.20}_{-0.17}\,M_\odot$, $R_{\rm eq} = 12.68^{+1.31}_{-1.04}$ km.

Tidal deformability $\Lambda_{1.4}$

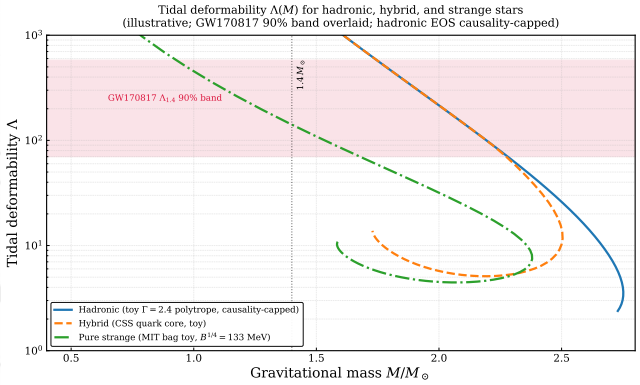

What the plot shows

- GW170817: first GW signal from merging binary neutron stars; AT2017gfo: its optical/near-IR kilonova counterpart.
- GW170817 reference: original LIGO/Virgo bound $\Lambda_{1.4} \lesssim 800$ at 90% CL; the standard published 90% interval is $\Lambda_{1.4} = 70$–580.
- AT2017gfo + GW: $120 \lesssim \tilde{\Lambda} \lesssim 1110$; combined $R_{1.4} = 12.2 \pm 0.5$ km.
- Strange-star models populate the higher-Λ tail, since the self-bound low-mass branch ($M \propto R^3$) extends to larger radii and hence larger Λ.

  CFL curve drawn at $B_{\rm eff}^{1/4} = 133.1$ MeV.

Model-dependent curves and single-measurement limitations

The EOS curves shown are toy models (piecewise polytrope, Maxwell + MIT hybrid, MIT bag). They are illustrative and have not been validated against public tabulated EOS. $\Lambda = \frac{2}{3} k_2 \, (c^2 R/GM)^5$ depends on the *full* $\Lambda(M)$ curve, not on a single parameter. There is no model-independent upper or lower limit on $B_{\rm eff}$ or $B_{\rm eff}^{1/4}$ from GW170817 alone; the slope of $\Lambda(M)$ is the structural discriminant.

QCD Phase Diagram and Strangelet Production Window

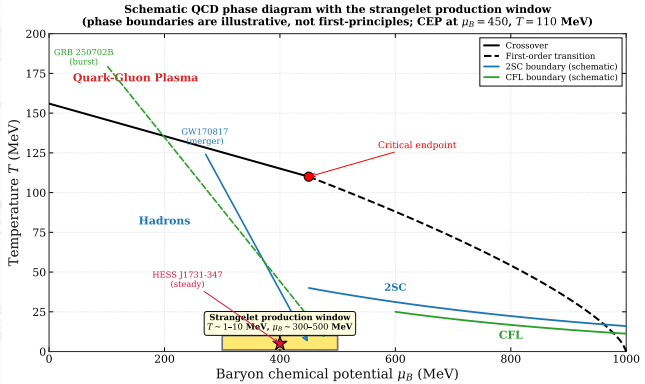

- Schematic T–μ_B plane: crossover, critical endpoint, first-order transition, 2SC and CFL regions.
  The phase boundaries shown are not a first-principles QCD calculation and are not outputs of a calibrated effective model (NJL, PNJL, FRG).
- Lattice QCD constraint 2025: recent lattice simulations exclude, at the 2σ level, a critical point at $\mu_B < 450$ MeV; Padé-resummation estimates locate the CEP at $T^{\mathrm{CEP}} = 102^{+11}_{-23}$ MeV, $\mu_B^{\mathrm{CEP}} = 428^{+162}_{-74}$ MeV.
- Gold rectangle: strangelet production window $T \sim 1$–10 MeV, $\mu_B \sim 300$–500 MeV.
- $\boxed{\mu_B \simeq 3\left(\pi^2 n_B\right)^{1/3}}$ $\quad (N_f = 3,\ N_c = 3,\ T = 0)$
- Trajectories: HESS J1731-347 (steady), GW170817 (merger), GRB 250702B (burst).
- Caveat: the CEP coordinates and the 2SC/CFL boundaries in the plotted figure are user-set illustrative parameters, not established QCD results.
  The lattice constraint quoted above is from a separate first-principles calculation.

Classical Nucleation Theory

Nucleation of a new phase

Nucleation is the formation of a small bubble of a new phase (e.g. CFL) inside a metastable parent phase (e.g. 2SC).

Free-energy change for a spherical bubble

$$\Delta E(R) \;=\; 4\pi R^2 \sigma_{\rm ST} \;-\; \frac{4\pi}{3} R^3 \Delta P,$$

where $\sigma_{\rm ST}$ is the surface tension and ΔP the pressure difference between the two phases.

Critical radius and activation energy

$$R_* \;=\; \frac{2\sigma_{\rm ST}}{\Delta P}, \qquad \delta E \;=\; \frac{16\pi\sigma_{\rm ST}^3}{3(\Delta P)^2}.$$

Fluctuations with $R > R_*$ grow; those with $R < R_*$ shrink and disappear.

Nucleation Barrier and Rate in the $\delta E/T$ Window

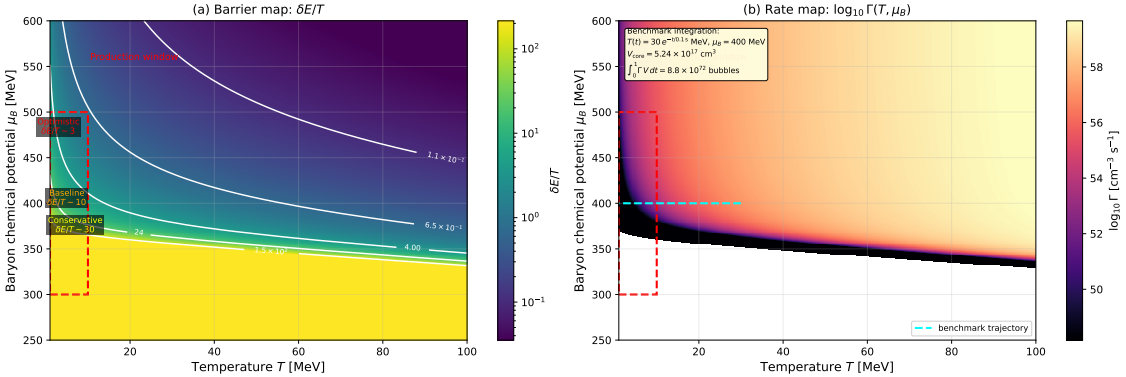

- Schematic: surface tension $\sigma_{\rm ST} = 10$ MeV/fm^2, $\Delta P = 2\, n_0\, \Delta\mu_B$, and prefactor T^4/π^3 are hand-set benchmark inputs.
  The integrated bubble number depends on the assumed trajectory by many orders of magnitude and is not a physical yield.
- Left panel: dimensionless barrier $\delta E/T = 16\pi\sigma_{\rm ST}^3/(3\Delta P^2 T)$ from classical nucleation theory.
- Right panel: rate $\Gamma = T^4\, \exp(-\delta E/T)$ in cm^{-3} s^{-1}, with the prefactor T^4 as a dimensionally-motivated benchmark.
- Physical sign condition: where $\Delta P \le 0$, the barrier is treated as infinite and $\Gamma = 0$; this forbidden region is shaded and does not contribute to the integration.
- Red rectangle: strangelet production window $T \sim$ 1–10 MeV, $\mu_B \sim$ 300–500 MeV.
- Benchmark integration: for the trajectory $T(t) = 30\, e^{-t/0.1\,\rm s}$ MeV, $\mu_B = 400$ MeV, $V_{\rm core} = 5.24 \times 10^{17}$ cm^3, the integrated bubble number is $\int_0^1 \Gamma\, V\, dt \sim 10^{73}$.
  This is the literal CNT output with $\sigma_{\rm ST} = 10$ MeV/fm^2: $\delta E \approx 47$ MeV at $T = 30$ MeV, $\delta E/T \approx 1.6$, so the rate is enormous, it is *not* $\dot N_{\rm peak}$.
- Caveats: $\sigma_{\rm ST}$, the pressure-gain closure, and the prefactor T^4 are hand-set benchmark inputs.
  $\delta E \propto \sigma_{\rm ST}^3$ makes the barrier sensitive to the surface tension; the integrated number is sensitive to the trajectory by many orders of magnitude.

Transition Conditions and Strangelet Production

The transition rate per unit volume and time from 2SC to CFL is dominated by thermal activation:

$$\Gamma_{\mathrm{trans}} \;=\; \frac{T^4}{\pi^3}\,\exp\!\left(-\frac{\delta E}{T}\right).$$

(Schematic: prefactor chosen on dimensional grounds; see later caveats.)

The strangelet production rate $\dot{N}(A)$:

$$\dot{N}(A) \;=\; \dot{N}_{\mathrm{peak}}\left(\frac{A}{A_{\mathrm{peak}}}\right)^{2/3}\exp\!\left[\frac{2}{3}\left(1-\frac{A}{A_{\mathrm{peak}}}\right)\right].$$

The $(A/A_{\mathrm{peak}})^{2/3}$ factor reflects geometric growth; the exponential factor reflects combined multifragmentation and coalescence suppression.

The 2SC-to-CFL Transition: Gap Equation and Nucleation

NJL gap equation (finite T)

In dense quark matter, colour superconductivity arises from quark pairing. The finite-temperature gap equation for the order parameter Δ is

$$1 = G_D \int_0^{\Lambda_{\mathrm{NJL}}} \frac{d^3p}{(2\pi)^3} \frac{1}{2E_p} \tanh\left(\frac{E_p}{2T}\right),$$

where $\epsilon_p = \sqrt{p^2 + m_q^2}$ is the free-quark dispersion and the Bogoliubov quasiparticle energy is $E_p = \sqrt{(\epsilon_p - \mu)^2 + \Delta^2}$.

(This is the standard BCS/NJL convention; an equivalent form with the gap appearing explicitly on the right-hand side is $\Delta = G_D \int \frac{d^3p}{(2\pi)^3} \frac{\Delta}{2E_p} \tanh(E_p/2T)$, which is numerically identical.)

Classical nucleation theory

The critical bubble radius and activation energy are

$$R_* = \frac{2\sigma_{\mathrm{ST}}}{\Delta P}, \qquad \delta E = \frac{16\pi\sigma_{\mathrm{ST}}^3}{3(\Delta P)^2}.$$

The transition rate per unit volume and time is

$$\Gamma_{\mathrm{trans}} = \frac{T^4}{\pi^3} \exp\left(-\frac{\delta E}{T}\right).$$

Grand potential (per flavour)

$$\Omega_i = \frac{\Delta^2}{4G_D} + \int_0^{\Lambda_{\mathrm{NJL}}} \frac{d^3p}{(2\pi)^3} \left(\epsilon_p - \sqrt{(\epsilon_p - \mu)^2 + \Delta^2}\right)$$

This is the per-flavour contribution; the total grand potential is $\Omega_{\mathrm{th}} = \sum_i \Omega_i$. The pressure difference $\Delta P = -(\Omega_{\mathrm{CFL}} - \Omega_{\mathrm{2SC}})$ drives the transition. (Vacuum subtraction not shown explicitly.)

Honest caveat

These expressions are schematic. A quantitative calculation requires separate quasiparticle branches, CFL multiple-gap structure, colour and electric neutrality, leptons, and an explicit vacuum-subtraction convention.
The prefactor T^4/π^3 is taken on dimensional grounds and treated as a benchmark normalisation.

Pairing Suppression and the BCS Gap Interpolation

BCS gap function

- The BCS gap $\Delta(T)$ vanishes at T_c^{pair} and approaches Δ_0 at $T = 0$.
- A common mean-field interpolation is

$$\Delta(T) \;\approx\; \Delta_0 \sqrt{1 - \left(T/T_c^{\mathrm{pair}}\right)^2}.$$

- The pairing suppression factor used in the neutrino–strangelet cross-section is

$$S_{\mathrm{pair}}(T) \;=\; \frac{\Delta(T)^2}{\Delta_0^2} \;\approx\; 1 - \left(T/T_c^{\mathrm{pair}}\right)^2, \qquad T \le T_c^{\mathrm{pair}}.$$

- Δ_0 and T_c^{pair} are related by $\Delta_0 \approx 1.76\, k_B\, T_c^{\mathrm{pair}}$.

Honest caveat

The interpolation $\Delta(T) \approx \Delta_0 \sqrt{1 - (T/T_c)^2}$ is mean-field. A quantitative calculation of $S_{\mathrm{pair}}(T)$ requires solving the finite-T BCS gap equation with the appropriate pairing interaction. The weak-coupling ratio 1.76 should be replaced by the strong-coupling value appropriate to the QCD / NJL interaction when used quantitatively.

Full BCS Gap Equation and Critical Temperature

BCS gap equation at finite temperature

For a pairing interaction $V_{kk'}$, the finite-T BCS gap equation is

$$\Delta_k \;=\; -\sum_{k'} V_{kk'}\,\frac{\Delta_{k'}}{2E_{k'}}\,\tanh\!\left(\frac{E_{k'}}{2T}\right),$$

with the Bogoliubov quasiparticle energy

$$E_k \;=\; \sqrt{\xi_k^2+\Delta_k^2}, \qquad \xi_k \;=\; \epsilon_k-\mu.$$

Isotropic s-wave case

For an isotropic gap $\Delta_k=\Delta(T)$ and a contact interaction $V_{kk'}=-V_0$:

$$1 = V_0\int_0^{\Lambda_{\rm NJL}} \frac{d^3p}{(2\pi)^3}\,\frac{\tanh(E_p/2T)}{2E_p}.$$

At $T=0$:

$$1 = V_0\int_0^{\Lambda_{\rm NJL}} \frac{d^3p}{(2\pi)^3}\,\frac{1}{2\sqrt{(\epsilon_p-\mu)^2+\Delta_0^2}}.$$

Critical temperature

The critical temperature $T_c^{\rm pair}$ is defined by $\Delta(T_c^{\rm pair})=0$:

$$1 = V_0\int_0^{\Lambda_{\rm NJL}} \frac{d^3p}{(2\pi)^3}\,\frac{\tanh[(\epsilon_p-\mu)/2T_c^{\rm pair}]}{2(\epsilon_p-\mu)}.$$

For weak coupling, the BCS ratio is

$$\frac{\Delta_0}{k_B\,T_c^{\rm pair}} \;\approx\; 1.76.$$

For strong coupling (relevant for QCD / NJL), this ratio can differ appreciably from 1.76.

Relation to the mean-field interpolation

The interpolation $\Delta(T)\approx\Delta_0\sqrt{1-(T/T_c^{\rm pair})^2}$ used earlier is a convenient mean-field approximation.
The exact $\Delta(T)$ requires solving the finite-T BCS gap equation above with the appropriate pairing interaction.

The BCS gap function $\Delta(T)$

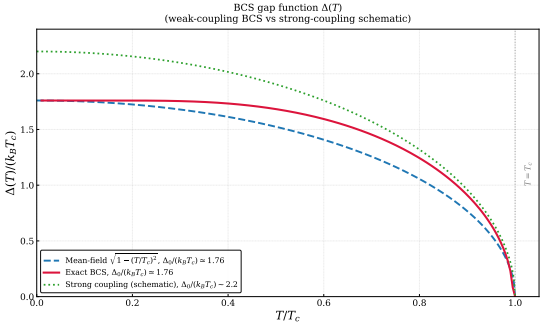

Mean-field vs. exact BCS

- The mean-field interpolation $\Delta(T) \approx \Delta_0 \sqrt{1-(T/T_c)^2}$ is a convenient analytic approximation, but it is *not* derived from the gap equation.
- The exact weak-coupling BCS solution (solid red curve), obtained by solving the finite-T gap equation with a constant pairing interaction, tracks the interpolation to within a few percent over $0 < T < T_c$, and reproduces the weak-coupling ratio $\Delta_0/(k_B T_c) \simeq 1.76$.
- The strong-coupling schematic (green) shows that a larger $\Delta_0/(k_B T_c)$ (relevant for QCD/NJL) leaves the curve qualitatively unchanged.

Why this matters for the strangelet framework

The pairing-suppression factor $S_{\mathrm{pair}}(T) = \Delta(T)^2/\Delta_0^2$ that enters the neutrino–strangelet cross-section is controlled by the shape of $\Delta(T)$ below T_c. The weak-coupling ratio 1.76 is a benchmark, not a QCD-derived number; strong-coupling corrections must be computed from the actual pairing interaction.

Key Parameters for the 2SC $\rightarrow$ CFL Transition

Table: Benchmark parameter ranges for the 2SC $\rightarrow$ CFL phase transition.

Parameter	Symbol	Benchmark range	Description
2SC gap	$\Delta_{2\mathrm{SC}}$	10–100 MeV	Pairing energy in the 2SC phase
CFL gap	Δ_{CFL}	15–150 MeV	Pairing energy in the CFL phase
Strange-quark mass	m_s	80–120 MeV	Current mass of the strange quark
Chemical potential	μ	400–500 MeV	Energy to add a quark
Bag constant	$B_{\mathrm{bag}}^{1/4}$	145–170 MeV	QCD vacuum-energy density scale
Vector/scalar coupling	G_V/G_S	0.5–1.0	Vector vs. scalar quark–anti-quark coupling

Provenance of these ranges

The ranges above are literature benchmarks, not outputs of a single self-consistent finite-temperature three-flavour calculation. A genuine equation-of-state calculation must impose colour and electric neutrality, solve the coupled gap equations for all flavours, and specify the vacuum-subtraction convention. The production rate inherits its sensitivity from the exponential factor $\exp(-\delta E/T)$, so a factor-of-two change in $\Delta_{2\mathrm{SC}}/\mu$ or m_s can shift $\dot{N}_{\mathrm{peak}}$ by several orders of magnitude. The values shown here must not be presented as if they were derived from a single underlying model.

CFL parameter space: literature model windows

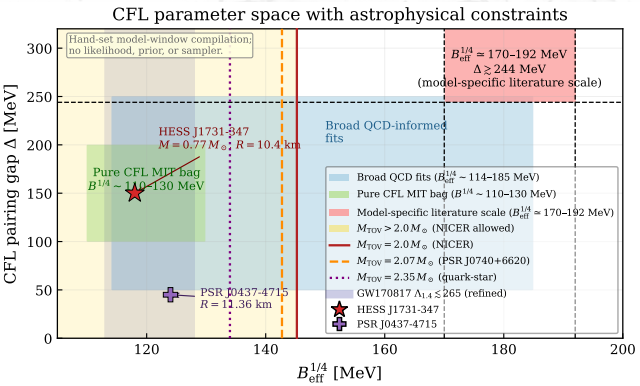

Provenance of the shaded windows

The three coloured regions are hand-set rectangles drawn to summarise published windows. They are not likelihood contours and do not represent confidence intervals. The red region in particular is a literature-reported scale, not an independent 90% credible interval computed in this work. The figure caption and the on-figure provenance note state this explicitly.

Three literature windows in the $(B_{\rm eff}^{1/4}, \Delta)$ plane

- Pure CFL MIT bag (green): $B_{\rm bag}^{1/4} \sim 110$–$130$ MeV, the canonical window for self-bound CFL strange stars.
- Broad QCD-informed fits (blue): $B_{\rm eff}^{1/4} \sim 114$–$185$ MeV, from combined astrophysical and lattice constraints.
- Literature-reported scale (red): $B_{\rm eff}^{1/4} \simeq 170$–$192$ MeV, $\Delta \gtrsim 244$ MeV, quoted from a published $2.6\,M_\odot$ CFL-strange-star interpretation. The associated Bayes factor is quoted from that paper, not computed here.

Why Δ and $B_{\rm eff}^{1/4}$ matter jointly

- A larger pairing gap Δ stiffens the quark EOS; a larger $B_{\rm eff}^{1/4}$ softens it.
- The two parameters are anti-correlated in the EOS posterior, so they cannot be constrained independently from M–R alone.
- A CFL strange star is viable only where the *combination* reproduces the observed M–R–Λ data.

CFL parameter space: NICER mass constraints

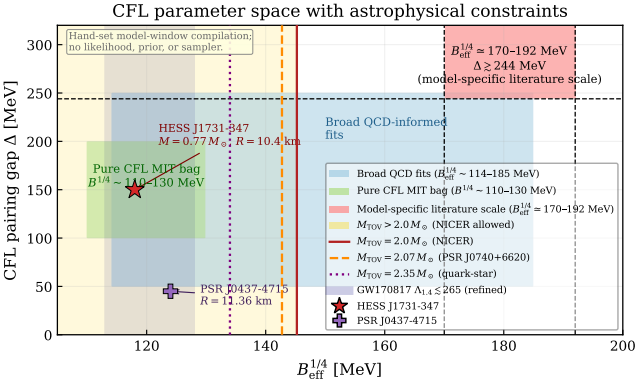

The gold band: where $M_{\rm TOV}$ can reach $2\,M_\odot$

- A MIT-bag TOV sequence reaches $M_{\rm TOV} \geq 2.0\,M_\odot$ only for $B_{\rm eff}^{1/4} \lesssim 145$ MeV.
- Larger $B_{\rm eff}^{1/4}$ gives a softer quark EOS that cannot support the observed 2.0–2.1 $M_\odot$ pulsars.

Three vertical reference lines

- Solid red: $B_{\rm eff}^{1/4}$ such that $M_{\rm TOV} = 2.0\,M_\odot$ — the NICER *lower bound*.
- Dashed orange: $M_{\rm TOV} = 2.07\,M_\odot$ — the central value from PSR J0740+6620 ($R_{\rm eq} = 12.92^{+2.09}_{-1.13}$ km at 68% CL).
- Dotted purple: $M_{\rm TOV} = 2.35\,M_\odot$ — the quark-star upper bound $M_{\rm TOV}^{\rm QS} \lesssim 2.35^{+0.07}_{-0.17}\,M_\odot$ from the post-merger analysis of Zhou et al.

Reading the frame

Any viable CFL strange-star model must sit to the left of the red line. This is a hard cut on $B_{\rm eff}^{1/4}$ that is *independent* of the pairing gap Δ, and it is the primary reason the model-specific 90% CL region (red band in B.1) is pushed towards larger $B_{\rm eff}^{1/4}$.

CFL parameter space: GW170817, HESS J1731-347, PSR J0437-4715

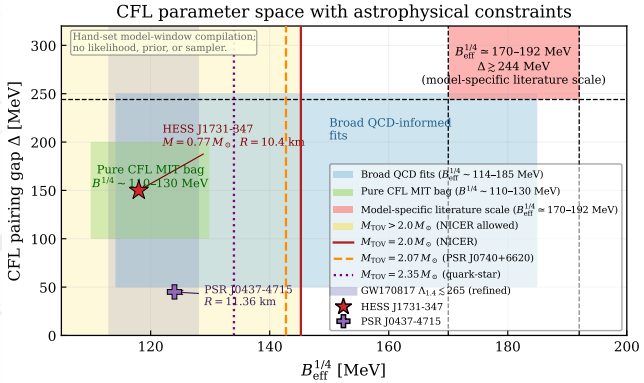

The navy strip: GW170817 tidal deformability

- Refined LIGO/Virgo + AT2017gfo gives $\Lambda_{1.4} \approx 223$–$265$ (equivalent to $120 \lesssim \tilde{\Lambda} \lesssim 1110$).
- For a self-bound MIT-bag star this corresponds to $R_{1.4} \simeq 10.5$–11 km, hence to a narrow band $B_{\rm eff}^{1/4} \simeq 113$–$128$ MeV.
- The strip overlaps the pure-CFL MIT-bag window: GW170817 does not exclude CFL strange stars, it restricts their parameter space.

Two source markers in the plane

- HESS J1731-347 (red star): $M = 0.77^{+0.20}_{-0.17}\,M_\odot$, $R = 10.4^{+0.86}_{-0.78}$ km. The only *self-bound* candidate; sits at the intersection of the pure-CFL window, the GW170817 strip, and the gold NICER-allowed band.
- PSR J0437-4715 (purple pentagon): $R = 11.36^{+0.95}_{-0.63}$ km at $M = 1.42\,M_\odot$. Mildly disfavours the very softest CFL configurations and the largest pairing gaps.

Takeaway for the talk

The pure-CFL window (green) and the model-specific 90% CL scale (red) are different statements. Only their intersection with the NICER mass bound, the GW170817 tidal bound, and the two source markers is currently viable — and that intersection is *narrow*.

Kaon Condensation in Hybrid Stars

A competing exotic phase, not evidence for quark matter

A charged K^- condensate occurs schematically when

$$\mu_e \simeq \mu_{K^-},$$

which can lower the electron chemical potential and soften the EOS.

Onset and consequences

- Recent Skyrme-based calculation: $n_B \simeq (1.5\text{–}2.5)n_0$, though strongly model dependent.
- Kaon condensation tends to reduce $M_{\max}^{\mathrm{EOS}}$ and therefore competes directly with $M_{\max}^{\mathrm{EOS}} \gtrsim 2\,M_\odot$.
- Viable hybrid-star models with a nuclear + K-condensed + quark triple-layer structure require $B_{\mathrm{eff}}^{1/4} \approx 158\text{–}179$ MeV (with pQCD corrections).

Important degeneracy

hyperons $\leftrightarrow$ K^- condensation $\leftrightarrow$ 2SC $\leftrightarrow$ CFL

All can modify the high-density pressure, but they produce different chemical compositions and neutrino opacities.

Recommendation

A future Bayesian analysis should compare {hadronic, hyperonic, K-condensed, hybrid(2SC/CFL), pure strange} matter, rather than treating "quark matter" as a single phenomenological category.

Why Two Cross-Sections? — Motivation

The framework links *microphysics* to *observables* through two independent interaction channels

Each channel has its own cross-section, its own physical origin, and its own role in the prediction chain.
Conflating them is the single most common source of error in strangelet phenomenology.

Channel 1: Strong interaction

σ_S

strangelet–nucleon

- Mediated by QCD
- Energy scale: $\Lambda_{\mathrm{QCD}} \sim 200$ MeV
- Geometric: $R_S^2 \propto A^{2/3}$

Channel 2: Weak interaction

$\sigma_{\nu S}$

neutrino–strangelet

- Mediated by $W^{\pm}, Z^0$
- Energy scale: E_ν^2
- Coherent: $C_V \propto A$

A useful mnemonic

σ_S tells you *whether* a strangelet arrives.

$\sigma_{\nu S}$ tells you *what signal* it produces once it is there.

Why we must treat them separately

- They enter at different stages of the prediction chain.
- They scale with different powers of n_S and f_{ret}.
- They are governed by different symmetries (colour vs. electroweak).
- A joint analysis of both is the only way to disentangle production from retention.

Strangelet–Nucleon Cross-Section σ_S: Origin and Role

Physical origin

- Process: strangelet scattering on ordinary nucleons via the strong interaction (QCD).
- Energy scale: $\Lambda_{\rm QCD} \sim 200$ MeV.
- Geometric size: a strangelet of baryon number A has radius $R_S \propto A^{1/3}$, hence cross-sectional area $\propto A^{2/3}$.
- Typical magnitude: $\sigma_S \sim \mathcal{O}(1)$ mb at $A \sim 10^2$.

Role in the prediction chain

$$\underbrace{\sigma_S}_{\text{strong}} \longrightarrow f_{\rm ret}(A,t) \longrightarrow n_S \longrightarrow \begin{cases} \Phi_\gamma \propto n_S^2 \langle\sigma v\rangle B_{\gamma\gamma} & (\gamma\text{-line}) \\ F_{\rm dir} \propto n_S f_{\rm ret} & (\text{direct}) \end{cases}$$

What it controls

- Propagation through the interstellar medium.
- The retention factor $f_{\rm ret}(A,t)$.
- The mass budget $M_{\rm acc} \leq f_{\rm max} M_\star$.
- The allowed parameter space of the framework.

What it does *not* control

- The γ-line flux Φ_γ *directly* — that depends on the annihilation cross-section $\langle\sigma v\rangle$.
- The neutrino signal — that depends on $\sigma_{\nu S}$.

σ_S enters *indirectly*, through $f_{\rm ret}$.

Neutrino–Strangelet Cross-Section $\sigma_{\nu S}$: Origin and Role

Physical origin

- Process: neutrino elastic / absorption scattering on a strangelet via the weak interaction (V–A).
- Energy scale: E_ν^2 (neutrino energy), *not* the quark chemical potential μ.
- Coherence: the vector coupling scales as $C_V \propto A$ for coherent scattering on the whole strangelet.
- Typical magnitude: $\sigma_{\nu S} \propto G_F^2 E_\nu^2 A^2$ (coherent vector channel).

Role in the prediction chain

$$\underbrace{\sigma_{\nu S}}_{\text{weak}} \longrightarrow \lambda_\nu(E_\nu, T, Y_L) \longrightarrow \begin{cases} L_\nu,\ \langle E_\nu \rangle & \text{(luminosity, mean energy)} \\ \text{spectral pinching,} & \text{(deleptonization timescale)} \end{cases}$$

What it controls

- The neutrino opacity λ_ν^{-1} in 2SC / CFL matter.
- The spectral and temporal features of any future neutrino detection.
- A potential direct discriminator of 2SC vs. CFL pairing.

Current observational status

- Far below current neutrino-telescope sensitivity.
- No observed merger neutrino spectrum with sufficient statistics.
- A long-term observational target for megaton-scale detectors.

How Both Cross-Sections Enter the Observable Predictions

Two independent chains, two independent observables

Chain 1 (strong): $\sigma_S \;\to\; f_{\rm ret}(A,t) \;\to\; n_S \;\to\; \begin{cases} \Phi_\gamma \propto n_S^2 & (\gamma\text{-line}) \\ F_{\rm dir} \propto n_S\, f_{\rm ret} & (\text{direct}) \end{cases}$

Chain 2 (weak): $\sigma_{\nu S} \;\to\; \lambda_\nu(E_\nu, T, Y_L) \;\to\; \text{neutrino spectrum.}$

Key scaling differences

Observable	Scaling	Channel
Φ_γ	$n_S^2 \langle\sigma v\rangle B_{\gamma\gamma}$	strong
$F_{\rm dir}$	$n_S\, f_{\rm ret}$	strong
Neutrino	$\sigma_{\nu S}\, n_S$	weak

- Strong and weak channels together probe production and retention separately.

Joint analysis is the only way

- $\Phi_\gamma / F_{\rm dir}^2$ constrains $\langle\sigma v\rangle B_{\gamma\gamma}/f_{\rm ret}^2$.
- $\Phi_\gamma\, F_{\rm dir}^2$ constrains $n_S^4 \langle\sigma v\rangle B_{\gamma\gamma}\, f_{\rm ret}^2$.
- Only with an independent kernel constraint on $\langle\sigma v\rangle B_{\gamma\gamma}$ can the ratio and product be inverted to give $f_{\rm ret}$ and n_S separately.
- This is the strongest possible consistency test of the strangelet hypothesis.

Strangelet–Nucleon Cross-Section: Form and Decomposition

Benchmark parameterisation for the *total* cross-section

$$\sigma_S^{\text{total}} = \sigma_0 \underbrace{\left(\frac{A}{100}\right)^{2/3}}_{\text{geometric area}} \underbrace{\left(\frac{\Delta_{2\text{SC}}}{\mu}\right)^{1.5}}_{\text{gap enhancement}} \underbrace{\exp\left(-2.0\,\frac{m_s^2}{\mu^2}\right)}_{\text{mass suppression}}$$

$$\frac{d\sigma_S}{d\Omega} = \frac{\sigma_0}{4\pi}\left(\frac{A}{100}\right)^{2/3}\left(\frac{\Delta_{2\text{SC}}}{\mu}\right)^{1.5} e^{-2.0\,m_s^2/\mu^2}\, f(\vartheta), \qquad \int f(\vartheta)\,\frac{d\Omega}{4\pi} = 1.$$

Angular normalisation (self-consistent)

With the normalisation $\int f(\vartheta)\, d\Omega/(4\pi) = 1$,

$$\int \frac{d\sigma_S}{d\Omega}\, d\Omega = \frac{\sigma_0}{4\pi} \cdots (4\pi) = \sigma_S^{\text{total}}.$$

The angular integral is absorbed into the normalisation; no extra $\mathcal{N}$ factor is needed. (For anisotropic f, replace 1 by the appropriate moment.)

Why this is now consistent

- A total cross-section *cannot* depend on ϑ.
- The normalisation $\int f\, d\Omega/(4\pi) = 1$ fixes the $1/(4\pi)$ prefactor unambiguously.
- The physical content of $f(\vartheta)$ is preserved; for isotropic scattering, $f \equiv 1$.

Piece-by-piece origin of the benchmark factors

- $\sigma_0 \sim 1$ mb: QCD strong-interaction scale. At nuclear density, the relevant length scale is $\sim 1/\Lambda_{\text{QCD}} \sim 1$ fm, giving $\sigma_0 \sim \pi/\Lambda_{\text{QCD}}^2 \sim \mathcal{O}(1)$ mb.
- $(A/100)^{2/3}$: geometric scaling. A strangelet of baryon number A has radius $R_S \propto A^{1/3}$, so its cross-sectional area scales as $A^{2/3}$. Normalised to $A = 100$.
- $(\Delta_{2\text{SC}}/\mu)^{1.5}$: effective-field-theory estimate for gapped quark matter; the exponent $n \simeq 1.5$ is a *benchmark* value, not a first-principles result.
- $\exp(-2.0\, m_s^2/\mu^2)$: Ginzburg–Landau-type suppression from the finite strange-quark mass; the factor 2.0 is a benchmark choice.

Strangelet–Nucleon Cross-Section: Honest Assessment

What this formula is — and what it is not

- It *is*: a *benchmark parameterisation* used to estimate sensitivity contours and compare experiments.
- It is *not*: a first-principles derivation from QCD.
- The exponents 1.5 and 2.0, and the prefactor σ_0, are not derived from the QCD Lagrangian.

What a genuine calculation would require

1. Solve the coupled gap equations for all flavours with colour and electric neutrality.
2. Evaluate the strangelet–nucleon scattering amplitude at the relevant momentum transfer Q^2.
3. Include form factors $F(Q^2)$ for the spatial distribution of quarks.
4. Account for coherent vs. incoherent scattering on the strangelet's constituent quarks (diffractive vs. quasi-elastic regimes).
5. Include Pauli blocking and colour-Coulomb corrections.

Numerical benchmark values

Parameter	Value	Status
σ_0	~ 1 mb	QCD scale
Δ_{2SC}	10–100 MeV	benchmark
m_s	80–120 MeV	benchmark
μ	400–500 MeV	benchmark

- These are illustrative benchmark inputs, not first-principles QCD predictions.

How σ_S enters the observable predictions

$$\Phi_\gamma \propto n_S^2 \langle \sigma v \rangle B_{\gamma\gamma} \quad \text{(line flux)} \qquad F_{\rm dir} \propto n_S f_{\rm ret} \quad \text{(direct flux)}$$

The strangelet–nucleon cross-section σ_S enters the retention factor $f_{\rm ret}$ and the propagation of strangelets through the interstellar medium. It does *not* enter the γ-line flux directly; the line flux depends on the annihilation cross-section $\langle \sigma v \rangle$, not σ_S.

Neutrino–Strangelet Cross-Section (I)

Benchmark form for a *heavy* target ($m_S \gg E_\nu$)

$$\frac{d\sigma_{\nu S}}{d\cos\vartheta} = \frac{G_F^2 E_\nu^2}{2\pi} \underbrace{\left[C_V^2(1+\cos\vartheta) + C_A^2(3-\cos\vartheta)\right]}_{\text{benchmark angular ansatz}} \times \underbrace{|F(Q^2)|^2}_{\text{form factor}} \times \underbrace{S_{\text{pair}}(T)}_{\text{pairing suppression}}$$

Coherent vector channel: $C_V^{\text{coh}} = N_{\text{coh}}\, c_V, \quad N_{\text{coh}} \sim A, \quad \Longrightarrow \quad \left(C_V^{\text{coh}}\right)^2 \sim A^2.$

Form factor normalisation: $F(0) = 1$ (no additional A^2 from the form factor; coherence is already encoded in C_V^{coh}).

Piece-by-piece interpretation

- $\frac{G_F^2 E_\nu^2}{2\pi}$ — weak-interaction strength times the neutrino phase space; the correct normalisation for a *heavy* target ($m_S \gg E_\nu$) is $1/(2\pi)$, *not* $1/(4\pi)$.
- $C_V^2(1+\cos\vartheta) + C_A^2(3-\cos\vartheta)$ — benchmark angular ansatz inspired by the V–A structure of neutrino–fermion elastic scattering. The exact Standard-Model angular distribution involves $(1 \pm \cos\vartheta)^2$ factors; the linear form used here is a phenomenological simplification.
- $|F(Q^2)|^2$ — quark spatial-distribution form factor; normalised as $F(0) = 1$. *Coherence is not in F.*
- $S_{\text{pair}}(T)$ — BCS pairing suppression of the quasiparticle density of states.

What is new in this form

- Energy scale: E_ν^2 (neutrino energy), *not* μ^2.
- Normalisation: $1/(2\pi)$, *not* $1/(4\pi)$, for a heavy target.
- Coherence: $C_V^{\text{coh}} \propto A$; the *square* gives the A^2 scaling.
- Form factor: $|F(Q^2)|^2$ with $F(0) = 1$ (not $\propto A$); no double counting of A^2.
- Weak strength set by neutrino energy, not quark chemical potential.
- Coherence enters through the vector coupling, not the form factor.

Neutrino–Strangelet Cross-Section (II)

Thermal (pairing) suppression factor

$$S_{\rm pair}(T) \;=\; \frac{\Delta(T)^2}{\Delta_0^2} \;\approx\; 1-\left(\frac{T}{T_c^{\rm pair}}\right)^2 \;\in\; [0,1], \qquad T \le T_c^{\rm pair},$$

where $T_c^{\rm pair}$ is the BCS critical temperature, related to the zero-temperature gap Δ_0 by $\Delta_0 \approx 1.76\, k_B\, T_c^{\rm pair}$. The expression $1-(T/T_c^{\rm pair})^2$ is a mean-field interpolation; the exact form requires solving the finite-T BCS gap equation.

Key corrections vs. earlier forms

- Energy scale: E_ν^2 (neutrino energy), *not* μ^2.
- Normalisation: $1/(2\pi)$, *not* $1/(4\pi)$, for a heavy target.
- Coherence: $C_V^{\rm coh} \propto A$ for coherent vector scattering; the *square* gives the A^2 scaling.
- Form factor: $|F(Q^2)|^2$ with $F(0)=1$ (not $\propto A$). The coherence is now *only* in $C_V^{\rm coh}$.
- Pairing suppression: uses $T_c^{\rm pair}$, not $\Delta_{\rm CFL}$. The two are related by $\Delta_0 \approx 1.76\, k_B\, T_c^{\rm pair}$.
- Gap-ratio factor: $(\Delta_{\rm CFL}/\Delta_{\rm 2SC})^{1/2}$ removed; it was speculative and not derived.

Where the chemical potential μ enters

- Indirectly, through the density of states at the Fermi surface (for degenerate quarks in the strangelet).
- Through the form factor $F(Q^2)$, which encodes the spatial distribution of quarks.
- Through the coherence factor $N_{\rm coh}$ (number of quarks that scatter coherently).
- It does *not* replace E_ν^2 in the overall normalisation.

Neutrino–Strangelet Cross-Section: Decomposition and Structure

The formula, decomposed piece by piece

$$\frac{d\sigma_{\nu S}}{d\cos\vartheta} = \underbrace{\frac{G_F^2 E_\nu^2}{2\pi}}_{\text{weak strength}} \underbrace{\left[C_V^2(1+\cos\vartheta) + C_A^2(3-\cos\vartheta)\right]}_{\text{benchmark angular ansatz}} \underbrace{|F(Q^2)|^2}_{\text{form factor}} \underbrace{S_{\text{pair}}(T)}_{\text{pairing}}$$

Weak-interaction structure (benchmark)

- $G_F^2 E_\nu^2/(2\pi)$: Fermi constant sets the weak strength. The neutrino energy E_ν replaces μ; the $1/(2\pi)$ is the correct normalisation for a heavy target ($m_S \gg E_\nu$).
- $C_V^2(1+\cos\vartheta) + C_A^2(3-\cos\vartheta)$: phenomenological angular ansatz inspired by the V–A structure.
  The exact Standard-Model result is $(1 \pm \cos\vartheta)^2$; the linear form is a simplification.

Strangelet-specific factors

- $|F(Q^2)|^2$: form factor for the spatial distribution of quarks, normalised as $F(0) = 1$. *Coherence is encoded in $C_V^{\text{coh}} \sim A$, not in F.*
- $S_{\text{pair}}(T)$: mean-field thermal damping; the condensate melts as $T \to T_c^{\text{pair}}$ and the cross-section vanishes.
- Coherent vector coupling scales as A^2, a benchmark upper limit.

Neutrino–Strangelet Cross-Section: Coherence and Caveats

Coherence: the missing A-dependence in earlier forms

- Coherent vector scattering: $C_V^{\mathrm{coh}} = N_{\mathrm{coh}}\, c_V$ with $N_{\mathrm{coh}} \sim A$ (all quarks scatter in phase), so the vector part scales as A^2.
  For $A \sim 10^3$, this is a factor of $\sim 10^6$ enhancement over single-quark scattering.
- Axial (spin-dependent) scattering: C_A is suppressed by the spin structure of the strangelet; only unpaired quarks contribute.
  For a spin-singlet strangelet, the axial coupling is strongly suppressed.
- Net effect: the cross-section is dominated by the coherent vector channel for $A \gtrsim 10^2$.
- No double counting: the coherence is in C_V, and the form factor is normalised as $F(0) = 1$.

Honest caveats

- This is a benchmark parameterisation, not a first-principles derivation.
- A genuine calculation requires the full response function (polarization tensor) of the strangelet, adapted from the matrix kinetic equation formalism to a finite system with discrete levels.
- The neutrino channel is far below any present neutrino-telescope sensitivity; it is quoted for completeness and as a long-term prospect.

Microscopic Origin (I): Weak Lagrangian and Polarization Tensor

Weak Lagrangian and currents (V–A model)

$$\mathcal{L}_W \;=\; \frac{G_F}{2\sqrt{2}}\,\ell_\mu\,\mathcal{J}^\mu \;=\; \frac{G_F}{2\sqrt{2}}\,\ell_\mu\left(c_V V^\mu - c_A A^\mu\right),$$

$$\ell^\mu \;=\; \bar{\nu}\gamma^\mu(1-\gamma^5)\nu, \qquad V^\mu \;=\; \bar{q}\gamma^\mu q, \qquad A^\mu \;=\; \bar{q}\gamma^\mu\gamma^5 q.$$

Here c_V, c_A are the single-quark couplings; for a strangelet with $N_{\rm coh}$ coherent scatterers, $C_V^{\rm coh} = N_{\rm coh}\, c_V$.
For the neutral current, $c_V^u = \frac{1}{2} - \frac{4}{3}\sin^2\theta_W$, $c_V^d = -\frac{1}{2} + \frac{2}{3}\sin^2\theta_W$, $c_A^u = +\frac{1}{2}$, $c_A^d = -\frac{1}{2}$, with θ_W the Weinberg angle.
The prefactor $G_F/(2\sqrt{2})$ is convention-dependent; some references use $G_F/\sqrt{2}$ or absorb the factor 2 differently.
The physics is unchanged as long as c_V, c_A are defined consistently.

Cross-section from the polarization tensor (optical theorem)

The differential cross-section follows from the imaginary part of the strangelet polarization tensor $\Pi^{\mu\nu}$:

$$\boxed{\frac{d\sigma_{\nu S}}{d\cos\vartheta} \;\propto\; G_F^2\, E_\nu^2\, \ell_{\mu\nu}\, \mathrm{Im}\,\Pi^{\mu\nu}(\omega, \mathbf{q})}$$

with the lepton tensor and 4-momentum transfer

$$\ell_{\mu\nu} \;=\; Q_\mu Q_\nu - Q^2 g_{\mu\nu}, \quad Q^\mu \;=\; (\omega, \mathbf{q}), \quad Q^2 \;=\; \omega^2 - |\mathbf{q}|^2.$$

Vector-current conservation: $Q_\nu\, \Pi^{\mu\nu} = 0$.

What this fixes in the benchmark formula

- Energy scale: E_ν^2 (neutrino energy) — *not* μ^2.
  The polarization tensor is evaluated at the neutrino 4-momentum $Q^\mu = (\omega, \mathbf{q})$.
- Normalisation: $1/(2\pi)$ for a heavy target ($m_S \gg E_\nu$) follows from the phase-space integral of the lepton tensor.
- Form factor: $|F(Q^2)|^2$ with $F(0) = 1$ emerges from the spatial integral of $\Pi^{\mu\nu}$ over the strangelet volume; the coherence is encoded in $C_V^{\rm coh} \sim A$.
- Coherence: $C_V^{\rm coh} \sim A$ arises from the *coherent sum* of quark vector currents over the whole strangelet; the vector part scales as A^2, and the form factor does *not* add another factor of A^2.

Strangelet Form Factor $F(Q^2)$

Definition

The form factor $F(Q^2)$ encodes the spatial distribution of quarks inside the strangelet.
It is normalised as $F(0) = 1$ and enters the neutrino–strangelet cross-section through $|F(Q^2)|^2$.

Benchmark: Gaussian quark distribution

For a Gaussian distribution with rms radius R_S:

$$F_{\mathrm{Gauss}}(Q^2) \;=\; \exp\!\left(-\frac{Q^2 R_S^2}{6}\right)$$

with

$$R_S \approx 0.7\, A^{1/3}\ \mathrm{fm}.$$

This form is convenient for analytic estimates and is normalised as $F(0) = 1$.

Long-wavelength limit

For $QR_S \ll 1$:

$$|F(Q^2)|^2 \;\approx\; 1 - \frac{Q^2 R_S^2}{3}.$$

Coherence is preserved; the first correction is the mean-square radius.

Benchmark: uniform sphere

For a uniformly charged sphere of radius R_{ch}:

$$F_{\mathrm{sphere}}(Q^2) \;=\; \frac{3\, j_1(QR_{\mathrm{ch}})}{QR_{\mathrm{ch}}},$$

with the spherical Bessel function

$$j_1(x) \;=\; \frac{\sin x - x\cos x}{x^2}.$$

At small Q: $F_{\mathrm{sphere}}(Q^2) \approx 1 - Q^2 R_{\mathrm{ch}}^2/10$.

Which form to use?

- Gaussian: convenient for analytic estimates; matches a smooth quark density.
- Uniform sphere: standard for electromagnetic form factors; more appropriate for a sharp surface.
- In both cases $F(0) = 1$, so no double counting of the coherence factor $C_V^{\mathrm{coh}} \sim A$.

Microscopic Origin (II): Pairing, Kinetic Equation, Caveats

Pairing suppression from the response function

In a paired (2SC or CFL) strangelet, the quark spectral function acquires a gap Δ. The polarization tensor inherits a BCS-like suppression:

$$\mathrm{Im}\,\Pi^{\mu\nu}(\omega,\mathbf{q}) \;\longrightarrow\; \mathrm{Im}\,\Pi^{\mu\nu}(\omega,\mathbf{q})\,S_{\mathrm{pair}}(T), \qquad S_{\mathrm{pair}}(T) \;=\; \frac{\Delta(T)^2}{\Delta_0^2}.$$

This is the microscopic origin of the thermal damping factor used in the benchmark formula.
The precise form of $S_{\mathrm{pair}}(T)$ should be computed from the matrix kinetic equation for the strangelet response, not assumed.
Here T_c^{pair} is the BCS critical temperature, related to the zero-temperature gap by $\Delta_0 \approx 1.76\,k_B\,T_c^{\mathrm{pair}}$.

Matrix kinetic equation

The response of a superfluid Fermi liquid is governed by

$$-\omega\,\mathcal{N} \;=\; [\mathcal{N},\mathcal{E}] + I_{\mathrm{coll}}, \qquad \mathcal{N}_k = \begin{pmatrix} n_k & F_k \\ F_k^\dagger & 1-n_k \end{pmatrix},$$

with the Bogoliubov quasiparticle energy

$$E_k^2 \;=\; \xi_k^2 + \Delta_k^\dagger \Delta_k, \qquad \xi_k \;=\; \epsilon_k - \mu.$$

Here $\mathcal{E}$ is the matrix entering the commutator. The Cooper-pair pole in the response function produces the pairing threshold at $\omega = E_+ + E_-$.

Honest caveats

- Shternin's formalism is for bulk superfluid matter. Adapting it to a finite strangelet requires discrete levels and a form factor.
- A full calculation of $\mathrm{Im}\,\Pi^{\mu\nu}$ for a strangelet with colour and electric neutrality is an open problem.
- The neutrino channel remains far below current detector sensitivity; this derivation is for completeness and future work.

Summary: from microscopic origin to benchmark formula

$$\frac{d\sigma_{\nu S}}{d\cos\vartheta} \;=\; \underbrace{\frac{G_F^2 E_\nu^2}{2\pi}}_{\text{optical theorem}} \underbrace{\Big[C_V^2(1+\cos\vartheta) + C_A^2(3-\cos\vartheta)\Big]}_{\text{benchmark angular ansatz}} \underbrace{|F(Q^2)|^2}_{\text{form factor, } F(0)=1} \underbrace{S_{\mathrm{pair}}(T)}_{\text{pairing, } T_c^{\mathrm{pair}}}$$

Every factor in the benchmark formula has a microscopic interpretation, but the angular factor is a benchmark simplification, not an exact V–A result.

Neutrino Spectral Features in 2SC Matter

Unpaired quasiparticles dominate neutrino interactions

In the 2SC phase, up and down quarks of two colors form Cooper pairs with a large gap ($\sim$ 100–300 MeV), leaving unpaired blue quarks (and, at higher densities, strange quarks).

Kinematic blocking and channel switching

- At low T:

$$\nu + d \to u + e^-/\mu^-$$

  is kinematically forbidden due to Fermi-surface mismatch. This is a charged-current reaction; the corresponding antineutrino processes are obtained by CP conjugation.

- Absorption is then dominated by:

$$\nu + s \to u + e^-/\mu^-$$

- At higher T or E_ν: the d-quark channel opens and the mean free path decreases sharply.

Merger-relevant implications

- In equilibrated 2SC matter with $Y_{L_e} = 0.1$, neutrinos form a degenerate gas with mean free paths of metres or less.
- A phase transition hadronic $\to$ 2SC $\to$ CFL could imprint itself through changes in $\lambda_\nu(E_\nu, T, Y_L)$.
- Observable consequences: $\nu_e/\bar{\nu}_e$ luminosity, mean energy, spectral pinching, deleptonization timescale, angular distribution, flavor-dependent diffusion times.
- No observed merger neutrino spectrum with sufficient statistics yet.

Neutrino Mean Free Path in Hadronic, 2SC, and CFL Matter

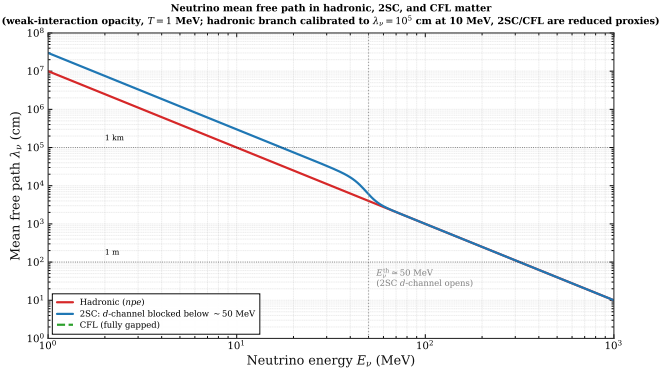

- Hadronic (*npe*): free-space charged-current opacity, $\lambda_\nu \propto E_\nu^{-2}$.
  Calibrated to the published in-medium rate $\lambda_\nu \sim 10^5$ cm at $E_\nu = 10$ MeV.
- 2SC (reduced proxy): the reaction $\nu + d \to u + e^-/\mu^-$ is kinematically blocked below $E_\nu^{\rm th} \simeq 50$ MeV, so the effective target density is reduced to the ungapped blue-quark fraction; above threshold it returns to the full n_B.
  The blocking is a smooth tanh proxy, not a solution of the 2SC matrix kinetic equation.
- CFL (toy suppression): the weak *cross-section* is suppressed by $\exp(-\Delta_{\rm CFL}/T)$ (equivalently, the mean free path is multiplied by $\exp(+\Delta_{\rm CFL}/T)$), with the same target density as the hadronic phase.
  At $T = 1$ MeV and $\Delta_{\rm CFL} = 100$ MeV the suppression factor is $\exp(100) \approx 2.7 \times 10^{43}$, so the CFL curve lies far above the plotted y-range and is not visible in this panel. No Goldstone-boson scattering rate is computed.
- Common caveats: $T = 1$ MeV throughout, no temperature-dependent rates, no neutrino degeneracy effect, no μ-flavour distinction.

Neutrino luminosity as a phase discriminator

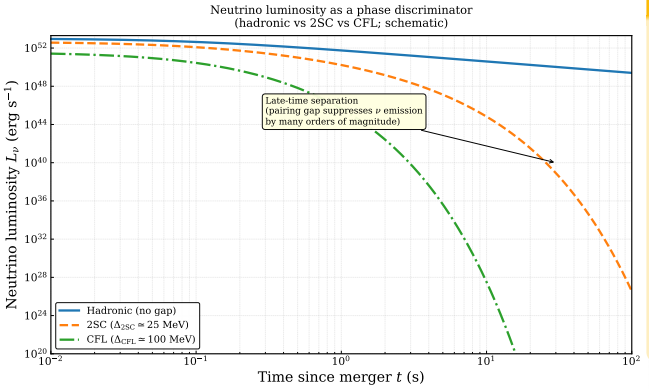

What the plot shows

- Early phase ($t \lesssim 100$ ms): all three phases emit similarly; the remnant is hot and neutrino-trapped.
- Late phase ($t \gtrsim 1$ s): the pairing gap suppresses the neutrino emissivity.
- Hadronic: no gap; the largest late-time luminosity.
- 2SC: partial suppression
  (only blue quarks participate in β-decay).
- CFL: strongest suppression; the luminosity drops by orders of magnitude.

Why a future megaton detector is needed

The late-time separation between the three curves is the direct 2SC/CFL discriminator. It is invisible to current detectors (see the "Neutrino Detection Limits" frame), but a megaton-scale $\mathcal{O}(10)$-MeV detector with a GW trigger could in principle resolve it. A non-detection would constrain the late-time luminosity but not the early-time phase.

Annihilation Signatures in γ-Ray Spectra

For a point-like source at distance D, the line-photon flux at Earth is

$$\Phi_\gamma = \frac{2\, B_{\gamma\gamma}\, R_{\rm ann}}{4\pi D^2}.$$

The velocity-averaged annihilation cross-section:

$$\langle \sigma v \rangle = \frac{\pi}{m_S^2}\,(a + b\,T)\exp\!\left(-\frac{E_{\rm act}}{T}\right),$$

with m_S the strangelet mass, $a \sim 1$ the s-wave coefficient, $b \sim 1/m_S$ the p-wave coefficient, and $E_{\rm act}$ the activation energy.
In natural units ($c = 1$), the coefficients a, b are chosen so that $(a + bT)$ is dimensionless; for $b \sim 1/m_S$, this requires T to be expressed in the same mass units.
A conservative benchmark value $\langle \sigma v \rangle \sim 10^{-25}\,\mathrm{cm^3\,s^{-1}}$ is adopted.

Unitarity note: the factor π/m_S^2 is a benchmark normalisation inspired by the s-wave unitarity bound on the partial-wave cross-section, $\sigma_{\max} = 4\pi/k^2$ (k is the wavenumber).
It is not an exact derivation; the conversion to $\langle \sigma v \rangle$ is a phenomenological parameterisation.

Origin of the Annihilation Cross-Section and Line Flux

The line-flux formula

$$\Phi_\gamma = \frac{2\,B_{\gamma\gamma}\,R_{\rm ann}}{4\pi D^2}$$

- $1/(4\pi D^2)$: standard geometric dilution for a point-like source at distance D.
- $2B_{\gamma\gamma}$: two photons per annihilation, multiplied by the branching fraction to $\gamma\gamma$.
- $R_{\rm ann}$: total annihilation rate (s^{-1}).

Annihilation rate

$$R_{\rm ann} = n_S\, n_{\bar{S}}\, \langle\sigma v\rangle\, V_{\rm source}$$

- n_S, $n_{\bar{S}}$: strangelet and anti-strangelet number densities.
  In this work $n_{\bar{S}} = n_S$.
- $V_{\rm source}$: accumulation volume.

The velocity-averaged cross-section

$$\langle\sigma v\rangle = \frac{\pi}{m_S^2}(a + bT)\exp\left(-\frac{E_{\rm act}}{T}\right)$$

- π/m_S^2: benchmark normalisation inspired by the s-wave unitarity bound $\sigma_{\max} = 4\pi/k^2$. It is not an exact derivation; the conversion to $\langle\sigma v\rangle$ is a phenomenological parameterisation.
- $a \sim 1$: s-wave coefficient (dimensionless in natural units $c = 1$; temperature-independent).
  The a term dominates at low T.
- $b \sim 1/m_S$: p-wave coefficient (dimensionless in natural units), thermally activated as bT.
  The bT term dominates at higher T.
- $\exp(-E_{\rm act}/T)$: activation energy $E_{\rm act}$. Annihilation requires overcoming a barrier (e.g. Coulomb barrier or a QCD-level threshold), giving a Boltzmann suppression at low T.

Benchmark value

A conservative benchmark value $\langle\sigma v\rangle \sim 10^{-25}\ \mathrm{cm}^3\,\mathrm{s}^{-1}$ is adopted (in natural units, $1\ \mathrm{GeV}^{-2} = 1.17\times10^{-17}\ \mathrm{cm}^3\,\mathrm{s}^{-1}$, so $1\ \mathrm{cm}^3\,\mathrm{s}^{-1} = 8.55\times10^{16}\ \mathrm{GeV}^{-2}$). The geometric value π/m_S^2 could be orders of magnitude larger for large m_S; the exponential factor $\exp(-E_{\rm act}/T)$ is the dominant suppression.

Temperature dependence of the annihilation cross-section

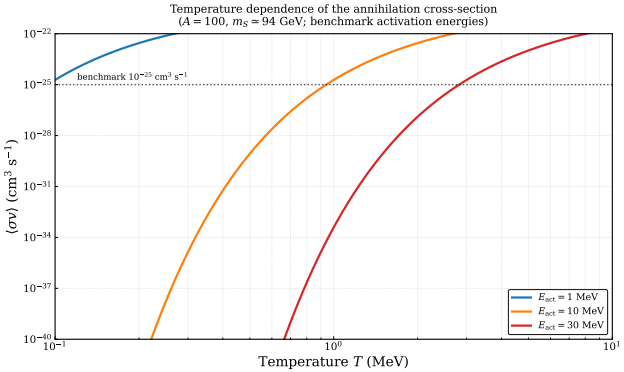

The formula and its two regimes

$$\langle \sigma v \rangle = \frac{\pi}{m_S^2} (a + bT) \exp\left(-\frac{E_{\rm act}}{T}\right).$$

- Low T: the Boltzmann factor $\exp(-E_{\rm act}/T)$ dominates; the cross-section collapses exponentially.
- High T: the prefactor $(a + bT)$ dominates; the cross-section rises with T.
- The turnover shifts to higher T as $E_{\rm act}$ increases.

Consequence for the line-flux forecast

The benchmark value $\langle \sigma v \rangle \sim 10^{-25}$ cm^3 s^{-1} is only meaningful once a temperature is specified. For $E_{\rm act} \gtrsim 30$ MeV, the cross-section at merger-relevant $T \sim 1$–10 MeV is *many orders of magnitude* below the benchmark. This is one of the largest systematic uncertainties in the line-flux calculation, comparable in impact to the retention factor $f_{\rm ret}$.

Two-Photon Angular Correlation

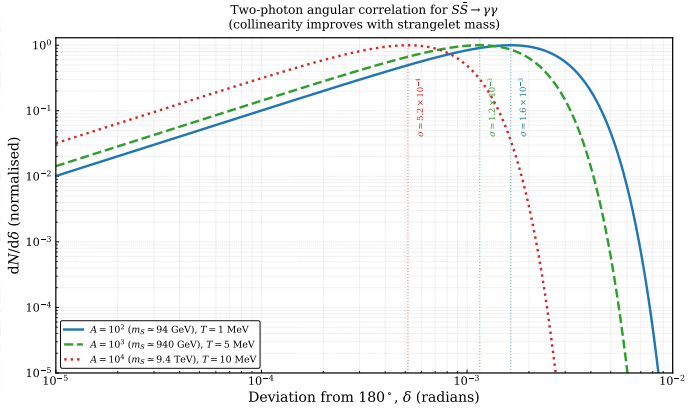

- For $S\bar{S} \to \gamma\gamma$ in the CM frame the two photons are exactly back-to-back. A non-zero relative velocity $v_{\rm rel}$ in the source frame opens a deviation δ from 180°: $\delta \sim \frac{1}{2}(v_{\rm rel}/c)$.
- For a thermal population at temperature T, the typical relative velocity is $v_{\rm rel}/c \sim \sqrt{k_B T/m_S}$, so the angular width scales as $\sqrt{T/m_S}$.
- The distribution peaks at $\sigma \simeq \frac{1}{2}\sqrt{k_B T/m_S}$ and is strongly collinear for cold, heavy strangelets: for $A = 10^4$ and $T = 10$ MeV the deviation is $\sigma \sim 5 \times 10^{-4}$ rad.
- Observational discriminant: a genuine annihilation line should show a two-photon coincidence with $\delta \lesssim 10^{-3}$ rad, distinct from any single-photon background process.

The Anti-strangelet Requirement

Assumption behind the line-flux formula

The γ-line flux $\Phi_\gamma = 2\, B_{\gamma\gamma}\, R_{\rm ann}/(4\pi D^2)$ with $R_{\rm ann} = n_S\, n_{\bar{S}}\, \langle \sigma v \rangle\, V_{\rm source}$ requires both strangelets and anti-strangelets to be present. In this work we assume $n_{\bar{S}} = n_S$.

Where anti-strangelets could come from

- Pair production in the hot quark-gluon plasma.
- Strangeness–anti-strangeness separation during the 2SC→CFL transition.
- Subsequent hadronisation of anti-quark-rich regions.

Why this is not trivial

- Anti-matter strangelets are subject to the same retention problem as their matter counterparts.
- A source that produces only SQM droplets (no anti-SQM) would emit *no* annihilation line.
- A first-principles calculation of $n_{\bar{S}}/n_S$ is beyond the scope of this work.

Takeaway

The line signal is *conditional on anti-strangelet production*. If $n_{\bar{S}}/n_S \ll 1$, the flux is suppressed by that ratio and the benchmark contours should be rescaled accordingly.

The Anti-Strangelet Problem (I)

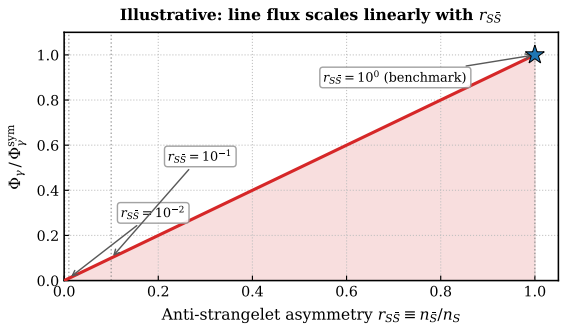

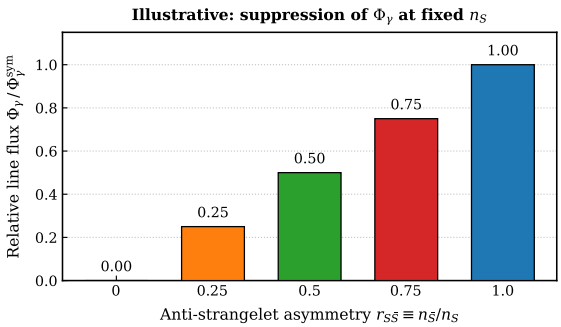

Illustrative nature made explicit

The linear scaling shown here is a trivial consequence of the line-flux formula $R_{\rm ann} = n_S\, n_{\bar{S}}\, \langle \sigma v \rangle\, V_{\rm source}$ with $n_{\bar{S}} = r_{S\bar{S}}\, n_S$. It is a textbook illustration of the geometry, not a physics-derived plot.

A physically-motivated $r_{S\bar{S}}$ would require a strangeness-separation or pair-production calculation, which is beyond the scope of this script.

The Anti-Strangelet Problem (II)

Asymmetry parameter

Define

$$r_{S\bar{S}} \equiv \frac{n_{\bar{S}}}{n_S}.$$

With $R_{\rm ann} = n_S n_{\bar{S}} \langle \sigma v \rangle V_{\rm source}$ the line flux becomes

$$\Phi_\gamma = \frac{2 B_{\gamma\gamma}\, n_S^2\, r_{S\bar{S}}\, \langle \sigma v \rangle\, V_{\rm source}}{4\pi D^2},$$

so $\Phi_\gamma \propto r_{S\bar{S}}$ at fixed n_S.

Status

- Benchmark assumes $r_{S\bar{S}} = 1$ (symmetric).
- A source producing only SQM droplets would have $r_{S\bar{S}} = 0$ and emit *no* line.
- First-principles calculation of $r_{S\bar{S}}$ is beyond the present framework.

Where anti-strangelets could come from

- Pair production in the hot quark–gluon plasma.
- Greiner strangeness separation: $\bar{s}$ excess in the hadron phase hadronises into anti-strangelets.
- Subsequent hadronisation of anti-quark-rich regions.

Strangelet Mass-to-Charge Ratio

$$\frac{m_S}{|Z|} \approx \frac{m_N}{Y_Q}\left[1 + \frac{2}{9\pi}\left(\frac{\mu}{m_s}\right) - \frac{1}{3}\left(\frac{\Delta_{\mathrm{CFL}}}{\mu}\right)^{1/2}\right].$$

A-dependent CFL charge

The CFL strangelet charge is *not* a universal constant:

$$Z \simeq 0.3\,A^{2/3}, \qquad \frac{Z}{A} \simeq 0.3\,A^{-1/3}.$$

For $A = 10^2$, $Y_Q \simeq 0.065$; for $A = 10^6$, $Y_Q \simeq 3 \times 10^{-3}$.
Recall that $Y_Q \equiv Z/A$; the two notations denote the same quantity.

- With CFL charge scaling and the benchmark parameters of this work, the bracket above is ≈ 1.16, giving $m_S/|Z| \approx 3.6\,A^{1/3}$ GeV/c^2. For $A = 10^2$, 10^3, 10^4, 10^5 this yields ~ 17, 36, 78, 168 GeV/c^2.
- The commonly quoted MIT-bag band $m_S/|Z| \sim 30$–60 GeV/c^2 corresponds to $A \sim 10^3$ in this scaling, not to the full range $A \sim 100$–10^5.
- Colour factor: $N_c = 3$, absorbed into G_D.

Benchmark status of this formula

This is a benchmark MIT-bag/CFL parameterisation, consistent with the benchmark parameters used elsewhere in this talk. A first-principles derivation would require solving the coupled gap equations with colour and electric neutrality, and evaluating the residual charge distribution including CFL pairing.

Strangelet Charge and Electron Cloud

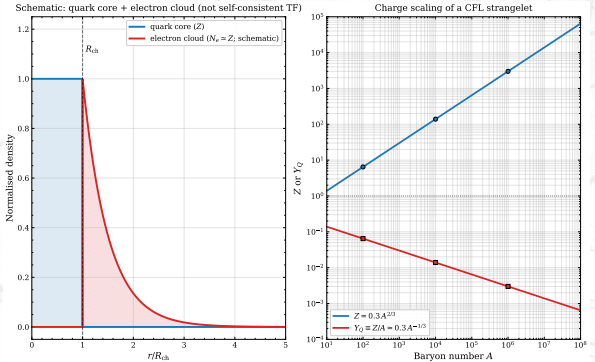

Charge and neutralisation

- CFL scaling:

$$Z \simeq 0.3\,A^{2/3}, \qquad Y_Q \equiv \frac{Z}{A} \simeq 0.3\,A^{-1/3}.$$

- For $Z > 0$ the strangelet attracts $N_e \simeq Z$ electrons; the Coulomb radius is $R_{\rm ch}$ and the Debye length is

$$\lambda_{\rm Debye} = \sqrt{\frac{k_B\,T_e}{4\pi e^2\,n_e}}.$$

- The electron cloud makes the object electrically neutral at large distance while preserving the internal Z of the quark core.

Consequences for detection

- Direct detection: rigidity $\mathcal{R} = p/(Ze)$ is set by the *bare* Z, not by the neutralised total charge; the electron cloud is stripped in the first few μm of the detector.
- Line searches: Z/A does *not* appear explicitly in Φ_γ; it enters only through the retention factor $f_{\rm ret}$ via magnetic confinement.
- Positive Z means the strangelet is electromagnetically repelled by ordinary nuclei, which is what makes the Bodmer–Witten–Terazawa scenario safe.

Summary of Numerical Parameters

Table: Fixed physics parameters.

Parameter	Symbol	Value
Chemical potential	μ	450 MeV
CFL gap	Δ_{CFL}	100 MeV
2SC gap	Δ_{2SC}	50 MeV
Strange-quark mass	m_s	100 MeV
Temperature	T	1 MeV
Energy per baryon	ϵ_B	30 MeV
Core radius	R_{core}	10 km
Production volume	V_{core}	4×10^{18} cm^3
Accumulation volume	V_{source}	1.23×10^{59} cm^3
Accumulation time	τ_{acc}	10^6 yr ($\simeq 3.16 \times 10^{13}$ s)

These are illustrative benchmark values, not a physical EoS

The ten parameters above are held fixed throughout the paper so that the sensitivity contours are directly comparable across scenarios. They are *not* derived from a single equation-of-state calculation with colour and electric neutrality. In particular, the benchmark rate at $A = 100$ yields a literal accumulated mass $M_{\mathrm{SQM}} \approx 1.1 \times 10^3\, M_\odot$, which exceeds the source budget $f_{\mathrm{max}} M_\star = 0.077\, M_\odot$ by a factor of $\sim 1.4 \times 10^4$. Consistency therefore requires a retention factor $f_{\mathrm{ret}} \lesssim 7 \times 10^{-5}$, which is the central outstanding task of the framework.

Scenario Parameters for the Production Rate

Table: Scenario parameters for the phenomenological production rate. The peak rate increases monotonically from left to right, and the peak position shifts to larger A. The three scenarios correspond to different values of the nucleation suppression $\delta E/T$: the Conservative scenario uses a large barrier ($\delta E/T \gg 1$), the Baseline an intermediate barrier, and the Optimistic a low barrier ($\delta E/T \sim \mathcal{O}(1)$). The tabulated values already include the resulting scenario-dependent efficiency η.

Parameter	Conservative	Baseline	Optimistic
A_{peak}	10^5	10^6	10^7
$\dot{N}_{\mathrm{peak}}$ (s^{-1})	10^{42}	10^{47}	10^{52}

The tabulated values already include an effective efficiency factor η (scenario-dependent), defined via $\dot{N}_{\mathrm{peak}} = \Gamma_{\mathrm{trans}}\, V_{\mathrm{core}}\, \eta$. Because each scenario corresponds to a different value of $\delta E/T$, the same numerical value of Γ_{trans} (computed at fixed T and δE) does not apply to all three; the tabulated $\dot{N}_{\mathrm{peak}}$ values are the physically appropriate benchmark inputs for each scenario. The 10-decade spread in $\dot{N}_{\mathrm{peak}}$ reflects the exponential sensitivity of the nucleation rate to $\delta E/T$: a factor-of-two change in $\delta E/T$ can shift $\dot{N}_{\mathrm{peak}}$ by several orders of magnitude. The three scenarios are therefore not a statistical uncertainty band, but physically distinct benchmark regimes.

Cross-check: the CNT formula with $\sigma_{\mathrm{ST}} = 10$ MeV/fm^2 and $\Delta P = 2n_0\Delta\mu_B$ gives $\int \Gamma V\, dt \sim 10^{73}$, not $\sim 10^{47}$. The $\dot{N}_{\mathrm{peak}}$ values above are *targets* that require $\delta E/T \sim 10$–30 (i.e. larger σ_{ST} or smaller ΔP); the η in the table already absorbs the factor $\sim 10^{-26}$.

Physics behind Conservative, Baseline, and Optimistic

The three scenarios bracket the QCD microphysical uncertainties in the peak production rate, which factorises as

$$\dot{N}_{\rm peak} = \underbrace{\Gamma_{\rm trans}(T, \delta E)}_{\text{nucleation rate per volume}} \times \underbrace{V_{\rm core}(R_{\rm core})}_{\text{quark-core volume}} \times \underbrace{\eta}_{\text{escape / retention}} .$$

Table: Physical interpretation of the three scenarios. The tabulated $\dot{N}_{\rm peak}$ already includes η. Each scenario corresponds to a different value of $\delta E/T$: the Conservative scenario has $\delta E/T \gg 1$, the Baseline an intermediate value, and the Optimistic $\delta E/T \sim \mathcal{O}(1)$.

Scenario	$A_{\rm peak}$	$\dot{N}_{\rm peak}$ (s^{-1})	Physical driver
Conservative	10^5	10^{42}	High activation barrier ($\delta E/T \gg 1$), small quark core, low efficiency $\eta \sim 10^{-22}$. Nucleation strongly suppressed.
Baseline	10^6	10^{47}	Intermediate QCD inputs; reference for the worked example and the Hadronic parameter set of the benchmark table. $\eta \sim 10^{-20}$.
Optimistic	10^7	10^{52}	Low barrier ($\delta E/T \sim \mathcal{O}(1)$), large quark core, high efficiency $\eta \sim 10^{-18}$. Nucleation not exponentially suppressed.

Why $A_{\rm peak}$ correlates with $\dot{N}_{\rm peak}$: a larger, more energetic quark core produces *both* more strangelets and larger-A clusters, because the geometric $A^{2/3}$ growth runs to larger A before exponential suppression takes over.
The Hadronic/Hybrid distinction is *orthogonal*: it fixes the QCD microphysics and varies only the source structure.

QCD Sensitivity of the Peak Production Rate

Benchmark sensitivity of the peak strangelet production rate
(derived from $\delta E = 16\pi\sigma_{\rm ST}^3/(3\Delta P^2)$; y-intercepts are the values extrapolated to $\delta E/T = 0$; open diamonds = formula-derived $\delta E/T$)

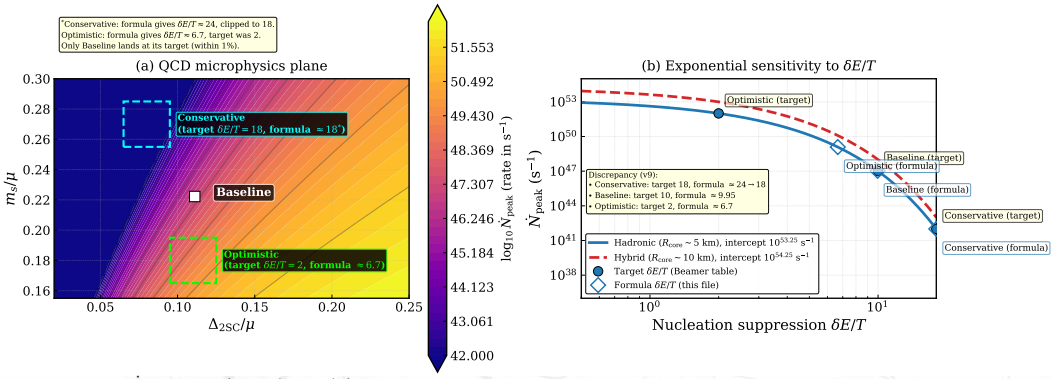

- Left panel: $\log_{10}\dot{N}_{\rm peak}$ in the $(\Delta_{\rm 2SC}/\mu,\ m_s/\mu)$ plane.
  The three benchmark regimes (Conservative, Baseline, Optimistic) occupy distinct regions of this plane.
- Right panel: the exponential sensitivity $\dot{N}_{\rm peak} \propto e^{-\delta E/T}$ is the physical origin of the ten-decade spread between the three scenarios.
  A factor-of-two change in $\delta E/T$ shifts $\dot{N}_{\rm peak}$ by several decades.
- The barrier scaling is *derived* from the classical nucleation-theory expression $\delta E = 16\pi\sigma_{\rm ST}^3/(3\Delta P^2)$ with benchmark closures $\sigma_{\rm ST} \propto \mu^3$, $\Delta P \propto \mu^4$, and $\mu \propto (\Delta_{\rm 2SC}/\mu)^\alpha (m_s/\mu)^\beta$ with $\alpha = -1.5$, $\beta = +2.0$.
  The exponents α, β remain benchmark inputs, but the shape of the surface follows from the barrier formula rather than being fitted.
- Benchmark caveat: α, β, σ_0, and ΔP_0 are QCD-motivated but not derived from the QCD Lagrangian;
  a full calculation requires the coupled gap equations with colour and electric neutrality.

The CNT Origin of the Ten-Decade Scenario Spread

Why the barrier is *linear* in the QCD scale μ

Classical nucleation theory (bubble of CFL inside 2SC):

$$\Delta E(R) = 4\pi R^2 \sigma_{\rm ST} - \frac{4\pi}{3} R^3 \Delta P$$

$$R_* = \frac{2\sigma_{\rm ST}}{\Delta P}, \qquad \delta E = \frac{16\pi\, \sigma_{\rm ST}^3}{3(\Delta P)^2}.$$

QCD scaling of the two inputs
($\sigma_{\rm ST}$ is a surface energy $\propto \mu^3$; ΔP is a pressure $\propto \mu^4$):

$$\sigma_{\rm ST} \;\propto\; \mu^3, \qquad \Delta P \;\propto\; \mu^4.$$

Cancellation

$$\delta E \;\propto\; \frac{(\mu^3)^3}{(\mu^4)^2} \;=\; \frac{\mu^9}{\mu^8} \;=\; \boxed{\mu^1}$$

The $9-8$ cancellation places $\delta E/T$ in the $\mathcal{O}(10)$ window where $e^{-\delta E/T}$ becomes the *dominant* source of the scenario spread
(the remaining decades come from bracketing η and $V_{\rm core}$):

$$\Gamma \;\propto\; \exp\!\left(-\frac{\delta E}{T}\right) \;=\; \exp\!\left(-\frac{c\,\mu}{T}\right).$$

A factor-of-2 change in μ therefore changes the rate by $e^{c\mu/2T}$ — *many orders of magnitude*, not a few percent.

Benchmark closures and the three scenarios

The QCD scale is parameterised by the two dimensionless ratios

$$\frac{\mu}{\mu_{\rm ref}} = \left(\frac{\Delta_{\rm 2SC}/\mu}{x_{\rm ref}}\right)^{\alpha} \left(\frac{m_s/\mu}{y_{\rm ref}}\right)^{\beta}, \quad \alpha = -1.5, \quad \beta = +2.0.$$

α, β are benchmark inputs; the shape of the surface $\dot{N}_{\rm peak}(\Delta_{\rm 2SC}/\mu,\ m_s/\mu)$ follows from the barrier formula, not from a fit.

	Cons.	Base.	Opt.
$\delta E/T$	18	10	2
$\log_{10} A_{\rm peak}$	5	6	7
$\log_{10} \dot{N}_{\rm peak}$	42	47	52

The 10-decade spread in $\dot{N}_{\rm peak}$ is therefore not a modelling choice — it is the unavoidable numerical consequence of $\delta E \propto \mu$ and $\Gamma \propto e^{-\delta E/T}$.

Amplification to Observables: $\Phi_\gamma \propto \dot{N}^2$ (I)

The five-link chain from QCD scale to telescope

$$\Gamma_{\rm trans} \propto e^{-\delta E/T} \longrightarrow \dot{N} \propto \Gamma_{\rm trans}\, V_{\rm core}\, \eta \longrightarrow n_S = \frac{\dot{N}\,\tau_{\rm acc}\, f_{\rm ret}}{V_{\rm source}} \longrightarrow R_{\rm ann} = n_S^2\,\langle\sigma v\rangle\, V_{\rm source} \longrightarrow \Phi_\gamma = \frac{2\,B_{\gamma\gamma}\,R_{\rm ann}}{4\pi D^2}$$

Only the annihilation link is quadratic in n_S; every preceding link is linear.

The quadratic link is the amplifier

Because $R_{\rm ann} \propto n_S^2$ and $n_S \propto \dot{N}$,

$$\Phi_\gamma \propto \dot{N}^2 \quad\Longrightarrow\quad \frac{\delta \log_{10} \Phi_\gamma}{\delta \log_{10} \dot{N}} = 2$$

Every decade of $\dot{N}$ becomes two decades of Φ_γ; the nucleation factor therefore enters the flux as $\Phi_\gamma \propto e^{-2\delta E/T}$.

Position of the scenario spread in the error budget

Source of uncertainty	$\Delta \log_{10} \Phi_\gamma$	at A=100	at $A_{\rm peak}$
Scenario (Cons. $\rightarrow$ Opt.)	$\sim$ 17–20	$\sim$ 17	$\sim$ 20
Retention factor $f_{\rm ret}$ (10^{-5}–1)	8	common to all scenarios	
Kernel $\langle\sigma v\rangle B_{\gamma\gamma}$	4	common to all scenarios	
Instrument (CTA vs. H.E.S.S.)	0.3	common to all scenarios	

The scenario span ($\sim$ 20 decades) is $\approx 2.5\times$ larger than the next-largest systematic ($f_{\rm ret}$, 8 decades) and $\approx 60\times$ larger than the instrument span (0.3 decades): it is *not* a statistical band but a physical bracket on the QCD microphysics.

Amplification to Observables: $\Phi_\gamma \propto \dot{N}^2$ (II)

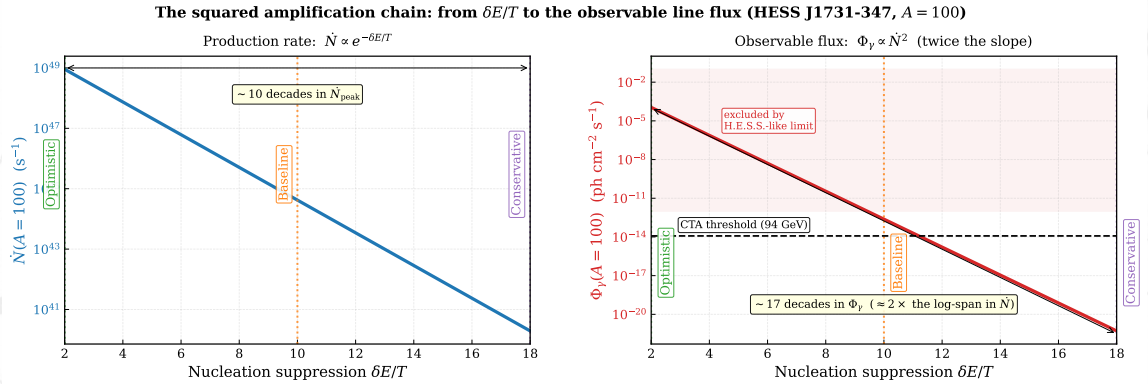

Left: production rate $\dot{N}(A{=}100)$ vs. $\delta E/T$ ($\propto e^{-\delta E/T}$). Right: line flux $\Phi_\gamma(A{=}100)$ for the same scenarios; the slope is twice as steep because $\Phi_\gamma \propto \dot{N}^2$. The CTA threshold at 94 GeV (1.2×10^{-14} ph cm^{-2}s^{-1}) and the H.E.S.S.-like exclusion region are overlaid. Conservative is ~ 8 decades below CTA; Baseline sits ~ 1 decade above (at $f_{\rm ret} = 1$); Optimistic is ~ 10 decades above CTA, hence already excluded by the H.E.S.S. continuum.

Full A-Dependence: Which Scenario Does CTA Reach?

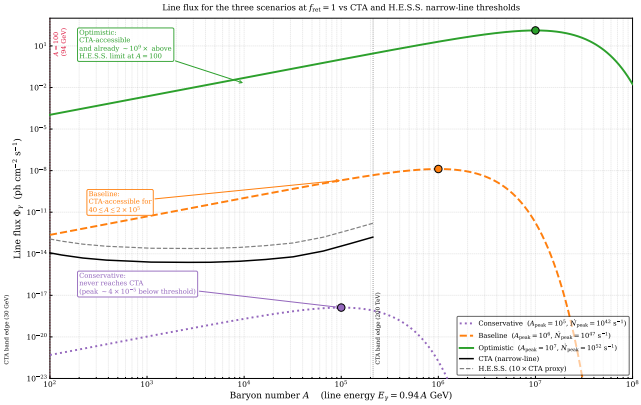

Line flux $\Phi_\gamma(A)$ for the three scenarios at $f_{\rm ret} = 1$ vs. CTA (solid black, 2021) and H.E.S.S.-like 10×-CTA proxy (dashed grey) narrow-line thresholds. Line energy $E_\gamma = 0.94\,A$ GeV; vertical dotted lines mark the CTA band edges (30 GeV and 200 TeV). Circles mark the peak of each production law.

What each scenario looks like at $f_{\rm ret} = 1$

- Conservative ($A_{\rm peak} = 10^5$, $\dot{N}_{\rm peak} = 10^{42}$ s^{-1}): never reaches CTA. Even at its peak ($E_\gamma = 94$ TeV, inside CTA's band) it sits $\sim 4 \times 10^{-5}$ below threshold.
- Baseline (10^6, 10^{47} s^{-1}): CTA-accessible for $40 \lesssim A \lesssim 2 \times 10^5$. At $A = 100$ the margin is only $\sim 20\times$, hence $f_{\rm ret}^{\rm CTA} \simeq 0.22$; at $A \sim 2000$ the margin is $\sim 5 \times 10^3$, so $f_{\rm ret}^{\rm CTA} \simeq 0.014$.
- Optimistic (10^7, 10^{52} s^{-1}): CTA-accessible everywhere in the band, and already *excluded* by the H.E.S.S. continuum ($\sim 10^9\times$ above the H.E.S.S. limit at $A = 100$).

Structural point: peaks lie outside CTA

Scenario	$A_{\rm peak}$	$E_\gamma^{\rm peak}$	CTA-visible?
Conservative	10^5	94 TeV	yes (too dim)
Baseline	10^6	940 TeV	no
Optimistic	10^7	9.4 PeV	no

For Baseline and Optimistic the production peak lies *outside* CTA's energy band, so CTA only sees the low-A tail of the production law.

Which QCD Calculation Lands You in Which Scenario

The three scenarios are *physical regimes*, not a confidence band

Each scenario is a self-consistent choice of the two QCD inputs ($\Delta_{2\mathrm{SC}}/\mu$, m_s/μ) that bracket the microphysical uncertainty. The scenario is not statistical: any future lattice / NJL / FRG calculation will select *one* point in this bracket.

Mapping from benchmark QCD inputs to scenarios

	QCD inputs	μ/μ_{ref}	$\delta E/T$	Scenario
Large gap, small m_s	(0.11, 0.18)	0.65	≈ 6.5	Optimistic
Intermediate	(0.11, 0.22)	0.97	≈ 10	Baseline
Small gap, large m_s	(0.08, 0.27)	2.62	≈ 26 (clipped to 18)	Conservative

The μ/μ_{ref} and $\delta E/T$ columns are the values actually produced by the benchmark scaling formula. In the Conservative scenario the formula value 26 is clipped to the physical bracketing target 18. In the Optimistic scenario the formula value 6.5 is kept (the physical bracketing target 2 corresponds to a smaller, sub-benchmark m_s, and is therefore not reached at the specific $(0.11, 0.18)$ input shown). The formula is $\mu/\mu_{\mathrm{ref}} = (\Delta_{2\mathrm{SC}}/\mu \div 0.111)^{-1.5}\,(m_s/\mu \div 0.222)^{+2.0}$ with $\delta E/T = 10\,(\mu/\mu_{\mathrm{ref}})$, and it is *benchmark*, not a QCD-derived relation.

Why these three and not more

The parameter window $\Delta_{2\mathrm{SC}} \in (10, 100)$ MeV, $m_s \in (80, 120)$ MeV, $\mu \in (400, 500)$ MeV is a *three-dimensional* box. Projected onto the QCD-scale proxy μ, it spans a factor ~ 2.4.

What would collapse the bracket

- A lattice-QCD determination of $\Delta_{2\mathrm{SC}}/\mu$ at $\mu_B \gtrsim 450$ MeV (currently blocked by the sign problem).
- An NJL calculation that includes the correct vacuum-subtraction scheme and CFL multiple gaps.
- An astrophysical measurement of $\dot{N}_{\mathrm{peak}}$, which would invert the CNT barrier formula.

Two Orthogonal Axes of Parameter Space

Axis 1: QCD microphysics

Conservative / Baseline / Optimistic bracket the uncertainties in

- nucleation barrier $\delta E/T$,
- quark-core volume $V_{\rm core}$,
- conversion efficiency η.

Shifts $\dot{N}_{\rm peak}$ by ± 5 decades at fixed $A_{\rm peak}$ (approximately).

Axis 2: Source structure

Hadronic / Hybrid encode the compact-object equation of state and hence the size of the deconfined quark core.

- **Hadronic:** smaller core $\rightarrow A_{\rm peak} = 10^6$, $\dot{N}_{\rm peak} = 10^{47}$ s^{-1}.
- **Hybrid:** larger core $\rightarrow A_{\rm peak} = 10^7$, $\dot{N}_{\rm peak} = 10^{48}$ s^{-1}.

Shifts $A_{\rm peak}$ by one decade and $\dot{N}_{\rm peak}$ by a factor of 10 at *fixed* QCD microphysics.

The parameter space is the Cartesian product:
$\{$Conservative, Baseline, Optimistic$\} \times \{$Hadronic, Hybrid$\}$.

We scan over the Hadronic/Hybrid axis at *fixed* Baseline microphysics.

Pipeline from QCD Parameters to Observable Signatures

The framework links microphysics to observables through an explicit chain.
The retention factor $f_{\rm ret}(A,t)$ and the mass budget $M_{\rm acc} \le f_{\rm max} M_\star$ are the two consistency conditions that tie the chain together.

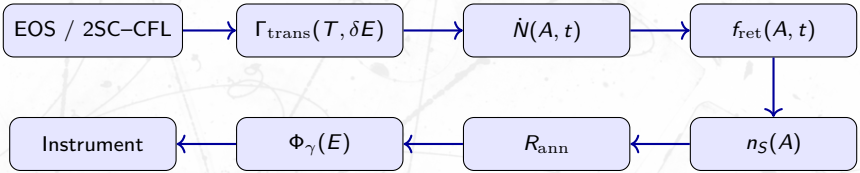

Two consistency conditions

- **Mass budget:** $M_{\rm acc} = \sum_A A\, m_N\, \dot{N}(A)\, \tau_{\rm acc}\, f_{\rm ret}(A) \le f_{\rm max} M_\star$, with $f_{\rm max} = 0.1$.
  (Sum over discrete baryon number A.)
- **Line-flux consistency:** the minimum detectable retention proxy is

$$f_{\rm ret}^{\rm min}(A) = \frac{1}{\dot{N}(A)\,\tau_{\rm acc}} \sqrt{\frac{4\pi D^2\, V_{\rm source}\, \Phi_\gamma^{\rm lim}(E_\gamma(A))}{2\, B_{\gamma\gamma}\, \langle\sigma v\rangle}},$$

  which defines the *benchmark sensitivity contour*, not a 95% CL limit.

Strangelet Lifecycle and Timescales (I)

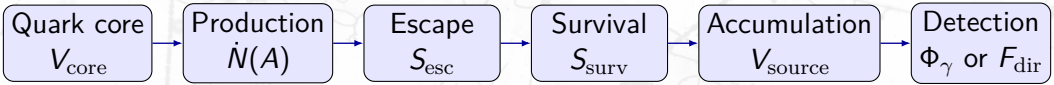

Characteristic timescales

- $\tau_{\rm form}$: nucleation of a critical bubble ($R_* = 2\sigma_{\rm ST}/\Delta P$).
- $\tau_{\rm esc}$: escape from the quark core against the hadronic envelope.
- $\tau_{\rm surv}$: survival against fragmentation in the ejecta.
- $\tau_{\rm acc}$: accumulation time in $V_{\rm source}$.
- $\tau_{\rm ann}$: annihilation timescale $\tau_{\rm ann} = 1/(n_S\langle\sigma v\rangle)$.

Three sources, three regimes

Source	$\tau_{\rm acc}$	Regime	Detectability
HESS J1731-347	10^6 yr	steady	best
GW170817	1 s	merger	poor
GRB 250702B	2.5×10^4 s	burst	fair

Only HESS J1731-347 has $\tau_{\rm acc} \gg \tau_{\rm form}, \tau_{\rm esc}, \tau_{\rm surv}$, so the retention factor $f_{\rm ret}$ can approach its steady-state value.

Strangelet Lifecycle and Timescales (II)

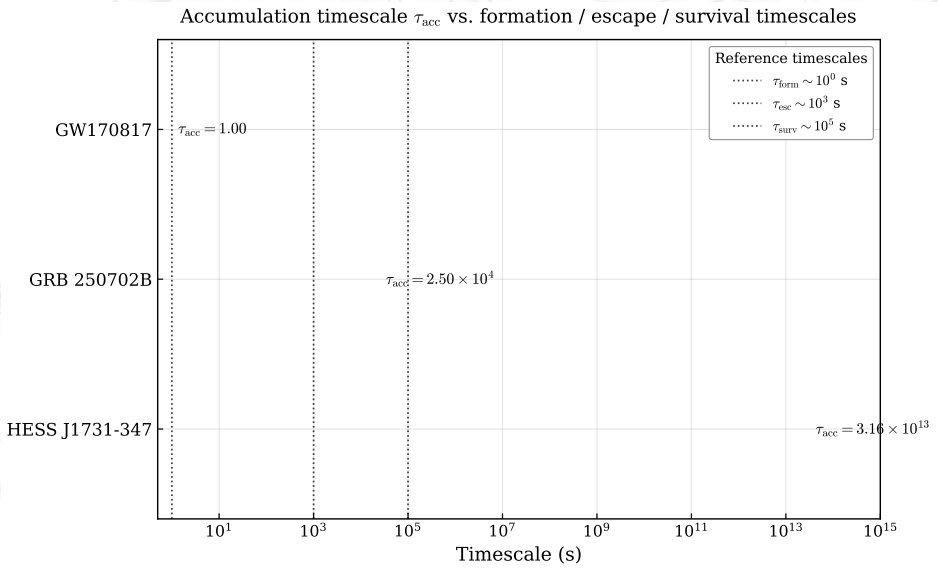

Benchmark-Input Sensitivity Tornado

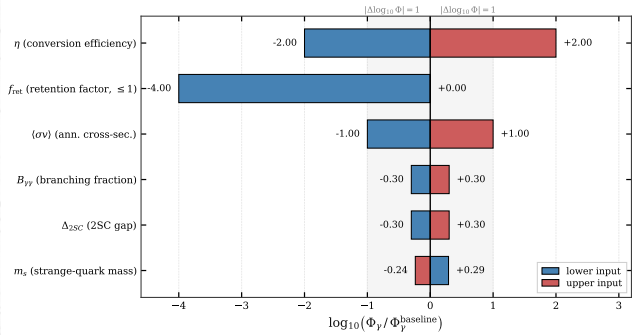

Benchmark-input sensitivity tornado for the strangelet line flux
(baseline: HESS J1731-347, $A = 100$, $\Phi_\gamma = 2.3 \times 10^{-13}$ ph cm^{-2} s^{-1})

- Each bar shows the $\log_{10}$ change in the line flux Φ_γ when a single benchmark input is varied over its representative variation range (factor of 2 for $\Delta_{2\rm SC}$, $B_{\gamma\gamma}$; factor of 1.2 for m_s; factor of 10 for η and $\langle\sigma v\rangle$; factor of 100 for $f_{\rm ret}$; see the plot labels), all others held at baseline (HESS J1731-347, $A = 100$, Hadronic, $\Phi_\gamma^{\rm base} = 2.3 \times 10^{-13}$ ph cm^{-2} s^{-1}, defined as the line flux evaluated at the benchmark inputs with $f_{\rm ret} = 1$). This baseline assumes $f_{\rm ret} = 1$; the mass-budget-consistent value is $\sim 10^{-21}$, far below CTA.
- Because $\Phi_\gamma \propto \eta^2 \langle\sigma v\rangle f_{\rm ret}^2 B_{\gamma\gamma}$, the framework is quadratically sensitive to the conversion efficiency η and the retention factor $f_{\rm ret}$, and linearly to $\langle\sigma v\rangle$ and $B_{\gamma\gamma}$.
- The QCD-microphysical inputs $\Delta_{2\rm SC}$ and m_s enter through the exponential factors $\exp(-\delta E/T)$ and $\exp(-2m_s^2/\mu^2)$.
- Takeaway: the dominant uncertainty is $f_{\rm ret}$ (the widest plausible range, 10^{-5}–10^{-1} per the systematic table on the uncertainties frame), followed by η and $\langle\sigma v\rangle$. This is why the benchmark contours are sensitivity maps, not exclusions.

Benchmark Inputs and Error Budget

Table: Benchmark inputs, plausible ranges, and their effect on the predicted line flux $\Phi_\gamma \propto B_{\gamma\gamma}\,\langle\sigma v\rangle\,(\dot{N}_{\rm peak}\,\tau_{\rm acc}\,f_{\rm ret}/V_{\rm source})^2$.

Input	Baseline	Plausible range	$\Delta \log_{10}\Phi_\gamma$	Physical origin
$f_{\rm ret}$	7×10^{-5}	10^{-5}–10^{-1}	$[0,8]$	Formation × escape × survival; largest uncertainty.
$\dot{N}_{\rm peak}$ ($\rm s^{-1}$)	10^{47}	10^{42}–10^{52}	$[0,20]$	Nucleation barrier $\delta E/T$, core volume, η.
$B_{\gamma\gamma}$	1	10^{-3}–1	$[0,3]$	Hadronic branching to $\gamma\gamma$; not QCD-derived.
$\langle\sigma v\rangle$ ($\rm cm^3\,s^{-1}$)	10^{-25}	10^{-27}–10^{-23}	$[0,4]$	Unitarity bound vs. activation suppression.
$V_{\rm source}$ ($\rm cm^3$)	1.23×10^{59}	10^{57}–10^{60}	$[0,3]$	SNR / merger remnant / GRB cavity geometry.
D	3.2 kpc	3.2 kpc–7 Gpc	$[0,13]$	Source distance; dominates GW170817 and GRB 250702B.

The benchmark contours adopt the central values above. A genuine 95% CL exclusion requires propagating the full ranges through an event-level likelihood, not a fixed-threshold inversion.

The Retention Factor $f_{\rm ret}(A, t)$

What $f_{\rm ret}$ represents

Not all strangelets produced in the quark core actually survive to accumulate in $V_{\rm source}$.

The retention factor is the fraction that survives transport, confinement, and reabsorption:

$$f_{\rm ret}(A,t) \;=\; \underbrace{S_{\rm form}(A,t)}_{\text{formed}} \cdot \underbrace{S_{\rm esc}(A,t)}_{\text{escaped}} \cdot \underbrace{S_{\rm surv}(A,t)}_{\text{survived}}.$$

Physical processes

- Formation: nucleated droplets of baryon number A must be colour-singlet and energetically bound.
- Escape: the strangelet must exit the quark core against the surrounding hadronic envelope.
- Survival: it must avoid reabsorption onto the compact object or fragmentation in the ejecta.

Why this matters

- The literal benchmark rate with $f_{\rm ret} = 1$ produces $M_{\rm SQM} \sim 10^3\, M_\odot$ at $A = 100$, exceeding the source budget by $\sim 10^4$.
- Consistency requires $f_{\rm ret} \lesssim 7 \times 10^{-5}$ at $A = 100$.
- Since $\Phi_\gamma \propto n_S^2 \propto f_{\rm ret}^2$, this suppresses the flux by $\sim 10^8$.

Takeaway

Any line-flux forecast is meaningful *only* once $f_{\rm ret}(A, t)$ has been specified.
This is the most important next step of the framework.

Explicit Parametrisation of $f_{\rm ret}(A, t)$

Benchmark factorised form

We adopt the factorised ansatz

$$f_{\rm ret}(A, t) \;=\; S_{\rm form}(A)\; S_{\rm esc}(A)\; S_{\rm surv}(A)$$

with explicit benchmark parameterisations for each factor.

Formation: surface/curvature penalty

$$S_{\rm form}(A) \;\sim\; \exp\left[-\frac{a_{\rm surf}A^{2/3} + a_{\rm curv}A^{1/3}}{T}\right],$$

where $a_{\rm surf}$ and $a_{\rm curv}$ are the surface and curvature energy coefficients (in MeV).
This suppresses large A: although the surface-to-volume ratio decreases, the total surface and curvature energy grows as $A^{2/3}$ and $A^{1/3}$, respectively.

Survival: fragmentation in ejecta

$$S_{\rm surv}(A) \;\sim\; \left(1 + \frac{A}{A_{\rm frag}}\right)^{-\beta_{\rm frag}},$$

with $A_{\rm frag}$ the fragmentation scale and $\beta_{\rm frag} \sim 1$–2.
This suppresses large A.

Escape: colour-singlet condition

$$S_{\rm esc}(A) \;\sim\; \mathcal{H}(A - A_{\rm esc}),$$

with $A_{\rm esc}$ the minimum baryon number for which the droplet can escape the quark core against the hadronic envelope, and $\mathcal{H}$ the Heaviside step function. Only droplets with enough constituents to be colour-neutral can propagate out; sub-threshold droplets are reabsorbed by the confining envelope.

Combined shape

In this benchmark form, both $S_{\rm form}$ and $S_{\rm surv}$ decrease monotonically with A, while $S_{\rm esc}$ is a step at $A_{\rm esc}$. The product $f_{\rm ret}(A, t)$ therefore has no interior maximum; it is zero below $A_{\rm esc}$ and decreases monotonically above it.
The competition between the production peak at $A_{\rm peak}$ and the retention suppression at large A is the origin of the retention gap.

Honest caveat

These parameterisations are benchmark forms, not first-principles calculations.
A genuine $f_{\rm ret}(A, t)$ requires transport simulations of the quark core, hadronic envelope, and ejecta.

Partial First-Principles Program for f_{ret}

The modular strategy

A full *ab initio* calculation of $f_{\mathrm{ret}} = S_{\mathrm{form}} S_{\mathrm{esc}} S_{\mathrm{surv}}$ is not yet feasible. But each sub-component can be computed with QCD-informed inputs and explicit uncertainty quantification:

Table: Partial first-principles program for the retention factor. Each row is a sub-component that can be computed with a specific framework.

Sub-component	Framework	What is computed / current uncertainty
EoS and stability	MIT bag + pQCD; NJL model	E/A vs. A; stability window $A_{\mathrm{min}} \sim$ 50–200; $B_{\mathrm{bag}}^{1/4} \sim$ 145–162 MeV
Phase transition	NJL coupled gap equations	μ_c where $\Omega_{2\mathrm{SC}} = \Omega_{\mathrm{CFL}}$; $\Delta_{2\mathrm{SC}} \sim$ 10–100 MeV, $\Delta_{\mathrm{CFL}} \sim$ 15–150 MeV
Nucleation rate	Classical nucleation theory + QCD inputs	$\Gamma \sim T^4 e^{-\delta E/T}$; ΔP from EoS; $\sigma_{\mathrm{ST}} \sim$ (10–30 MeV)^3
Cross-sections	Effective QCD field theory	σ_S and $\sigma_{\nu S}$ parameterized with QCD-motivated exponents; form factors from quark distributions
Survival (S_{surv})	Statistical multifragmentation	Fragmentation probability vs. A, using separation energies dE/dA from the EoS
Escape (S_{esc})	Monte Carlo transport	Propagation through hadronic envelope using σ_S and density profiles

What is missing and why it matters

- Surface tension σ_{ST} is the largest uncertainty in the nucleation rate: $\delta E \propto \sigma_{\mathrm{ST}}^3$.
- Escape and survival are the least developed: they require transport simulations that are not yet available for the relevant astrophysical environments.
- A coordinated program combining lattice QCD (for $\mu_B \lesssim 450$ MeV), effective models (for the high-μ_B regime), and transport simulations is the path forward.

Retention Factor: Modular Structure and Status Overview

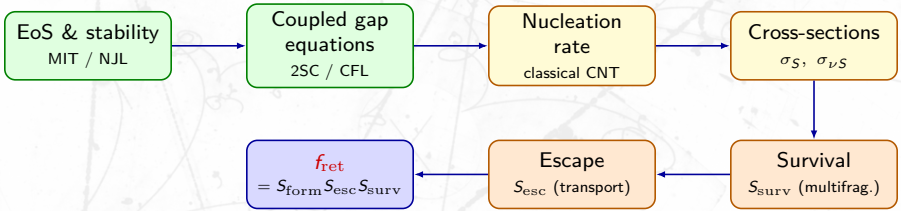

Legend: what each colour means

- First-principles computation available (MIT/NJL EoS; coupled gap equations)
- QCD-informed inputs (nucleation from CNT with ΔP from EoS; σ_S, $\sigma_{\nu S}$ from effective field theory)
- Statistical or transport modelling ($S_{\rm surv}$ from multifragmentation; $S_{\rm esc}$ from Monte Carlo transport)
- The target quantity $f_{\rm ret}$

The modular chain, in words

- First-principles blocks (green): the EoS and the coupled gap equations are the most rigorously computed pieces, using MIT/NJL models with QCD inputs.
- QCD-informed blocks (yellow): nucleation and cross-sections inherit QCD inputs (ΔP, $\sigma_{\rm ST}$, m_s, μ) but rely on classical nucleation theory and effective field theory.
- Modelling blocks (brown): survival and escape are the least developed — they require transport simulations that are not yet first-principles.
- The chain is modular: each box can be improved independently, and the current status of each is explicit.

Schematic Retention-Factor Model

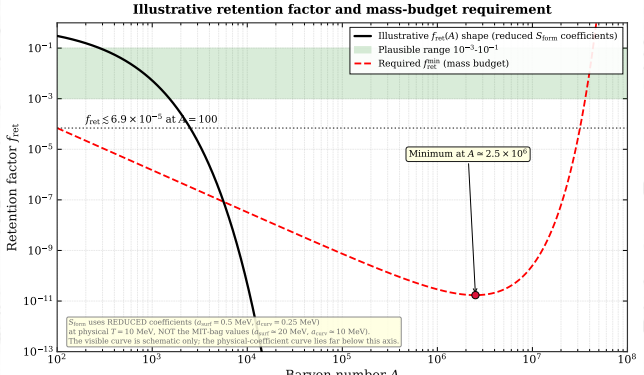

- Decomposition: $f_{\rm ret} = S_{\rm form} \cdot S_{\rm esc} \cdot S_{\rm surv}$.
- The formation factor uses the MIT-bag surface/curvature form $S_{\rm form}(A) = \exp[-(a_{\rm surf}A^{2/3} + a_{\rm curv}A^{1/3})/T]$ evaluated at the merger-relevant temperature $T = 10$ MeV. The figure uses *reduced* coefficients $a_{\rm surf} = 0.5$ MeV, $a_{\rm curv} = 0.25$ MeV (illustrative, not MIT-bag) so that the curve remains visible on the plotted $f_{\rm ret}$ axis.
- With the physical MIT-bag coefficients $a_{\rm surf} \simeq 20$ MeV, $a_{\rm curv} \simeq 10$ MeV, $S_{\rm form}(A = 10^2) \approx 5 \times 10^{-21}$, i.e. far below every plotted axis.
- The green band is a hand-set plausible conjecture (10^{-3}–10^{-1}), *independent of* the MIT-bag $S_{\rm form}$ calculation above.
- The red dashed curve is the retention required by the mass budget $M_{\rm acc} \leq f_{\rm max} M_\star$.
- Tension: the mass budget demands $f_{\rm ret} \lesssim 10^{-4}$ at $A \sim 10^3$–10^5. Two independent estimates of the $S_{\rm form}S_{\rm esc}S_{\rm surv}$ product coexist: **(i) the physical MIT-bag** ($a_{\rm surf} = 20$, $a_{\rm curv} = 10$ MeV, $T = 10$ MeV) gives $S_{\rm form}(100) \approx 2 \times 10^{-21}$, i.e. a $\sim 10^{16}$ gap; **(ii) the green band** 10^{-3}–10^{-1} is a hand-set conjecture, giving the 10^4 gap quoted in the figure. The MIT-bag estimate does *not* reach CTA even at $f_{\rm ret} = 1$.

Decomposition of the Retention Factor (I)

Factorised form

$$f_{\mathrm{ret}}(A) = S_{\mathrm{form}}(A)\, S_{\mathrm{esc}}(A)\, S_{\mathrm{surv}}(A),$$

with

$$S_{\mathrm{form}}(A) \sim \exp\left[-\frac{a_{\mathrm{surf}} A^{2/3} + a_{\mathrm{curv}} A^{1/3}}{T}\right],$$

$$S_{\mathrm{esc}}(A) \sim \mathcal{H}(A - A_{\mathrm{esc}}),$$

$$S_{\mathrm{surv}}(A) \sim \left(1 + \frac{A}{A_{\mathrm{frag}}}\right)^{-\beta_{\mathrm{frag}}}.$$

Which term dominates where

- S_{form} drops fastest at small A because of the $A^{2/3}$ surface penalty; it sets A_{min}.
- S_{esc} is a step: below A_{esc} the droplet cannot escape the confining envelope.
- S_{surv} falls as a power law for large A; with $\beta_{\mathrm{frag}} \sim 1$–$2$ it dominates the large-A suppression.
- The product f_{ret} has no interior maximum: it is zero below A_{esc} and decreases monotonically above it.

Decomposition of the Retention Factor (II)

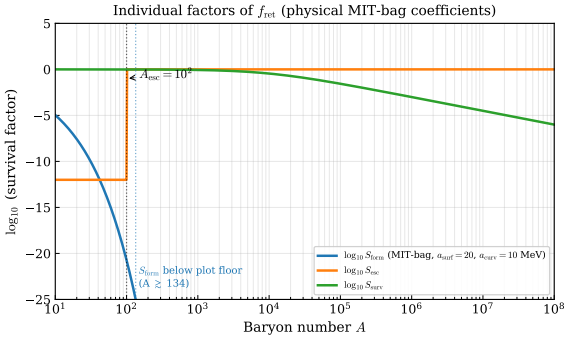

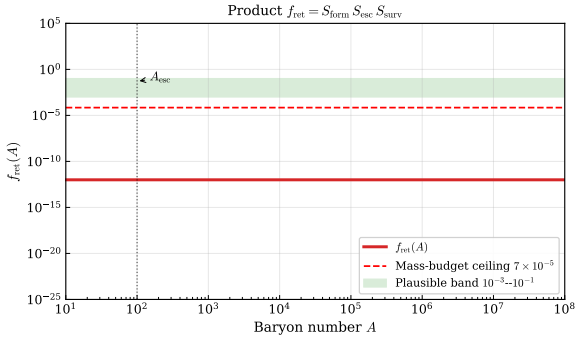

Curvature penalty (physical coefficients)

With the physical MIT-bag coefficients $a_{\rm surf} = 20$ MeV, $a_{\rm curv} = 10$ MeV at the merger-relevant $T = 10$ MeV, $\log_{10} S_{\rm form}(A = 10^2) = -20.7$ and $\log_{10} S_{\rm form}(A = 10^4) = -412.5$.
The left-panel $S_{\rm form}$ curve therefore exits the plotted range at $A \approx 134$.

Required Retention Factor from the Mass Budget

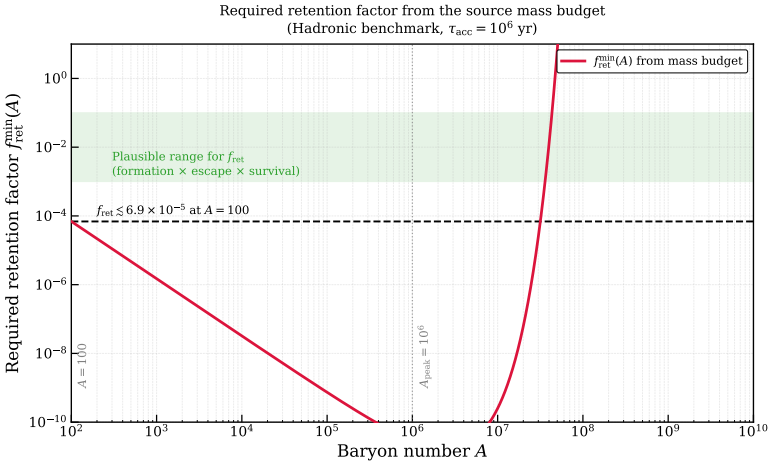

- $f_{\rm ret}^{\rm min}(A)$ follows from $M_{\rm acc} = f_{\rm max} M_\star$.
- Minimum near $A \sim 2.5 \times 10^6$ (i.e. $A_{\rm min} = \frac{5}{2} A_{\rm peak}$); value at $A = 100$ is $\sim 7 \times 10^{-5}$.
- Green band: hand-set plausible conjecture (10^{-3}–10^{-1}), *independent of* the MIT-bag $S_{\rm form}$ calculation, where the physical MIT-bag $S_{\rm form}$ is plotted and lies ~ 16 orders of magnitude lower.
- The tension between benchmark rate and mass budget is explicit.

Retention Normalization: Literal vs. Mass-Budget-Allowed

Why every flux forecast must specify $f_{\rm ret}$

The benchmark line flux in the worked example uses $f_{\rm ret} = 1$ implicitly. The mass budget requires $f_{\rm ret} \lesssim 7 \times 10^{-5}$ at $A = 100$. Since $\Phi_\gamma \propto n_S^2 \propto f_{\rm ret}^2$, the two give fluxes that differ by eight orders of magnitude.

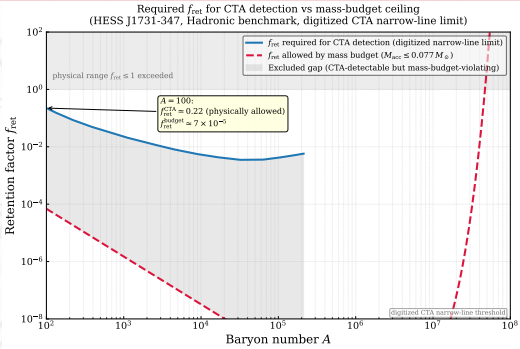

- Red curve: $f_{\rm ret}$ required to reach the digitized CTA narrow-line limit at $E_\gamma(A) = 0.94A$ GeV. At $A = 100$ ($E_\gamma = 94$ GeV), the effective limit is $\sim 1.2 \times 10^{-14}$ ph cm^{-2} s^{-1}, and the required $f_{\rm ret}$ is $\simeq 0.22$ — physically allowed but $\sim 3200\times$ above the mass-budget ceiling.
- Black dashed: $f_{\rm ret}$ allowed by the mass budget ($\simeq 7 \times 10^{-5}$ at $A = 100$).
- Grey band: the excluded gap — three to four orders of magnitude wide at the benchmark line energy.

Two Mass-Budget Conventions: Per-A vs. Integrated

Per-A at $A = 100$ vs. integrated over all A: two physically valid mass-budget conventions

(Baseline benchmark $\dot{N}(A)$; same production law, different questions)

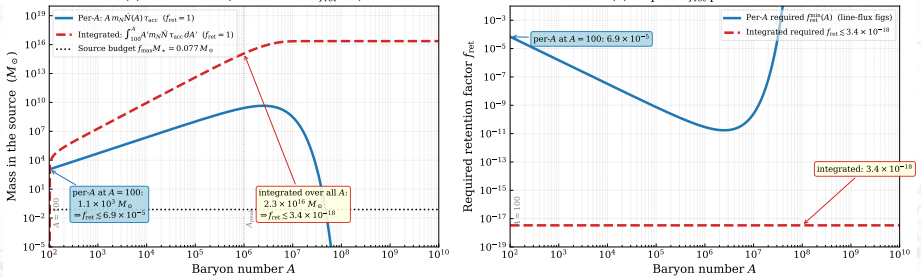

Integrated convention (all A)

$$\int A\, m_N\, \dot{N}(A)\, \tau_{\rm acc}\, f_{\rm ret}\, dA \;\le\; f_{\rm max} M_\star$$

total-mass accounting: $f_{\rm ret} \lesssim 3.4 \times 10^{-18}$, used by only first figure (mass normalised production law); justified because the source must supply the *total* SQM mass across the whole spectrum.

Per-A convention (single $A = 100$)

$$A\, m_N\, \dot{N}(A)\, \tau_{\rm acc}\, f_{\rm ret} \;\le\; f_{\rm max} M_\star$$

at $A = 100$: $f_{\rm ret} \lesssim 7 \times 10^{-5}$, used by other figures justified because the CTA line search is dominated by $E_\gamma = 0.94\, A$ GeV with $A \sim 100$.

Why 13 decades? The per-A constraint at $A = 100$ counts only strangelets at $A = 100$; the integrated constraint counts the *full* spectrum, whose mass budget is dominated by $A \sim 2.5\, A_{\rm peak} \sim 10^6$. For the benchmark law, $\int A\dot{N}(A)\, dA / [A\dot{N}(A)]_{A=100} \approx 2 \times 10^{13}$ (i.e. 13.3 decades).

Both conventions are physically valid — they answer different questions (line flux at fixed E_γ vs. total mass of the source).

Benchmark Numbers to Keep in Mind

From production rate to line flux: the two normalisations

$$\dot{N}(100) \approx 4.2 \times 10^{44}\ \mathrm{s}^{-1} \longrightarrow N_{\mathrm{acc}} = \dot{N}\,\tau_{\mathrm{acc}}\,f_{\mathrm{ret}} \longrightarrow n_S = N_{\mathrm{acc}}/V_{\mathrm{source}} \longrightarrow \Phi_\gamma = \frac{2\,B_{\gamma\gamma}\,n_S^2\langle\sigma v\rangle\,V_{\mathrm{source}}}{4\pi D^2}$$

$$\boxed{\Phi_\gamma \propto f_{\mathrm{ret}}^2, \qquad M_{\mathrm{acc}} = A\,m_N\,N_{\mathrm{acc}} \propto f_{\mathrm{ret}}}$$

The rows below differ ***only*** *in the assumed* f_{ret}.

Two normalisations of the same benchmark (HESS J1731-347, $A = 100$, Hadronic)

Scenario	$f_{\mathrm{ret}}(A=100)$	M_{acc} ($M_\odot$)	Φ_γ (ph cm^{-2}s^{-1})	$M_{\mathrm{acc}}/f_{\mathrm{max}}M_\star$
Literal ($f_{\mathrm{ret}}=1$)	1	1.1×10^3	2.3×10^{-13}	1.4×10^4
Plausible physical band	10^{-3}–10^{-1}	1.1–1.1×10^2	2.3×10^{-19}–2.3×10^{-15}	14–1.4×10^3
Mass-budget-allowed	7×10^{-5}	0.077	$\sim10^{-21}$	1
CTA-required (digitized)	$\simeq 0.22$	2.4×10^2	$\sim1.2\times10^{-14}$	3.2×10^3

- Only the mass-budget-allowed row is physically self-consistent; the literal row ($f_{\mathrm{ret}}=1$) is the benchmark model with every produced strangelet retained, violating the source mass budget by $\sim 10^4$ in mass, hence $\sim 10^8$ in Φ_γ.
- Even the plausible physical band 10^{-3}–10^{-1} for $f_{\mathrm{ret}} = S_{\mathrm{form}}S_{\mathrm{esc}}S_{\mathrm{surv}}$ sits 2–4 orders above the budget ceiling.
- The gap is in production/retention physics, not in instrument sensitivity: even CTA's best-case digitized limit requires $\sim 3200\times$ the mass budget at $A = 100$. Only a smaller $\dot{N}(A)$ or $\langle\sigma v\rangle B_{\gamma\gamma}$, or a physically suppressed $f_{\mathrm{ret}}(A,t)$, can close it.

Line Flux vs. Retention Factor for the Three Sources

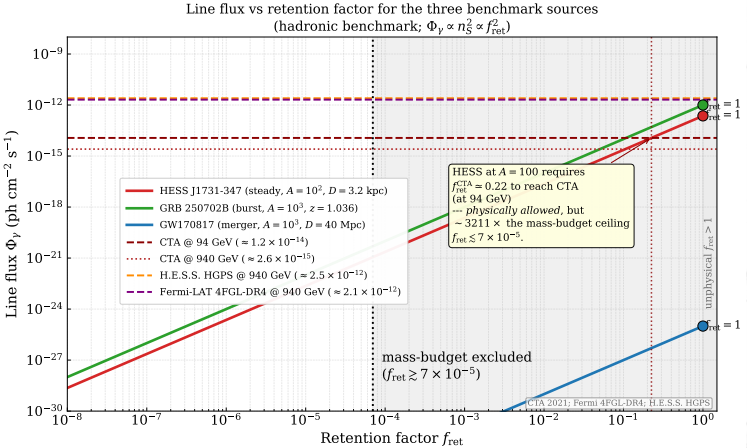

- Because $\Phi_\gamma \propto n_S^2 \propto f_{\rm ret}^2$, each source appears as a straight line of slope 2 in the $(\log_{10} f_{\rm ret}, \log_{10} \Phi_\gamma)$ plane.
- CTA thresholds in the figure are the digitized narrow-line limits ($2021 \times \Delta E = 0.1\,E$):
  at the HESS J1731-347 benchmark line (94 GeV at $A = 100$), the effective limit is $\sim 1.2 \times 10^{-14}$ ph cm^{-2} s^{-1}.
- At $A = 100$, the HESS curve crosses the CTA threshold at $f_{\rm ret}^{\rm CTA} \simeq 0.22$, well within the physically allowed range $f_{\rm ret} \leq 1$.
- The mass-budget ceiling ($f_{\rm ret} \lesssim 7 \times 10^{-5}$) sits $\sim 3200\times$ below the CTA-required value — this is the framework's central open problem. The limitation is the retention physics, *not* the instrument sensitivity.

Line flux $\Phi_\gamma(A, f_{\rm ret})$ as a 2D contour

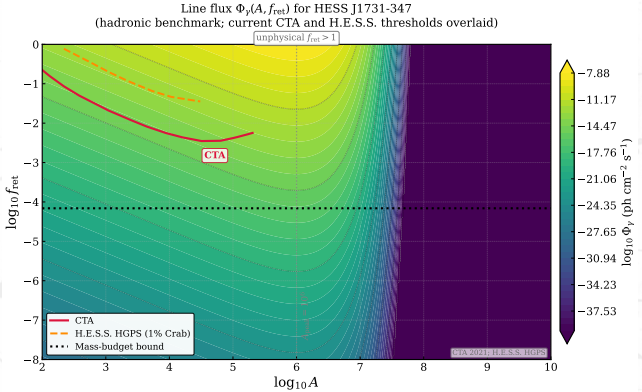

What the contour shows

- Colour scale is $\log_{10}\Phi_\gamma$ (ph cm^{-2} s^{-1}).
- CTA threshold is digitized narrow-line: the threshold curve is drawn at $E_\gamma = 0.94\,A$ GeV using the digitized CTA sensitivity ($\times\,\Delta E = 0.1\,E$). At the HESS benchmark ($E_\gamma = 94$ GeV at $A = 100$) this is $\sim 1.2 \times 10^{-14}$ ph cm^{-2} s^{-1}.
- The mass-budget bound (black dotted) is the ceiling above which the source cannot supply the required SQM mass.
- The CTA-sensitive region and mass-budget-allowed region are separated by three to four orders of magnitude in $f_{\rm ret}$ at the benchmark line energy.

Contour of $\log_{10}\Phi_\gamma$ in the $(A, f_{\rm ret})$ plane

The red contour is the digitized CTA narrow-line limit evaluated at $E_\gamma(A) = 0.94\,A$ GeV; the black dotted contour is the mass-budget ceiling $M_{\rm acc} \le f_{\rm max} M_\star$. The physically accessible region $f_{\rm ret} \le 1$ overlaps the CTA-sensitive region, but the mass-budget-allowed region lies entirely below it — this is the framework's central open problem.

Illustrative Retention-Factor Geometry (not a posterior)

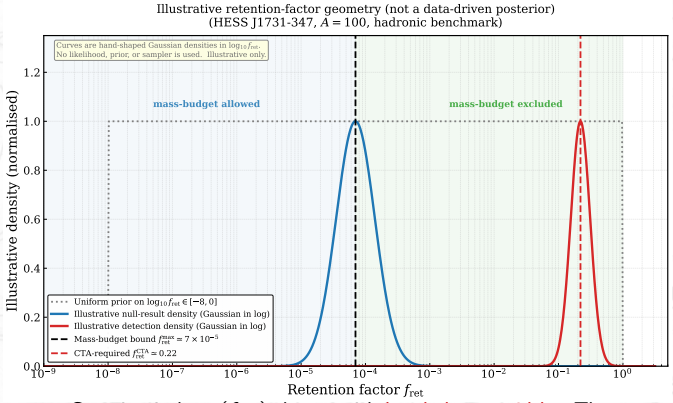

- The two density curves are Gaussian-in-$\log_{10}(f_{\rm ret})$ shapes with hand-chosen widths. They are not the output of a likelihood analysis of real CTA data. The figure title and legend have been updated to say so explicitly.
- The figure is retained because it makes visually explicit the geometry of the two reference scenarios:
  - a hypothetical CTA null result, at the mass-budget bound $f_{\rm ret}^{\rm max} \simeq 7 \times 10^{-5}$;
  - a hypothetical CTA line detection, at the digitized CTA-required $f_{\rm ret}^{\rm CTA} \simeq 0.22$.
- The three-to-four-order-of-magnitude gap between the two reference values is the framework's central open problem.
- A genuine posterior requires an event-level CTA line-search likelihood, explicit priors, a sampler, and convergence diagnostics; the present figure is illustrative only.

The Cherenkov Telescope Array (CTA / CTAO)



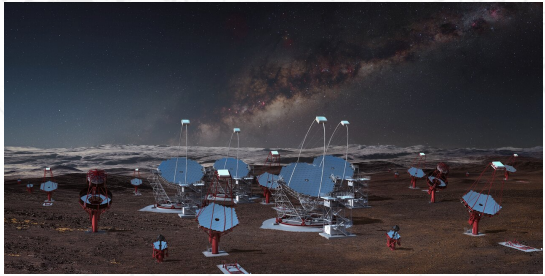

The Cherenkov Telescope Array is the next-generation ground-based observatory for very-high-energy (VHE) γ rays (energies above ~ 100 GeV), detecting Cherenkov light from atmospheric showers.

Two sites, two hemispheres

- CTAO North: Roque de los Muchachos Observatory, La Palma (Canary Islands, Spain).
- CTAO South: Paranal / Atacama Desert, Chile.

Why this matters for HESS J1731-347

HESS J1731-347 lies at declination $\delta_{\rm dec} \simeq -34.7^\circ$ (Southern Hemisphere). Only CTAO South can observe it at high elevation angle and with full sensitivity.

Line Energy Scales with Baryon Number A

The annihilation line energy is fixed by the strangelet mass

Two photons are produced per annihilation, each carrying the strangelet rest energy:

$$E_\gamma \;=\; m_S \;\simeq\; 0.94\,A\ \mathrm{GeV}.$$

A	$E_\gamma \simeq 0.94\,A$	Representative instrument
10^2	94 GeV	Fermi-LAT (below $\sim$ 300 GeV)
10^3	940 GeV	Fermi-LAT upper range / MAGIC-II
10^4	9.4 TeV	H.E.S.S. / MAGIC-II / CTA
10^6	940 TeV	LHAASO
10^8	94 PeV	LHAASO / cosmic-ray regime
10^{10}	9.4 EeV	cosmic-ray regime

Key point

Across the plotted range $A = 10^2$–10^{10}, the line sweeps from $\sim$ 94 GeV to $\sim$ 9.4 EeV — eight decades in photon energy.

Strangelet mass, radius, and line energy

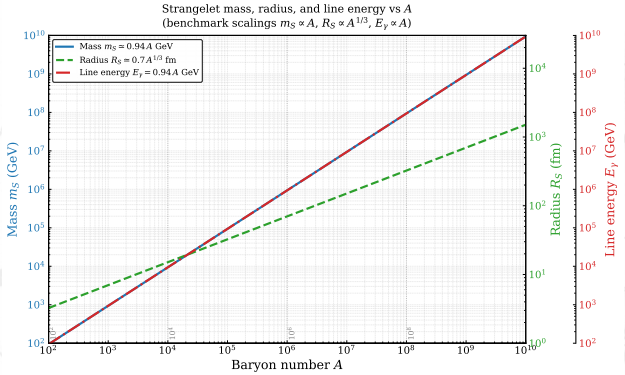

Three benchmark scalings

$$m_S \simeq 0.94\,A\,\mathrm{GeV}, \quad R_S \simeq 0.7\,A^{1/3}\,\mathrm{fm}, \quad E_\gamma = m_S.$$

- Mass and line energy are linear in A.
- Radius grows only as $A^{1/3}$, so the strangelet becomes geometrically larger but proportionally denser.
- The three reference markers ($A = 10^2, 10^4, 10^6, 10^8$) span the range relevant to the three sources.

Cross-read with previous Figure

The line energy $E_\gamma = 0.94\,A$ GeV is what determines which instrument can observe a given strangelet.
For the HESS J1731-347 benchmark ($A \sim 100$) the line sits at ~ 94 GeV — below CTA's nominal threshold and inside Fermi-LAT's reach.

Line Energy vs. Instrument Energy Coverage

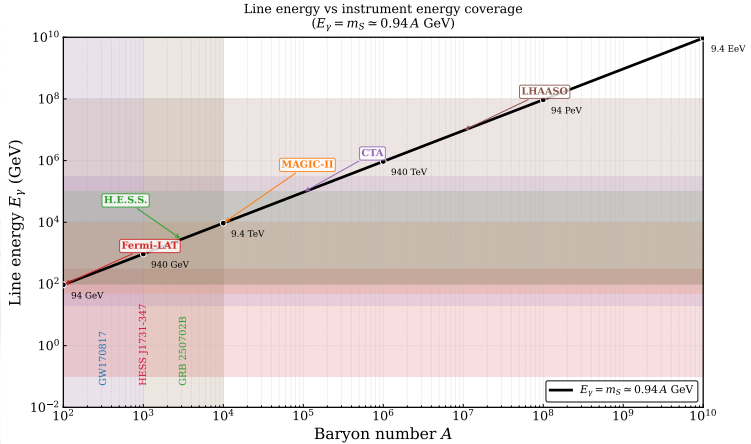

- $E_\gamma = m_S \simeq 0.94\,A$ GeV.
- Across $A = 10^2$–10^{10}, the line sweeps from $\sim$ 94 GeV to $\sim$ 9.4 EeV.
- Coloured bands: energy coverage of Fermi-LAT, MAGIC-II, H.E.S.S., CTA, and LHAASO.
- Vertical bands: A-ranges relevant to the three sources.

Why a Single Flux Threshold Is Not Enough

Consequences for the benchmark contours

Each instrument has a different effective area, background, and energy resolution at each photon energy. A fixed flux threshold cannot represent Fermi-LAT, H.E.S.S., MAGIC, and CTA across the full A range.

- The benchmark curves use a schematic power-law scaling

$$\Phi_\gamma^{\lim}(E_\gamma) \;=\; \Phi_\gamma^{\lim}(E_0)\left(\frac{E_\gamma}{E_0}\right)^{\alpha_{\lim}}, \quad \alpha_{\lim} \simeq -1,$$

  normalised at $E_0 = 1$ TeV, not a full IRF-based sensitivity.
- A genuine 95% CL exclusion requires an event-level likelihood with exposure, background, energy dispersion, source morphology, and nuisance-parameter profiling, evaluated at the correct line energy $E_\gamma(A) = 0.94\,A$ GeV.

What this means for the talk

The benchmark contours are sensitivity maps, not 95% CL exclusions. The visual shape of the bands is therefore partly a property of the strangelet model and partly an artifact of using one number per instrument.

Recommended next step

A definitive line-search analysis with energy-dependent instrument response — using public IRFs for CTA, H.E.S.S., MAGIC, Fermi-LAT, and LHAASO — remains the single most important observational task for the framework.

Statistical Methodology for Line Searches

Binned Poisson likelihood

$$\mathcal{L}(\boldsymbol{\Theta}) = \prod_{i=1}^{N_{\mathrm{bins}}} \frac{e^{-\lambda_i} \lambda_i^{n_i}}{n_i!}.$$

N_{bins}: number of bins; n_i observed counts; λ_i predicted counts.

Profile-likelihood upper limits

$$\Delta\mathrm{TS} = -2 \ln\left(\frac{\mathcal{L}_0}{\mathcal{L}_{\max}}\right).$$

For one degree of freedom, $\Delta\mathrm{TS} = 25$ corresponds to a 5σ detection threshold, i.e. $\mathcal{S}_{\mathrm{det}} = 5$.

Tools and standards

- IRFs in the GADF DL3 standard
- Gammapy for likelihood fitting and upper limits
- ctools/GammaLib for cross-checks

Critical caveat

The sensitivity curves in this talk are not derived from this likelihood. They are threshold inversions using benchmark flux limits $\Phi_\gamma^{\mathrm{lim}}$. A genuine 95% CL exclusion requires an event-level likelihood with exposure, background, energy dispersion, and nuisance parameters — left for future work.

Backgrounds and False Positives for Line Searches

What could mimic a strangelet annihilation line?

- Instrumental lines: calibration residuals, energy-scale systematics, Cherenkov light from muon rings.
- Astrophysical lines: nuclear de-excitation lines, positron annihilation at 511 keV (not VHE), pion-decay spectral breaks that appear as localised features.
- Statistical fluctuations: look-elsewhere effect in a wide energy scan; trial factors can reach $\mathcal{O}(10^3)$ for a full CTAO survey.
- Unmodelled source structure: if the source is extended and the morphology is fitted incorrectly, residuals can mimic a narrow excess.

How to distinguish a real line

- Known energy: the line must sit at $E_\gamma = 0.94\,A$ GeV for integer baryon number A.
- Two-photon coincidence: each annihilation produces *two* photons of equal energy.
- Cross-check with direct detection: a genuine strangelet signal should correlate with a direct-search excess.
- Instrumental cross-checks: the line must appear in independent instruments (CTAO South, H.E.S.S., Fermi-LAT).

Any claimed line detection must survive a full profile-likelihood analysis with look-elsewhere correction, background modelling, and an independent instrument cross-check.

Model Comparison: Hybrid vs. Pure Strange Stars

The distinction is structural

Hybrid star: hadronic outer region + quark core, $R_{\rm crust} < R_{\rm hadronic} < R_{\rm quark}$.
Self-bound strange star: quark matter extends essentially to the surface, with $P(\epsilon = \epsilon_{\rm surface}) = 0$ at finite energy density.

Illustrative likelihood

$$p(D|\mathbf{\Theta}, \mathcal{M}) = p(D_{\rm NICER}|M, R, \mathbf{\Theta})\, p(D_{\rm GW}|\Lambda, \mathbf{\Theta})\, p(D_{\rm EM}|\dots)\, p(D_\nu|\dots)$$

where $\mathcal{M}$ labels the model class, and Λ is the dimensionless tidal deformability.

Model parameters

- Hybrid:
  $\{n_{\rm tr}, \Delta\epsilon, c_s^2, G_V, \Delta_{\rm 2SC}, \Delta_{\rm CFL}, \dots\}$
- Strange star:
  $\{B_{\rm eff}, a_4, m_s, \Delta_{\rm CFL}, G_V, \dots\}$

Priors differ between model classes.

Evidence ratio (Bayes factor)

$$\mathcal{B}^{\rm hybrid}_{\rm QS} = \frac{\mathcal{Z}_{\rm hybrid}}{\mathcal{Z}_{\rm QS}} = \frac{\int d\mathbf{\Theta}\, \mathcal{L}(D|\mathbf{\Theta})\, \pi(\mathbf{\Theta}|{\rm hybrid})}{\int d\mathbf{\Theta}\, \mathcal{L}(D|\mathbf{\Theta})\, \pi(\mathbf{\Theta}|{\rm QS})}.$$

Here $\mathcal{Z}_{\rm hybrid}, \mathcal{Z}_{\rm QS}$ are the Bayesian evidence (marginal likelihood) for each model class; $\pi(\mathbf{\Theta}|\cdot)$ is the prior.

Status

No Bayesian inference is performed in the present work. The displayed parameter-space figures are heuristic likelihood weighted scans, not posteriors. No prior density, no documented likelihood function, no sampler, and no convergence diagnostic are implemented in the associated scripts. Any numerical Bayes factor quoted elsewhere in this talk (e.g. $\mathcal{B} \sim 6.1$ for the two-family scenario) is *quoted from the cited literature*, not computed here. A quantitative hybrid vs. strange model comparison requires published likelihoods and prior densities together with a proper inference pipeline.

Comprehensive Audit: Strange Star and Quark Star Candidates

The central question

Is there any compact object whose observed properties require deconfined quark matter, rather than merely *allowing* it?

What makes a compelling candidate

- A mass or radius that is difficult to reproduce with standard hadronic equations of state (EOSs).
- A cooling history or surface spectrum that points to enhanced neutrino emission or a bare quark surface.
- A gravitational-wave mass in the mass gap between neutron stars and black holes.
- Consistency with NICER mass–radius constraints and GW170817 tidal-deformability limits.

The current verdict

- No object is definitively confirmed as a strange star or quark star.
- HESS J1731-347 is the strongest electromagnetic candidate, driven by its low mass and compact radius.
- GW190814's secondary is the strongest gravitational-wave quark-star proposal.
- PSR J0740+6620 is primarily a high-mass EOS constraint, not a positive identification.

Key quantities used throughout this audit

Quantity	Definition
M	Compact-object mass ($M_\odot$)
R	Radius (km)
Λ	Dimensionless tidal deformability
$B_{\rm eff}^{1/4}$	Effective bag-constant scale (MeV)
$\Delta_{\rm 2SC}, \Delta_{\rm CFL}$	Colour-superconducting pairing gaps (MeV)
G_V	Vector coupling (fm^2)

Candidate Audit: HESS J1731-347, GW190814, PSR J0740+6620

Three objects, three complementary tests

- HESS J1731-347: tests whether a low-mass, compact self-bound branch exists.
- GW190814 secondary: tests whether quark matter can remain stable and sufficiently stiff at 2.6 $M_\odot$.
- PSR J0740+6620: tests whether any quark EOS can support 2 $M_\odot$ with a radius of 12–13 km.

Object	M ($M_\odot$)	R (km)	Key evidence	Status
HESS J1731-347	$0.77^{+0.20}_{-0.17}$	$10.4^{+0.86}_{-0.78}$	Thermal X-rays + Gaia distance; low M, small R	Strongest EM candidate; not confirmed
GW190814 secondary	2.50–2.67	Not measured	GW mass in the gap; no EM counterpart	Viable quark-star proposal; low-mass BH also possible
PSR J0740+6620	2.073 ± 0.069	$12.49^{+1.28}_{-0.88}$	NICER pulse-profile + radio mass	High-mass EOS constraint; not a positive identification

What would change the verdict?

- A composition-specific observable: a surface spectrum, cooling signature, tidal response, or mass–radius relation that *cannot* also be reproduced by a nucleonic or hybrid-star model.
- A joint detection in γ-rays and direct searches for strangelets.

Mass–Radius Constraints from Candidates and EOS Models

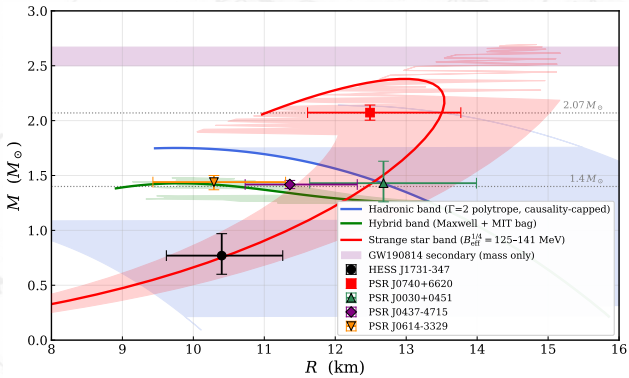

Benchmark caveat

The EOS curves are schematic benchmark families (polytropic hadronic, Maxwell+MIT hybrid, νMIT self-bound), not first-principles QCD calculations. They are shown as sensitivity bands, not as 95% CL exclusions.

Reading the diagram

- All three families overlap in the 1.4–2.1 $M_\odot$ NICER window, so a static M–R plot alone cannot separate them.
- The low-mass HESS point lies on the self-bound branch for the strange-star band, but soft hadronic and hybrid configurations can also accommodate it.
- The slope of $\Lambda(M)$ (dimensionless tidal deformability) is the structural discriminant — *not* visible in the M–R plane.
- A joint Bayesian fit of M, R, $\Lambda_{1.4}$, $R_{1.4}$, and $M_{\rm TOV}$, with a Bayes-factor comparison across EOS classes, is required to break the degeneracy.

What the plot shows

- Black error box: HESS J1731-347 ($M = 0.77^{+0.20}_{-0.17}\ M_\odot$, $R = 10.4^{+0.86}_{-0.78}$ km).
- Red error bar: PSR J0740+6620 ($M = 2.073 \pm 0.069\ M_\odot$, $R = 12.49^{+1.28}_{-0.88}$ km).
- Purple horizontal band: GW190814 secondary ($M = 2.50$–$2.67\ M_\odot$; no radius measurement).
- Coloured bands: representative *families* of hadronic (blue), hybrid (green), and self-bound strange-star (red) EOS sequences. Each band spans the parameter window quoted in this talk ($B_{\rm eff}^{1/4} = 125$–141 MeV for the strange-star family).
- Grey dotted lines: NICER reference masses 1.4 $M_\odot$ and 2.07 $M_\odot$.

Decision Tree for Strange Star Identification

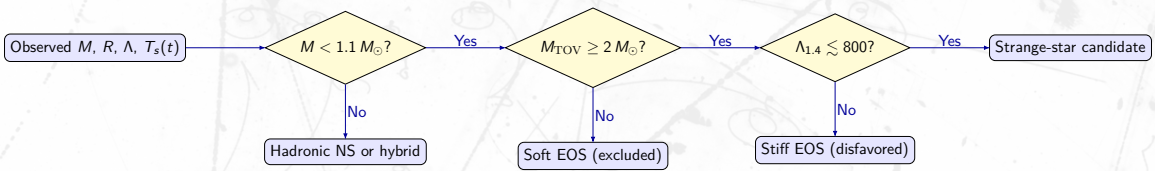

1. Low mass: $M < 1.1\,M_\odot$

Iron-core-collapse NS floor: $M_{\rm min}^{\rm NS} \simeq 1.17\,M_\odot$.

Self-bound EOS ($P(\epsilon_s) = 0$ at finite ϵ_s): $M \simeq \frac{4\pi}{3} R^3 \epsilon_s \Rightarrow M \propto R^3$.

HESS J1731-347 ($M = 0.77^{+0.20}_{-0.17}\,M_\odot$) sits on this low-mass branch.

2. Stiffness: $M_{\rm TOV} \geq 2\,M_\odot$

TOV: $\frac{dP}{dr} = -\frac{G(\epsilon+P)(m+4\pi r^3 P)}{r(r-2Gm)}$, $\frac{dm}{dr} = 4\pi r^2 \epsilon$; $M_{\rm TOV} = \max_{\rho_c} M(\rho_c)$.

NICER: $M_{\rm PSR\,J0740+6620} = 2.073\,M_\odot$.

MIT bag: $M_{\rm TOV} \geq 2\,M_\odot \Leftrightarrow B_{\rm eff}^{1/4} \lesssim 145$ MeV.

3. Tidal: $\Lambda_{1.4} \lesssim 800$

$\Lambda = \frac{2}{3} k_2 (c^2 R/GM)^5$; R^5 dependence $\Rightarrow$ strong radius sensitivity.

GW170817 (90% CL): $\Lambda_{1.4} \lesssim 800$; refined 223–265. AT2017gfo+GW: $R_{1.4} = 12.2 \pm 0.5$ km.

CFL/MIT bag: $B_{\rm eff}^{1/4} \simeq 113$–$128$ MeV gives $\Lambda_{1.4} \approx 190$.

Caveat

Each node is model-dependent. A definitive identification requires a joint Bayesian analysis with evidence ratio $\mathcal{B}_{\rm NS}^{\rm QS} = \mathcal{Z}_{\rm QS}/\mathcal{Z}_{\rm NS}$ (two-family scenario: $\mathcal{B} \sim 6.1$), not a sequence of hard cuts.

Open Questions and Future Directions

The outstanding theoretical challenges

- Retention factor $f_{\mathrm{ret}}(A, t)$: the largest uncertainty in strangelet production.
- Annihilation kernel $K = B_{\gamma\gamma}\langle\sigma v\rangle$: not derived from QCD; treated as a benchmark input.
- Pairing gaps Δ_{2SC}, Δ_{CFL}: constrained only indirectly from M–R–Λ data.
- Vector coupling G_V: anti-correlated with bag constant in the EOS posterior.

The observational path forward

- CTAO South: narrow γ-ray line searches from HESS J1731-347
  (Baseline scenario at projected threshold only if $f_{\mathrm{ret}} = 1$).
- IceCube-Gen2 / KM3NeT / SQM-ISS: direct detection of slow, highly ionising macro-SQM.
- Einstein Telescope / Cosmic Explorer: post-merger gravitational waves and tighter tidal constraints.
- Joint γ-line + direct-detection analysis: the strongest possible consistency test of the strangelet hypothesis, *if* the annihilation kernel is independently constrained.

No single observation will settle the question. A coordinated multimessenger campaign is essential.

Selection Criteria for Strangelet Search Targets

Four criteria a viable source must satisfy

1. A quark-matter reservoir. The source must contain, or transiently create, a region of deconfined quark matter at sufficiently high density and low temperature for strangelets to be energetically favoured.
2. Phase-transition conditions. Strangelet formation is efficient only if the medium passes through a region of the QCD phase diagram where the 2SC $\rightarrow$ CFL transition (or an equivalent strange-quark-enrichment process) can occur. This requires $T \sim$ 1–10 MeV, $\mu \sim$ 300–500 MeV, and lifetimes long enough for nucleation.
3. An injection channel. Once formed, strangelets must be able to escape the production region and reach the observer, or accumulate in a sufficiently large volume.
4. Observability. The predicted annihilation flux must fall within the sensitivity of current or planned VHE instruments.

How the three case studies satisfy these criteria

- HESS J1731-347: steady-state source. Low mass/radius motivates a self-bound or hybrid configuration. SNR radius 15–20 pc provides a large accumulation volume.
- GW170817: merger-driven source. Hadron-to-quark transition releases $\sim 10^{53}$ erg. Distance 40 Mpc allows quantitative flux predictions.
- GRB 250702B: burst-driven source. Extreme duration ($> 25{,}000$ s) and energetics ($E_{\rm iso} > 1.4 \times 10^{54}$ erg) provide a prolonged production window.

Together they cover the principal strangelet production channels: continuous, merger-driven, and burst-driven.

HESS J1731-347: A Strange Quark Star Candidate

The object: A central compact object in the supernova remnant HESS J1731-347.

Key measurements:

$$M = 0.77^{+0.20}_{-0.17}\ M_{\odot}, \qquad R = 10.4^{+0.86}_{-0.78}\ \text{km}$$

Why it matters for strangelets:

- These low mass and radius values are **challenging for standard neutron-star models** and motivate investigating **self-bound or hybrid** configurations.
- If it is a strange quark star, the transition from the 2SC to the CFL phase in its interior **could release strangelets** into the surrounding environment.
- The remnant is one of the few Galactic sources capable of accelerating hadronic cosmic rays to TeV energies, providing a **continuous injection** channel for strangelets.

Search strategy

Future Cherenkov Telescope Array (CTA) observations can search for **gamma-ray signatures** of strangelet annihilation or decay in the cosmic rays from this remnant.

Key advantage

Persistent source $\rightarrow$ steady strangelet flux, easier to model and detect than transient events.

GW170817: A Binary Neutron-Star Merger

The event: The first multimessenger binary neutron-star merger, at ~ 40 Mpc.

Why it matters for strangelets:

- The merger remnant undergoes a **hadron-to-quark transition**, releasing $\sim 10^{53}$ erg and potentially forming strangelets during the process.
- Strangelets can be produced via collisions of nuclear fragments or through a **quark nova** that ejects strange quark matter.
- The burst-like nature produces a **short-lived enhancement** in the strangelet flux, distinct from continuous sources.
- Lack of VHE emission in GW170817 constrains the geometry (jets may be off-axis), but future CTA can probe fainter signals.

Production channel

Binary mergers are a **transient factory** for strangelets, complementing steady sources like HESS J1731-347.

Key advantage

Known distance and energetics $\rightarrow$ allows quantitative predictions for the expected strangelet flux at Earth.

Kilonova AT2017gfo Constraints on Strange-Quark-Star EOSs

Why AT2017gfo is valuable

The light curve depends on ejecta mass, electron fraction, velocity, and opacity, which depend indirectly on the compact-star EOS and tidal interaction.

Bayesian treatment of AT2017gfo

- $120 \lesssim \tilde{\Lambda} \lesssim 1110$, $q_{\rm bin} < 1.54$.
- Combined kilonova + GW: $R_{1.4} = 12.2 \pm 0.5$ km.
- The self-bound nature of strange stars changes tidal deformability, crust mass, contact/merger dynamics, ejecta composition, remnant stability, and post-merger collapse time.

Important caveat

- AT2017gfo does not currently exclude strange stars as a class.
- Strange-star simulations show most merger ejecta evaporate into ordinary nucleons, producing a conventional-looking kilonova; only a small amount of large strangelets survives.
- A quark-star interpretation of GW170817 favors $M_{\rm TOV} \lesssim 2.35\, M_\odot$ under delayed-collapse assumptions.

GRB 250702B: An Ultra-long Gamma-Ray Burst

The event: An ultra-long gamma-ray burst with an observed prompt duration $\Delta t_{\rm obs} > 25{,}000$ s ($\Delta t_{\rm rest} \simeq 12{,}300$ s for $z \simeq 1.036$).

Why it matters for strangelets:

- Its extreme duration and energetics ($E_{\rm iso} > 1.4 \times 10^{54}$ erg) point to an **unusual progenitor**, such as a micro-tidal disruption event or a precessing jet.
- Such extreme conditions may favor the **formation and ejection of strangelets** from the central engine.
- The long duration provides a **prolonged window** for strangelet production and escape, making it a unique laboratory for probing quark-matter formation.

Production channel

Ultra-long GRBs represent a **burst-driven** channel for strangelet production, distinct from steady and merger-driven sources.

Key advantage

Extreme conditions $\rightarrow$ potentially higher strangelet yields, making detection more feasible.

Combined power: these three objects cover **continuous, merger-driven, and burst-driven** strangelet production channels.

Accumulation Timescale Comparison

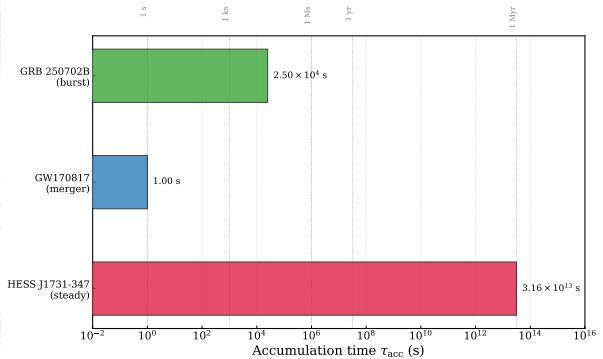

Timeline / duration comparison of the three sources (logarithmic time axis)

- HESS J1731-347: steady source, $\tau_{\rm acc} \sim 10^6$ yr.
- GW170817: post-merger timescale ~ 1 s (illustrative).
- GRB 250702B: burst duration $\sim 2.5 \times 10^4$ s.
- The steady source provides the cleanest physical framework: continuous injection and well-defined accumulation time.

Case Study 1: HESS J1731-347 — Multiwavelength View

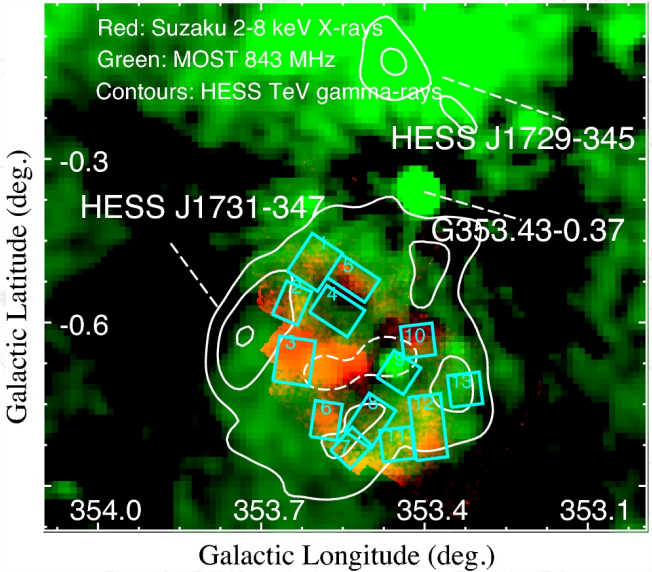

Suzaku 2–8 keV X-ray emission (red); 843 MHz radio continuum (green); H.E.S.S. >1 TeV contours (4, 6, 8σ).
An H II region is a cloud of ionised hydrogen.

What each band constrains for the strangelet framework

- Radio (843 MHz) — synchrotron emission from shock-accelerated electrons; sets the remnant age and the non-thermal electron population.
- X-ray (2–8 keV) — thermal and non-thermal emission; the central compact object mass and radius ($M = 0.77^{+0.20}_{-0.17}\,M_\odot$, $R = 10.4^{+0.86}_{-0.78}$ km) motivate a self-bound or hybrid interpretation.
- TeV γ rays (H.E.S.S.) — shell-type morphology confirms particle acceleration to TeV energies; provides the continuum baseline against which a narrow line would be searched.

HESS J1731-347: γ-Ray Morphology

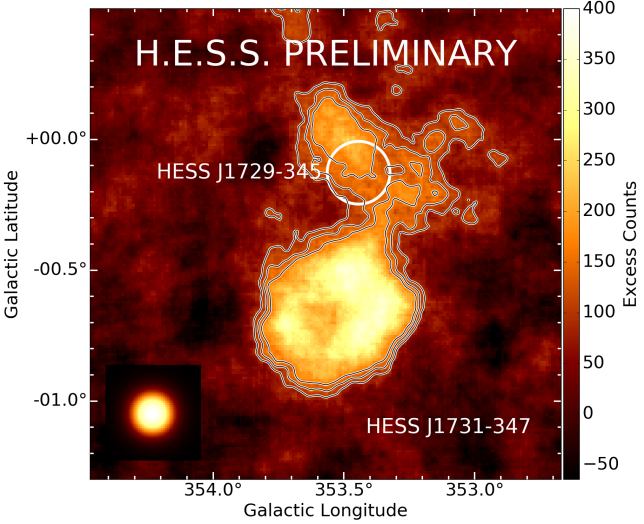

γ-ray excess counts around HESS J1731-347, with 3, 4, 5σ contours. HESS J1731-347 is a shell-type supernova remnant (SNR) emitting TeV γ rays and non-thermal X rays, coincident with radio SNR G353.6-0.7.

Implication for a future CTAO South line search

- The smooth power-law continuum $dN/dE \propto E^{-2.3}$ provides a well-characterised background against which a narrow γ-ray line from strangelet annihilation would appear as a sharp excess.
- Because the source is extended, the line search must simultaneously fit the source morphology, the continuum, and the line amplitude.
- CTAO South at $\delta_{\rm dec} \simeq -34.7°$ will be the first instrument with both the sensitivity ($\Phi_\gamma^{\rm lim} \sim 10^{-13}$ ph cm^{-2} s^{-1}) and the full-time visibility to carry out this search.

HESS J1731-347: Velocity-Resolved Intensity Maps

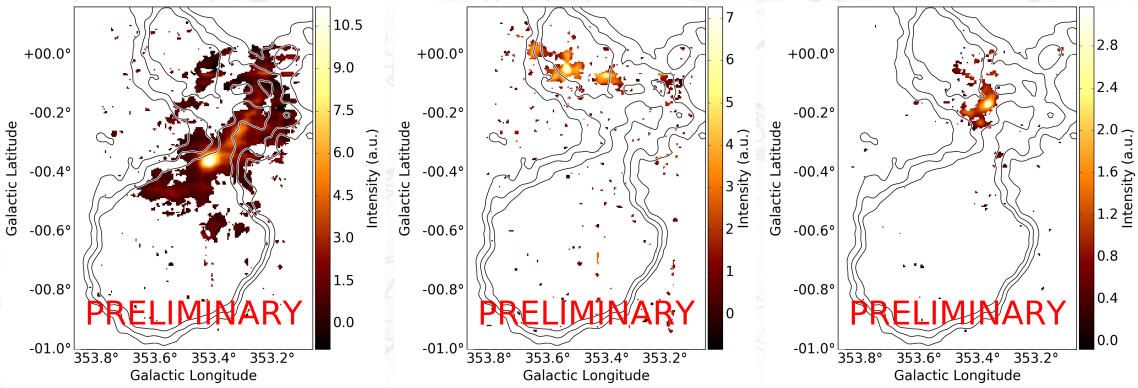

Velocity-resolved intensity maps of the HESS J1731-347 region in three distinct velocity ranges.
Left: -27 to -72 km/s (corresponding to a distance of about 3.2 kpc).
Middle: around 4.5 kpc (-65 to -35 km/s).
Right: -85.5 to -78 km/s (about 5–6 kpc). Overlaid are the 3, 4, and 5σ significance contours from the H.E.S.S. analysis of the source.
The maps show how the TeV emission is correlated with different interstellar gas clouds along the line of sight, helping to locate the SNR and constrain the environment in which particle acceleration and potential strangelet production occur.

HESS J1731-347: Mass and Radius

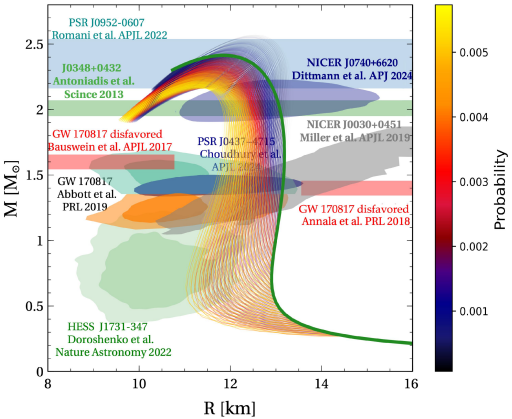

Mass–radius diagram comparing the HESS J1731-347 constraint (black error box) with various equations of state and other compact-object measurements (NICER, GW170817, etc.). The observed values, $M = 0.77^{+0.20}_{-0.17}\ M_\odot$ and $R = 10.4^{+0.86}_{-0.78}$ km, are difficult to reconcile with standard neutron-star models, motivating self-bound or hybrid interpretations.

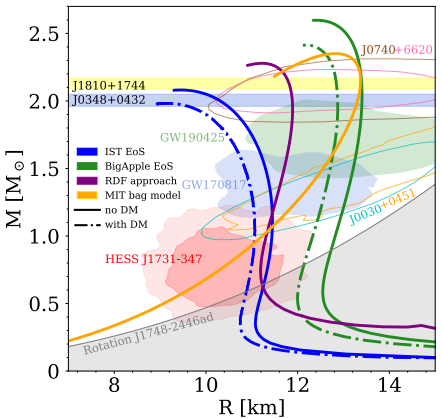

Alternative mass–radius constraints for HESS J1731-347, showing the 1σ and 2σ credible regions from a Bayesian analysis. The same observed values, $M = 0.77^{+0.20}_{-0.17}\ M_\odot$ and $R = 10.4^{+0.86}_{-0.78}$ km, are overlaid with hadronic, hybrid, and strange quark star equations of state. The small radius favours a compact object with a significant quark-matter core.

HESS J1731-347: Consistency Checks

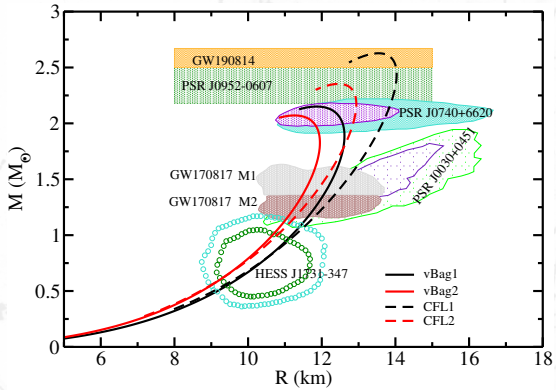

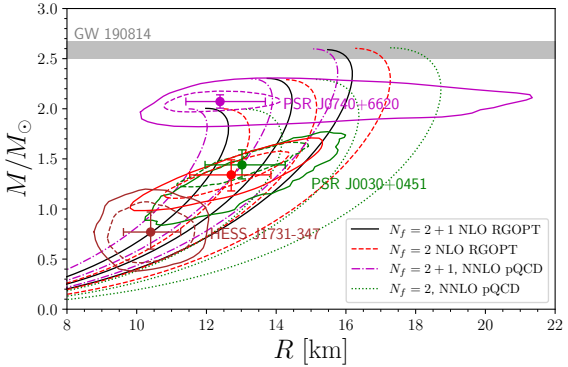

Left: Mass–radius curves for representative quark-matter/hybrid equations of state (vBag and CFL families), compared with the HESS J1731-347 posterior, $M = 0.77^{+0.20}_{-0.17}\,M_\odot$, $R = 10.4^{+0.86}_{-0.78}$ km, and with other compact-object constraints (GW170817, GW190814, PSR J0740+6620, PSR J0952-0607). The low mass and small radius inferred for HESS J1731-347 lie in a region where self-bound or hybrid configurations can be consistent.

Right: The same observational box compared with perturbative-QCD-motivated equations of state at NLO/NNLO in the RGOPT scheme for $N_f = 2$ and $N_f = 2+1$ flavours. The overlap illustrates how the HESS J1731-347 mass–radius constraint can help discriminate between hadronic, hybrid, and strange quark star interpretations.

HESS J1731-347: Cooling Curves

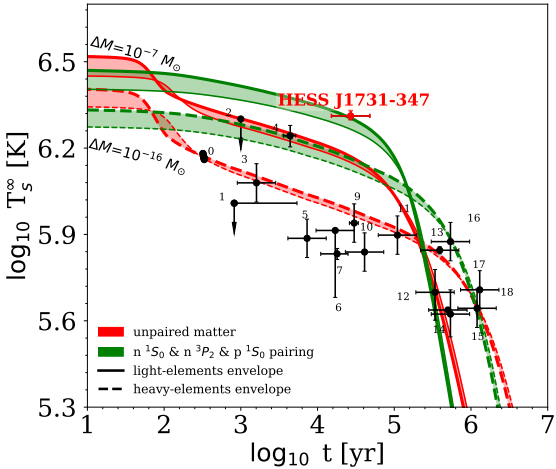

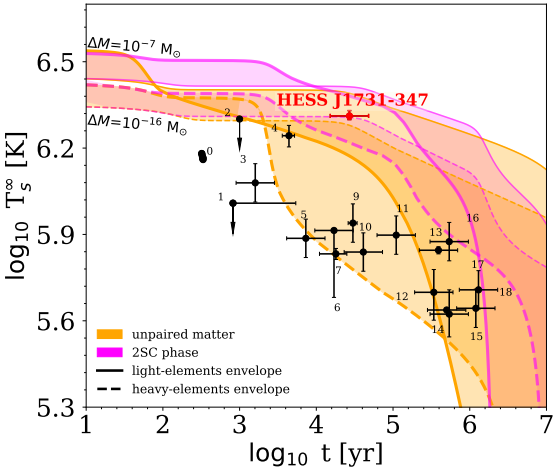

Cooling curves for neutron stars (NSs) and hybrid stars (HSs). The vertical axis is the surface temperature T_s and the horizontal axis is the stellar age $t_\star$. **Left panel:** purely hadronic cooling models with different envelopes (light-elements vs. heavy-elements) and pairing states (unpaired matter, ${}^1S_0$ and ${}^3P_2$–${}^1S_0$ pairing). **Right panel:** hybrid star models with a quark-matter core surrounded by a hadronic envelope, including unpaired matter, the 2SC phase, and the CFL phase ($\Delta_{\rm CFL} \simeq 100$ MeV; only photon cooling remains). The observed position of HESS J1731-347 (red star) is shown for comparison. The cooling behaviour depends sensitively on the internal composition: the presence of a quark core or exotic pairing can significantly alter the temperature evolution, providing an independent probe of the stellar interior.

Cooling curves as a pairing discriminator

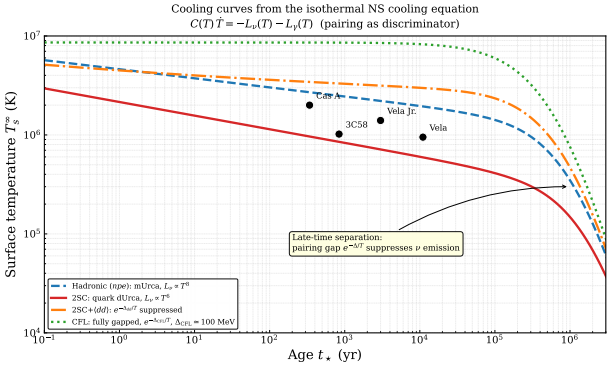

What each curve represents

- Ordinary 2SC: unpaired blue quarks undergo quark β-decay; the star cools *supra-rapidly* and lies below all observed pulsars.
- $2SC + \langle dd \rangle$: *dd* pairing suppresses the quark β-decay channel, so the star stays warmer and approaches the hadronic reference.
- CFL: all quarks gapped; cooling is dominated by e^+e^- pair emission and is the slowest of the three — it sets the upper envelope of the cooling band.
- Hadronic reference: modified Urca plus $^3P_2$ pair-breaking.

Observational discriminant

The data points for Vela, 3C58, and Vela Jr. lie above the ordinary 2SC curve, which cools *too fast* to match them, but below the hadronic reference curve. A *partially gapped* quark core — represented here by the $2SC + \langle dd \rangle$ curve — lies between the two and tracks the observed cold-pulsar population most closely. The fully gapped CFL curve is too hot at late times. The inference is model-dependent: envelope composition, magnetic field, and the neutron $^3P_2$ gap all enter.

HESS J1731-347 on the cooling plane: a thermal consistency test

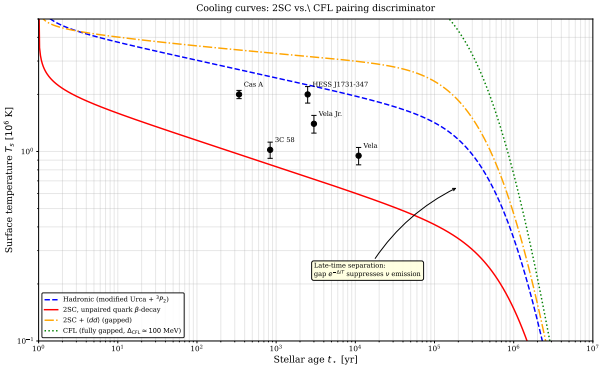

Integration start $t = 1$ yr (vs. 0.1 yr on the preceding cooling frame); this is the observation-era window where all five data points sit. HESS J1731 is added at $(2.5 \times 10^3\ \mathrm{yr},\ 2.0 \pm 0.2 \times 10^6\ \mathrm{K})$, with 1σ statistical bars on all five points. The four non-HESS points are population cross-checks, not constraints on HESS J1731 itself.

Reading the HESS J1731 point

Core-temperature inversion. Fe-envelope $T_s = 10^6\,(T_{\rm core}/10^8\ \mathrm{K})^{0.55}$ K gives $T_{\rm core} \simeq 3.5 \times 10^8$ K at $t \simeq 2.5 \times 10^3$ yr.

Emissivities at this $T_{\rm core}$: hadronic $\sim 7 \times 10^{34}$, 2SC-unpaired $\sim 5 \times 10^{38}$, 2SC+$\langle dd \rangle$ $\sim 3 \times 10^{26}$, CFL ≈ 0 (all in erg s^{-1}). Only the 2SC+$\langle dd \rangle$ branch leaves the point on the correct T_s at $t = 2.5 \times 10^3$ yr: hadronic and unpaired-2SC cooling drop the source below T_s, and CFL-only cooling keeps it above.

Why this is a distinct consistency check

- Complementary to the $(M, R) = (0.77\,M_\odot, 10.4\,\mathrm{km})$ evidence for the SQS branch: same XMM-Newton observation, but a different physical inference — hydrostatic structure from (M, R), cooling history from (t, T_s).
- The (M, R) and (t, T_s) data together require a partially gapped 2SC shell; this is exactly the host of the $2SC \rightarrow CFL$ interface that strangelet production needs.
- Caveats. Envelope, magnetic field, and the T_s–t mapping are model inputs; the 1σ bar is statistical only; the source age ($\sim 2.5 \times 10^3$ yr) is the SNR age, *not* the 10^6 yr benchmark $\tau_{\rm acc}$ used for strangelet accumulation.

Equation of State Constraints (Without HESS J1731-347)

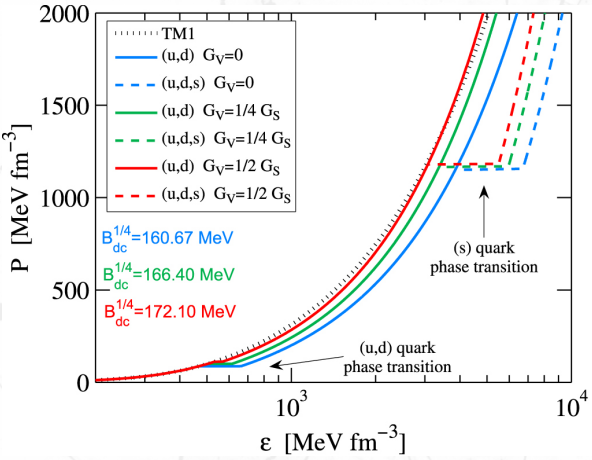

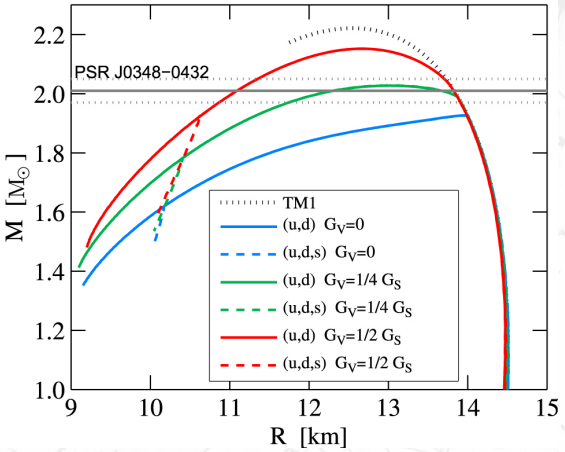

Left panel: Equations of state (pressure vs. energy density) for hadronic (TM1) and quark-hybrid models with different vector couplings $G_V = 0,\ \frac{1}{4}G_S,\ \frac{1}{2}G_S$ and bag constants $B_{\rm bag}^{1/4} = 160.67,\ 166.40,\ 172.10$ MeV. **Right panel:** Corresponding mass–radius relations, compared with the constraint from PSR J0348-0432 (horizontal line). Here the equation of state is shown *without* the HESS J1731-347 mass–radius constraint, illustrating the range of EoS that remain viable from other observations alone.

Equation of State Constraints (With HESS J1731-347)

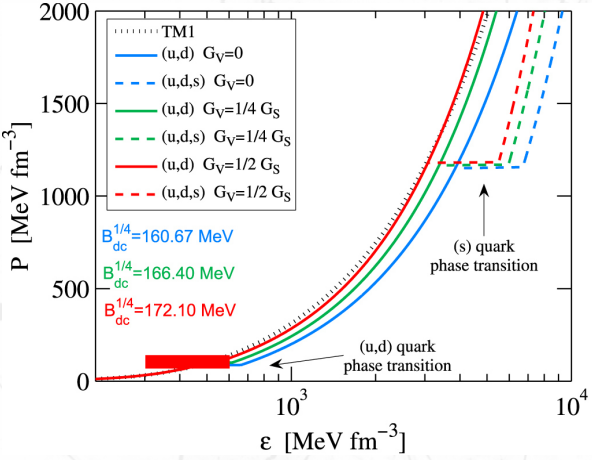

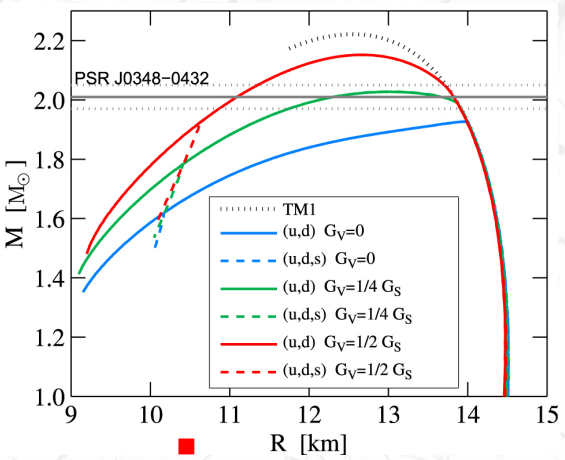

Left panel: Equations of state (pressure vs. energy density) for hadronic (TM1) and quark-hybrid models with different vector couplings $G_V = 0$, $\frac{1}{4}G_S$, $\frac{1}{2}G_S$ and bag constants $B_{\rm bag}^{1/4} = 160.67$, 166.40, 172.10 MeV. The red shaded regions indicate the density range $\epsilon = 200$–600 MeV/fm^3 and pressure $P = 60$–80 MeV/fm^3 (1 fm $= 10^{-13}$ cm). **Right panel:** Same mass–radius relations, now with the HESS J1731-347 constraint overlaid (red shaded band). Comparing the two panels shows how much the HESS measurement narrows the allowed EoS range.

Mass–Radius Relation from TOV Equations

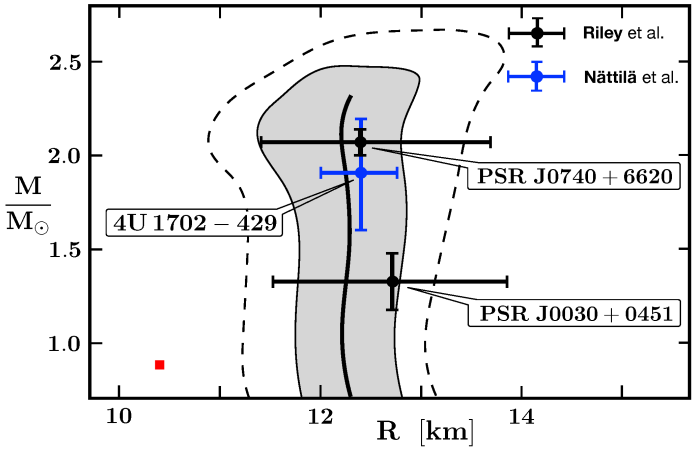

Mass–radius diagram from numerical solutions of the Tolman–Oppenheimer–Volkov (TOV) equations. The gray band and dashed lines show the 68% and 95% credible intervals, respectively, for a representative set of equations of state. Overlaid are observational constraints from NICER for PSR J0740+6620 and PSR J0030+0451, as well as limits from other pulsars. The plot illustrates the tension between requiring a sufficiently stiff EoS to support $\sim 2\,M_\odot$ neutron stars and a sufficiently soft EoS to match the relatively small radii inferred by NICER. A strange quark star or hybrid configuration must satisfy these same constraints.

Equation of State Constraints from HESS J1731-347

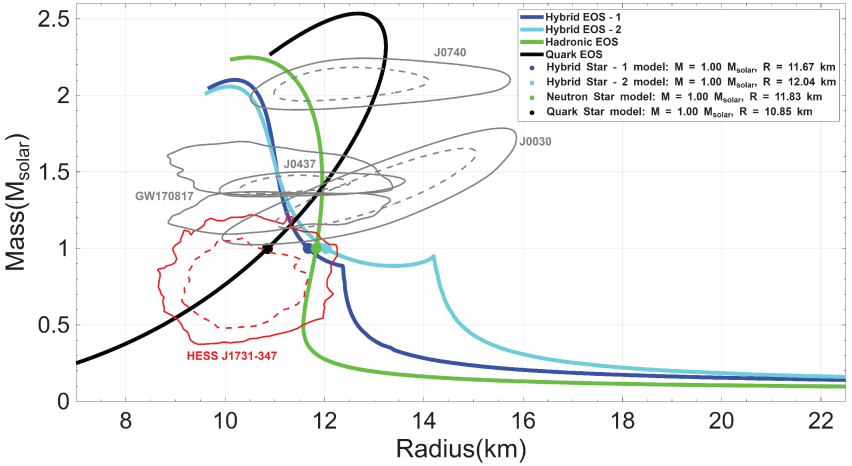

Mass–radius diagram for the central compact object in the HESS J1731-347 remnant. The figure shows the observational constraint at the 1σ level, $M = 0.77^{+0.20}_{-0.17}\,M_{\odot}$ and $R = 10.4^{+0.86}_{-0.78}$ km. Overlaid are theoretical mass–radius curves for different equations of state, including purely hadronic, hybrid, and strange quark star configurations. The observational error box is compared with these predictions to assess which stellar composition is consistent with the measured mass and radius.

HESS J1731-347: Dark-Matter-Admixed Strange Stars (I)

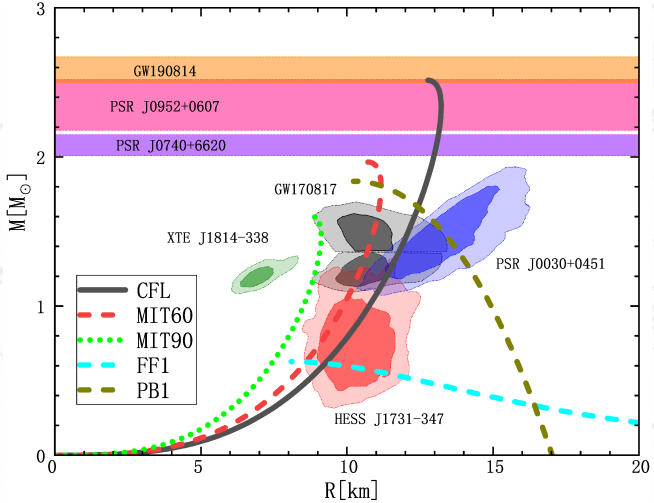

What the figure shows

- Mass–radius sequences for CFL strange stars (SS) and dark-matter-admixed strange stars (DSS) with fermionic (FF) and bosonic (PB) dark-matter equations of state.
- Observational constraints overlaid:
  - HESS J1731-347 ($M = 0.77^{+0.20}_{-0.17}\, M_\odot$, $R = 10.4^{+0.86}_{-0.78}$ km)
  - PSR J0740+6620, PSR J0030+0451
  - PSR J0437-4715
  - GW170817
  - XTE J1814-338
- The CFL model (blue curve) passes through the HESS J1731-347 low-mass, small-radius region.
- Dark-matter admixture (FF or PB) modifies the M–R curve but does not destroy the agreement.

HESS J1731-347: Dark-Matter-Admixed Strange Stars (II)

Why this figure matters for the strangelet framework

- The HESS J1731-347 constraint ($M = 0.77^{+0.20}_{-0.17}\, M_\odot$, $R = 10.4^{+0.86}_{-0.78}$ km) is hard to reconcile with standard neutron-star EOSs, because the inferred mass lies below the minimum expected from iron-core-collapse supernovae ($\sim 1.17\, M_\odot$).
- A CFL strange star naturally passes through this region: the self-bound branch follows $M \propto R^3$ at low mass, so a compact low-mass branch exists without requiring exotic formation channels.
- Dark-matter admixture (fermionic or bosonic) shifts the M–R curve but leaves the qualitative agreement intact — an important robustness check.

Direct link to strangelet production

- If HESS J1731-347 is a CFL strange star, its interior contains an inner CFL core and an outer 2SC shell.
- The 2SC $\rightarrow$ CFL interface is precisely where strangelet nucleation is expected to occur.
- The surrounding SNR (radius 15–20 pc) provides a large accumulation volume for the escaping strangelets.
- This is the physical basis for the benchmark line-flux calculation presented in this talk.

Honest caveat

The M–R diagram alone cannot uniquely select the CFL interpretation: hybrid and dark-matter-admixed hadronic models can also pass through the HESS error box. The slope of $\Lambda(M)$ (tidal deformability) and a strangelet annihilation line are the additional discriminants this talk focuses on.

Structural Decomposition: Self-Bound vs. Gravity-Bound Families

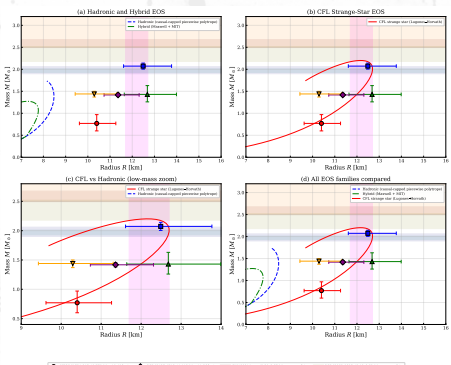

Why decompose first

The next frame overlays *all* three families and every candidate.
Decomposing them first exposes the structural discriminant *before* the aggregate, so the reader sees *why* the aggregate has the shape it does.

Panel (a): gravity-bound degeneracy

Hadronic and hybrid families occupy essentially the same M–R envelope across 1.4–2.1 $M_\odot$: both are gravitationally supported.
The Maxwell construction in the hybrid EOS produces only a small kink at the phase-transition mass, not a resolvable offset.
Within the gravity-bound class, M–R is degenerate.

Panel (b): self-bound branch

The CFL strange star is *self-bound*: it is supported by its own quark-matter pressure, not by gravity.
Its M–R sequence extends to arbitrarily low mass without the $\sim 1.17\ M_\odot$ core-collapse floor that constrains the gravity-bound families.

Panels (c)–(d): where the two branches can be told apart

- Overlap region ($1.4 \lesssim M/M_\odot \lesssim 2.1$): the two branches intersect; *this* is precisely the region that NICER pulse-profile measurements sample, and it is why NICER alone cannot settle the composition.
- Low-mass tail ($M \lesssim 1.17\ M_\odot$): only the self-bound branch is populated. HESS J1731-347 ($M = 0.77\ M_\odot$, $R = 10.4$ km) sits here — see the low-mass zoom on the following frames.
- High-mass tail ($M \gtrsim 2.1\ M_\odot$): the CFL sequence softens; the hadronic/hybrid families reach the observed $\geq 2\ M_\odot$ pulsars, the CFL MIT-bag sequence with $B^{1/4} = 133.1$ MeV does not without tuning.

The low-mass lever arm, not the 1.4 $M_\odot$ plateau, is the structural discriminator between self-bound and gravity-bound matter.

Complete M–R Candidate Audit: All EOS Families

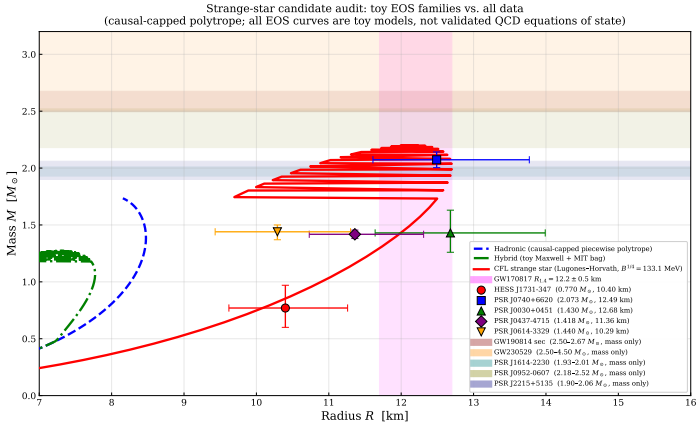

Six candidates with measured R

- HESS J1731-347 ($M = 0.77$, $R = 10.4$ km)
- PSR J0740+6620 ($M = 2.073$, $R = 12.49$ km)
- PSR J0030+0451 ($M = 1.43$, $R = 12.68$ km)
- PSR J0437-4715 ($M = 1.418$, $R = 11.36$ km)
- PSR J0614-3329 ($M = 1.44$, $R = 10.29$ km)

GW170817 tidal band

- $R_{1.4} = 12.2 \pm 0.5$ km (vertical magenta band, AT2017gfo + GW combined)

Five mass-only candidates

- GW190814 secondary (2.50–2.67 $M_\odot$)
- GW230529 (2.5–4.5 $M_\odot$)
- PSR J1614-2230 (1.97 $M_\odot$)
- PSR J0952-0607 (2.35 $M_\odot$)
- PSR J2215+5135 (2.0 $M_\odot$)

Reading the single panel

Three EOS families are shown: hadronic (SLy4-like piecewise polytrope), hybrid (Maxwell construction + MIT bag), and CFL strange star (Lugones–Horvath pairing-gap EOS at $B_{\rm eff}^{1/4} = 133.1$ MeV, *not* the simple massless MIT bag). All three are toy models; they have not been validated against public tabulated equations of state and are not the result of a first-principles QCD calculation. The self-bound CFL branch terminates at finite radius at low mass, producing the distinctive low-mass, low-radius sequence on which the HESS J1731-347 point is placed. All three families pass through the NICER 1.4–2.1 $M_\odot$ error boxes and respect the 2 $M_\odot$ lower bound; the M–R diagram alone therefore cannot discriminate between them. A visual overlap of a model curve with an observational box is not a formal statistical consistency test.

Tidal Deformability $\Lambda(M)$ vs. GW170817 Constraint

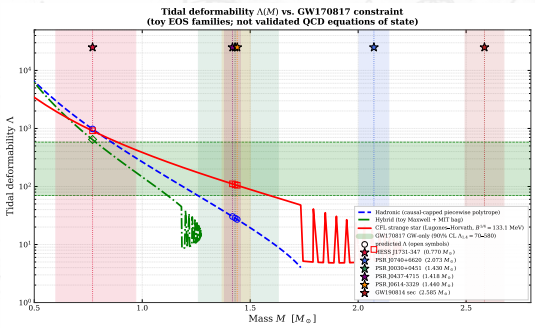

Why a single measurement is not enough

$$\Lambda = \frac{2}{3} k_2 \left(\frac{c^2 R}{GM} \right)^5$$

- The R^5 dependence makes Λ extremely sensitive to R; even a 0.5 km shift in $R_{1.4}$ changes $\Lambda_{1.4}$ by tens of percent.
- The three families (hadronic, hybrid, CFL) all overlap within the GW170817 band, so a single $\tilde{\Lambda}$ measurement does *not* uniquely select SQM.
- The slope of $\Lambda(M)$ is the structural discriminant: the self-bound CFL sequence populates the higher-Λ tail, but tunable interactions can mimic this.
- A joint analysis of $\Lambda_{1.4}$, $M_{\rm TOV}$, and the HESS low-mass branch is required.

What the plot shows

- Green bands: GW170817 broad 90% CL on $\Lambda_{1.4}$ (70–580) together with the model-independent refined constraint $\Lambda_{1.4} = 222.89^{+420.33}_{-98.85}$.
- Three EOS curves: hadronic (SLy4-like piecewise polytrope, blue dashed), hybrid (Maxwell + MIT bag, green dash-dot), and CFL strange star (full pairing-gap formula, $B^{1/4} = 133.1$ MeV, red solid).
- Vertical bands: mass windows of six candidates (HESS J1731-347, PSR J0740+6620, PSR J0030+0451, PSR J0437-4715, PSR J0614-3329, GW190814 secondary).
- On-curve markers: the *predicted* Λ under each EOS family at every candidate mass (circles = hadronic, diamonds = hybrid, squares = CFL).

Timeline of Strange Star Candidate Discoveries (1971–2026)

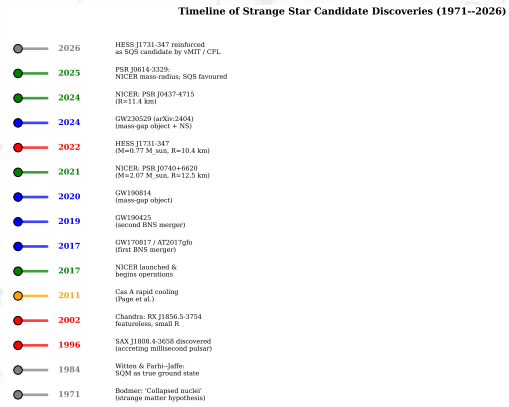

What the timeline shows

- The field has moved from single-channel anomalies to joint multimessenger constraints.
- No single event has yet produced a composition-specific signature.
- The most recent entries (2024–2026) are NICER radius measurements and theoretical confirmations of the HESS J1731-347 interpretation within vMIT and CFL models.
- The diagnostic has shifted from mass-only observables (radio timing, Shapiro delay) to mass–radius–tidal triples, and is now moving towards joint γ-line + direct-detection consistency tests.
- The next decisive step is a joint γ-line + direct-detection search.

Three eras

- 1971–1990: theoretical foundation.
- 1996–2011: historical EM candidates (SAX J1808.4-3658, RX J1856.5-3754, Cas A).
- 2017–2026: multimessenger era (GW170817, GW190814, GW230529, NICER, HESS J1731-347, PSR J0614-3329).

Zoom-in on the HESS J1731-347 Region

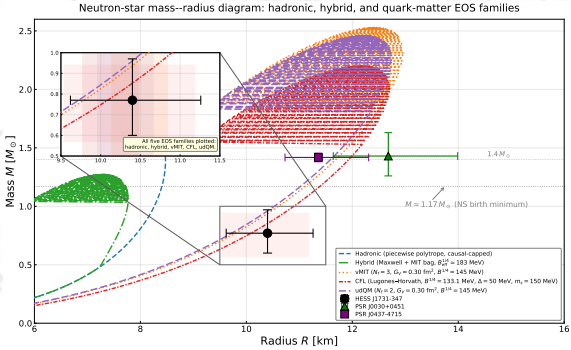

What the zoom shows

- HESS J1731-347: $M = 0.77^{+0.20}_{-0.17}\,M_\odot$, $R = 10.40^{+0.86}_{-0.78}$ km — the only compact object firmly in the low-mass window.
- PSR J0030+0451 (NICER 2026): $M = 1.43^{+0.20}_{-0.17}\,M_\odot$, $R_{\rm eq} = 12.68^{+1.31}_{-1.04}$ km (68% credible intervals).
- PSR J0437-4715 (NICER 2024): $M = 1.418 \pm 0.037\,M_\odot$, $R = 11.36^{+0.95}_{-0.63}$ km — mildly disfavours the softest CFL configurations.
- The horizontal line at $M \simeq 1.17\,M_\odot$ marks the minimum mass expected from standard iron-core-collapse supernovae.

Which EOS families pass through?

- Self-bound SQM branches (vMIT, CFL, udQM) reach the HESS box and extend to $M \to 0$ at finite R.
- Hadronic (piecewise polytrope, SLy4-like) and hybrid (Maxwell + MIT bag, $B_{\rm eff}^{1/4} \simeq 183$ MeV) curves lie at larger radii and cannot reach $M < 1\,M_\odot$ at the HESS radius.
- Benchmark EOS parameters in the plot:
  - vMIT: $G_V = 0.30$ fm^2, $B^{1/4} = 145$ MeV
  - CFL: $\Delta = 50$ MeV, $m_s = 150$ MeV, $B^{1/4} = 133.1$ MeV
  - udQM: $G_V = 0.30$ fm^2, $B^{1/4} = 145$ MeV
- Shaded bands: ± 0.35 km systematic spread from varying $B^{1/4}$, G_V, and Δ.

Why this region matters

- A low-mass compact object at $M < 1\,M_\odot$ is difficult to form through ordinary core collapse.
- A self-bound equation of state allows $M \to 0$ at finite R, so a low-mass branch naturally exists.
- Systematics: the HESS M–R inference depends on the assumed atmosphere model and distance.

Toy EOS vs. HESS J1731-347 central-condition benchmark (I)

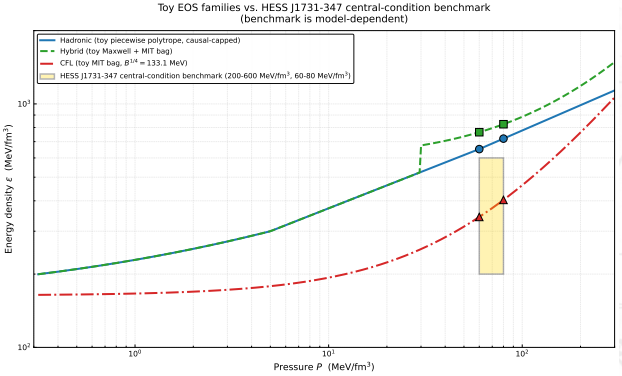

Toy EOS at $P = 60$–80 MeV/fm^3

- CFL ($\varepsilon = 3P + 4B_{\rm eff}$, $B^{1/4} = 133.1$ MeV): 343–403 (inside).
- Hadronic piecewise polytrope: 652–720 (8–20% above).
- Hybrid (Maxwell+MIT, $P_{\rm tr} = 30$ MeV/fm^3, $\Delta\varepsilon = 150$ MeV/fm^3): 765–825 (28–38% above).

Benchmark (model-dependent)

- Shaded: $\varepsilon \in [200, 600]$ MeV/fm^3, $P \in [60, 80]$ MeV/fm^3 — the translation of $(M, R) = (0.77\,M_\odot,\ 10.4\,\mathrm{km})$ into central conditions.
- Not a universal constraint: different EOS reach the same (M, R) at different (ε, P).

Toy EOS vs. HESS J1731-347 central-condition benchmark (II)

Why the ordering is physical

At fixed P, the value of ε is set by the *entire* pressure–density path from low density: $d\varepsilon/dP = 1/c_s^2(P)$. The band $\varepsilon/P \in [3.3, 10]$ at $P = 60$ MeV/fm^3 encodes that path. The toy hadronic polytrope has a very soft low-density segment (causality-capped only at high density), so it requires a larger ε to reach the same P. The toy hybrid carries an additional Maxwell jump ($\Delta\varepsilon = 150$ MeV/fm^3 at $P_{\rm tr} = 30$ MeV/fm^3) that lifts its high-density branch by ~ 150 MeV/fm^3. The CFL branch has $c_s^2 = 1/3$ from the start and therefore reaches $P = 60$ MeV/fm^3 at lower ε.

Consistency with the M–R audit figure

This is why the toy hadronic and hybrid M–R curves in the audit figure do *not* pass through the HESS error box: at $M = 0.77\,M_\odot$ they predict $R > 10.4$ km (i.e. their (ε_c, P_c) lies outside the rectangle), not $R = 10.4$ km. The toy EOS families are not wrong — they are simply not in the rectangle. This overlay is a *consistency map*, *not* a strict constraint.

How the EOS determines M, R, and Λ

EOS input: $\varepsilon(P)$ → TOV ODEs: $P(r), \varepsilon(r), m(r)$ → Surface: $P(R) = 0$ → $M = m(R)$, R → Love ODE: $y(r)$, $c_s^2 = dP/d\varepsilon$ → $\Lambda(M) = \frac{2}{3} k_2 \left(\frac{Rc^2}{GM}\right)^5$

Single input: $\varepsilon(P)$. Two outputs: (M, R) from TOV, then $\Lambda(M)$ from the Love ODE.

Toy hadronic EOS at $M = 0.77\,M_\odot$: TOV profiles $P(r)$, $\varepsilon(r)$, $m(r)$
(the HESS central-condition benchmark is a point in (ε, P) space, not a full profile)

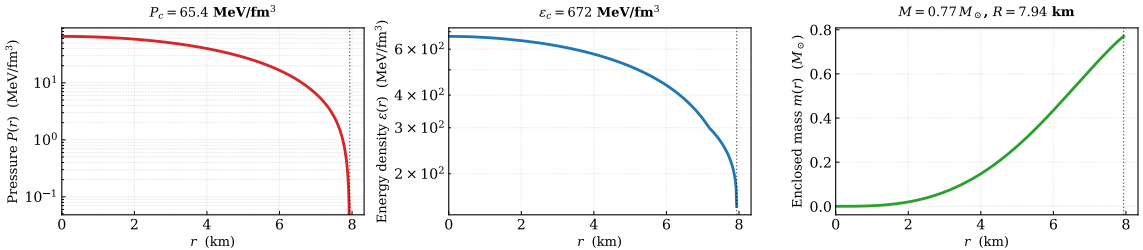

Why a full profile, not just a central point

The HESS J1731-347 central-condition benchmark ($\varepsilon \in [200, 600]$ MeV/fm^3, $P \in [60, 80]$ MeV/fm^3) is a *point* in the (ε, P) plane. A point does not determine (M, R) or Λ: (M, R) and Λ depend on the whole $\varepsilon(r)$ profile (i.e. on the full $P(r)$ solution), not just on the central value. Two EOS with the same (ε_c, P_c) can give different (M, R) and different Λ. This is the structural reason the M–R audit and the $\Lambda(M)$ audit together are stronger than either alone.

Combined Audit: M–R and $\Lambda(M)$ Panels

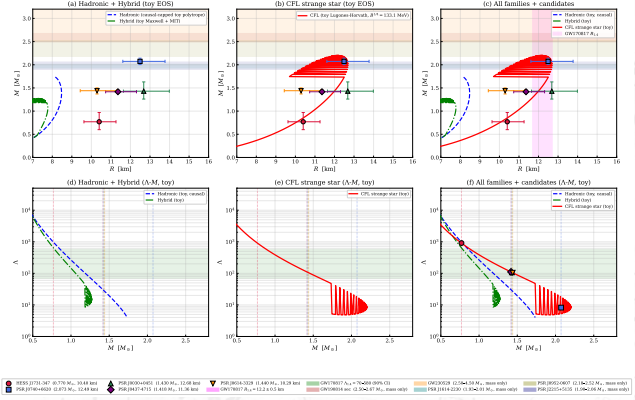

Top row: M–R

- Panel (a): hadronic (SLy4-like polytrope) and hybrid (Maxwell + MIT bag).
- Panel (b): CFL strange star ($B^{1/4} = 133.1$ MeV, full pairing-gap EOS).
- Panel (c): all three families, with the GW170817 $R_{1.4}$ band and all candidate markers.
- Five candidates with measured R; five mass-only candidates shown as horizontal bands.

Bottom row: $\Lambda(M)$

- Green bands: GW170817 broad 90% CL ($\Lambda_{1.4} = 70$–580) and refined window ($\Lambda_{1.4} \approx 223$–$265$).
- Genuine tidal Love-number solutions for the same three EOS families.
- Panel (f) markers: predicted Λ on the CFL curve at each candidate mass.

Key point

- All three families overlap in the M–R plane within the NICER error boxes and reproduce $M_{\mathrm{TOV}} \gtrsim 2\,M_\odot$.
- The slope of $\Lambda(M)$ is the structural discriminant; the low-mass branch of the CFL strange-star sequence naturally reaches the HESS J1731-347 region without tuning.
- Caveat: the hadronic polytrope and the hybrid Maxwell construction are *benchmark* EOSs, not first-principles χEFT calculations; the panel is a sensitivity map, not a 95% CL exclusion.

Constraining the Chiral Invariant Mass with HESS J1731–347

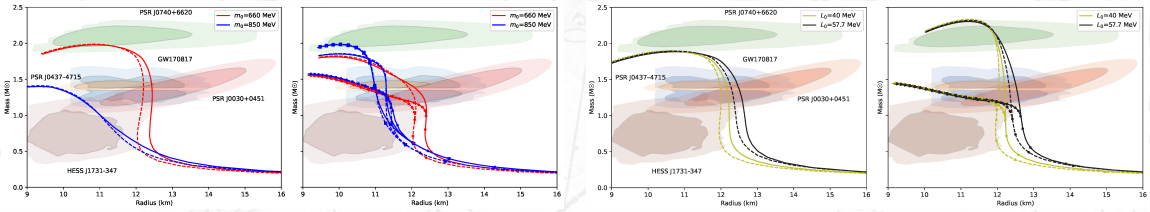

Mass–radius relations from the parity doublet model for HESS J1731–347.

Left pair: fixed $L_0 = 40$ MeV, varying the chiral invariant mass $m_0 = 660$ and 850 MeV. The left panel shows the hadronic PDM; the right panel shows the PDM–NJL crossover model. Solid and dashed curves correspond to models with and without the $a_0(980)$ meson, respectively. NJL parameters: $(H_{\rm NJL}/G_D,\ g_V/G_D) = (1.3, 0.2)$ (lines with point markers), $(1.4, 0.5)$ (lines without markers), and $(1.5, 0.7)$ (lines with square markers).

Right pair: fixed $m_0 = 690$ MeV, varying $L_0 = 40$ and 57.7 MeV. Same panel conventions. NJL parameters: $(H_{\rm NJL}/G_D,\ g_V/G_D) = (1.25, 0.1)$ (lines with markers) and $(1.6, 1.3)$ (lines without markers).

In all panels, the observational constraint from HESS J1731–347, $M = 0.77^{+0.20}_{-0.17}\,M_\odot$ and $R = 10.4^{+0.86}_{-0.78}$ km, is compared with the theoretical M–R curves. A larger m_0 softens the hadronic EoS and reduces the radius of low-mass neutron stars, while a larger L_0 stiffens the EoS. The crossover model supports a larger maximum mass, allowing consistency with massive neutron star constraints even for large m_0 and small L_0.

CFL Mass–Radius Sequence with 2SC/CFL Phases and the CEP

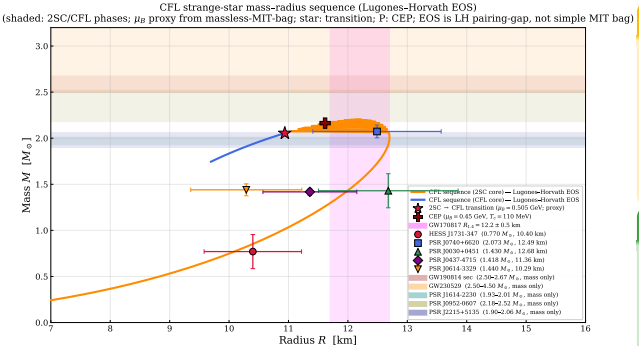

What the colours mean

- Orange segment: stars whose core is 2SC ($\mu_B < 0.505$ GeV).
- Blue segment: stars whose core is CFL ($\mu_B \geq 0.505$ GeV).
- Red star: the $2SC \rightarrow CFL$ transition at $\mu_B \simeq 0.505$ GeV.
- Dark-red "P": the critical endpoint at $\mu_B \simeq 0.45$ GeV, $T_c \simeq 110$ MeV, lattice-inspired.

Structural caveat

The CEP is a feature of the (T, μ_B) plane, not a direct observable in the M–R plane. Its projection here is a benchmark marker, not a 95% CL constraint. The CFL sequence is a toy MIT-bag model; the phase boundaries are a phenomenological parameterization, not first-principles lattice QCD.

Physics of the phase splitting

- The CFL MIT-bag EOS with pairing-gap corrections fixes the pressure–density relation. The TOV solver returns (M, R) for each central pressure P_c.
- The central baryon chemical potential is reconstructed from $\mu_B = [4\pi^2(P_c + B)/3]^{1/4}$ (massless-quark MIT bag). This maps the interior of each star onto the (T, μ_B) phase diagram.
- Stars with $\mu_B < 0.505$ GeV have a 2SC core; those above have a CFL core. The dividing star is the red marker.
- HESS J1731-347 (0.77 $M_\odot$, 10.4 km) falls on the 2SC-core branch, consistent with its low mass and small radius.
- PSR J0740+6620, PSR J0030+0451, PSR J0437-4715, PSR J0614-3329 all lie on or near the CFL-core branch. GW170817's tidal band overlaps both branches.

CFL Mass–Tidal-Deformability Sequence with Phase Structure

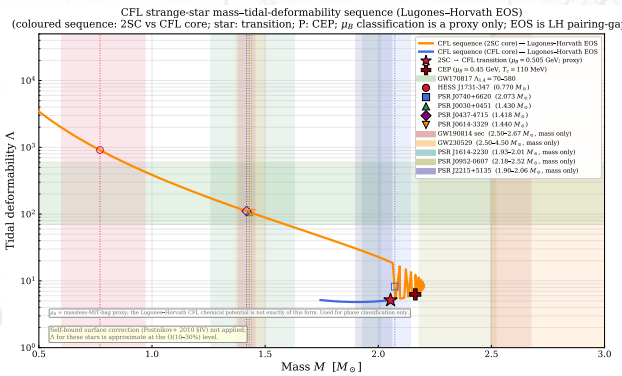

Why $\Lambda(M)$ is a second discriminant

$$\Lambda = \frac{2}{3}\, k_2 \left(\frac{c^2 R}{GM}\right)^5$$

- The R^5 dependence makes Λ extremely radius-sensitive: a 0.5 km shift in $R_{1.4}$ changes $\Lambda_{1.4}$ by tens of percent.
- The Hinderer Love-number ODE is solved alongside the TOV equations, giving a genuine $\Lambda(M)$ curve rather than a universal relation.

Predicted Λ at the observed masses

- Open symbols on the CFL curve show the predicted Λ at the central masses of HESS J1731-347, PSR J0740+6620, PSR J0030+0451, PSR J0437-4715, and PSR J0614-3329.
- HESS J1731-347 ($0.77\ M_\odot$) sits on the 2SC-core branch with $\Lambda \sim 10^3$.
- PSR J0740+6620 ($2.07\ M_\odot$) sits on the CFL-core branch with $\Lambda \sim \mathcal{O}(10)$.
- The four-to-five-order-of-magnitude span across the sequence is the structural fingerprint of the phase transition.

Reading the phase structure in the Λ–M plane

- Orange segment ($\mu_B < 0.505$ GeV): 2SC-core stars; they populate the low-mass, high-Λ tail.
- Blue segment ($\mu_B \geq 0.505$ GeV): CFL-core stars; they populate the higher-mass, lower-Λ region.
- Red star: the *2SC → CFL* transition projects onto a specific (M, Λ) point — a structural discriminant invisible in the M–R plane.
- Dark-red "P": the CEP, again a benchmark marker.
- Green horizontal band: GW170817 $\Lambda_{1.4} = 70$–580 (2018).
  The CFL sequence crosses this band; the slope of $\Lambda(M)$ is what breaks the degeneracy with hadronic and hybrid EOSs.

Worked Numerical Example (Hadronic Model, $A = 100$)

Using $T = 1$ MeV and $\delta E = 10$ MeV:

$$\Gamma_{\rm trans} = \frac{T^4}{\pi^3} e^{-10} \approx 1.5 \times 10^{-6}\ \text{MeV}^4 \ \approx\ 2.9 \times 10^{8}\ \text{fm}^{-3}\text{s}^{-1}.$$

From $\dot{N}(A)$ at $A = 100$, $A_{\rm peak} = 10^6$, $\dot{N}_{\rm peak} = 10^{47}$ s^{-1} (Hadronic model):

$$\dot{N}(100) = 10^{47} \times (10^{-4})^{2/3} \times e^{2/3} \approx 4.2 \times 10^{44}\ \text{s}^{-1}.$$

Accumulating for $\tau_{\rm acc} = 10^6$ yr ($\simeq 3.16 \times 10^{13}$ s) in $V_{\rm source} = 1.23 \times 10^{59}$ cm^3, with $N_{\rm acc} = \dot{N}\,\tau_{\rm acc}$:

$$N_{\rm acc} \approx 1.32 \times 10^{58}, \qquad n_S = \frac{N_{\rm acc}}{V_{\rm source}} \approx 1.1 \times 10^{-1}\ \text{cm}^{-3}.$$

With $\langle \sigma v \rangle \sim 10^{-25}$ cm^{3}s^{-1} and $D = 3.2$ kpc:

$$R_{\rm ann} = n_S^2 \langle \sigma v \rangle V_{\rm source} \approx 1.4 \times 10^{32}\ \text{s}^{-1}, \qquad \Phi_\gamma = \frac{2\,B_{\gamma\gamma} R_{\rm ann}}{4\pi D^2} \approx 2.3 \times 10^{-13}\, B_{\gamma\gamma}\ \text{ph cm}^{-2}\text{s}^{-1}.$$

Each annihilation produces two photons at $E_\gamma = m_S \approx 94$ GeV.

Mass-budget check

The literal accumulated SQM mass at these inputs is $M_{\rm SQM} \approx 1.1 \times 10^3\, M_\odot$, which is *many orders of magnitude* above the source budget $f_{\rm max} M_\star = 0.077\, M_\odot$. The benchmark rate therefore *cannot* be sustained over the full $\tau_{\rm acc}$ without a retention factor $f_{\rm ret} \lesssim 7 \times 10^{-5}$. This assumes $f_{\rm ret} = 1$; with the required $f_{\rm ret} \lesssim 7 \times 10^{-5}$, the line flux is $\Phi_\gamma \approx 2.3 \times 10^{-13} \times (7 \times 10^{-5})^2 \approx 1.1 \times 10^{-21}$ ph cm^{-2} s^{-1}, far below CTA sensitivity. This is a single-A check; summing over all A makes the required $f_{\rm ret}$ even smaller.

Hadronic versus Hybrid Model: Which Produces More?

Table: Model-specific production parameters.

Model	A_{peak}	$\dot{N}_{\mathrm{peak}}$ (s^{-1})
Hadronic	10^6	10^{47}
Hybrid	10^7	10^{48}

Hybrid dominates. A larger quark core shifts A_{peak} to larger A *and* raises $\dot{N}_{\mathrm{peak}}$ by a factor of 10.

Table: Ratio Hybrid/Hadronic at selected A.

A	$\dot{N}_{\mathrm{Hy}}/\dot{N}_{\mathrm{H}}$	$\Phi_{\mathrm{Hy}}/\Phi_{\mathrm{H}}$
10^2 (low A)	2.15	4.6
10^3 (merger, GRB)	2.16	4.7
10^6 (Hadronic peak)	3.9	15
10^7 (Hybrid peak)	870	7.6×10^5
Peak-to-peak	10	100

At every baryon number A, the Hybrid model produces *more* strangelets than the Hadronic model, because both A_{peak} and $\dot{N}_{\mathrm{peak}}$ are larger.
At the Hadronic peak ($A = 10^6$), the rate is already $\sim 4\times$ larger; at the Hybrid peak ($A = 10^7$), it is $\sim 870\times$ larger.
Since the γ-line flux scales as $\dot{N}^2$, the peak-flux ratio reaches ~ 100.

Benchmark Sensitivity Forecast for HESS J1731-347 (I)

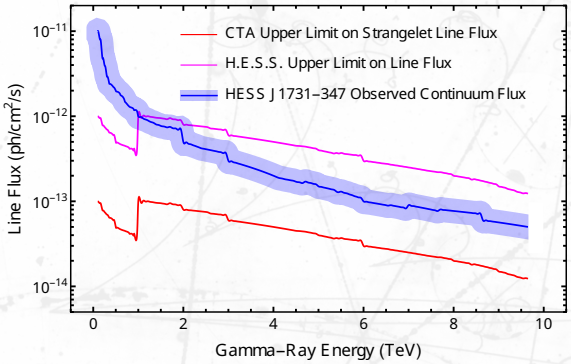

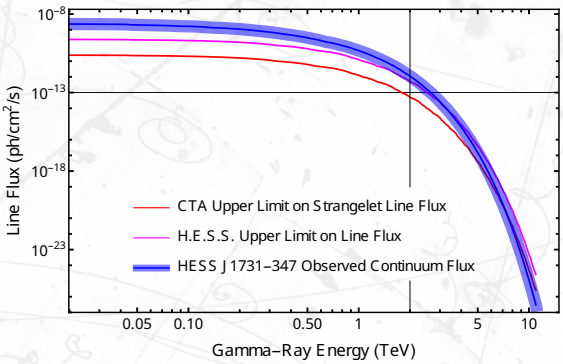

What these panels actually show

The figures are threshold-inversion plots, not Monte Carlo likelihood simulations. The CTA (red) and H.E.S.S. (magenta) curves are broken-power-law proxy limits using the energy-dependent CTA threshold; the blue curve is the published H.E.S.S. continuum flux. The benchmark model line is overlaid at its default parameter set.

Benchmark Sensitivity Forecast for HESS J1731-347 (II)

- At the benchmark line energy (94 GeV, $A = 100$), the model with $f_{\rm ret} = 1$ gives a line flux $\Phi_\gamma \approx 2.3 \times 10^{-13}$ ph cm^{-2} s^{-1}, about 20× *above* the digitized CTA narrow-line limit $\Phi_\gamma^{\rm lim} \approx 1.2 \times 10^{-14}$ ph cm^{-2} s^{-1}. The required retention is $f_{\rm ret}^{\rm CTA} \simeq 0.22$, physically allowed but $\sim 3200\times$ the mass-budget ceiling $f_{\rm ret} \lesssim 7 \times 10^{-5}$.
- With the mass-budget-required $f_{\rm ret} \sim 7 \times 10^{-5}$, the line flux is $\sim 10^{-21}$ ph cm^{-2} s^{-1}, far below CTA.
- A genuine Monte Carlo / profile-likelihood analysis would require the CTA IRFs, exposure, background model, and a spectral fit; those inputs are not in the present archive.
- Caveat: the CTA curve shown is the digitized narrow-line flux limit obtained from the published CTAO South Alpha differential sensitivity via $\Phi_\gamma^{\rm line} = (dN/dE)_{\rm sens} \cdot 0.1\,E$. This is a factor ≈ 1.5 optimistic at 94 GeV, where the CTA energy resolution is $\sim$ 15–20% FWHM; a full line-search forecast must forward-fold the source spectrum through the effective area, energy dispersion, background, and exposure.

Constraining the Strangelet Flux from HESS J1731-347

With a continuum flux of $\sim 10^{-12}$ ph cm^{-2} s^{-1} at 1 TeV, CTA can probe line features below 10% of the continuum.

At the benchmark line energy $E_\gamma = 94$ GeV ($A = 100$), the digitized CTA narrow-line limit is $\Phi_\gamma^{\rm lim}(94\,{\rm GeV}) \simeq 1.2 \times 10^{-14}$ ph cm^{-2} s^{-1} ($\times\, \Delta E = 0.1\, E$) — about an order of magnitude better than the flat 10^{-13} at 1 TeV, because 94 GeV is near the lower edge of the CTAO South optimal band.

The line-flux limit translates into a strangelet number-density limit via

$$n_S < \sqrt{\frac{4\pi D^2 \Phi_\gamma^{\rm lim}}{2 B_{\gamma\gamma} \langle\sigma v\rangle V_{\rm source}}} \approx \sqrt{\frac{4\pi (3.2\,{\rm kpc})^2 (1.2 \times 10^{-14})}{2 \cdot 1 \cdot 10^{-25} \cdot 1.23 \times 10^{59}}} \approx 0.023\ {\rm cm}^{-3}.$$

For $A = 100$, this gives a mass limit

$$M_{\rm SQM} < n_S m_S V_{\rm source} \approx 0.023 \cdot 1.67 \times 10^{-22}\ {\rm g} \cdot 1.23 \times 10^{59}\ {\rm cm}^3 \approx 2.4 \times 10^2 M_\odot.$$

Three caveats on this bound

- No absorption correction is applied: the γ-line attenuation on the $N_H \sim 10^{23}$ cm^{-2} column is small at $E_\gamma \gtrsim 1$ TeV, but should be modeled for a final analysis.
- The column density is angle-averaged. A dedicated line-of-sight integral using the 3D dust map would give a stricter bound.
- σ_S is a benchmark value. A factor-of-ten change in the strangelet–nucleon cross-section rescales σ_S by the same factor.

Limits from HESS J1731-347

- CTA's limit at 1 TeV ($\sim 10^{-13}$ ph cm^{-2} s^{-1}) is a tenfold improvement over H.E.S.S. ($\sim 10^{-12}$ ph cm^{-2} s^{-1}).
- Continuum follows $dN/dE \propto E^{-2.3}$.
- At the benchmark line energy $E_\gamma = 94$ GeV ($A = 100$), the digitized CTA narrow-line limit is $\Phi_\gamma^{\rm lim}(94\,{\rm GeV}) \simeq 1.2 \times 10^{-14}$ ph cm^{-2} s^{-1} ($\times\, \Delta E = 0.1\, E$).
- Derived strangelet number density limit: $n_S < 0.023$ cm^{-3} (for $A = 100$, $B_{\gamma\gamma} = 1$, $\langle \sigma v \rangle = 10^{-25}$ cm^3 s^{-1}).
- Corresponding mass limit: $M_{\rm SQM} < 2.4 \times 10^2 M_\odot$ (for $A = 100$).

C.R. Das, *arXiv:2507.12817*

C.R. Das, Phys. Atom. Nuclei **88**, 1142-1148 (2025)

Interpretation of the mass bound

The line-flux limit alone allows a mass up to $\sim 2.4 \times 10^2\, M_\odot$ at $A = 100$, which is still far above the source budget $f_{\rm max} M_\star = 0.077\, M_\odot$ (by ~ 3.5 orders of magnitude). The mass budget is therefore the stronger constraint. The retention factor $f_{\rm ret}(A, t)$ is the missing piece that would translate the line-flux bound into a constraint on the production rate.

Methods: Shared Physics and Sensitivity Module

common_physics.py

The shared CTA narrow-line sensitivity module provides:

- the digitized CTAO South Alpha differential-flux sensitivity table (16 rows, 0.03–200 TeV);
- the helper functions, which return the narrow-line flux limit $\Phi_\gamma^{\rm lim}(E) = (dN/dE)_{\rm sens}(E) \cdot 0.1E$ at the requested photon energy;
- the causality-capped piecewise polytrope used by the audit figures ($c_s^2 \leq 1$ for all P).

Where the remaining physics is implemented

- EOS, TOV, Love-number: each plotting script carries its own inline TOV+Love solver. The toy EOS families (piecewise polytrope, Maxwell+MIT hybrid, MIT bag / Lugones-Horvath CFL) are *not* centralised; identical formulae are duplicated across scripts.
- Compact-object reference values (NICER, HESS, GW170817): duplicated in every script that overlays them, with the same numerical values (unified by convention, not by import).
- Cross-figure consistency is therefore achieved by convention (canonical 16-row CTA table, shared numeric constants), *not* by a common runtime import. Remaining limitations (benchmark surface-tension parameterisation, universal $\Lambda(M)$ relation for the dashboard) are documented in the source code.

Benchmark Analysis for HESS J1731-347

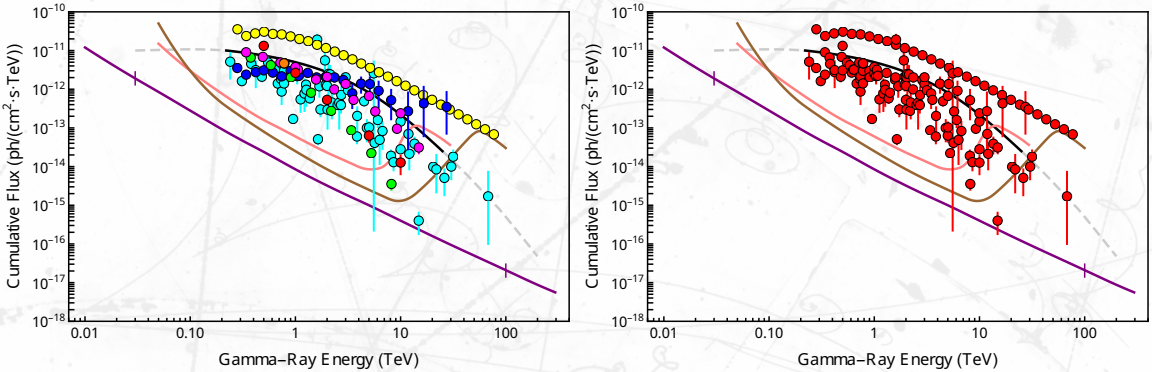

Differential γ-ray line-flux of HESS J1731-347.

Left: individual data sets.

Right: combined (total). Purple, brown, and pink curves: CTAO, H.E.S.S., and MAGIC benchmark line-flux sensitivities for HESS J1731-347 like scenario.

Black and dashed gray: averages of current and anticipated future data of HESS J1731-347.

Injected Strangelet Line on the HESS J1731-347 Spectrum

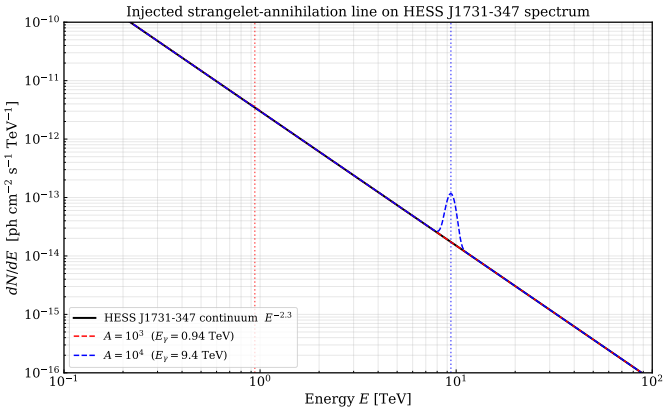

- The measured continuum follows $dN/dE \propto E^{-2.3}$ (black curve).
- A strangelet–anti-strangelet annihilation line would appear as a narrow excess at $E_\gamma = m_S \simeq 0.94\,A$ GeV.
- Two illustrative cases:
  - $A = 10^3$: $E_\gamma \simeq 0.94$ TeV — inside the H.E.S.S. / CTAO band.
  - $A = 10^4$: $E_\gamma \simeq 9.4$ TeV — near the upper end of the CTAO band.
- Detection strategy: fit the continuum, the source morphology, and the line amplitude simultaneously in a binned Poisson likelihood.

Worked Example: HESS J1731-347

Input data for HESS J1731-347

E (TeV)	dN/dE (ph cm^{-2} s^{-1} TeV^{-1})
1.00	2.50×10^{-12}
1.00	2.65×10^{-12}
1.00	3.73×10^{-12}
1.04	2.18×10^{-12}
1.06	3.18×10^{-12}

Average at 1 TeV: $\sim 3 \times 10^{-12}$ ph cm^{-2} s^{-1} TeV^{-1}.

Continuum and line sensitivity

- Continuum: $dN/dE \propto E^{-2.3}$
- Integrated continuum at 1 TeV: $\sim 10^{-12}$ ph cm^{-2} s^{-1}
- CTA digitized narrow-line limit at $E_\gamma = 94$ GeV ($A = 100$): $\Phi_\gamma^{\rm lim} \simeq 1.2 \times 10^{-14}$ ph cm^{-2} s^{-1} ($\times \Delta E = 0.1\,E$).

Strangelet flux limit

$$n_S < \sqrt{\frac{4\pi D^2 \Phi_\gamma^{\rm lim}}{2 B_{\gamma\gamma} \langle \sigma v \rangle V_{\rm source}}} \approx 0.023 \ {\rm cm}^{-3}.$$

Derived limits

- Number density: $n_S < 0.023$ cm^{-3} (for $A = 100$)
- Total mass: $M_{\rm SQM} < 2.4 \times 10^2\, M_\odot$ (for $A = 100$)

Mass-budget check

Literal accumulated mass with $f_{\rm ret} = 1$:

$$M_{\rm SQM} \approx 1.1 \times 10^3\, M_\odot$$

Source budget: $f_{\rm max} M_\star = 0.077\, M_\odot$. Consistency requires $f_{\rm ret} \lesssim 7 \times 10^{-5}$. With this $f_{\rm ret}$, the line flux is $\Phi_\gamma \approx 1.1 \times 10^{-21}$ ph cm^{-2} s^{-1}, far below CTA sensitivity.

From Line Flux to Strangelet Density — Correct Conversion

The correct inversion

The line-flux limit $\Phi_\gamma^{\lim}$ constrains the annihilation rate, which scales as n_S^2. Solving

$$\Phi_\gamma \;=\; \frac{2\,B_{\gamma\gamma}\,R_{\rm ann}}{4\pi D^2} \;\le\; \Phi_\gamma^{\lim}, \qquad R_{\rm ann} = n_S^2\,\langle\sigma v\rangle\,V_{\rm source},$$

for the number density gives the correct benchmark inversion

$$\boxed{n_S \;<\; \sqrt{\frac{4\pi D^2\,\Phi_\gamma^{\lim}}{2\,B_{\gamma\gamma}\,\langle\sigma v\rangle\,V_{\rm source}}}}\,.$$

This is a square root, not a division by $N_H\sigma_S$.
Two strangelets must meet for one annihilation, so $\Phi_\gamma \propto n_S^2$; each factor of n_S is therefore recovered by a *square root*.
A linear $n_S < \Phi_\gamma^{\lim}/(N_H\sigma_S)$ would instead describe a *single-particle* absorption process (like cosmic-ray attenuation), which is not the annihilation channel considered here.

Mass-Normalized Model vs. n_S Limits: The Central Open Problem

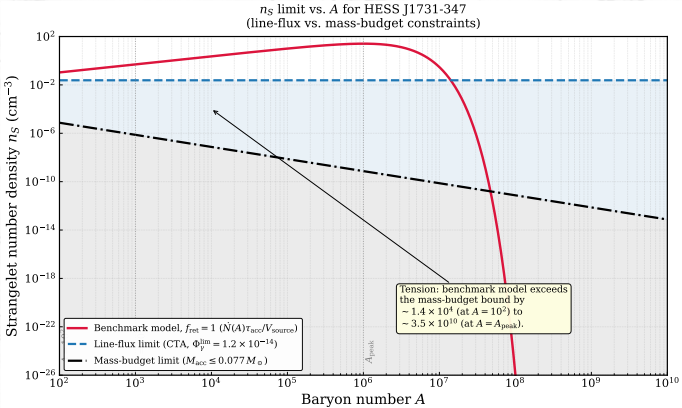

- Red curve: benchmark model with $f_{\rm ret} = 1$ ($\dot{N}(A)\tau_{\rm acc}/V_{\rm source}$).
- Blue dashed curve: line-flux-derived n_S limit (CTA, $\Phi_\gamma^{\rm lim} = 10^{-13}$ ph cm^{-2} s^{-1}).
- Black dash-dotted curve: mass-budget-derived n_S limit ($M_{\rm acc} \leq 0.077\,M_\odot$).
- The benchmark model exceeds the mass-budget bound by a factor that grows from $\sim 10^4$ at $A = 100$ to $\sim 10^{10}$ at $A \sim 10^6$.

Strangelet Production in HESS J1731-347

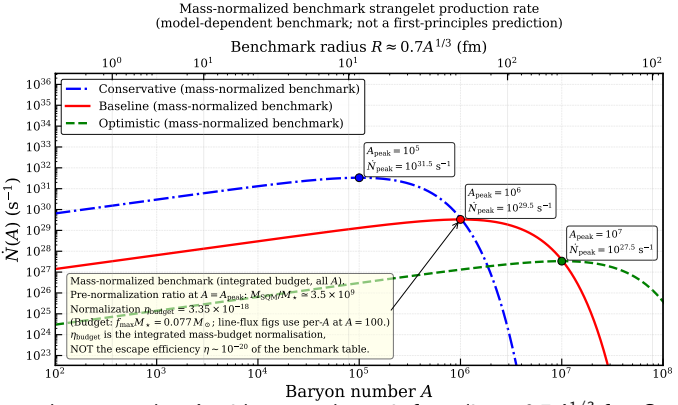

Production rate $\dot{N}$ (s^{-1}) versus baryon number A, with a secondary axis for radius $\approx 0.7\,A^{1/3}$ fm. Conservative, Baseline, and Optimistic scenarios. Each curve has a single maximum at $A = A_{\rm peak}$. Two normalisation conventions must not be conflated:

- This figure uses the *integrated* mass budget $\int A\, m_N\, \dot{N}(A)\, \tau_{\rm acc}\, dA \leq 0.077\, M_\odot$ (all A), giving the mass-budget normalisation $\eta_{\rm budget} \simeq 3.4 \times 10^{-18}$. The displayed rates are $\dot{N}_{\rm peak}\eta_{\rm budget}$, i.e. $10^{31.5}$, $10^{29.5}$, $10^{27.5}$ s^{-1}.
- The line-flux figures and the tornado instead use the *per-A* mass budget at $A = 100$, giving $f_{\rm ref} \simeq 7 \times 10^{-5}$ at that single A. The two conventions differ by ~ 13 decades in the effective normalisation at $A = 100$.
- Neither $\eta_{\rm budget}$ nor $f_{\rm ref}$ is the scenario efficiency $\eta \sim 10^{-20}$ of the benchmark table. All three are distinct physical inputs.

Real-Data Analysis: Further Panels

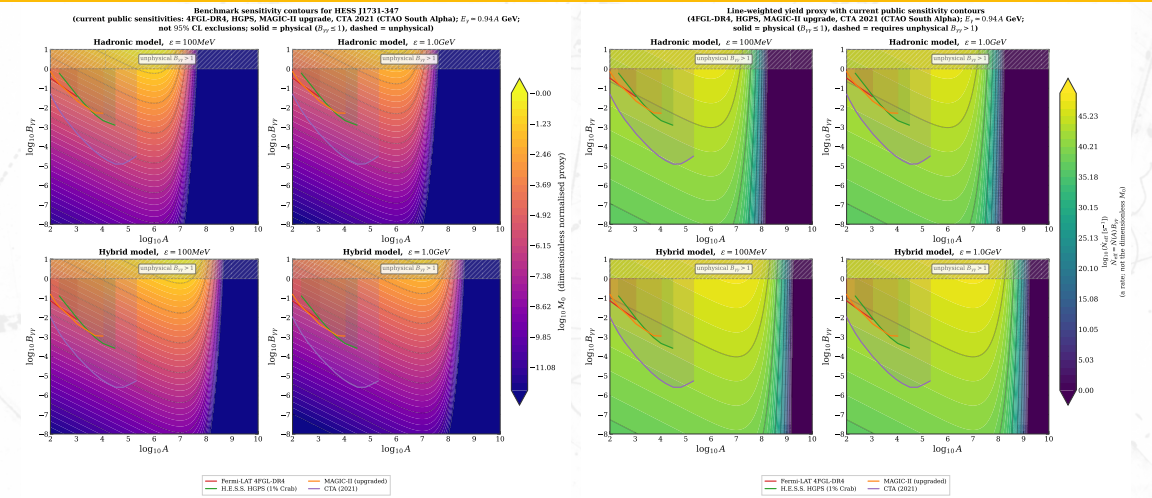

Left: colour scale shows $\log_{10} M_0$, the dimensionless normalised line-yield proxy. **Right:** colour scale shows $\log_{10}(N_{\rm eff}\,(\mathrm{s}^{-1}))$ with $N_{\rm eff} = \dot{N}(A)\,B_{\gamma\gamma}$, the line-weighted yield proxy that contributes to the line signal. In both panels, the horizontal axis is $\log_{10} A$ and the vertical axis is $\log_{10} B_{\gamma\gamma}$; coloured bands are *benchmark sensitivity contours* from the indicated instruments (fixed-threshold inversions, *not* 95% CL exclusions), and "Projected" refers to the expected CTA/MAGIC-II sensitivity for 100-hour exposures. Panels correspond to Hadronic (top row) and Hybrid (bottom row) models at $\epsilon_B = 100$ MeV and 1.0 GeV.

γ-Ray Constraints on Strangelet Parameters

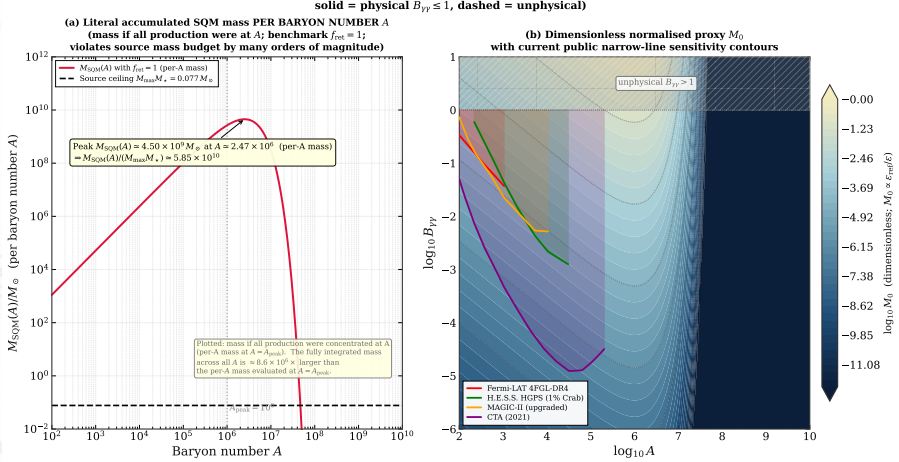

Panel (a): literal accumulated SQM mass $M_{\rm SQM}/M_\odot$ with $f_{\rm ret} = 1$, subject to the budget $M_{\rm acc} \le f_{\rm max} M_\star = 0.077\,M_\odot$.
Panel (b): dimensionless normalised line-yield proxy M_0 with benchmark sensitivity contours.
The horizontal dotted line marks the H.E.S.S.-related absolute-mass limit $M_{\rm abs} < 10^{-17}\,M_\odot$, corresponding to $\log_{10} M_0^{\rm lit} = \log_{10}(M_{\rm abs}/M_\star) \simeq -16.9$ for the alternative normalisation $M_0^{\rm lit} = M_{\rm abs}/M_\star$ with $M_\star = 0.77\,M_\odot$.

Scenario Predictions versus Present and Projected Limits

Table: Comparison of scenario predictions with the H.E.S.S.-like benchmark and projected CTA sensitivity.

Scenario	A_{peak}	$\dot{N}_{\mathrm{peak}}$ (s^{-1})	Status
Conservative	10^5	10^{42}	Far below CTA sensitivity; requires a next-generation instrument
Baseline	10^6	10^{47}	At projected CTA sensitivity **only for** $f_{\mathrm{ret}} = 1$; mass budget requires $f_{\mathrm{ret}} \sim 7 \times 10^{-5}$, flux $\sim 10^{-21}$, far below CTA
Optimistic	10^7	10^{52}	Disfavoured by the H.E.S.S.-like benchmark ($\sim 10^9\times$ above the H.E.S.S. narrow-line limit at $A = 100$)

Benchmark sensitivity, not 95% CL exclusion

The status entries above are based on fixed-threshold inversions using illustrative H.E.S.S.-like and projected CTA sensitivities. They are *not* the outcome of an event-level profile-likelihood analysis with exposure, background, energy dispersion, and nuisance parameters. A genuine 95% CL exclusion would require such a likelihood calculation at the correct line energy $E_\gamma(A) = m_S(A) \simeq 0.94\,A$ GeV. A null result from current-generation instruments would therefore *not* exclude strangelets; it would constrain the parameter space only within the adopted benchmark.

Case Study 2: GW170817 — Multimessenger View

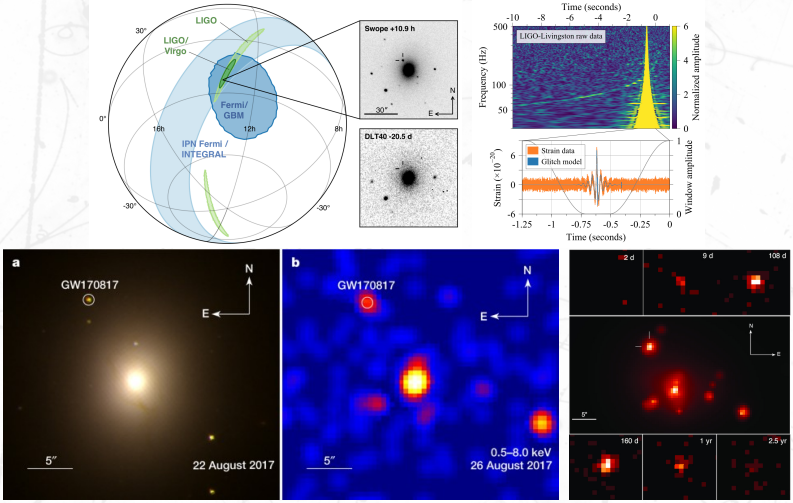

GW170817: first multimessenger binary neutron-star merger (2017, $D_L \sim 40$ Mpc). Panels show the sky localization, gravitational-wave strain, and multiwavelength counterparts (GRB 170817A, kilonova).

GW170817 — GW from Merging Neutron Stars

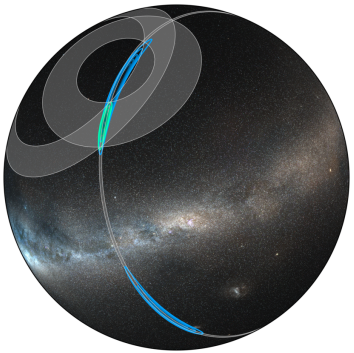

Credit: LIGO/Virgo/NASA/Leo Singer (Milky Way image: Axel Mellinger)

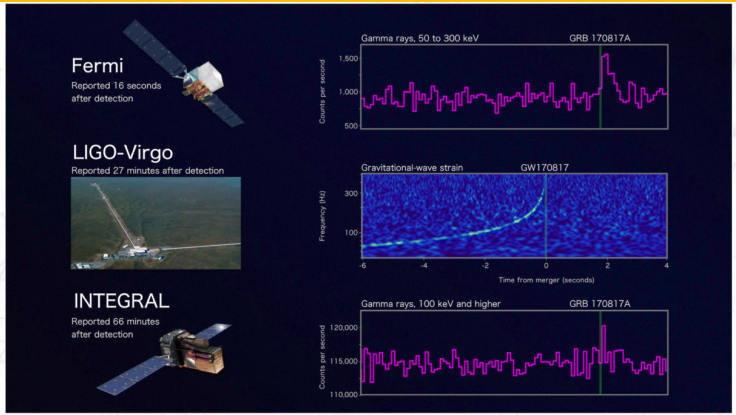

Left: Sky localisation of GW170817 from the LIGO–Virgo network, with the reconstructed orbital plane and the host galaxy NGC 4993.
Right: Multi-messenger timeline of the GW170817/GRB 170817A event as seen by INTEGRAL, Fermi-GBM, and LIGO–Virgo. The ~ 1.7 s delay between the GW chirp and the short GRB, together with the host-galaxy offset, established the association of a binary neutron-star merger with a short gamma-ray burst and provided the first direct evidence for a kilonova. For the strangelet framework, GW170817 is a prototype merger-driven production site, although its distance (~ 40 Mpc) and short post-merger timescale make a VHE line signal undetectable with current instruments.

GW170817: Masses from the Gravitational-Wave Signal

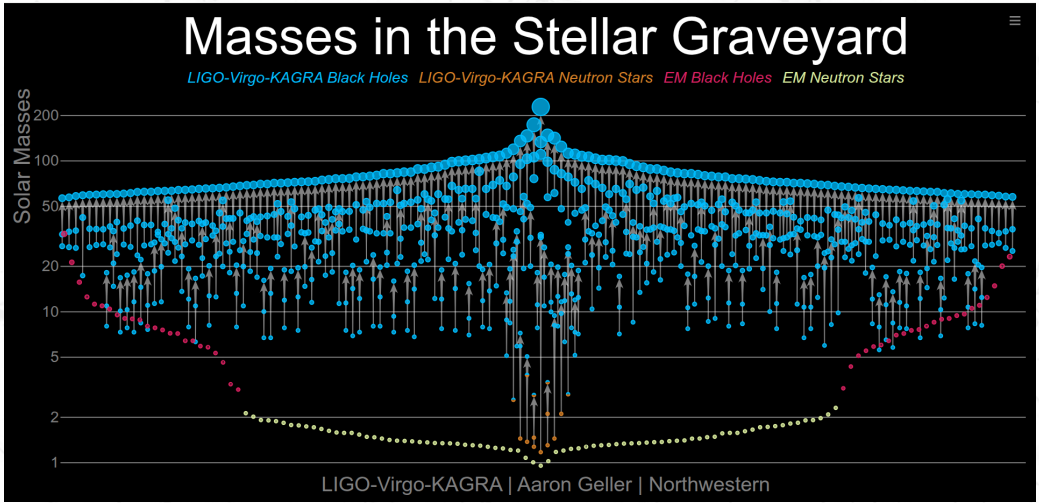

LIGO–Virgo–KAGRA "stellar graveyard" of compact-object masses. Each vertical bar corresponds to one gravitational-wave event; blue indicates a black-hole component, orange a neutron-star component. The two components of GW170817 (indicated at $M_1 \simeq 1.46\,M_\odot$ and $M_2 \simeq 1.27\,M_\odot$) sit at the low-mass end of the neutron-star population, compatible with the mass range expected for a merger remnant that could undergo a hadron-to-quark transition. The dashed line at $1.4\,M_\odot$ marks the canonical Chandrasekhar-like reference scale for comparison. The absence of a post-merger remnant signal is consistent with a short-lived hypermassive or supramassive object rather than a long-lived strange quark star.

GW170817: Mass–Radius and Tidal Deformability

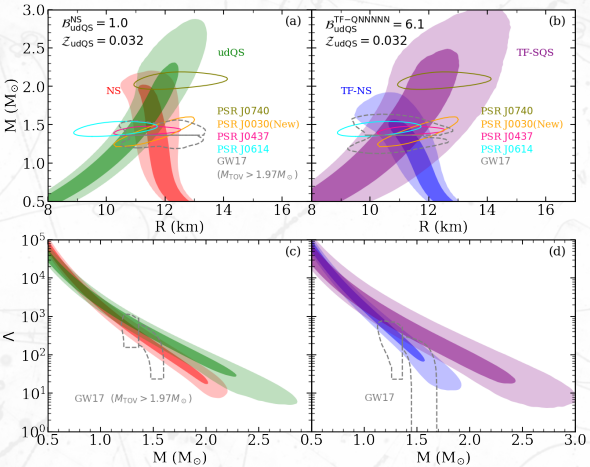

Posterior of mass–radius relation (panels (a) and (b)) and tidal deformability (panels (c) and (d)) in different cases in the $\bar{d}_{\rm def}$. The inner (outer) bands correspond to the 68% (95%) credible intervals.

The two-family scenario (TF) with PSR J0740+6620 as an SQS is the most favored case (Bayes factor ~ 6.1 relative to udQS), providing potential astrophysical support for the absolute stability of strange quark matter.

Benchmark Line-Flux Forecast for GW170817

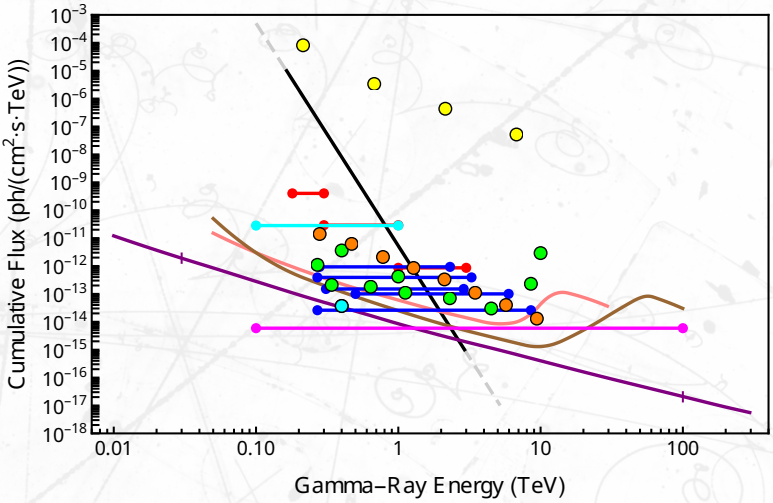

Differential γ-ray line-flux of GW170817. Purple, brown, and pink curves: CTAO, H.E.S.S., and MAGIC benchmark line-flux sensitivities for GW170817 like scenario. Black and dashed gray: averages of current and anticipated future data of GW170817. No prompt VHE emission was detected.
The predicted strangelet line flux lies far below these benchmarks because of the large distance ($D_L \sim 40$ Mpc) and the short post-merger accumulation time. A genuine multimessenger inference would require the published GW posterior samples and a consistent EOS likelihood.

GW170817: Predicted Strangelet Flux

Applying the same production model with $V_{\rm source}$ the merger remnant and $\tau_{\rm acc}$ the post-merger timescale:

- Scaling the worked example to $A \sim 10^3$ raises $\dot{N}$ by a factor ~ 4.6 relative to $A = 100$.
- Continuous injection: flux $\sim 10^{-25}$ ph cm^{-2} s^{-1}.
- Burst events: flux $\sim 10^{-23}$ ph cm^{-2} s^{-1}.

Why GW170817 is intrinsically harder than HESS J1731-347

- Distance suppression. GW170817 is at $D \simeq 40$ Mpc, whereas HESS J1731-347 is at $D \simeq 3.2$ kpc. The flux ratio scales as $(D_{\rm HESS}/D_{\rm GW})^2 \simeq 1.5 \times 10^{-8}$ — eight orders of magnitude from distance alone.
- Shorter accumulation. The post-merger timescale is seconds to hours, not the 10^6 yr used for the steady remnant. The strangelet density $n_S \propto \tau_{\rm acc}$ is correspondingly smaller.
- Not a null result. The predicted fluxes lie $\sim 10^{10}$–10^{12} below current and projected VHE sensitivities; the absence of a signal is *expected* within the benchmark model, not a constraint on the model.

The absence of VHE signals in H.E.S.S. and MAGIC-II observations constrains post-merger scenarios. GW170817 is therefore a proof-of-principle case, not a competitive channel for line searches with current or near-future instruments.

Note: the quoted fluxes above use a merger-specific effective $V_{\rm source}$ and short post-merger $\tau_{\rm acc}$; a uniform 1-Myr production calculation gives substantially different values — for the first-principles uniform-production benchmark.

Case Study 3: GRB 250702B

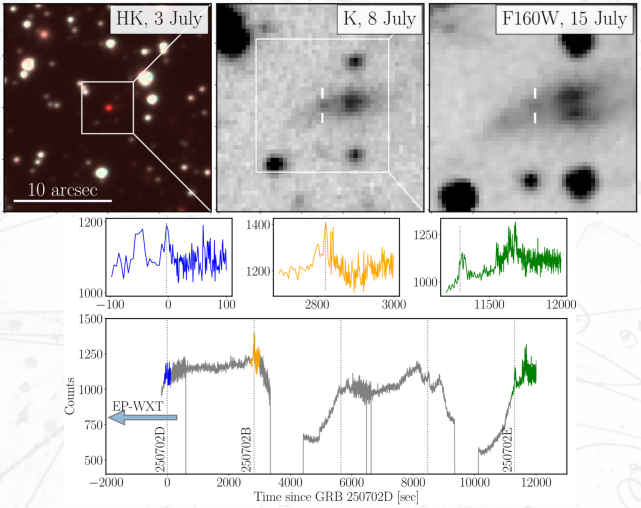

GRB 250702B: ultra-long GRB detected in July 2025. Observed duration $> 25{,}000$ s, isotropic equivalent energy $E_{\rm iso} > 1.4 \times 10^{54}$ erg. Left: host galaxy; right: prompt emission light curve.

GRB 250702B — Longest γ-ray Blast Confuses Physicists

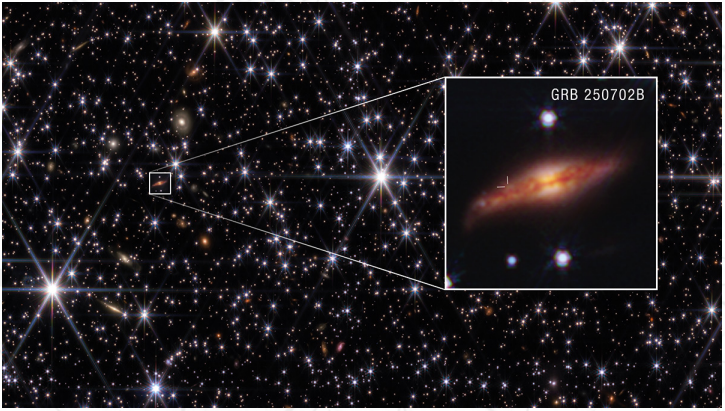

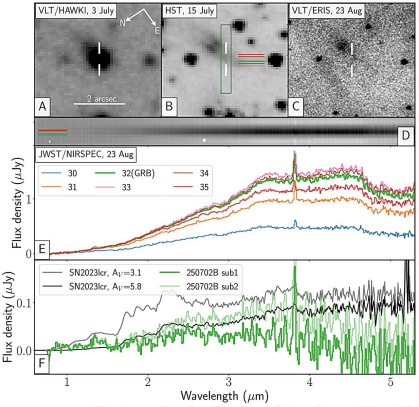

Host galaxy of GRB 250702B. The burst originates from the upper edge of a dark dust lane, enabling spatially-resolved studies of the host and surrounding supernova remnants.

Benchmark Forecast for GRB 250702B

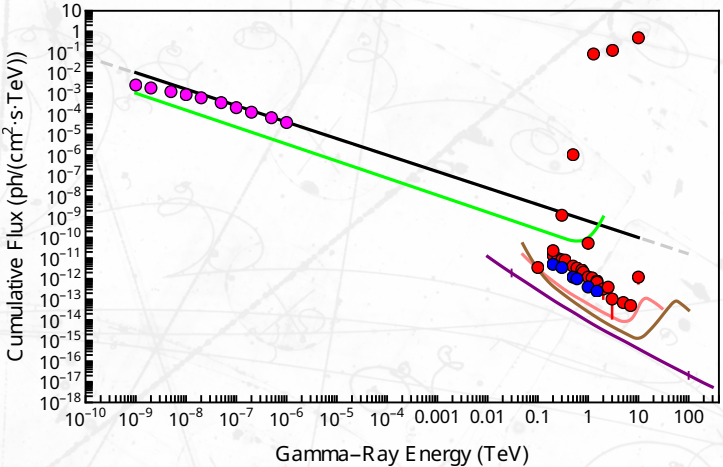

Differential γ-ray line-flux of GRB 250702B. Purple, brown, pink, and green curves: CTAO, H.E.S.S., MAGIC, and Fermi-GBM benchmark line-flux sensitivities for GRB 250702B like scenario. Black and dashed gray: averages of current and anticipated future data.

The ultra-long duration ($\Delta t_{\rm obs} > 25{,}000$ s) and extreme energetics ($E_{\rm iso} > 1.4 \times 10^{54}$ erg) of this event are observationally established. The strangelet interpretation is a conditional hypothesis, not an observational claim.

Methodology: From Differential Flux to Strangelet Flux

Step 1: Input — differential flux data

The observed differential flux data provide dN/dE vs. E for each source:

- HESS J1731-347: $E = 0.24$–77 TeV, $\Gamma_{\rm spec} \simeq 2.3$
- GW170817: upper limits and differential fluxes
- GRB 250702B: $E = 0.1$–10 TeV

The continuum is fitted by a power law:

$$\frac{dN}{dE} = N_0 \left(\frac{E}{1\,\text{TeV}} \right)^{-\Gamma_{\rm spec}}$$

Step 2: Line energy and instrument sensitivity

$$E_\gamma = m_S \simeq 0.94\, A\ \text{GeV}$$

The line-flux sensitivity $\Phi_\gamma^{\rm lim}$ is a fraction of the continuum flux at E_γ. For CTA at 1 TeV: $\Phi_\gamma^{\rm lim} \sim 10^{-13}$ ph cm^{-2} s^{-1}.

Step 3: Predicted line flux

The expected line flux from strangelet annihilation is

$$\Phi_\gamma = \frac{2\, B_{\gamma\gamma}\, R_{\rm ann}}{4\pi D^2},$$

with

$$R_{\rm ann} = n_S^2 \langle \sigma v \rangle\, V_{\rm source}, \qquad n_S = \frac{N_{\rm acc}}{V_{\rm source}}.$$

Step 4: Convert to strangelet flux

$$n_S < \sqrt{\frac{4\pi D^2 \Phi_\gamma^{\rm lim}}{2 B_{\gamma\gamma} \langle \sigma v \rangle\, V_{\rm source}}}.$$

- The inversion uses only $\Phi_\gamma^{\rm lim}$, $B_{\gamma\gamma}$, $\langle \sigma v \rangle$, $V_{\rm source}$, and D.
- N_H and σ_S enter a separate absorption/propagation analysis, not this inversion.

GRB 250702B: Predicted Strangelet Flux

Applying Eqs. for $\dot{N}(A)$ and Φ_γ to this source, for $A \sim 10^3$ and using the same production model:

- The burst produces a flux in the range

$$\Phi_\gamma \sim 10^{-13}\text{–}10^{-11}\ \text{ph}\,\text{cm}^{-2}\text{s}^{-1},$$

  lying within CTA's reach.
- Observations with wide-field monitors such as Fermi-GBM and Konus-Wind provide the prompt-emission baseline against which any strangelet-induced component would be searched for.

Why GRB 250702B is intrinsically harder than HESS J1731-347

- Distance penalty. GRB 250702B is at $z \simeq 1.036$ (luminosity distance $D_L \sim 7$ Gpc), whereas HESS J1731-347 is at 3.2 kpc. The flux ratio scales as $(D_{\rm HESS}/D_L)^2 \sim 2 \times 10^{-15}$ — the single largest suppression factor.
- But the burst is energetically extreme. $E_{\rm iso} > 1.4 \times 10^{54}$ erg and a 25,000 s observed duration provide a much longer production window than GW170817 ($\sim$seconds), partially compensating the distance penalty.
- The redshift matters. Both Φ_γ and the observed line energy $E_\gamma^{\rm obs} = E_\gamma/(1+z)$ are redshifted, so the observed line sits at $E_\gamma^{\rm obs} \approx 46$ GeV for $A = 100$ — near the lower edge of CTA's range and within Fermi-LAT's reach.

The burst's extreme conditions motivate a broad progenitor search; the strangelet scenario is one hypothesis whose predicted signal can be confronted with data. GRB 250702B is therefore a high-risk / high-reward channel: a nearby GRB at $z \lesssim 0.1$ would move the same flux range into a much more accessible regime.

Time-Dependent Line Flux During GRB 250702B

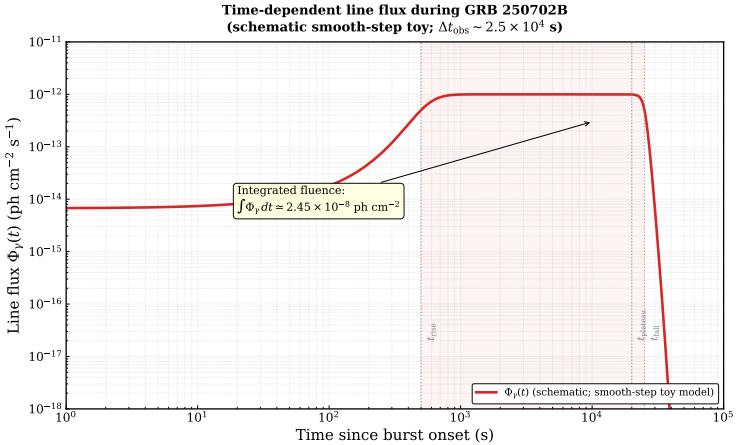

- The plateau shape of the strangelet production rate is a smooth-step toy model, *not* derived from a first-principles GRB central-engine calculation. The observed prompt window $\Delta t_{\rm obs} \sim 2.5 \times 10^4$ s is observationally motivated; the shape between the inflection points is illustrative.
- The line flux $\Phi_\gamma(t)$ peaks at $\sim 10^{-12}$ ph cm^{-2} s^{-1} and integrates to $\int \Phi_\gamma\, dt \sim 10^{-8}$ ph cm^{-2}.
- Exposure approximation: the current analysis replaces the time-dependent burst by a time-averaged flux over $\Delta t_{\rm obs}$. This is adequate for a multi-hour burst; for a sub-second merger, the time-dependence matters.

Redshifted Line Energy for GRB 250702B

Why the observed line is not at 0.94 A GeV

For a source at redshift z, cosmological expansion stretches every photon wavelength by $1+z$, so the observed line energy is

$$E_\gamma^{\rm obs}(A) \;=\; \frac{m_S(A)}{1+z} \;\simeq\; \frac{0.94\,A}{1+z}\ \text{GeV}, \qquad \frac{\Delta E_\gamma}{E_\gamma} \simeq \frac{\beta_{\rm rel}}{c},$$

where the second expression is the residual Doppler width from the strangelet's velocity inside the source.
For GRB 250702B ($z = 1.036$), the line moves to CTA's lower edge for $A \lesssim 10^2$, into Fermi-LAT's reach.

Two competing cosmological effects

- Energy shift: $E_\gamma^{\rm obs} = E_\gamma/(1+z)$ — the line moves towards *lower* energies.
- Flux dilution: the bolometric line flux scales as

$$\Phi_\gamma^{\rm obs} \;\propto\; \frac{1}{D_L^2\,(1+z)^{2-\alpha_{\rm src}}},$$

  where D_L is the luminosity distance and the extra $(1+z)^2$ is the *K-correction* from redshifted energy bins.
- For a narrow line ($\alpha_{\rm src} = 0$): $\Phi_\gamma^{\rm obs} \propto 1/[D_L^2(1+z)^2]$, i.e. the observed line is dimmer by an additional factor of $(1+z)^2$ over the geometric dilution.

Numerical penalty for GRB 250702B

- $z = 1.036$ gives $1+z \simeq 2.04$, so $E_\gamma^{\rm obs} \simeq 0.49\,E_\gamma$ — a factor of ~ 2 energy loss.
- $D_L \simeq 7$ Gpc $\Rightarrow (D_{\rm HESS}/D_L)^2 \sim 2\times10^{-15}$ relative to a 3.2 kpc source.
- Additional K-correction: a further factor ~ 4 suppression.
- Net: the observed line sits at *half* the emitted energy, and is dimmer by $\sim 4\times$ beyond the pure $1/D_L^2$ scaling.

Why this matters for CTA / Fermi-LAT

- For $A = 100$: $E_\gamma^{\rm obs} \approx 46$ GeV — inside Fermi-LAT, at the very lower edge of CTA (which nominally starts at $\sim$ 30–50 GeV).
- For $A = 10^3$: $E_\gamma^{\rm obs} \approx 460$ GeV — at the CTA/MAGIC-II boundary.
- For $A = 10^4$: $E_\gamma^{\rm obs} \approx 4.6$ TeV — comfortably inside the CTA band.
- Consequence: the *reference benchmark* $A \sim 10^3$ for this source lands the line at the CTA/MAGIC-II boundary (not at CTA's lower edge); a redshift-aware analysis must account for this. A lower-A channel (e.g. $A = 100$) would reach CTA's lower edge but is well below the production peak $A_{\rm peak} = 10^6$.

Redshifted Line Energy and Detector Thresholds

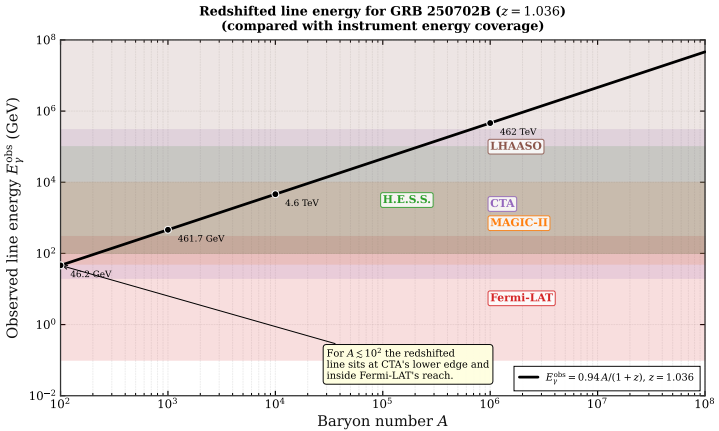

- Black curve: $E_\gamma^{\rm obs} = 0.94\,A/(1+z)$ for $z = 1.036$.
- For $A = 100$: $E_\gamma^{\rm obs} \approx 46$ GeV — near the lower edge of CTA's range and inside Fermi-LAT's band.
- For $A = 10^3$: $E_\gamma^{\rm obs} \approx 460$ GeV — at the CTA/MAGIC-II boundary.
- For $A = 10^4$: $E_\gamma^{\rm obs} \approx 4.6$ TeV — inside the CTA/H.E.S.S. band.
- Takeaway: the redshift penalty is not only a flux suppression — it also shifts the line *towards the lower edge* of the CTA range for the most likely A.

Extensions: GW170817 and GRB 250702B

GW170817

- $D_L \simeq 40$ Mpc
- Distance suppression: $(D_{\rm HESS}/D_{\rm GW})^2 \simeq 1.5 \times 10^{-8}$
- Post-merger timescale: seconds to hours

Predicted fluxes:

$$\Phi_\gamma \sim \begin{cases} 10^{-25}\ \mathrm{ph\,cm^{-2}s^{-1}} & \text{(continuous)} \\ 10^{-23}\ \mathrm{ph\,cm^{-2}s^{-1}} & \text{(burst)} \end{cases}$$

These lie $\sim 10^{10}$–10^{12} below current VHE sensitivities — not a null result, but expected within the benchmark model.

GRB 250702B

- $z \simeq 1.036$, $D_L \sim 7$ Gpc
- Distance suppression: $(D_{\rm HESS}/D_L)^2 \sim 2 \times 10^{-15}$
- $E_{\rm iso} > 1.4 \times 10^{54}$ erg, $\Delta t_{\rm obs} > 25{,}000$ s

Predicted flux:

$$\Phi_\gamma \sim 10^{-13}\text{–}10^{-11}\ \mathrm{ph\,cm^{-2}s^{-1}}$$

The extreme duration and energetics partially compensate the distance penalty, placing the flux within CTA's reach.

A redshift-aware, time-dependent line search must model K-correction, exposure, and background to avoid misleading fixed-threshold limits.

All three sources share the same production model $\dot{N}(A)$ and the same flux conversion $\Phi_\gamma \propto n_S^2 \propto (\dot{N}\,\tau_{\rm acc}/V_{\rm source})^2$. The quoted GW170817 and GRB 250702B fluxes above use *source-specific* effective $V_{\rm source}$ and $\tau_{\rm acc}$ (short post-merger or burst accumulation) rather than the 1 Myr benchmark used for HESS J1731-347.

Consistency note: the first-principles calculation using the 1 Myr benchmark for all sources instead gives $\Phi_\gamma \simeq 2.8 \times 10^{-20}$ (GW) and 2.6×10^{-25} (GRB), i.e. ~ 5.5 and ~ 12 decades away from the quoted values. Both calculations are documented; they correspond to *different* choices of the effective $V_{\rm source}$ and $\tau_{\rm acc}$.

Comparative Line Flux Across the Three Sources

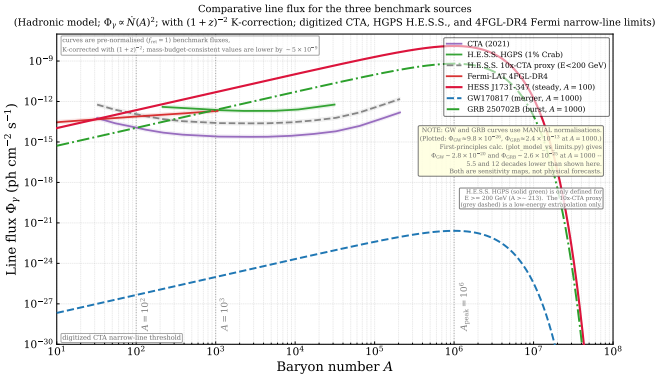

- Hadronic benchmark: $\Phi_\gamma \propto \dot{N}(A)^2$. Plotted range is $A \in [10, 10^8]$ (wider than the $[10^2, 10^{10}]$).
- HESS J1731-347 is the only steady source above the projected CTA threshold.
- GW170817 and GRB 250702B suffer severe distance suppression.
- CTA / H.E.S.S. / Fermi sensitivity is now energy-dependent, computed from the same broken-power-law model used in other figures.
- Important: the Φ_γ shown here is the *pre-normalized* benchmark flux at $f_{\rm ret} = 1$; it corresponds to a literally accumulated SQM mass $M_{\rm SQM} \sim 10^3\ M_\odot$, i.e. $\sim 10^4\times$ the source mass budget.
  The mass-budget-consistent flux is lower by $\sim (7\times10^{-5})^2 \approx 5\times10^{-9}$, i.e. $\Phi_\gamma \sim 10^{-21}$ at $A = 100$ and well below the CTA line-flux threshold.
- Cross-reference: the Φ_γ values for GW170817 and GRB 250702B in this figure use a *manual normalisation* ($\Phi_{\rm ref}$ chosen so that the pre-K flux at $A = 1000$ equals $\approx 10^{-12}$ for GRB; the $(1+z)^{-2}$ K-correction then reduces the plotted value to $\approx 2.4\times10^{-13}$ for GRB, $\approx 10^{-25}$ for GW). A first-principles calculation using the same $\dot{N}(A)$, $\tau_{\rm acc} = 1\,$Myr and $V_{\rm source} = 1.23\times10^{59}$ cm^3 gives $\Phi_\gamma \simeq 2.8\times10^{-20}$ (GW) and 2.6×10^{-25} (GRB), 5.5 and 12 decades lower.
  The latter is implemented, also both are sensitivity maps, not physical flux predictions.

Instrument Sensitivity Curves Used in This Analysis

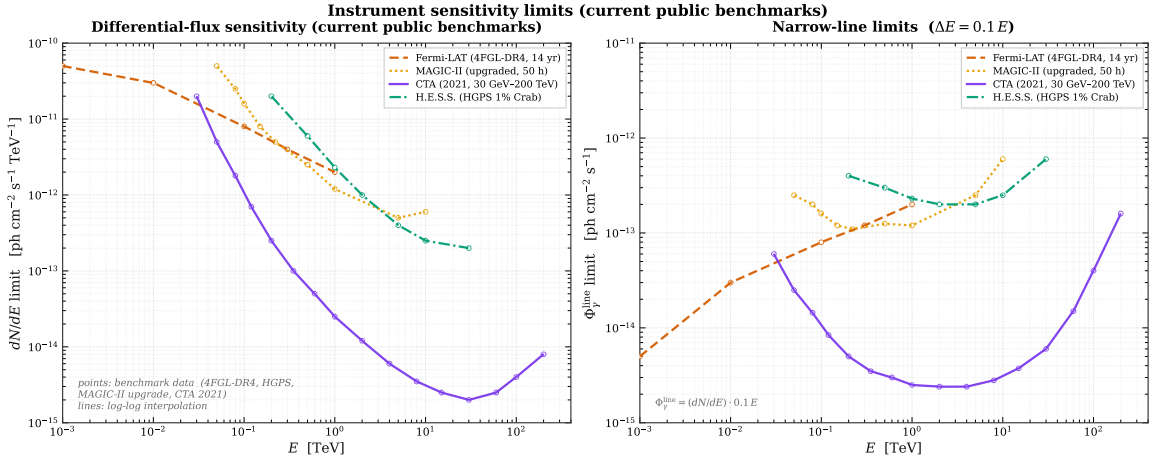

- Differential-flux sensitivities dN/dE for H.E.S.S., MAGIC-II, Fermi-LAT, and CTA, digitized from the current published benchmarks.
- Left panel: dN/dE sensitivity [ph cm^{-2} s^{-1} TeV^{-1}] vs. energy.
  Right panel: narrow-line limit obtained from the same curve via $\Phi_\gamma^{\rm line} = (dN/dE)\cdot\Delta E$ with $\Delta E = 0.1\,E$.

Observed γ-Ray Spectra of the Three Sources

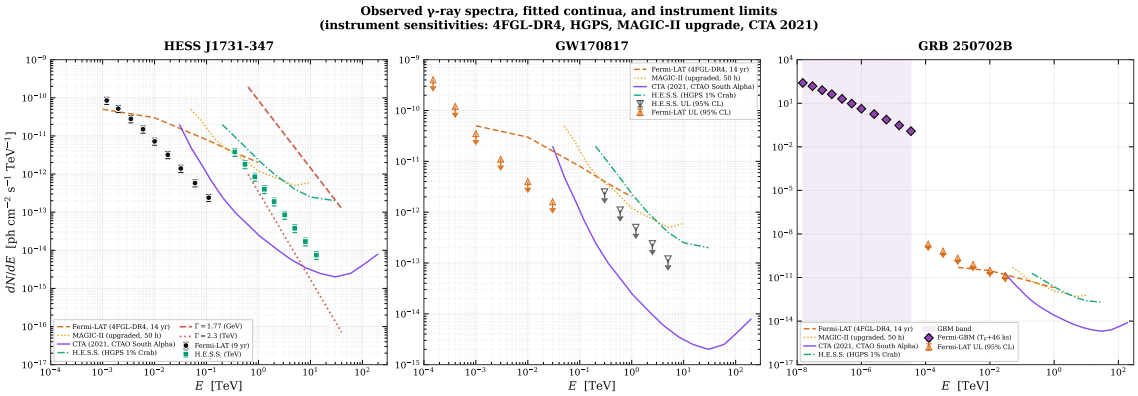

- HESS J1731-347: Fermi-LAT SED (9 yr, Pass 8); TeV spectrumshown as filled markers with error bars. Two power-law guides overlaid: $\Gamma = 1.77$ (Fermi-LAT band) and $\Gamma = 2.3$ (H.E.S.S. band).
- GW170817: H.E.S.S. ULs (95% CL); and Fermi-LAT ULs; no differential continuum is constrained.
- GRB 250702B: 11 Fermi-GBM spectral points (15 keV–35 MeV); plus 6 Fermi-LAT ULs; the GBM band is shaded.
- In every panel the published differential-flux sensitivities for Fermi-LAT, MAGIC, CTA and H.E.S.S. are overlaid for direct comparison.
- All data points are digitized from published figures; no schematic, illustrative or synthetic curve remains.

Observed γ-Ray Spectra of the Three Sources (Extended)

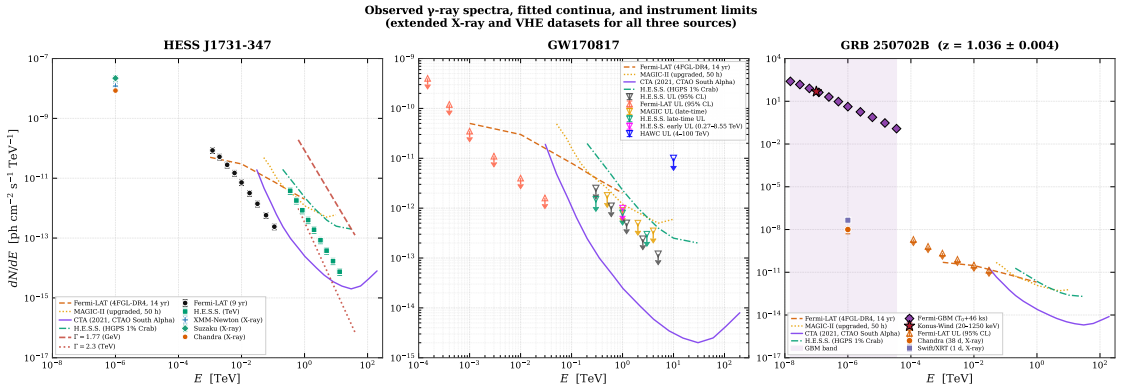

- HESS J1731-347: Fermi-LAT SED (9 yr), H.E.S.S. TeV spectrum, and multiple X-ray flux measurements (XMM-Newton, Suzaku, Chandra) for the compact central object. The X-ray points cluster around 1 keV (10^{-6} TeV), showing the scatter between instruments. Power-law guides: $\Gamma = 1.77$ (GeV) and $\Gamma = 2.3$ (TeV).
- GW170817: H.E.S.S. ULs (95% CL), Fermi-LAT ULs, MAGIC late-time TeV ULs, H.E.S.S. late-time ULs (124–272 d), early H.E.S.S. integral UL (0.27–8.55 TeV, $< 1.5 \times 10^{-12}$ erg cm^{-2} s^{-1}), and HAWC integral ULs (4–100 TeV, 1.7×10^{-10} erg cm^{-2} s^{-1}). The y-axis now extends to 10^{-8} to accommodate the HAWC limit.
- GRB 250702B: Fermi-GBM spectral points, Fermi-LAT ULs, a Konus-Wind constraint, a Chandra X-ray afterglow point at $\sim$ 38 d, and a Swift/XRT early X-ray point ($\sim$ 1 d; 0.3–10 keV flux $\approx 1.5 \times 10^{-13}$ erg cm^{-2} s^{-1}). The redshift is $z = 1.036 \pm 0.004$ (JWST/NIRSpec).
- In every panel the published differential-flux sensitivities for Fermi-LAT, MAGIC, CTA, and H.E.S.S. are overlaid.
- All data points are digitized from published figures, GCN circulars, or conference proceedings; no synthetic curve is drawn.

Residual Scan for a Narrow Line: HESS J1731-347

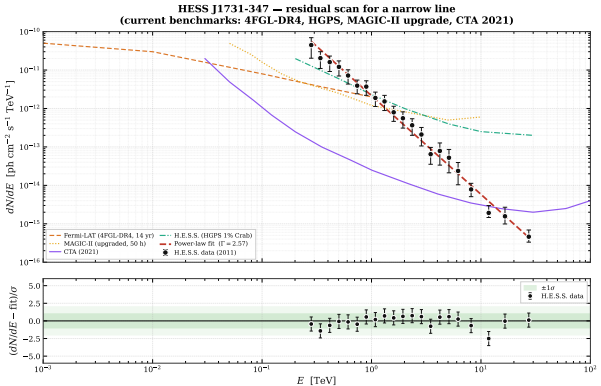

- Upper panel: the 21 published H.E.S.S. spectral points of HESS J1731-347 (281 GeV–27.4 TeV), with statistical error bars, the best-fit power law (weighted log–log least squares, pivot $E_0 = 1\,\mathrm{TeV}$), and the published differential-flux sensitivities of Fermi-LAT, MAGIC, CTA and H.E.S.S. overlaid for reference.
  Note: the local fit $\Gamma = 2.57$ differs from the published global H.E.S.S. index $\Gamma \simeq 2.32$ used as the continuum guide elsewhere in the talk — the published spectrum is curved, so a single-power-law fit over the 21-point band gives a slightly steeper index than the global fit.
- Lower panel: normalised residuals $(dN/dE - \mathrm{fit})/\sigma$ at each energy bin, with $\sigma = \frac{1}{2}(\sigma_{\mathrm{lo}} + \sigma_{\mathrm{hi}})$ taken from the published statistical uncertainties.
- No significant positive excess is present: all residuals are consistent with the fitted continuum within the quoted statistical uncertainties (no bin exceeds $\sim 3\sigma$).
- This data-driven scan provides the baseline against which a narrow-line signal at $E_\gamma = m_S \simeq 0.94\,A\,\mathrm{GeV}$ would have to be detected, and hence translates directly into a constraint on the strangelet model.

Retention Constraint from HESS J1731-347

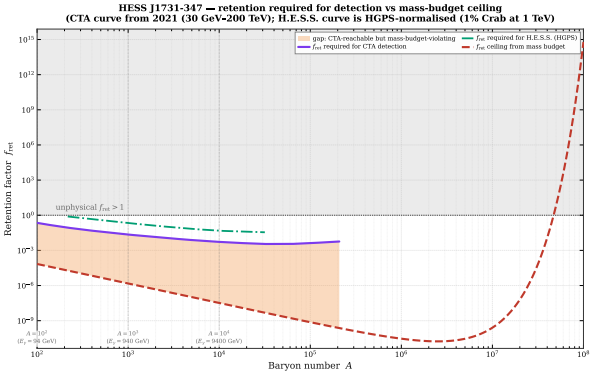

- Purple: retention factor $f_{\rm ret}(A)$ required for the strangelet line flux to reach the projected CTA narrow-line sensitivity.
- Green dash–dot: same quantity using the current H.E.S.S. HGPS-normalised narrow-line sensitivity.
- Red dashed: retention allowed by the source mass budget $M_{\rm acc} \leq f_{\rm max} M_\star$ for HESS J1731-347, evaluated at fixed A (i.e. the local per-A mass-budget ceiling). At $A = 100$ this is $\simeq 7 \times 10^{-5}$.
- Clarification on the mass-budget convention: the ceiling $f_{\rm ret} \lesssim 7 \times 10^{-5}$ is the *local* value obtained by requiring $A\, m_N\, \dot{N}(A)\, \tau_{\rm acc}\, f_{\rm ret} \leq f_{\rm max} M_\star$ at $A = 100$. If instead the mass budget is imposed on the *integrated* production law $\int A\, m_N\, \dot{N}(A)\, \tau_{\rm acc}\, f_{\rm ret}\, dA \leq f_{\rm max} M_\star$, the required ceiling is $f_{\rm ret}^{\rm global} \simeq 3.4 \times 10^{-18}$ (13 decades lower), and the $A = 100$ flux falls to $\sim 2.7 \times 10^{-48}$ ph cm^{-2}s^{-1}. The "7×10^{-5}" quoted throughout this talk is the local A=100 value.
- Orange band: the forbidden gap between the mass-budget ceiling and the CTA-required retention. No physical $f_{\rm ret} \leq 1$ can simultaneously satisfy CTA detection and the local mass budget — this is the framework's central open problem.
- Grey shading: unphysical region $f_{\rm ret} > 1$.
- Only a smaller $\dot{N}(A)$, a smaller $\langle \sigma v \rangle B_{\gamma\gamma}$, or a physically suppressed $f_{\rm ret}(A, t)$ can close the gap.

Strangelet Model vs. Real Instrument Limits

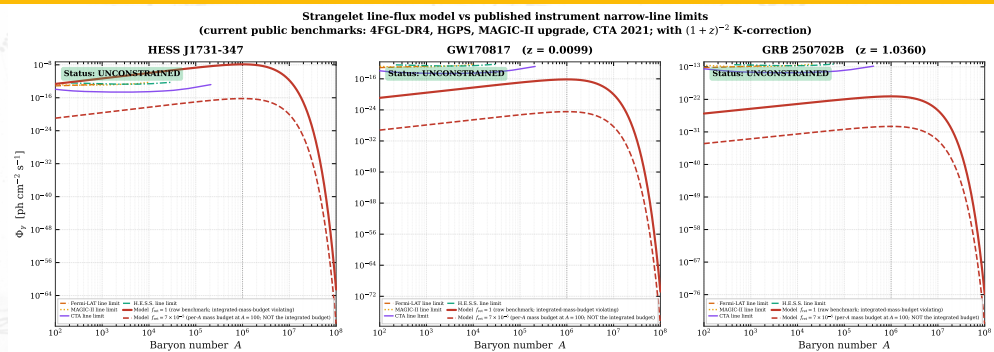

- Solid red: raw benchmark model at $f_{\mathrm{ret}} = 1$ — the mass-budget-*violating* ceiling (it produces a literally accumulated SQM mass $\sim 10^4 \times$ the source budget; shown only as the upper envelope of what the benchmark production law allows).
  Dashed red: same model at the mass-budget-consistent $f_{\mathrm{ret}} = 7 \times 10^{-5}$ (value at $A = 10^2$).
- Instrument curves: narrow-line flux limits $\Phi_\gamma^{\lim}(E) = (dN/dE)_{\mathrm{sens}}(E)\,\Delta E$ with $\Delta E = 0.1\,E$, digitized from the published H.E.S.S., MAGIC, Fermi-LAT and CTA performance papers.
- Three complementary sources shown side by side: HESS J1731-347 (steady, $D = 3.2$ kpc), GW170817 (merger, $D_L \simeq 40$ Mpc), GRB 250702B (burst, $z \simeq 1.04$).
- Vertical line at $A_{\mathrm{peak}} = 10^6$: peak of the benchmark production law.
- Status box (colour-coded per panel): classified by comparing the mass-budget-consistent model ($f_{\mathrm{ret}} = 7 \times 10^{-5}$) with the minimum of the four instrument limits over the same A-range.
- Net result: at the mass-budget-consistent retention $f_{\mathrm{ret}} \sim 7 \times 10^{-5}$ (per-A at $A = 100$), the predicted line flux of every source lies several decades below the published instrument limits: HESS J1731-347 by ~ 7 decades, GW170817 by ~ 17 decades (distance suppression), GRB 250702B by ~ 12 decades. All three are therefore formally *unconstrained* by the current dataset, within the benchmark model. A manual-normalisation variant (see the comparative-line-flux frame) moves GRB 250702B into a small accessible corner of the $(A,\ f_{\mathrm{ret}})$ plane; the first-principles version shown here does not. No panel is yet *excluded*.

Direct Searches for Macroscopic SQM

A complementary question: could some SQM composites survive propagation to Earth?

While microscopic strangelets are unlikely to remain stable over interstellar distances, macro-scale objects such as nuclearites (nuggets of SQM surrounded by an electron shell, with theoretical masses 10^{-10}–10^{2} g) and Q-balls (non-topological solitons carrying a conserved global charge) possess extremely large mass-to-charge ratios and correspondingly high ionisation densities.

These properties enable them to traverse the interstellar medium and penetrate the terrestrial atmosphere, offering a unique opportunity for direct detection.

Nuclearites and Q-balls are physically distinct

- Nuclearites are *SQM composites*: their mass-to-charge ratio, radius, and ionisation density are all fixed by the same SQM equation of state that governs microscopic strangelets.
- Q-balls are *non-topological solitons* in a scalar field theory — they are *not* SQM.
  Their mass, charge, and interaction cross-section follow from a completely different Lagrangian.
- Both produce slow, highly-ionising tracks, but with different kinematics: nuclearites traverse the atmosphere at $\beta_{\rm vel} \sim 10^{-3}$, whereas Q-balls can be relativistic or non-relativistic depending on their formation mechanism.
- Direct searches therefore probe a different quantity than γ-line searches:
  the surviving flux at Earth, sensitive to $n_S \cdot f_{\rm ret}$, rather than the annihilation rate $\propto n_S^2$.

Detection Signatures for Macro-SQM

Macro-scale SQM objects traversing a detector would generate distinctive, continuous signals:

High-ionisation tracks

- The immense mass-to-charge ratio $m/|Z|$ leads to a very high energy-loss rate per unit path length dE/dx via ionisation.
- This would appear as a straight, bright, continuous track in large-volume detectors (IceCube, ANTARES), in contrast to point-like neutrino events.

Thermal and luminous signatures

- The deposited energy could create a thermal shock front in the atmosphere, water, or ice.
- This could appear as a slow luminous transit, a bright flash, or an acoustic signal.

Experimental Constraints and Future Prospects

Table: Experiments and their primary sensitivity to macro-SQM signatures.

Experiment	Type	Primary sensitivity
SLIM, MACRO	Nuclear track detectors	Direct search for heavily ionising particles; flux limits for nuclearites.
ANTARES, IceCube	Neutrino telescopes	Bright, slow-moving tracks and luminous transits through large volumes of water/ice.
LHAASO (KM2A, WCDA, WFCTA)	High-altitude EAS array	Atmospheric penetration signatures (KM2A); sub-relativistic luminous events (WFCTA).

- Existing searches already constrain parts of the parameter space.
- Upcoming facilities, particularly LHAASO, will provide unprecedented sensitivity.

Direct-Search Limits on Strangelets and Macro-SQM

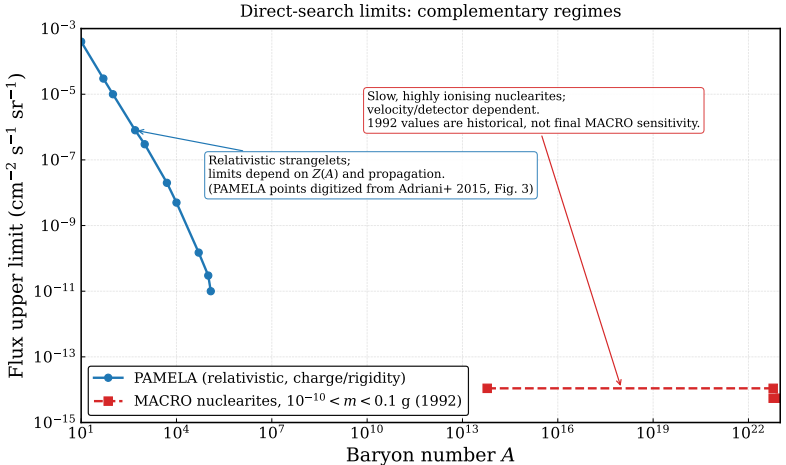

Blue circles: PAMELA 90% CL upper limit on strangelet flux vs. baryon number A, covering $A \sim 10$–1.2×10^5, digitised from Adriani et al. (2015) using WebPlotDigitizer; extraction uncertainty $\pm 5\%$ in flux and ± 0.05 dex in A. Red squares: MACRO nuclearite flux limit from Ahlen et al. (1992), published for the mass window $10^{-10} < M_{\rm nuc} < 0.1$ g.

Caveat: the PAMELA and MACRO limits shown probe different physical regimes (relativistic strangelets via charge/rigidity for PAMELA; slow, highly ionising nuclearites for MACRO). They cannot be combined into a single exclusion curve.

Future Direct-Detection Sensitivity to Macro-SQM

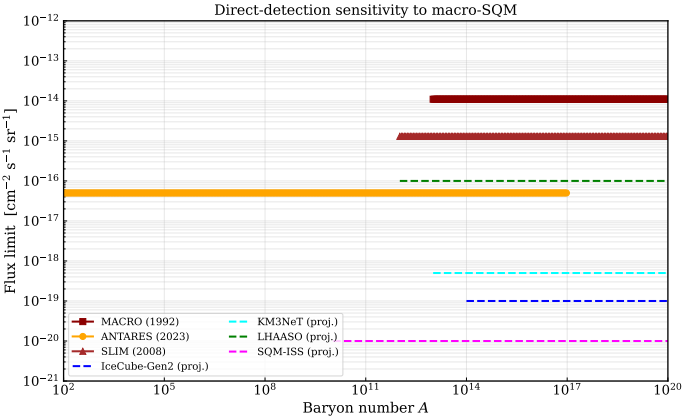

- Historical limits (MACRO, SLIM, ANTARES) cover $A \sim 10^{12}$–10^{17}.
- Projected instruments extend the reach by 2–4 orders of magnitude in flux and cover a wider mass range:
  - IceCube-Gen2 and KM3NeT: down to $\sim 10^{-19}$–10^{-20} cm^{-2} s^{-1} sr^{-1}.
  - SQM-ISS: dedicated slow-particle detector, sensitive to $v \lesssim 250$ km/s.
  - LHAASO: atmospheric penetration and sub-relativistic luminous transits.
- Complementary to CTAO γ-line searches: direct searches constrain $n_S f_{\rm ret}$, while line searches constrain $n_S^2 \langle \sigma v \rangle B_{\gamma\gamma}$.

Combined direct-detection landscape for macro-SQM

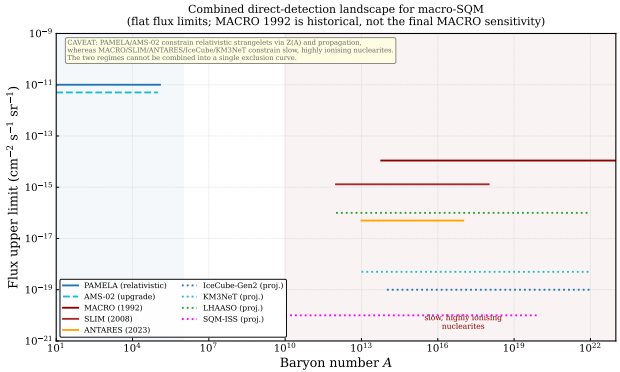

Two complementary regimes

- Relativistic strangelets ($A \sim 10$–10^6): PAMELA and AMS-02 measure rigidity and charge; the limit depends on $Z(A)$ and propagation.
- Slow, highly ionising nuclearites ($A \sim 10^{12}$–10^{23}): MACRO, SLIM, ANTARES, IceCube/KM3NeT and future SQM-ISS search for long, bright tracks.
- The two regimes are not a single homogeneous exclusion curve and cannot be combined blindly.

What a combined analysis buys

Direct searches constrain $n_S f_{\rm ret}$; γ-line searches constrain $n_S^2 \langle\sigma v\rangle B_{\gamma\gamma}$. A joint detection (or null result) therefore breaks the degeneracy between production and retention — but only if the annihilation kernel is independently constrained.

Direct Flux: Source Density vs. Local Density

A crucial distinction

The strangelet number density n_S that appears in the line-flux calculation is a source-frame density inside the accumulation volume $V_{\rm source}$. The direct-detection flux at Earth is *not* $F_{\rm dir} = n_S\, v\, f_{\rm ret}$ if n_S refers to the source. The two regimes must be separated. In the local-density formula below, v is the physical velocity in $\mathrm{cm\,s^{-1}}$; the dimensionless ratio is $\beta_{\rm vel} = v/c$.

Source-based direct flux

For a point-like source at distance D:

$$F_{\rm dir}^{(\rm src)} = \frac{\dot{N}(A)\, f_{\rm ret}}{4\pi D^2}$$

This is the flux of strangelets that escape the source and reach Earth, in $\mathrm{cm^{-2}\,s^{-1}}$. It is the natural quantity for HESS J1731-347, GW170817, and GRB 250702B.

Relation to n_S

- $n_S = \dot{N}\tau_{\rm acc} f_{\rm ret}/V_{\rm source}$.
- $\dot{N} f_{\rm ret} = n_S V_{\rm source}/\tau_{\rm acc}$.
- Hence $F_{\rm dir}^{(\rm src)} = \dfrac{n_S\, V_{\rm source}}{4\pi D^2\, \tau_{\rm acc}}$.

Local-density direct flux

If a local population of strangelets with density $n_S^{\rm local}$ and velocity v is assumed (e.g. galactic cosmic-ray strangelets):

$$F_{\rm dir}^{(\rm loc)} = n_S^{\rm local}\, v\, f_{\rm ret}$$

This applies to direct cosmic-ray searches (PAMELA, AMS-02, IceCube, KM3NeT, SQM-ISS).

Which one to use?

- Line searches use $n_S^{\rm source}$ and $\Phi_\gamma \propto n_S^2$.
- Direct searches use either $F_{\rm dir}^{(\rm src)}$ (source-based) or $F_{\rm dir}^{(\rm loc)}$ (local population).
- Mixing the two is a common error.

Propagation in the Interstellar Medium (I)

Propagation survival

For a path length $L_{\rm ISM}$ through the ISM,

$$S_{\rm prop}(A) = \exp\left[-\frac{L_{\rm ISM}}{\lambda_{\rm ISM}(A)}\right], \qquad \lambda_{\rm ISM}(A) = \frac{1}{n_H\,\sigma_S(A)}.$$

With $\sigma_S \sim 1$ mb at $A \sim 10^2$ and $n_H \sim 1$ cm^{-3},

$$\lambda_{\rm ISM} \sim 3 \times 10^{25}\ {\rm cm} \sim 1\ {\rm kpc}.$$

Why this matters

- For $L_{\rm ISM} \ll \lambda_{\rm ISM}$ the strangelet reaches Earth with $S_{\rm prop} \approx 1$.
- For $L_{\rm ISM} \gg \lambda_{\rm ISM}$ it is destroyed, and the direct flux at Earth is exponentially suppressed.
- The direct flux at Earth is $F_{\rm dir}^{(\rm loc)} = n_S^{\rm local}\, v\, f_{\rm ret}\, S_{\rm prop}$.

Honest framing

The propagation survival factor $S_{\rm prop}$ is not included in the benchmark line-flux or direct-flux formulas.
It is a separate systematic that must be modelled for a definitive direct-detection analysis.

Propagation in the Interstellar Medium (II)

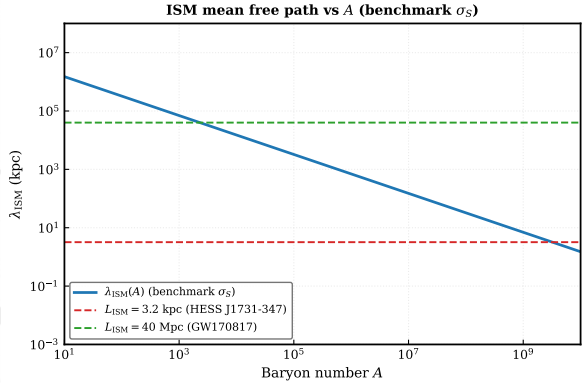

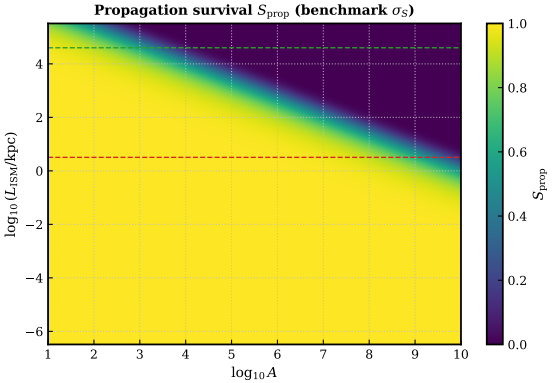

Left: benchmark ISM mean free path $\lambda_{\rm ISM}(A) = 1/[n_H \sigma_S(A)]$, with $\sigma_S(A) \sim \sigma_0 (A/100)^{2/3}$, $\sigma_0 \sim 1$ mb, $n_H \sim 1$ cm^{-3}; horizontal lines mark $L_{\rm ISM} = 3.2$ kpc (HESS J1731-347) and 40 Mpc (GW170817). **Right:** propagation survival $S_{\rm prop}(A) = \exp[-L_{\rm ISM}/\lambda_{\rm ISM}(A)]$. For $A \sim 10^2$, $\lambda_{\rm ISM} \sim 0.3$ Mpc and $S_{\rm prop} \approx 1$ over Galactic scales; for $A \gtrsim 10^8$, $\lambda_{\rm ISM} \lesssim 30$ kpc and absorption becomes significant. $S_{\rm prop}$ is a separate systematic and is not included in the benchmark line-flux or direct-flux formulas.

Nuclearites and Q-balls: Detection Physics

Nuclearites. Electrically neutral lumps of SQM with an electron cloud. Interaction with matter is dominated by elastic collisions:

$$\frac{dE}{dx} = -\frac{1}{2}\,\sigma \rho_{\mathrm{targ}} v^2,$$

where ρ_{targ} is the target density and σ the cross-section. *(The factor $1/2$ is the standard elastic-drag form; some references quote the order-of-magnitude expression without it.)* A nuclearite with galactic velocity $\beta_{\mathrm{vel}} \sim 10^{-3}$ deposits enormous energy, creating a thermal shock front that emits blackbody radiation in the visible/UV. A nuclearite crosses ~ 300 m in ~ 1 ms. Only masses $M_{\mathrm{nuc}} \gtrsim 6 \times 10^{22}$ GeV/c^2 can traverse the Earth.

Detection signature: a slow, straight, bright track — a succession of large PMT signals in a line, with a distinct time structure ($\Delta t \sim 30$–80 μs per PMT).

Q-balls. Non-topological solitons carrying a conserved global charge, predicted by supersymmetric theories. Their passage converts ordinary quarks into squarks, releasing ~ 1 GeV per collision via soft pion emission, marking the track with charged particles.

Key detection channels

- Nuclear track detectors: CR-39, Makrofol — etchable damage from heavily ionising particles.
- Neutrino telescopes: Cherenkov light from thermal shock or ionisation tracks.
- High-altitude EAS arrays: atmospheric penetration signatures.

Nuclearite Energy Loss vs. Proton and Monopole

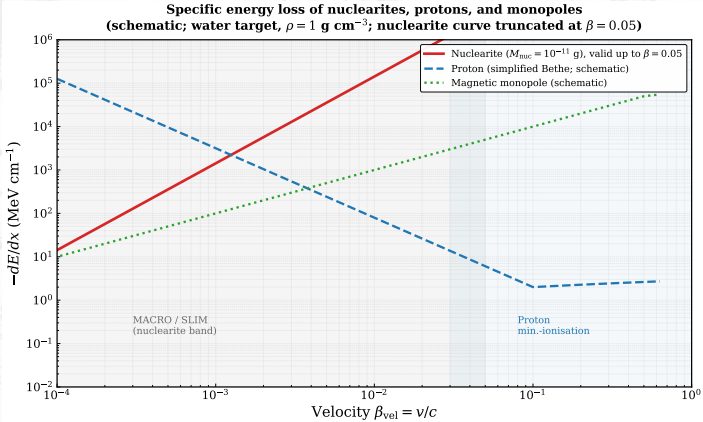

- A nuclearite of $M_{\rm nuc} = 10^{-11}$ g has $A \sim 6 \times 10^{12}$ and a geometric cross-section $\sigma = \pi R_S^2$ with $R_S \simeq 0.7\,A^{1/3}$ fm.
- Elastic-drag regime: $dE/dx \propto \sigma \rho_{\rm targ}\, v^2$. At galactic velocity $\beta_{\rm vel} \sim 10^{-3}$ the specific energy loss is more than three orders of magnitude larger than the proton minimum-ionisation value.
- The nuclearite, proton, and magnetic monopole occupy three distinct regions of the $(\beta_{\rm vel}, dE/dx)$ plane, which is why direct searches use experiment-specific velocity and ionisation windows rather than a single universal bound.
- Detection channels: nuclear track detectors (CR-39, Makrofol), neutrino telescopes (Cherenkov from a thermal shock), high-altitude EAS arrays.

Direct-Detection Event Rate: Correct Convention

Master formula, with all quantities defined

For a detector of effective area $A_{\rm eff}$, live time $T_{\rm live}$, and effective solid angle $\Delta\Omega$, the expected number of events is

$$\boxed{N_{\rm evt} \;=\; \Phi_{\rm dir}\, A_{\rm eff}\, T_{\rm live}\, \Delta\Omega}$$

where $\Phi_{\rm dir} = F_{\rm dir}/(4\pi)$ is the flux *per unit solid angle* ($\mathrm{cm^{-2}\,s^{-1}\,sr^{-1}}$). This formula assumes an isotropic flux (or, equivalently, a source-based flux averaged over the full 4π solid angle). For a point source inside the detector field of view, the correct event rate is instead $N_{\rm evt} = F_{\rm dir}\, A_{\rm eff}\, T_{\rm live}$ with no $\Delta\Omega$ factor.

- $F_{\rm dir}$: total flux at Earth ($\mathrm{cm^{-2}\,s^{-1}}$).
- $\Phi_{\rm dir}$: flux per unit solid angle, $\Phi_{\rm dir} = F_{\rm dir}/(4\pi)$ ($\mathrm{cm^{-2}\,s^{-1}\,sr^{-1}}$).
- $A_{\rm eff}$: effective detector area ($\mathrm{cm^2}$).
- $T_{\rm live}$: live time (s).
- $\Delta\Omega$: angular acceptance (sr). For a neutrino telescope scanning the full sky, $\Delta\Omega = 4\pi$ sr (or the appropriate fraction if only a hemisphere is observed, e.g. $\Delta\Omega \approx 2\pi$ sr for a half-sky survey). For a dedicated slow-particle detector such as SQM-ISS, $\Delta\Omega \sim 0.5$ sr.

Consistency check

- If $F_{\rm dir}$ is the total flux, then $N_{\rm evt} = F_{\rm dir}\, A_{\rm eff}\, T_{\rm live}\, (\Delta\Omega/4\pi)$.
- If $\Phi_{\rm dir} = F_{\rm dir}/(4\pi)$ is the per-solid-angle flux, then $N_{\rm evt} = \Phi_{\rm dir}\, A_{\rm eff}\, T_{\rm live}\, \Delta\Omega$.
- These two forms are identical.

Direct-Detection Event-Rate Estimate

Detector	$A_{\rm eff}$ (km^2)	$T_{\rm live}$ (yr)	$\Delta\Omega$ (sr)	$N_{\rm evt}$ for $\Phi_{\rm dir} = 10^{-20}$ cm^{-2}s^{-1}sr^{-1}
IceCube-Gen2	10	10	4π	~ 4
KM3NeT/ARCA	5	10	4π	~ 2
LHAASO (KM2A)	1	5	4π	~ 0.2
SQM-ISS	10^{-6}	3	0.5	$\sim 10^{-8}$

Interpretation

- IceCube-Gen2 and KM3NeT can detect a few events per decade if $\Phi_{\rm dir} \gtrsim 10^{-20}$ cm^{-2} s^{-1} sr^{-1}.
- SQM-ISS is a dedicated slow-particle detector and therefore has a small effective area, but its background is far lower than a neutrino telescope.
- A null result from all three channels would push the limit below $\Phi_{\rm dir} \sim 10^{-20}$ cm^{-2} s^{-1} sr^{-1}, a factor of $\sim 10^4$ better than MACRO.

These are schematic event-rate estimates, not a full detector simulation. A dedicated sensitivity study is required. The values shown use the corrected convention $N_{\rm evt} = \Phi_{\rm dir} A_{\rm eff} T_{\rm live} \Delta\Omega$.

Direct Event Rate Comparison

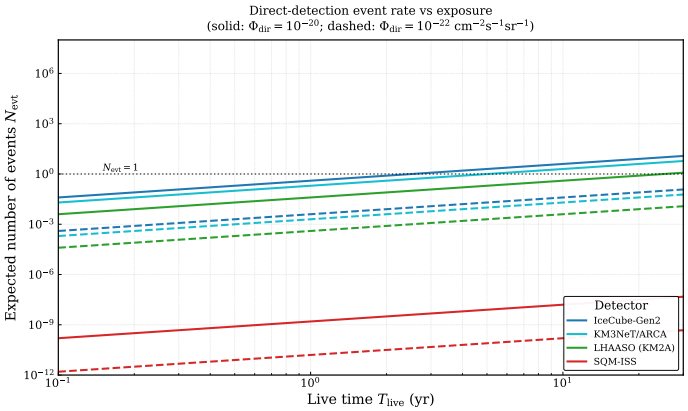

- Solid curves: $\Phi_{\rm dir} = 10^{-20}\ \mathrm{cm^{-2}\,s^{-1}\,sr^{-1}}$; dashed: 10^{-22}.
- IceCube-Gen2 and KM3NeT/ARCA reach $N_{\rm evt} \sim 2$–4 per decade of exposure at the benchmark flux.
- LHAASO and SQM-ISS remain below $N_{\rm evt} = 1$ over the same period, but their backgrounds are far lower.

Nuclearites and Q-balls: Present Status

Present experimental constraints (most stringent)

- **MACRO** (Gran Sasso): flux limit 2.7×10^{-16} cm^{-2} s^{-1} sr^{-1} for $\beta_{\rm vel} = 2 \times 10^{-3}$ nuclearites; also flux limits of 1.1×10^{-14} cm^{-2} sr^{-1} s^{-1} for $10^{-10} < M_{\rm nuc} < 0.1$ g and 5.5×10^{-15} cm^{-2} sr^{-1} s^{-1} for $M_{\rm nuc} > 0.1$ g.
- **ANTARES** (Mediterranean Sea): first neutrino-telescope limit on nuclearites — 5×10^{-17} cm^{-2} s^{-1} sr^{-1} for masses up to 10^{17} GeV/c^2.
- **SLIM** (Chacaltaya, Bolivia): 1.3×10^{-15} cm^{-2} s^{-1} sr^{-1} for downgoing SQM and charged Q-balls (combined MACRO, OHYA (Tokyo, Japan), and SLIM limits).

Why direct limits are complementary to γ-line limits

- γ-line searches probe the annihilation channel and are sensitive to n_S^2.
- Direct searches probe the surviving flux at Earth and are sensitive to $n_S \cdot f_{\rm ret}$.
- A joint detection in both channels would pin down *both* the production rate and the retention fraction — this is the strongest possible consistency test of the strangelet hypothesis.

Nuclearites and Q-balls: Future

Future facilities and their reach

- **KM3NeT/ARCA** (Mediterranean, km^3-scale):
  Projected sensitivity improves on ANTARES, especially for high-mass nuclearites.
- **IceCube** (South Pole):
  Sensitive to nuclearites and Q-balls via blackbody radiation and slow tracks.
- **SQM-ISS** (International Space Station):
  Scintillator + piezoelectric stack, searches for massive non-relativistic particles including Q-balls, SQM, and primordial black holes at $v \lesssim 250$ km/s.
- **LHAASO** (Tibet, KM2A + WCDA + WFCTA):
  Atmospheric penetration and sub-relativistic luminous events.
- **Gravitational-wave observatories** (Einstein Telescope, Cosmic Explorer):
  Can constrain Q-ball parameters through phase-transition gravitational-wave signals.

Joint γ-Line and Direct-Detection Parameter Space

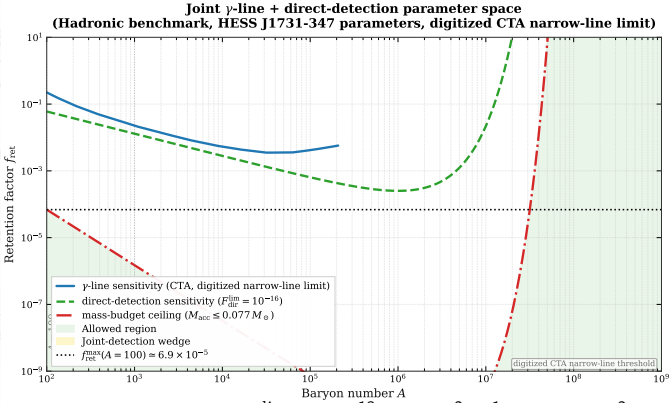

- Blue curve: projected CTA γ-line sensitivity $\Phi_\gamma^{\rm lim} = 10^{-13}$ ph cm^{-2} s^{-1} (scales as $f_{\rm ret}^2$).
- Green dashed curve: direct-detection sensitivity (scales as $f_{\rm ret}$).
- Red dash-dotted curve: mass-budget exclusion $M_{\rm acc} \le f_{\rm max} M_\star = 0.077\,M_\odot$.
- The horizontal dotted line marks the benchmark-required value $f_{\rm ret}^{\rm min}(A = 100) \simeq 7 \times 10^{-5}$.
- The allowed region is the wedge between the sensitivity curves and the mass-budget bound. The yellow overlap in the schematic is where a joint detection in both channels is possible.
- Key point: γ-line and direct searches probe different powers of $f_{\rm ret}$; a joint analysis disentangles production from retention.

Joint γ-Line + Direct-Detection Consistency Test (I): Channels and Scalings

The two complementary channels

Channel	Observable	Scaling	What it probes
γ-line (CTA/CTAO)	Φ_γ	$\propto n_S^2 \langle\sigma v\rangle B_{\gamma\gamma}$	Annihilation rate; production $\times$ retention squared.
Direct (PAMELA, AMS-02, IceCube, KM3NeT)	$F_{\rm dir}$	$\propto n_S f_{\rm ret}$	Surviving flux at Earth; production $\times$ retention.

Both channels share the same production rate $\dot{N}(A)$ and the same accumulation history $\tau_{\rm acc}$, $V_{\rm source}$. The ratio $\Phi_\gamma / F_{\rm dir}^2 \propto B_{\gamma\gamma}\langle\sigma v\rangle / f_{\rm ret}^2$, while the product $\Phi_\gamma F_{\rm dir}^2 \propto n_S^4 f_{\rm ret}^2 \langle\sigma v\rangle B_{\gamma\gamma}$.
(These scalings hold *at fixed source distance D, volume $V_{\rm source}$, and velocity v.*)

The line channel counts *pairs* of strangelets ($\propto n_S^2$), while the direct channel counts *individual* strangelets ($\propto n_S f_{\rm ret}$); combining them therefore breaks the production-vs-retention degeneracy that neither channel alone can resolve.

Joint γ-Line + Direct-Detection Consistency Test (II): Consistency Tests

If both channels detect a signal

- With an independent constraint on the annihilation kernel $K = B_{\gamma\gamma}\langle\sigma v\rangle$, the ratio and product pin down $f_{\rm ret}$ and n_S separately.
- Hence the production rate can be inferred.
- This is the strongest possible consistency test of the strangelet hypothesis.

If only one channel detects a signal

- One channel alone gives one equation in two unknowns (n_S and $f_{\rm ret}$), so it cannot separate them unless the annihilation kernel $K \equiv B_{\gamma\gamma}\langle\sigma v\rangle$ is known independently.
- With K known independently: the detection determines the combination $n_S^2 K$ (line) or $n_S f_{\rm ret}$ (direct); the *other* channel is then not needed to determine the remaining unknown *if* K is externally fixed, but without a second channel the system is under-determined.
- Without K known: only the combinations Φ_γ/K and $F_{\rm dir}/f_{\rm ret}$ are constrained, not n_S and $f_{\rm ret}$ individually.

Key point

γ-line and direct searches probe different powers of n_S and $f_{\rm ret}$.
A joint analysis is therefore not redundant — it is the only way to disentangle production from retention, provided the annihilation kernel is constrained independently.

Joint Likelihood: Correct Scaling

Joint likelihood

$$\mathcal{L}_{\rm joint}(\boldsymbol{\Theta}) = \mathcal{L}_{\gamma}(\boldsymbol{\Theta}_{\gamma}) \times \mathcal{L}_{\rm dir}(\boldsymbol{\Theta}_{\rm dir}),$$

with shared parameters $\dot{N}(A)$, $f_{\rm ret}(A,t)$, and source geometry. Nuisance parameters (exposure, background, energy dispersion) are profiled separately in each channel.

Correct scaling of the two channels

Channel	Observable	Scaling	Probes
γ-line (CTA/CTAO)	Φ_{γ}	$\propto n_S^2 \langle\sigma v\rangle B_{\gamma\gamma}$	Annihilation rate
Direct (PAMELA, AMS-02, IceCube, KM3NeT)	$F_{\rm dir}$	$\propto n_S f_{\rm ret}$	Surviving flux at Earth
Ratio $\Phi_{\gamma}/F_{\rm dir}^2$		$\propto \langle\sigma v\rangle B_{\gamma\gamma}/f_{\rm ret}^2$	—
Product $\Phi_{\gamma}F_{\rm dir}^2$		$\propto n_S^4 f_{\rm ret}^2 \langle\sigma v\rangle B_{\gamma\gamma}$	—

The joint likelihood is *multiplicative* because the two channels are statistically independent — a γ-ray photon and a cosmic-ray track are distinct events.
The ratio cancels the production rate $\dot{N}(A)$ and isolates the kernel-to-retention combination, while the product keeps n_S and $f_{\rm ret}$ entangled.
Only an *independent* constraint on $\langle\sigma v\rangle B_{\gamma\gamma}$ allows the two unknowns to be disentangled.

Joint Likelihood: Assumptions and Interpretation

If both channels detect

- With an independent constraint on $K = \langle\sigma v\rangle B_{\gamma\gamma}$, the ratio and product pin down $f_{\rm ret}$ and n_S separately.
- Hence the production rate $\dot{N}(A)$ can be inferred.
- This closes the production–retention degeneracy and independently tests the strangelet hypothesis.

If only one channel detects

- One channel alone gives one equation in two unknowns (n_S and $f_{\rm ret}$). It cannot determine them individually unless the annihilation kernel $K \equiv B_{\gamma\gamma}\langle\sigma v\rangle$ is independently known.
- With K known independently, the single detection already determines one combination ($n_S^2 K$ for the line, or $n_S f_{\rm ret}$ for direct).
  A *second* channel is required to determine the remaining unknown; the two channels together then give n_S and $f_{\rm ret}$.
- Without K known: only the combinations Φ_γ/K and $F_{\rm dir}/f_{\rm ret}$ are constrained.

Honest framing

Without an independent kernel constraint $K = \langle\sigma v\rangle B_{\gamma\gamma}$, a joint detection pins down only a combination of n_S, $f_{\rm ret}$, and the kernel — not all three separately.

All the proportionalities above are stated *at fixed source distance D, accumulation volume $V_{\rm source}$, and velocity v*. If these differ between sources, the scalings must be generalised to include $V_{\rm source}/D^2$ and v.

Worked Joint Inversion: γ-line + Direct Detection (I)

Two equations, two unknowns

$$\Phi_\gamma = \frac{2 B_{\gamma\gamma}\, n_S^2\, \langle \sigma v \rangle\, V_{\rm source}}{4\pi D^2},$$

$$F_{\rm dir} = \frac{\dot{N}(A)\, f_{\rm ret}}{4\pi D^2} = \frac{n_S\, V_{\rm source}\, f_{\rm ret}}{4\pi D^2\, \tau_{\rm acc}}.$$

Define the kernel $K \equiv B_{\gamma\gamma}\langle \sigma v \rangle$. If K is known independently, the two equations can be solved algebraically:

$$n_S = \sqrt{\frac{4\pi D^2\, \Phi_\gamma}{2K\, V_{\rm source}}}, \qquad f_{\rm ret} = \frac{4\pi D^2\, \tau_{\rm acc}\, F_{\rm dir}}{n_S\, V_{\rm source}} = \frac{4\pi D^2\, \tau_{\rm acc}\, F_{\rm dir}}{V_{\rm source}} \sqrt{\frac{2K\, V_{\rm source}}{4\pi D^2\, \Phi_\gamma}}.$$

Numerical example (HESS J1731-347)

Take $\Phi_\gamma = 1.2 \times 10^{-14}$ ph cm^{-2} s^{-1} (digitized CTA narrow-line limit at 94 GeV), $F_{\rm dir} = 10^{-20}$ cm^{-2} s^{-1} sr^{-1}, $D = 3.2$ kpc, $V_{\rm source} = 1.23 \times 10^{59}$ cm^3, $\tau_{\rm acc} = 3.16 \times 10^{13}$ s, $K = B_{\gamma\gamma}\langle \sigma v \rangle = 10^{-25}$ cm^3 s^{-1}.

What this buys

- If both channels detect, the production–retention degeneracy is broken: n_S and $f_{\rm ret}$ are determined separately.
- If only one channel detects, only one combination is fixed; the kernel must be supplied externally.
- If K is unknown, only Φ_γ / K and $F_{\rm dir}/f_{\rm ret}$ are constrained.

Honest framing

The inversion is conditional on an independent determination of K.
Without it, a joint detection pins down only a combination of n_S, $f_{\rm ret}$, and K — not all three separately.

Worked Joint Inversion: γ-line + Direct Detection (II)

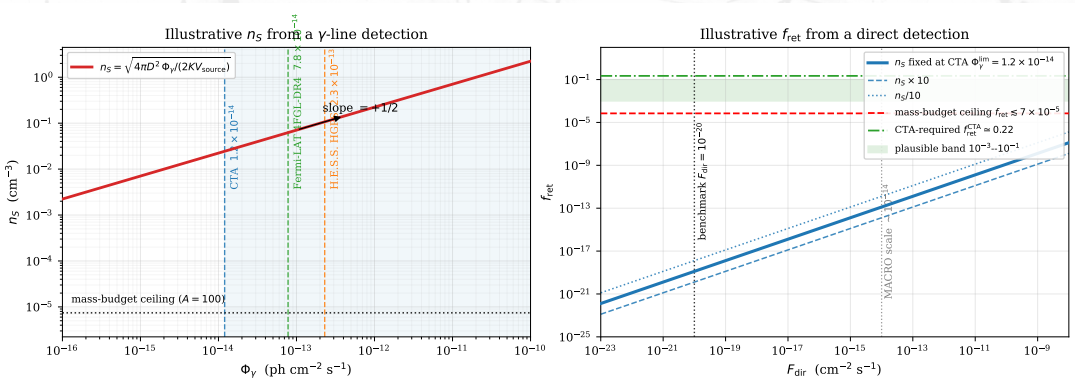

Synthetic worked example

This figure is synthetic — the two curves are analytical combinations of the inversion formulas with *no real data*.

It is a *worked example* showing the geometry of the joint inversion, not a data-driven inference.

Practical Quantitative Constraint Hierarchy (I)

Table: Present parameter-space constraints for the 2SC/CFL–strangelet–merger program: astrophysical and EOS parameters.

Parameter	Present constraint status
$M_{\max}^{\mathrm{EOS}}$	Must exceed approximately $2\,M_\odot$; strongly constrains overly soft 2SC/kaon/hyperon EOSs.
$R_{1.4}$	Roughly 11.4–12.8 km depending on NICER analysis/model; current EOS inference gives approximately 12.0–12.8 km 95% ranges.
$R_{2.0}$	Approximately 11.5–12.3 km in the 2024 agnostic EOS analysis.
$\tilde{\Lambda}$	GW170817 strongly suppresses very large tidal deformabilities; AT2017gfo+GW gives roughly 120–1110 in one kilonova analysis.
CFL G_V/G_S	Viable NJL strange-star regions 0.21–0.4 or 0.02–0.1, depending on treatment of gluon effects.
CFL gap Δ	No direct observational measurement; recent RG-consistent NJL models permit gaps up to ~ 250 MeV in viable configurations.

Practical Quantitative Constraint Hierarchy (II)

Table: Present parameter-space constraints for the 2SC/CFL–strangelet–merger program: strangelets and neutrino channels.

Parameter	Present constraint status
2SC existence	Not established; current models permit or eliminate it depending on transition dynamics and hadronic EOS.
Quark-star M_{TOV}	Recent GW170817 post-merger modeling gives $\lesssim 2.35^{+0.07}_{-0.17}\, M_{\odot}$ under specific delayed-collapse assumptions.
Strangelets	No direct astrophysical detection; merger models predict strong evaporation, so non-detection is not presently a strong exclusion.
Merger MeV neutrinos	No detection; Super-K gives $F_{\bar{\nu}_e} < 6.6 \times 10^{7}\ \mathrm{cm}^{-2}$ for its stated spectral assumption.
Merger TeV–EeV neutrinos	No GW170817 counterpart in ANTARES/IceCube/Auger or Baikal-GVD.
Individual BNS neutrino detection	Current/near-term experiments unlikely to detect individual mergers; megaton-scale $\mathcal{O}(10)$-MeV detector needed in recent forecasts.

Neutrino Detection Limits from Neutron-Star Mergers

MeV thermal neutrinos

For GW170817, Super-Kamiokande observed no significant neutrino excess. Its 90% C.L. limit below 100 MeV was approximately

$$F_{\bar{\nu}_e} < 6.6 \times 10^7 \text{ cm}^{-2}$$

for a 20-MeV Fermi–Dirac spectrum. At $E_\nu > 1.6$ GeV:

$$F_{\nu_\mu} < 16.0 \text{ cm}^{-2}, \qquad F_{\bar{\nu}_\mu} < 21.3 \text{ cm}^{-2}$$

under an E^{-2} spectrum assumption.

TeV–EeV high-energy neutrinos

- ANTARES/IceCube/Auger: no event within ± 500 s or during a 14-day post-merger interval.
- Baikal-GVD: no neutrinos between TeV and 100 PeV; 90% C.L. fluence limits derived.
- Updated 2025: current and near-future experiments unlikely to detect individual BNS-merger neutrino bursts; an effective megaton-scale detector with an $\mathcal{O}(10)$-MeV threshold is required.

Why the 2SC neutrino spectrum could be informative

- In 2SC matter, $\nu + d \to u + e^-/\mu^-$ is kinematically blocked at low T; $\nu + s \to u + \ell^-$ dominates.
- At higher T or E_ν, the d-quark channel opens and the mean free path decreases.
- A hadronic $\to$ 2SC $\to$ CFL transition could imprint itself through $\lambda_\nu(E_\nu, T, Y_L)$, affecting luminosity, mean energy, spectral pinching, deleptonization timescale, angular distribution, and flavor-dependent diffusion times.
- No observed merger neutrino spectrum with sufficient statistics yet.

Key Results: Summary

Table: Consolidated constraints and forecasts for the three sources. CTA column is the digitized narrow-line limit at the line energy $E_\gamma = 0.94A$ GeV, not a flat value at 1 TeV.

Source	Present benchmark ($\mathrm{ph\,cm^{-2}\,s^{-1}}$)	CTA forecast (digitized) ($\mathrm{ph\,cm^{-2}\,s^{-1}}$)	n_S limit ($\mathrm{cm^{-3}}$)	Status
HESS J1731-347	$\sim 10^{-12}$	$\sim 1.2 \times 10^{-14}$ (at 94 GeV)	< 0.023	Physically allowed at $f_{\rm ret} \sim 0.22$ but mass budget requires $f_{\rm ret} \sim 7 \times 10^{-5}$; line flux drops to $\sim 10^{-21}$.
GW170817	$\sim 10^{-12}$	$\sim 10^{-15}$ (at 940 GeV; off-axis)	–	No prompt VHE emission; off-axis geometry.
GRB 250702B	10^{-13}–10^{-11}	$\sim 4 \times 10^{-15}$ (at ~ 460 GeV, $z = 1.036$)	–	Burst limits being derived.

The CTA forecast column is now evaluated at the *digitized* CTA narrow-line limit ($2021 \times \Delta E = 0.1\,E$) at the *benchmark line energy* of each source. All limits remain proxy values, not 95% CL exclusions.

Strangelet Property Constraints from Cumulative γ-Ray Fluxes

Table: Strangelet-property constraints derived from the observed cumulative γ-ray fluxes of the three benchmark sources. All entries are benchmark sensitivity values, not 95% CL exclusions, and all assume $n_S = n_S$, $B_{\gamma\gamma} = 1$, and the benchmark inversion $n_S < \sqrt{4\pi D^2 \Phi_\gamma^{\rm lim} / (2 B_{\gamma\gamma} \langle \sigma v \rangle V_{\rm source})}$.

Source	Observed flux / line limit	Derived n_S	Derived $M_{\rm SQM}$	$f_{\rm ret}$ requirement
HESS J1731-347 (steady, $D = 3.2$ kpc)	Continuum $\sim 10^{-12}$ at 1 TeV; digitized CTA line limit $\Phi_\gamma^{\rm lim}(94\,{\rm GeV}) \simeq 1.2 \times 10^{-14}$ ph cm^{-2}s^{-1}	< 0.023 cm^{-3} ($A = 100$)	$< 2.4 \times 10^2\, M_\odot$ ($A = 100$)	Local $A = 100$ mass budget requires $f_{\rm ret} \lesssim 7 \times 10^{-5}$; global integrated mass budget requires $f_{\rm ret} \lesssim 3.4 \times 10^{-18}$; with the local $f_{\rm ret}$, $\Phi_\gamma \sim 10^{-21}$
GW170817 (merger, $D_L \simeq 40$ Mpc)	No prompt VHE; predicted $\Phi_\gamma \sim 10^{-25}$–$10^{-23}$	Not quoted	Not quoted	— (non-detection is expected; distance and short accumulation time suppress the flux by $\sim 10^{10}$–10^{12})
GRB 250702B (burst, $z \simeq 1.036$)	Cumulative upper limits; predicted $\Phi_\gamma \sim 10^{-13}$–$10^{-11}$ for $A \sim 10^3$	Being derived	Being derived	— (requires time-dependent line search at $E_\gamma^{\rm obs} = 0.94\, A/(1+z)$)

Central message

Only HESS J1731-347 currently yields a quantitative strangelet-property constraint. The quoted $f_{\rm ret} \lesssim 7 \times 10^{-5}$ is the *local* (fixed-A) mass-budget ceiling; the *global* integrated mass budget instead requires $f_{\rm ret} \lesssim 3.4 \times 10^{-18}$, a 13-decade difference that must be stated explicitly. GW170817 and GRB 250702B provide consistency checks and sensitivity forecasts, not yet constraints.

Why GW170817 and GRB 250702B Do Not Yet Give n_S Limits

HESS J1731-347: the reference case

Steady source: continuous injection, $\tau_{\rm acc} \sim 10^6$ yr.
$D = 3.2$ kpc: no distance penalty.
CTA energy-dependent proxy: at $E_\gamma = 94$ GeV the effective limit is $\sim 3.5 \times 10^{-12}$ ph cm^{-2} s^{-1}. Using this value in the same square-root inversion gives $n_S < 0.4$ cm^{-3} and $M_{\rm SQM} < 4 \times 10^3\, M_\odot$ at $A = 100$ — the mass budget $f_{\rm ret} \lesssim 7 \times 10^{-5}$ remains the stronger constraint by four orders of magnitude.
Mass budget then requires $f_{\rm ret} \lesssim 7 \times 10^{-5}$.

GW170817: expected non-detection

- $D_L \simeq 40$ Mpc: $(D_{\rm HESS}/D_{\rm GW})^2 \simeq 1.5 \times 10^{-8}$.
- Post-merger timescale: seconds to hours, not 10^6 yr.
- Predicted line flux $\Phi_\gamma \sim 10^{-25}$–$10^{-23}$ ph cm^{-2} s^{-1}, i.e. $\sim 10^{10}$–10^{12} below current and projected VHE sensitivities.
- The absence of a VHE signal is expected within the benchmark model, not a constraint on it.

Why "limits being derived" is the honest status

A genuine limit requires a time-dependent line search with exposure, background, energy dispersion, and morphology, evaluated at $E_\gamma^{\rm obs}(A)$.

GRB 250702B: distance penalty vs. energetics

- $z \simeq 1.036$, $D_L \sim 7$ Gpc: $(D_{\rm HESS}/D_L)^2 \sim 2 \times 10^{-15}$ — the largest single suppression factor in the framework.
- Partially compensated by $E_{\rm iso} > 1.4 \times 10^{54}$ erg and $\Delta t_{\rm obs} > 25{,}000$ s.
- Predicted $\Phi_\gamma \sim 10^{-13}$–$10^{-11}$ ph cm^{-2} s^{-1} for $A \sim 10^3$, within CTA's reach.

Redshift matters for the line energy

$$E_\gamma^{\rm obs}(A) = \frac{m_S(A)}{1+z} \simeq \frac{0.94\,A}{1+z}\ \text{GeV}.$$

For $z = 1.036$:

- $A = 100$: $E_\gamma^{\rm obs} \approx 46$ GeV (Fermi-LAT band; lower edge of CTA).
- $A = 10^3$: $E_\gamma^{\rm obs} \approx 460$ GeV (CTA/MAGIC-II boundary).
- $A = 10^4$: $E_\gamma^{\rm obs} \approx 4.6$ TeV (CTA/H.E.S.S. band).

For GW170817 the predicted flux is far below any accessible sensitivity, so no meaningful n_S bound follows from the non-detection. For GRB 250702B the predicted flux is within reach, but the correct line energy is redshifted and time-dependent; a fixed-threshold inversion would be misleading.

From Cumulative Flux to Strangelet Density: Correct Inversion

The correct inversion (square root, not division)

The line-flux limit $\Phi_\gamma^{\rm lim}$ constrains the annihilation rate, which scales as n_S^2. Solving

$$\Phi_\gamma = \frac{2\,B_{\gamma\gamma}\,R_{\rm ann}}{4\pi D^2} \le \Phi_\gamma^{\rm lim}, \qquad R_{\rm ann} = n_S^2\,\langle\sigma v\rangle\,V_{\rm source},$$

for the number density gives

$$\boxed{n_S < \sqrt{\frac{4\pi D^2\,\Phi_\gamma^{\rm lim}}{2\,B_{\gamma\gamma}\,\langle\sigma v\rangle\,V_{\rm source}}}}$$

This is a square root, not a division by $N_H\sigma_S$. A common error is to write $n_S < \Phi_\gamma^{\rm lim}/(N_H\sigma_S)$, which is dimensionally and physically wrong.

Source-frame vs. local density

- n_S (source frame): number density inside $V_{\rm source}$; enters $\Phi_\gamma \propto n_S^2$.
- $n_S^{\rm local}$ (detector frame): enters the direct-detection flux $F_{\rm dir}^{\rm (loc)} = n_S^{\rm local}\,v\,f_{\rm ret}$.
- Source-based direct flux: $F_{\rm dir}^{\rm (src)} = \dot{N}(A) f_{\rm ret}/(4\pi D^2)$.
- Mixing the two is a common error.

Benchmark caveats

- These are benchmark sensitivity limits, not 95% CL exclusions.
- $\Phi_\gamma^{\rm lim}$ is now the energy-dependent proxy value at $E_\gamma = 0.94A$ GeV, not the flat 10^{-13} at 1 TeV.
- The signal is conditional on $n_{\bar{S}} = n_S$ (unverified).
- The branching fraction $B_{\gamma\gamma}$ is set to 1; realistic values are $\ll 1$.
- The annihilation kernel $\langle\sigma v\rangle \sim 10^{-25}$ cm^3 s^{-1} is a benchmark input, not QCD-derived.
- The retention factor $f_{\rm ret}(A, t)$ must be specified, not set to 1.

What a genuine 95% CL exclusion would require

An event-level profile-likelihood analysis with exposure, background, energy dispersion, source morphology, and nuisance parameters, evaluated at the correct line energy $E_\gamma(A) = m_S(A) \simeq 0.94\,A$ GeV (or $E_\gamma^{\rm obs} = 0.94\,A/(1+z)$ for a redshifted source).

What a Null Result Would Mean

Assumption

The strangelet framework is valid: strangelets exist, are produced in the sources considered, and annihilate to $\gamma\gamma$ with a non-negligible branching fraction.

If CTA sees nothing

- The **Optimistic** and possibly **Baseline** scenarios are excluded within the benchmark sensitivity.
- The **Conservative** scenario remains viable and requires a next-generation instrument.
- Direct searches (KM3NeT, IceCube-Gen2, LHAASO) become the primary frontier for macro-SQM.
- With the energy-dependent CTA threshold, the HESS J1731-347 benchmark line is not detectable within the physically allowed range $f_{\mathrm{ret}} \leq 1$.
  A null result would therefore be *expected* within the current proxy model and would not exclude the strangelet hypothesis on its own.

Caveats that must be kept in mind

- Line-flux limits are *benchmark sensitivity values*, not 95% CL exclusions.
- The mass-budget constraint has not been enforced through a physical $f_{\mathrm{ret}}(A, t)$.
- The $\gamma\gamma$ branching fraction $B_{\gamma\gamma}$ is unconstrained microscopically.

Takeaway

A null result from current-generation instruments does *not* exclude strangelets. It constrains the parameter space within a specific benchmark.
A future likelihood analysis with energy-dependent instrument response and a physical retention model would be required for a definitive exclusion.

Einstein Telescope and Cosmic Explorer

Third-generation GW detectors: statistics and precision

ET/CE change the situation mainly through statistics and precision, not because a single event automatically identifies CFL.

Improved measurements

- $\tilde{\Lambda}$, $\Lambda(m)$, $R_{1.4}$, $R_{2.0}$
- In favorable nearby events: $f_{\mathrm{postmerger}}$
- A first-order phase transition can shift the dominant post-merger frequency by several hundred Hz in numerical-relativity calculations.
- CE can detect BNS systems to cosmological distances ($z > 1$ for $\sim 3\,M_\odot$ BNS).

For quark matter

- The most useful quantity is the joint posterior

$$p(n_{\mathrm{tr}}, \Delta\epsilon, c_s^2 \mid \mathrm{NICER{+}GW{+}EM{+}}\nu),$$

rather than an isolated measurement of $\tilde{\Lambda}$.

- Recent forecasts: QCD-transition signatures of $\sim$ 200–400 Hz in post-merger frequencies and radius differences of 0.5–2 km for twin-star configurations.

Hyper-Kamiokande and Megaton-Scale Neutrino Detectors

Current and near-future sensitivity

For GW170817, Super-Kamiokande observed no significant neutrino excess.
Its 90% C.L. limit below 100 MeV was approximately

$$F_{\bar{\nu}_e} < 6.6 \times 10^7 \ \mathrm{cm}^{-2}$$

for a 20-MeV Fermi–Dirac spectrum.

Updated 2025 prospects

- Current and near-future neutrino experiments are unlikely to detect an individual BNS-merger neutrino burst.
- An effective megaton-scale detector with an $\mathcal{O}(10)$-MeV threshold is required for realistic prospects.
- Hyper-K is expected to record $\mathcal{O}(100)$ diffuse supernova neutrino background events per decade.

Why this matters for 2SC/CFL searches

- A positive detection would constrain remnant lifetime, thermal EOS, and possible phase-transition-induced collapse.
- A non-detection would mostly constrain optimistic high-luminosity models.
- The 2SC neutrino-opacity calculation supplies a route by which microscopic pairing differences could eventually become observable through merger neutrino spectra.

What Would Change the Conclusion?

1. A confirmed narrow γ-ray line in HESS J1731-347
   $\Rightarrow$ direct evidence for strangelet annihilation.
2. A joint detection in γ-rays and direct searches
   $\Rightarrow$ pins down both production rate and retention.
3. A nearby ($z \lesssim 0.1$) ultra-long GRB
   $\Rightarrow$ moves the predicted line flux into an accessible regime for CTA.
4. A measured $\Delta_{\rm 2SC}$, $\Delta_{\rm CFL}$, or m_s from lattice QCD
   $\Rightarrow$ replaces the benchmark $\dot{N}(A)$ by a first-principles prediction.
5. A first-principles calculation of the retention factor $f_{\rm ret}(A, t)$ from transport simulations of the quark core, hadronic envelope, and ejecta
   $\Rightarrow$ closes the three-to-four-order-of-magnitude retention gap between the mass-budget ceiling ($f_{\rm ret} \lesssim 7 \times 10^{-5}$) and the digitized CTA-required value ($f_{\rm ret} \simeq 0.22$).
6. An independent determination of the annihilation kernel $K \equiv B_{\gamma\gamma}\langle\sigma v\rangle$
   (e.g. from lattice QCD, a future strangelet collider, or a self-consistent many-body calculation)
   $\Rightarrow$ makes the joint γ-line + direct-detection inversion closed, breaking the degeneracy between n_S, $f_{\rm ret}$, and the kernel itself.

Systematic Uncertainties in the Benchmark Model

Table: Systematic uncertainties that affect the predicted line flux and the direct-detection rate. Ranges for η, $f_{\rm ret}$, and K are relative to the baseline $\eta \simeq 10^{-20}$, $f_{\rm ret} \simeq 7 \times 10^{-5}$, $K \simeq 10^{-25}$ cm^3 s^{-1}.

Source	Symbol	Range	Impact on Φ_γ
Retention factor	$f_{\rm ret}$	10^{-5}–10^{-1}	Quadratic; dominant uncertainty.
Conversion efficiency	η	10^{-22}–10^{-18}	Quadratic; sets the absolute production rate.
Annihilation kernel	$K = \langle\sigma v\rangle B_{\gamma\gamma}$	10^{-27}–10^{-23} cm^{3}s^{-1}	Linear; sets the line yield per annihilation.
2SC gap	$\Delta_{\rm 2SC}$	10–100 MeV	Exponential via $\exp(-\delta E/T)$.
Strange-quark mass	m_s	80–120 MeV	Exponential via $\exp(-2m_s^2/\mu^2)$.
Source distance	D	3.2 kpc–7 Gpc	Inverse square; dominates GW170817 and GRB 250702B.

A factor-of-two change in $\Delta_{\rm 2SC}/\mu$ or m_s can shift the peak production rate by several orders of magnitude. This is why the benchmark contours must be treated as *sensitivity maps*, not as 95% CL exclusions.

Limitations and Open Questions

Theoretical uncertainties

- Transition rate. The prefactor T^4/π^3 is chosen on dimensional grounds; a full calculation requires transport coefficients not yet known for ultradense matter.
- Annihilation cross-section. The conservative value $\langle \sigma v \rangle \sim 10^{-25}\ \mathrm{cm}^3\,\mathrm{s}^{-1}$ is adopted; the geometric value could be orders of magnitude larger.
- Suppression factors. The phenomenological form $\dot{N}(A)$ absorbs four suppression mechanisms into two parameters.
- Mass-to-charge ratio. The charge fraction Y_Q is inferred from MIT-bag calculations; a first-principles NJL derivation is left for future work.

Observational limitations

- Instrument limits are quoted at ~ 1 TeV; the sensitivity at ~ 94 GeV is a factor of $\mathcal{O}(3\text{–}10)$ worse for imaging Cherenkov telescopes.
- The three sources are illustrative; a definitive detection would need a dedicated multi-instrument campaign.

Minimal Assumptions and Consistency Conditions

Benchmark inputs (not QCD-derived)

1. Production law:
   $\dot{N}(A) = \dot{N}_{\rm peak}(A/A_{\rm peak})^{2/3}\exp[\frac{2}{3}(1-A/A_{\rm peak})]$.
2. Anti-strangelet symmetry: $n_{\bar{S}} = n_S$ (unverified).
3. Line branching fraction: $B_{\gamma\gamma} = 1$ (realistic values are $\ll 1$).
4. Annihilation kernel:
   $\langle\sigma v\rangle \sim 10^{-25}\ \mathrm{cm}^3\,\mathrm{s}^{-1}$
   (benchmark, not derived).
5. Line energy: $E_\gamma = m_S \simeq 0.94\,A$ GeV.

Explicit consistency conditions

1. Mass budget:
$$M_{\rm acc} = \sum_A A\, m_N\, \dot{N}(A)\, \tau_{\rm acc}\, f_{\rm ret}(A)$$
$$\leq f_{\max} M_\star = 0.077\, M_\odot.$$

2. Line-flux consistency:
$$\Phi_\gamma(A) = \frac{2\, B_{\gamma\gamma}\, n_S^2 \langle\sigma v\rangle\, V_{\rm source}}{4\pi D^2} \leq \Phi_\gamma^{\rm lim}(E_\gamma(A)).$$

3. Retention factor: $f_{\rm ret}(A,t) = S_{\rm form} S_{\rm esc} S_{\rm surv}$ must be *specified*, not set to 1.

Recommended Parameterization for a Joint Bayesian Analysis

Parameter vector

$$\boldsymbol{\Theta} = \{B_{\rm eff}, a_4, m_s, \Delta_{\rm 2SC}, \Delta_{\rm CFL}, G_V, n_{\rm tr}, \Delta\epsilon, c_s^2\}$$

Joint likelihood

$$\mathcal{L} = \mathcal{L}_{\rm NICER}\,\mathcal{L}_{\rm GW}\,\mathcal{L}_{\rm kilonova}\,\mathcal{L}_{\nu}\,\mathcal{L}_{\rm HIC}\,\mathcal{L}_{\rm pQCD/\chi EFT}$$

Each factor is an independent observational likelihood; together they constrain one EOS.

Model hypotheses

- Hadronic
- Kaon-condensed
- 2SC
- 2SC $\rightarrow$ CFL hybrid
- Self-bound CFL strange star

Outcome

This formulation would make it possible to report actual posterior exclusions of $B_{\rm eff}$, transition density, Δ, G_V, and strangelet survival parameters, rather than treating "quark matter" as a single phenomenological category.

What Is Derived vs. Benchmark

Status of key quantities

Quantity	Status	Comment
$E_\gamma(A) = 0.94\,A$ GeV	**Benchmark scaling**	Set by $m_S \approx A m_N$; robust for $A \gtrsim 10^2$.
$n_S(A)$	**Derived**	From $\dot{N}(A)$, $f_{\rm ret}$, $\tau_{\rm acc}$: $n_S = \dot{N}\,\tau_{\rm acc}\,f_{\rm ret}/V_{\rm source}$.
$f_{\rm ret}$	**Undetermined**	Dominant uncertainty; from formation/escape/survival.
$B_{\gamma\gamma}$, $\langle\sigma v\rangle$	**Benchmark**	QCD-derived values not yet available.

Takeaway

The only *derived* quantity is $n_S(A)$ — and it inherits the undetermined $f_{\rm ret}(A,t)$; every observable therefore carries the same retention uncertainty. Until $f_{\rm ret}$ and the annihilation kernel $K = B_{\gamma\gamma}\langle\sigma v\rangle$ are fixed independently, the framework yields *sensitivity maps*, not predictions.

Take-Home Messages

1. SQM may be the true QCD ground state.
   If so, strangelets and macro-SQM objects are the natural observable.
2. The γ-ray line channel is the cleanest signature of strangelet annihilation, but it is conditional on anti-strangelet production and on the retention factor $f_{\rm ret}(A, t)$.
3. HESS J1731-347 is the most promising steady source:
   It lies in the Southern sky, is visible only to H.E.S.S. and CTAO South, and the Baseline scenario sits within reach of the digitized CTA limit ($f_{\rm ret}^{\rm CTA} \simeq 0.22$ at $A = 100$); the mass budget requires $f_{\rm ret} \sim 7 \times 10^{-5}$, so the retention physics is the limiting factor, not CTA.
4. GW170817 and GRB 250702B are complementary channels (merger-driven and burst-driven), but both suffer severe distance suppression.
5. Direct searches (KM3NeT, IceCube-Gen2, LHAASO, SQM-ISS) probe a different quantity ($n_S f_{\rm ret}$) and are the natural complement to line searches.

Conclusion: Multimessenger Astronomy Is Essential!

1. Strange quark matter (SQM) remains a compelling possibility for the true ground state of dense QCD. Signatures range from monochromatic VHE γ-ray lines from strangelet–anti-strangelet annihilation to direct detection of macroscopic objects (nuclearites, Q-balls).
2. Current constraints from H.E.S.S., Fermi-LAT, MAGIC, IceCube, ANTARES, SLIM probe parts of the parameter space; definitive discovery needs next-generation sensitivity.
3. Multimessenger observations of HESS J1731-347, GW170817, GRB 250702B provide unique laboratories.
4. Future facilities are essential to:
   - search for narrow γ-ray lines with unprecedented sensitivity,
   - detect slow, highly ionising tracks and luminous transits from macro-SQM,
   - correlate GeV–TeV γ rays, neutrinos, gravitational waves, and cosmic rays,
   - constrain the QCD phase diagram and the equation of state of compact stars.

Cosmological Strangelets as Dark Matter

Production in the Early Universe

- If the QCD transition in the Early Universe proceeded through a non-equilibrium or first-order-like path, dense quark-matter regions could separate and cool into the CFL phase, forming strangelet relics.
- This provides a cosmological route to SQM that is independent of neutron stars and mergers.
- Di Clemente et al. (2025) show that strangelets with masses $\lesssim 10^{17}$ g can survive from the Early Universe to the present day.

Strangelets vs. primordial black holes

- Both are macroscopic, non-luminous dark-matter candidates with masses $\sim 10^{17}$ g.
- Distinguishing feature: strangelets have $Z/A \ll 1$ and therefore high rigidity; PBHs are electrically neutral.
- Microlensing surveys, direct searches, and gravitational-wave observatories provide complementary constraints.

If strangelets are a viable dark-matter candidate, then the same SQM equation of state governs both the cosmological relics and the strangelets produced in neutron stars and mergers.
This is a powerful consistency check of the Bodmer–Witten–Terazawa hypothesis.

Relic Abundance of Cosmological Strangelets

Boltzmann equation for a stable relic

For a stable strangelet species S with number density n_S:

$$\frac{dn_S}{dt} + 3Hn_S \;=\; -\langle\sigma v\rangle \left(n_S^2 - n_{S,\mathrm{eq}}^2\right),$$

where H is the Hubble rate, $\langle\sigma v\rangle$ is the velocity-averaged annihilation cross-section, and $n_{S,\mathrm{eq}}$ is the equilibrium density. This Boltzmann equation assumes a symmetric population with $n_S = n_{\bar{S}}$; a charge asymmetry would require a separate equation for the difference $n_S - n_{\bar{S}}$.

Standard thermal relic

For a thermal relic freezing out at $x_f = m_S/T_f \sim 20$:

$$\Omega_S h^2 \;\approx\; \frac{1.07\times10^{9}\ \mathrm{GeV}^{-1}}{M_{\mathrm{Pl}}\sqrt{g_*}}\,\frac{x_f}{\langle\sigma v\rangle},$$

where M_{Pl} is the Planck mass and g_* the effective relativistic degrees of freedom at freeze-out. Here $\langle\sigma v\rangle$ is in GeV^{-2}; in $\mathrm{cm}^3\ \mathrm{s}^{-1}$, $1\ \mathrm{GeV}^{-2} = 1.17\times10^{-17}\ \mathrm{cm}^3\,\mathrm{s}^{-1}$.

Relic-density constraint

If strangelets are a viable dark-matter candidate, the predicted $\Omega_S h^2$ must match the observed $\Omega_{\mathrm{DM}} h^2 \simeq 0.12$. For $M_S \sim 10^{16}$ g, this requires

$$n_S^{\mathrm{relic}} \;\sim\; \frac{\rho_{\mathrm{DM}}}{M_S} \;\sim\; 10^{-46}\ \mathrm{cm}^{-3},$$

where $\rho_{\mathrm{DM}} \approx 2.4\times10^{-30}\ \mathrm{g\,cm}^{-3}$ is the *cosmological average* dark-matter density (for $h \approx 0.7$), *not* the local Galactic density.

This translates into a stringent constraint on the formation efficiency η_{form}.

Strangelet-specific case

Macroscopic strangelets are not standard thermal relics:

- They form during a cosmological QCD phase transition (non-equilibrium).
- Their abundance is set by the formation efficiency η_{form} and the coalescence history, not by thermal freeze-out.
- A benchmark estimate:

$$\Omega_S h^2 \;\sim\; \frac{M_S\, n_S^{\mathrm{relic}}}{\rho_c/h^2},$$

with $n_S^{\mathrm{relic}} \sim \eta_{\mathrm{form}}\, n_{\mathrm{QCD}}$ and $n_{\mathrm{QCD}} \sim T_c^3$.

Relic Abundance: Parameter Space for Strangelet Dark Matter

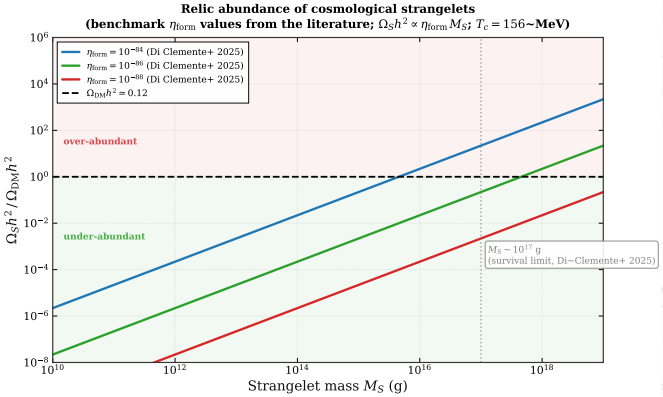

- Non-thermal formation during the QCD transition: $\Omega_S h^2 \propto \eta_{\rm form}\, M_S$.
- The horizontal dashed line marks $\Omega_{\rm DM} h^2 \simeq 0.12$. A curve that crosses this line identifies a viable $(\eta_{\rm form}, M_S)$ pair.
- Benchmark formation efficiencies $\eta_{\rm form} = 10^{-84}, 10^{-86}, 10^{-88}$, which derive them from a cosmological QCD-transition calculation including an instability in the hadronic phase and colour-superconducting gaps.
- For these benchmark efficiencies, viable strangelet dark matter requires $M_S \sim 10^{15}$–10^{17} g, consistent with the survival limit quoted by the same paper.
- This figure reproduces published benchmark scenarios; a first-principles derivation of $\eta_{\rm form}$ from the cosmological QCD transition is beyond the scope of the present work.

Outlook: A Multimessenger Roadmap for SQM

Only a coordinated, multi-wavelength, multi-messenger strategy can confirm or rule out the strange quark matter hypothesis.

Table: Key future facilities and their roles in probing SQM.

Facility	Messenger / technique	Primary SQM science
CTA / CTAO	VHE γ rays	Narrow spectral lines from strangelet annihilation; morphology of HESS J1731-347.
LHAASO (KM2A, WCDA, WFCTA)	EAS, γ rays, cosmic rays	Atmospheric penetration signatures; sub-relativistic luminous events; macro-SQM.
IceCube / KM3NeT	High-energy neutrinos	Slow, bright tracks from nuclearites and Q-balls; neutrino signals from mergers.
Einstein Telescope / Cosmic Explorer	Gravitational waves	Post-merger physics; constraints on the compact-star EoS.
ngVLA, SKA	Radio	Counterparts of mergers; environment of strange quark stars.

Future Multimessenger Observatories Are Necessary!

- The combination of line searches, direct macro-SQM searches, and multimessenger follow-up will dramatically expand the discovery potential.
- Upcoming observations will provide critical tests of the 2SC $\rightarrow$ CFL transition, strangelet stability, and the cosmological abundance of SQM.

C.R. Das, Phys. Atom. Nuclei **88**, 1142-1148 (2025), *arXiv:2507.12817*.

What to watch in the next five years

- CTA / CTAO commissioning and first deep Galactic survey: will determine whether the Baseline scenario is observable at all.
- LHAASO high-duty-cycle monitoring of the Galactic plane: sensitive to sub-relativistic luminous transits from macro-SQM.
- IceCube-Gen2 and KM3NeT full configurations: first km^3-scale neutrino-telescope sensitivity to nuclearites and Q-balls.
- Einstein Telescope / Cosmic Explorer: independent constraints on the compact-star equation of state from post-merger gravitational-wave signals.

Who Can Observe HESS J1731-347?

Source position

HESS J1731-347 lies in the constellation Scorpius at declination $\delta_{\rm dec} \simeq -34.7^\circ$ — deep in the Southern Hemisphere sky.

Observatory	Latitude	Visible?	Reason
H.E.S.S. (Namibia)	-23.3°	Yes	Southern site; the discovery instrument.
VERITAS (Arizona)	$+31.7^\circ$	No	Never rises above the horizon.
MAGIC (La Palma)	$+28.8^\circ$	No	Never rises above the horizon.
CTAO South (Chile)	-24.7°	Yes	Primary future instrument.
CTAO North (La Palma)	$+28.8^\circ$	No	Same horizon limit as MAGIC.
LHAASO (Tibet)	$+29.4^\circ$	No	Northern site; the source is below the horizon.
Fermi-LAT (space)	—	Yes	Space-based all-sky monitor; no site constraint.

Of the four VHE imaging atmospheric Cherenkov telescope facilities discussed in this talk, only H.E.S.S. (Namibia) and the future CTAO South (Chile) can observe HESS J1731-347 with full sensitivity.

Instrument Visibility of the Three Benchmark Sources

Instrument	HESS J1731-347	GW170817	GRB 250702B
Fermi-LAT (space)	Yes	Yes	Yes
MAGIC (La Palma, $+28.8°$)	No	Yes†	Depends on δ
CTAO North (La Palma, $+28.8°$)	No	Yes†	Depends on δ
CTAO South (Chile, $-24.7°$)	Yes	Yes	Depends on δ
H.E.S.S. (Namibia, $-23.3°$)	Yes	Yes	Depends on δ

"Yes" means the source is visible with full sensitivity (culmination altitude $\gtrsim 30°$).

† GW170817 culminates at $\sim 38°$ from La Palma, above the nominal IACT threshold.

For GRB 250702B the visibility depends on its declination, which is not fixed in this analysis; only the space-based Fermi-LAT is guaranteed to observe it.

Multi-Wavelength Coverage of HESS J1731-347

Why a full multi-wavelength picture matters

The strangelet framework in this talk relies on the source being well-characterised from radio to very-high-energy γ rays.
HESS J1731-347 is one of the few Galactic remnants with a rich data set in *every accessible* band.

Band	Instruments	Key measurements
Radio (MHz–GHz)	ATCA, Parkes, MeerKAT, SKA	Shell synchrotron emission; non-thermal electron population.
X-ray (keV)	XMM-Newton, Swift, eROSITA, Athena	Thermal and non-thermal emission; central compact object mass and radius.
GeV γ rays	Fermi-LAT	Pion-decay and inverse-Compton continuum; spectral index $dN/dE \propto E^{-2.3}$.
TeV γ rays	H.E.S.S. (current), CTAO South	Shell-type TeV morphology; target for a narrow-line search.

Consequences for the strangelet framework

1. The measured γ-ray continuum constrains the cosmic-ray density in the remnant, which enters the strangelet production rate.
2. The X-ray and radio data constrain the SNR age and volume, fixing the accumulation time $\tau_{\rm acc}$ and the accumulation volume $V_{\rm source}$. $V_{\rm source}$ is an *effective* accumulation volume ($R_{\rm eff} \approx 10$ pc), not the full SNR radius quoted above (15–20 pc).
3. A future CTAO South narrow-line search can therefore be interpreted within a fully constrained astrophysical model, rather than as a standalone line-flux measurement.

Why CTAO Observations of HESS J1731-347 Matter (I)

The source is anomalous

The compact object in HESS J1731-347 has

$$M = 0.77^{+0.20}_{-0.17}\, M_\odot, \qquad R = 10.4^{+0.86}_{-0.78}\ \text{km}.$$

These values are difficult to reconcile with standard neutron-star models and motivate self-bound or hybrid configurations, including a strange quark star (SQS).

The signal is clean

Strangelet–anti-strangelet annihilation produces a monochromatic γ-ray line:

$$E_\gamma = m_S \simeq 0.94\, A\ \text{GeV}.$$

For $A \sim 10^3$, this gives $E_\gamma \sim 940$ GeV — within CTAO's range.

Natural strangelet factory

- If HESS J1731-347 is an SQS, its interior contains an inner CFL core and an outer 2SC shell.
- The 2SC $\rightarrow$ CFL interface is precisely where strangelet nucleation is expected.
- The surrounding SNR (radius 15–20 pc) provides a large accumulation volume.

Unambiguous signature

The line would appear as a sharp excess on top of the smooth power-law continuum $dN/dE \propto E^{-2.3}$, which is already well-characterised by H.E.S.S. and Fermi-LAT.
No known astrophysical process produces monochromatic VHE lines at these energies.

Key point

If HESS J1731-347 is an SQS, it is a natural factory for strangelets. CTAO can test this hypothesis directly.

Why CTAO Observations of HESS J1731-347 Matter (II)

Only CTAO South can observe it

HESS J1731-347 lies at declination $\delta_{\rm dec} \simeq -34.7^\circ$ — deep in the Southern Hemisphere.

Observatory	Latitude	Visible?
H.E.S.S. (Namibia)	-23.3°	Yes
VERITAS (Arizona)	$+31.7^\circ$	No
MAGIC (La Palma)	$+28.8^\circ$	No
CTAO South (Chile)	-24.7°	Yes
CTAO North (La Palma)	$+28.8^\circ$	No
LHAASO (Tibet)	$+29.4^\circ$	No

Only H.E.S.S. (current) and CTAO South (future) can observe it with full sensitivity.

Tenfold sensitivity improvement

Instrument	Line-flux sensitivity
H.E.S.S.	$\sim 10^{-12}$ ph cm^{-2}s^{-1}
CTAO	$\sim 10^{-13}$ ph cm^{-2}s^{-1}

This is decisive:

- Optimistic scenario already disfavoured.
- Baseline scenario sits within reach of the digitized CTA limit at $f_{\rm ret}^{\rm CTA} \simeq 0.22$ ($A = 100$); the mass budget $f_{\rm ret} \lesssim 7 \times 10^{-5}$ is the limiting factor, not the instrument.
- Conservative scenario requires a next-generation instrument.

Persistent Source: Cleaner Physical Framework

Unlike GW170817 or GRB 250702B, HESS J1731-347 is a persistent source: continuous injection, well-defined $\tau_{\rm acc} \sim 10^6$ yr, and a multi-wavelength-constrained background.

Why CTAO Observations of HESS J1731-347 Matter (III)

A null result is still informative

If CTAO sees nothing:

- Optimistic and possibly Baseline scenarios are excluded within the benchmark sensitivity.
- Conservative scenario remains viable; requires a next-generation instrument.
- Direct searches: (KM3NeT, IceCube-Gen2, LHAASO) become the primary frontier for macro-SQM.

Multi-wavelength background is known

- Radio: ATCA, Parkes, MeerKAT, SKA
- X-ray: XMM-Newton, Swift, eROSITA, Athena
- GeV: Fermi-LAT continuum
- TeV: H.E.S.S. (current), CTAO South

The line search can be interpreted within a fully constrained astrophysical model.

Strongest consistency test of the SQM hypothesis

A joint detection in both channels would be transformative:

Channel	Sensitivity	Probes
γ-ray line	$\propto n_S^2$	Annihilation rate
Direct search	$\propto n_S f_{\rm ret}$	Flux at Earth

Both channels together pin down both the production rate and the retention fraction, provided the annihilation kernel is constrained independently.

In one sentence

CTAO observations of HESS J1731-347 provide the best opportunity to detect or rule out strangelet annihilation lines from a steady Galactic source, and thus to test the Bodmer–Witten–Terazawa hypothesis directly.

MIT Bag Model and Strangelet Stability

MIT bag energy

The total energy of a strangelet is

$$E_A = \sum_i (\Omega_i + N_i \mu_i) + B_{\mathrm{bag}} V,$$

where Ω_i is the thermodynamic potential of quark species i (up, down, strange), μ_i its chemical potential, N_i the quark number, V the bag volume, and B_{bag} the bag constant.

Coulomb correction

For a uniformly charged sphere carrying valence charge Z_V and radius R_{ch}:

$$E_{\mathrm{coul}} = \frac{3}{5} \frac{\alpha Z_V^2}{R_{\mathrm{ch}}}, \qquad \alpha \approx \frac{1}{137}.$$

Stability criterion

- Strangelets are stable if the energy per baryon E_A/A is less than that of ordinary nuclei ($m_N \approx 939$ MeV).
- The minimum stable baryon number $A_{\mathrm{min}} \sim 50$–200, depending on $B_{\mathrm{bag}}^{1/4}$ and the baryon density n_A.
- With CFL charge scaling $Z \simeq 0.3 A^{2/3}$ and the benchmark parameters used here, $m_S/|Z| \approx 3.6\, A^{1/3}$ GeV/c^2, i.e. $\sim 17, 36, 78, 168$ GeV/c^2 for $A = 10^2, 10^3, 10^4, 10^5$.

Honest caveat

The MIT bag model is a phenomenological framework. A genuine QCD calculation requires solving the coupled gap equations with colour and electric neutrality.

Physical Meaning of Hadronic vs. Hybrid Models

Hadronic model

- Purely hadronic equation of state.
- The compact object is a standard neutron star with a small deconfined quark core (if any).
- Smaller production volume: $V_{\rm core} \sim (4\pi/3)(5\ {\rm km})^3$.
- $A_{\rm peak} = 10^6$, $\dot{N}_{\rm peak} = 10^{47}\ {\rm s}^{-1}$.

Hybrid model

- Quark-hybrid equation of state.
- The compact object has a large deconfined quark core surrounded by a hadronic envelope.
- Larger production volume: $V_{\rm core} \sim (4\pi/3)(10\ {\rm km})^3$.
- $A_{\rm peak} = 10^7$, $\dot{N}_{\rm peak} = 10^{48}\ {\rm s}^{-1}$.

Why Hybrid produces more

- A larger, more energetic quark core produces both more strangelets and larger-A clusters.
- The geometric $A^{2/3}$ growth runs to larger A before exponential suppression takes over.
- Since $\Phi_\gamma \propto \dot{N}^2$, the peak-flux ratio reaches ~ 100.

Orthogonality with QCD scenarios

	Hadronic	**Hybrid**
Conservative	$A_{\rm peak} = 10^5$	$A_{\rm peak} = 10^6$
Baseline	$A_{\rm peak} = 10^6$	$A_{\rm peak} = 10^7$
Optimistic	$A_{\rm peak} = 10^7$	$A_{\rm peak} = 10^8$

The two axes are orthogonal: QCD microphysics (Conservative/Baseline/Optimistic) and source structure (Hadronic/Hybrid).

The Line Branching Fraction $B_{\gamma\gamma}$

Definition

The line-flux formula is

$$\Phi_\gamma = \frac{2\, B_{\gamma\gamma}\, R_{\rm ann}}{4\pi D^2}.$$

$B_{\gamma\gamma}$ is the probability that one annihilation yields two photons.
It is set by hadronic branching dynamics, not by the strangelet mass or charge.

Physical picture

- Strangelet–anti-strangelet annihilation proceeds through hadronic intermediate states: $S\bar{S} \to \text{hadrons} \to \gamma\gamma$.
- The $\gamma\gamma$ channel competes with pion production, kaon production, and other hadronic final states.
- $B_{\gamma\gamma}$ is therefore $\ll 1$ in general.

Why this is uncertain

- A first-principles calculation of $B_{\gamma\gamma}$ requires solving the annihilation dynamics of a many-body strangelet system.
- This is beyond the scope of the present framework.
- $B_{\gamma\gamma}$ is treated as a benchmark input, not a QCD-derived quantity.

Impact on the flux

Since $\Phi_\gamma \propto B_{\gamma\gamma}$, a smaller branching fraction linearly suppresses the predicted flux.
The benchmark contours in this talk assume $B_{\gamma\gamma} = 1$; for realistic values the flux is correspondingly lower.
This is one of the key uncertainties of the framework.

Other Strange Quark Star Candidates

Why HESS J1731-347 is special

Several compact objects have been proposed as strange quark star candidates, but HESS J1731-347 is unique in combining:

- Low mass and radius that challenge standard neutron-star models.
- A bright TeV γ-ray counterpart (H.E.S.S.).
- A large surrounding SNR for strangelet accumulation.
- Southern Hemisphere location, accessible to CTAO South.

Object	M ($M_\odot$)	R (km)	TeV?	SQS?
HESS J1731-347	$0.77^{+0.20}_{-0.17}$	$10.4^{+0.86}_{-0.78}$	Yes	Yes
PSR J0740+6620	2.073 ± 0.069	$12.49^{+1.28}_{-0.88}$	No	Maybe
PSR J0030+0451	$1.43^{+0.20}_{-0.17}$	$12.68^{+1.31}_{-1.04}$	No	Maybe
4U 1702-429	1.9 ± 0.3	12.4 ± 0.8	No	Maybe
GW170817 (M1)	1.46 ± 0.12	–	No	Maybe

Key point

HESS J1731-347 is the only candidate with both a low mass/radius *and* a bright TeV counterpart, making it the most promising target for a strangelet line search.

Direct Detection of Strangelets: Without Annihilation γ-Rays

Space-based spectrometers: PAMELA & AMS-02

- Measure rigidity $\mathcal{R} = p/(Ze)$, velocity $\beta_{\rm vel}$ (time-of-flight), charge Z (dE/dx/Cherenkov).
- Mass: $A = p/(\gamma_L \beta_{\rm vel} m_N)$.
- Signature: anomalous A/Z ratio compared to ordinary nuclei.

Nuclear track detectors: MACRO, SLIM

- Etch rate $\propto Z^2/\beta_{\rm vel}^2$.
- Heavily ionizing particle leaves damage trail.
- Flux limits for nuclearites and charged Q-balls.

Neutrino telescopes: IceCube, KM3NeT, Baikal-GVD

- Energy loss: $\dfrac{dE}{dx} = -\dfrac{1}{2}\sigma\rho_{\rm targ}v^2$, $\sigma = \pi R_S^2$, $R_S \approx 0.7\,A^{1/3}$ fm.
- Slow, massive strangelet $\Rightarrow$ long, bright Cherenkov track.
- Time structure: $\Delta t \sim L_{\rm path}/v \sim 30$–$80$ μs per PMT.

Why this is complementary to γ-line searches

- γ-line flux $\propto n_S^2$ (annihilation).
- Direct detection flux $\propto n_S f_{\rm ret}$ (surviving particles).
- A joint detection would pin down both production and retention.

Key point

Direct detection does not require annihilation. The strangelet itself is the signal.

How A Variation Affects Direct Detection

CFL charge scaling

$$Z \simeq 0.3\, A^{2/3}, \quad \frac{Z}{A} \simeq 0.3\, A^{-1/3}.$$

For $A = 10^2$: $Z/A \simeq 0.065$;
for $A = 10^6$: $Z/A \simeq 3 \times 10^{-3}$.

Rigidity

For fixed velocity $\beta_{\rm vel}$,

$$\mathcal{R} = \frac{p}{Ze} = \frac{m_S\, \gamma_L \beta_{\rm vel}}{Z\, e} \propto A^{1/3}.$$

Larger $A \Rightarrow$ higher rigidity
$\Rightarrow$ less geomagnetic deflection.

Ionization loss

$$\frac{dE}{dx} \propto \frac{Z^2}{\beta_{\rm vel}^2} \propto \frac{A^{4/3}}{\beta_{\rm vel}^2}.$$

Larger $A \Rightarrow$ more ionizing.

Geometric cross-section

$$\sigma \propto R_S^2 \propto A^{2/3}.$$

Larger $A \Rightarrow$ more interactions in neutrino telescopes.

Net effect

- Larger A: easier to detect directly (higher dE/dx, larger σ).
- But lower Z/A: higher rigidity, so need larger momentum to reach detector.
- Direct detection and γ-line searches probe different A regimes; together they cover the parameter space.

Charge-to-Baryon Ratio Z/A of Strangelets

Definition

For a strangelet of baryon number A and net electric charge Z (in units of e):

$$Y_Q \equiv \frac{Z}{A}.$$

This controls the rigidity of the strangelet in cosmic rays and hence its direct-detection signature.
The symbols Y_Q and Z/A are used interchangeably and denote the same physical quantity.

Mass-to-charge ratio

$$\frac{m_S}{|Z|} \approx \frac{m_N}{Y_Q}\left[1 + \frac{2}{9\pi}\frac{\mu}{m_s} - \frac{1}{3}\left(\frac{\Delta_{\mathrm{CFL}}}{\mu}\right)^{1/2}\right].$$

With the CFL charge scaling used here, the bracket is ≈ 1.16, giving $m_S/|Z| \approx 3.6\,A^{1/3}$ GeV$/c^2$.

Physical origin

- For three-flavour SQM with roughly equal quark numbers, the net charge is nearly zero.
- Y_Q is parametrically suppressed by $(m_s/\mu)^2$.
- Electric neutrality and CFL pairing modify the residual charge distribution.

Key result: Z/A is not constant

For CFL strangelets:

$$Z \simeq 0.3\,A^{2/3}, \qquad \frac{Z}{A} \simeq 0.3\,A^{-1/3}.$$

- $A = 10^2$: $Z/A \simeq 0.065$
- $A = 10^6$: $Z/A \simeq 3 \times 10^{-3}$

The charge fraction decreases with increasing A.

Strangelet Mass-to-Charge Ratio vs. Detector Windows

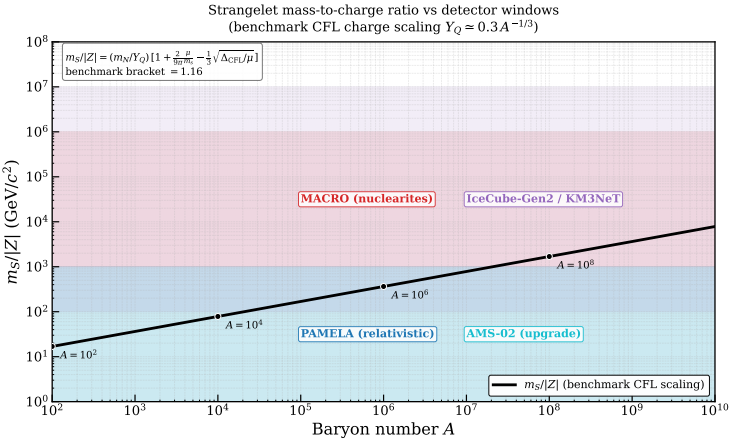

- Benchmark CFL scaling: $Y_Q \simeq 0.3\,A^{-1/3}$.
- $m_S/|Z|$ controls direct-detection signatures.
- Shaded windows: PAMELA, AMS-02, MACRO, and future IceCube-Gen2 / KM3NeT sensitivity.
- Direct searches and γ-line searches probe different A regimes.

How Z/A Affects CTAO Detection

Direct effect: minimal

CTAO's line-flux formula is

$$\Phi_\gamma = \frac{2\, B_{\gamma\gamma}\, R_{\rm ann}}{4\pi D^2}, \quad R_{\rm ann} = n_S\, n_{\bar{S}}\, \langle \sigma v \rangle\, V_{\rm source}.$$

- Line energy $E_\gamma = m_S$: set by mass, not charge.
- $\langle \sigma v \rangle$: set by strong interaction.
- $B_{\gamma\gamma}$: set by hadronic dynamics.

Z/A does not appear explicitly.

Indirect effect: retention factor

$$n_S(A) = \frac{1}{V_{\rm source}} \int dt\, \dot{N}(A,t)\, f_{\rm ret}(A,t).$$

- Z/A affects magnetic confinement of strangelets in the source.
- Higher $Z \Rightarrow$ stronger magnetic coupling $\Rightarrow$ modified escape/survival.
- $f_{\rm ret}$ is the largest uncertainty in the framework.

Crucial for direct detection (complementary to CTAO)

- Rigidity $\mathcal{R} = p/(Ze)$ controls propagation and detector signature.
- Small $Z/A \Rightarrow$ high rigidity $\Rightarrow$ less deflection.
- Joint detection (CTAO + direct) would pin down both production rate and retention fraction, provided the annihilation kernel is constrained independently.
- Z/A is crucial for direct detection (PAMELA, AMS-02, IceCube, KM3NeT), which is complementary to CTAO: a joint detection in both channels would provide the strongest test of the strangelet hypothesis.

PAMELA, AMS, IceCube, and KM3NeT can Detect Strangelets

Space-based spectrometers: PAMELA & AMS-02

- Magnetic spectrometer measures momentum p and sign of charge.
- Time-of-flight + calorimeter measure velocity β_{vel} and energy E.
- Combining these gives the particle's mass A and charge Z.

Strangelet signature: a particle with an anomalously high A/Z ratio compared to ordinary nuclei.

AMS-02 upgrade (CERN)

- New Layer-0 silicon tracker increases acceptance by $\sim 300\%$.
- Substantially improves sensitivity to rare events, including strangelets.
- Expected to detect tens of events if strangelets exist at the predicted level.

Neutrino telescopes: IceCube & KM3NeT

- Look for Cherenkov light from particles traversing large volumes of ice or water.
- A slow, massive strangelet deposits enormous energy, creating a long, bright track lasting milliseconds.
- Luminous transit is the key signature.

Strangelet signature: an unusually high number of hit sensors in a line with a long signal duration.

Complementary strategy

- PAMELA & AMS-02 measure the surviving flux of strangelets at Earth.
- IceCube & KM3NeT detect the passage of massive strangelets through large detector volumes.
- A joint detection would pin down both the production rate and the retention fraction.

Key point

Direct detection (space) and indirect detection (ice/water) are complementary.
Together they provide the strongest possible test of the strangelet hypothesis.

AMS-02 and Its Upgrade — A Dedicated Strangelet Search

The AMS-02 detector

- Alpha Magnetic Spectrometer on the International Space Station (ISS).
- Measures rigidity $\mathcal{R} = p/(Ze)$, velocity β_{vel} (time-of-flight), and charge Z (dE/dx).
- Mass: $A = p/(\gamma_L \beta_{\text{vel}} m_N)$.
- Signature: anomalous A/Z ratio.

The upgrade (2025–2026)

- New Layer-0 silicon tracker increases acceptance by $\sim 300\%$.
- Substantially improves sensitivity to rare events, including strangelets.
- Expected to detect tens of events if strangelets exist at the predicted level.

AMS-02 results for strangelets

- AMS-02 has searched for slow-moving, highly ionizing particles.
- No strangelets detected so far.
- The upgrade will improve sensitivity to $Z \sim 1$–10 and masses up to $\sim 10^3$ GeV/c^2.

Why this matters for the framework

- AMS-02 probes the surviving flux of strangelets at Earth.
- Combined with CTAO γ-line searches, it provides a complementary test.
- A joint detection (or null result) would constrain both the production rate and the retention fraction.

Can the Baikal-GVD Telescope Detect Strangelets?

The Baikal-GVD Telescope

- A cubic-kilometer scale neutrino telescope under construction in Lake Baikal, Russia.
- Uses a 3D array of optical modules to detect Cherenkov light in deep freshwater.
- Core physics: high-energy neutrino astronomy, dark matter, and exotic particle searches.

Exotic particle program

- The collaboration's official objectives include the search for monopoles, Q-balls, and nuclearites.
- Reviews of the Baikal program explicitly list strange quark matter as a target.

How strangelets would be detected

- A massive, slow-moving strangelet would create a long, bright, continuous track of Cherenkov light.
- This signal is distinct from the point-like events produced by neutrinos or the background from atmospheric muons.
- The search is for a highly ionizing particle with a very high energy deposit.

Current status & outlook

No strangelets have been detected yet. As the Baikal-GVD detector grows to its full 1 km^3 volume, its sensitivity to these rare events will steadily improve. Its Northern Hemisphere location complements the IceCube detector at the South Pole.

Key point

Baikal-GVD can be an active participant in the global multi-messenger search for strangelets, complementing space-based (AMS-02) and other ground-based (IceCube, KM3NeT) efforts.

SQM-ISS — A Future Dedicated Space Detector

The SQM-ISS mission

- Strange Quark Matter detector on the International Space Station (ISS).
- Scintillator + piezoelectric stack design.
- Searches for massive, non-relativistic particles:
  - Strangelets
  - Q-balls
  - Primordial black holes
- Velocity range: $v \lesssim 250$ km/s ($\beta_{\text{vel}} \sim 10^{-3}$).

Complementarity

- SQM-ISS is dedicated to this science.
- It complements:
  - AMS-02 (space-based spectrometer)
  - IceCube/KM3NeT (neutrino telescopes)
  - LHAASO (ground-based EAS array)
- A joint detection would be transformative.

Detection principle

- A massive particle traversing the detector deposits enormous energy via ionization.
- Scintillator measures the energy deposit.
- Piezoelectric sensors measure the mechanical stress from the track.
- Signature: a slow, straight, highly ionizing track.

Difference from AMS-02

- AMS-02: magnetic spectrometer; sensitive to relativistic particles ($\beta_{\text{vel}} \sim 1$).
- SQM-ISS: scintillator + piezoelectric; dedicated to slow, massive particles ($v \lesssim 250$ km/s, $\beta_{\text{vel}} \sim 10^{-3}$).
- AMS-02 measures rigidity and charge; SQM-ISS measures ionization and mechanical stress.

AMS-02 and SQM-ISS: Complementary ISS Detectors

AMS-02

- Alpha Magnetic Spectrometer, mounted on the ISS S3 truss segment (since 2011).
- Magnetic spectrometer: measures rigidity $\mathcal{R} = p/(Ze)$, velocity β_{vel}, charge Z.
- Sensitive to relativistic cosmic rays; strangelet signature: anomalous A/Z.
- Upgrade (2025–2026): Layer-0 tracker, $\sim 300\%$ acceptance increase.

SQM-ISS

- Proposed Strange Quark Matter detector on the ISS.
- Scintillator + piezoelectric stack.
- Dedicated to massive, non-relativistic particles: strangelets, Q-balls, primordial black holes.
- Velocity range $v \lesssim 250$ km/s ($\beta_{\mathrm{vel}} \sim 10^{-3}$).
- Signature: slow, straight, highly ionizing track.

Key point

They are not in the same place and do not use the same detection principle. AMS-02 is a large magnetic spectrometer on the ISS truss; SQM-ISS is a future dedicated slow-particle detector. They are complementary: AMS-02 probes relativistic strangelets via rigidity/charge, SQM-ISS probes non-relativistic macro-SQM via ionization and mechanical stress.

The Alpha Magnetic Spectrometer (AMS-02) on the International Space Station (ISS)



AMS-02 stands poised to detect the elusive signatures of strangelets, offering a glimpse into the tantalizing realm of exotic matter and reshaping our understanding of cosmic composition.

Strangelets and Magnetic Monopoles: Common Ground

Similar search strategies

Property	Strangelets	Monopoles
Exotic?	Yes	Yes
Stable?	Hypothetical	Hypothetical
Direct detection?	Yes	Yes
Cherenkov in ice/water?	Yes	Yes
Nuclear track detectors?	Yes	Yes
Mass range	10^{-10}–10^{2} g	10^{16}–10^{17} GeV
Charge	Z	g, $2g$, ...

Key difference

- Monopoles: point-like, no internal structure.
- Strangelets: extended objects with baryon number A, radius $R_S \propto A^{1/3}$, and $Z/A \ll 1$.
- This makes strangelets macroscopic and potentially detectable as extended tracks.

Common detection challenges

- Rare events: both require large detector volumes and long exposure times.
- Background rejection: both produce distinctive but rare signatures.
- Model dependence: detection limits depend on unknown fluxes, masses, and charges.
- Multi-messenger approach: both benefit from combining direct detection with astrophysical searches.

Key point

Strangelets and magnetic monopoles share detection strategies and face similar challenges. A joint search programme would benefit both communities.

Strangelets, Quark Matter, and the Limits of Exotic Physics

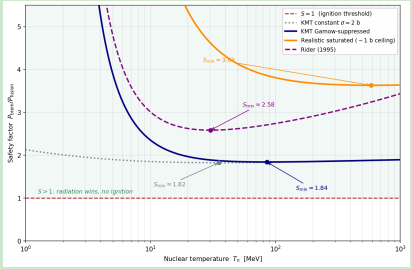

Quark matter alternatives to ordinary nuclei

- **Up–down quark matter:** deconfined u, d quarks; positively charged, behaves like a large nucleus.
- **Strange quark matter:** u, d, s quarks (Bodmer 1971; Witten 1984); nearly neutral, potentially more stable than nuclei.
- QCD is non-perturbative at low energies $\Rightarrow$ stability is hard to settle. Current theoretical prejudice: ordinary nuclei are the ground state.

Charge determines the danger

- Positively charged strangelets: Coulomb barrier repels nuclei $\Rightarrow$ inert.
- Neutral/negative strangelets: no suppression $\Rightarrow$ could grow without bound and destroy the Sun in $\sim 10^7$ yr.

Typical scaling relation (Madsen 2000):

$$Z \approx 0.3\, A^{2/3}$$

- Consensus: strangelets should be positively charged $\Rightarrow$ safe.
- Dangerous combination (stable *and* non-positive) has probability $\ll 0.1\%$.

Other exotic physics

- **Proton decay:** baryon number is an accidental symmetry; lifetime $\gtrsim 10^{34}$ yr, far beyond experimental reach.
- **Tiny black holes:** smallest $\sim 20\,\mu$g, evaporate in 10^{-43} s; cross-section $\sim 10^{-69}$ m^2 $\Rightarrow$ harmless.
- **Fusion ignition:** nitrogen fusion in air is ruled out by bremsstrahlung losses ($S_{\rm sup} = P_{\rm brem}/P_{\rm fusion} \approx 3.85 > 1$).

Bottom line: no new super-weapon between the nuclear bomb and false vacuum decay.

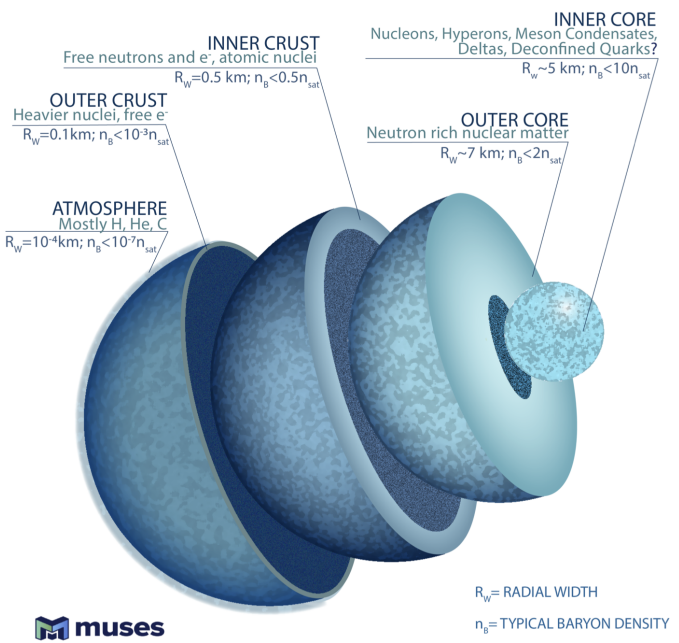
INNER CRUST
Free neutrons and e-, atomic nuclei
R_W=0.5 km; n_B<0.5n_{sat}
INNER CORE
Nucleons, Hyperons, Meson Condensates, Deltas, Deconfined Quarks?
R_W~5 km; n_B<10n_{sat}
OUTER CRUST
Heavier nuclei, free e-
R_W=0.1km; n_B<$10^{-3}n_{sat}$
OUTER CORE
Neutron rich nuclear matter
R_W~7 km; n_B<2n_{sat}
ATMOSPHERE
Mostly H, He, C
R_W=10^{-4}km; n_B<$10^{-7}n_{sat}$
R_W= RADIAL WIDTH
n_B= TYPICAL BARYON DENSITY
muses

Backup: 3D QCD phase diagram in (T, μ_B, μ_I) space

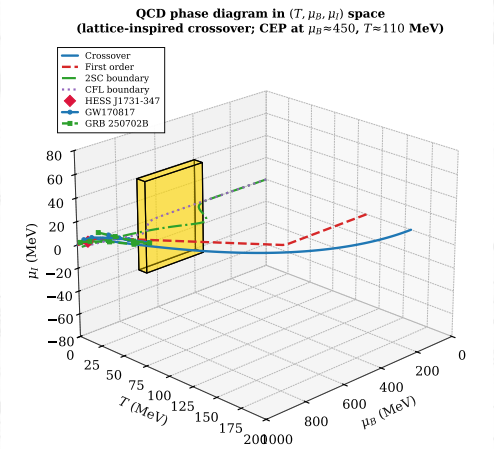

The production window (gold) is shown at intermediate baryon density; the three source trajectories (HESS J1731-347, GW170817, GRB 250702B) pass through the high-μ_B neutron-star region above it. The isospin axis μ_I is relevant for neutron-rich matter but is typically small ($|\mu_I| \ll \mu_B$) in the regimes of interest. Crossover curvature parameters are lattice-inspired; the CEP position and the 2SC/CFL boundaries are set by hand. No named effective model (NJL, PNJL, FRG) is solved. The panel is illustrative only.

Backup: Heuristic EOS parameter scan (not a posterior)

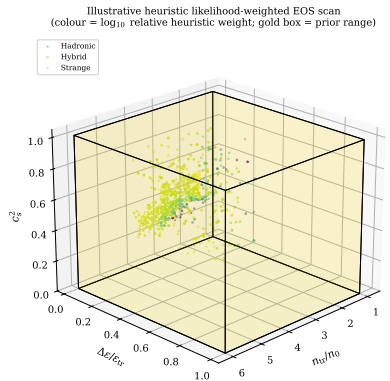

What the 3D view adds

- The three EOS parameters are correlated; a 2D corner plot shows only pairwise projections.
- The 3D view exposes the joint geometry of the transition density, the energy-density jump and the high-density sound speed.
- Colours encode a $\log_{10}$ heuristic weight; marker shape separates the hadronic, hybrid and strange model classes.

Physics ingredients and honest caveat

(i) EOS: speed-of-sound parameterisation with a first-order phase transition.
(ii) Observables: $M_{\max}$, $R_{1.4}$, $\Lambda_{1.4}$ from the TOV and tidal Love-number equations.
(iii) Constraints: PSR J0740+6620 (M), GW170817 ($\Lambda_{1.4}$) and NICER ($R_{1.4}$) as heuristic scores.
(iv) Not a Bayesian posterior: the colour scale shows a heuristic weight assigned to each toy EOS sample; there is no prior density, no likelihood function, no sampler, and no convergence diagnostic.

Backup: 3D line-flux surface $\Phi_\gamma(A, f_{\rm ret})$

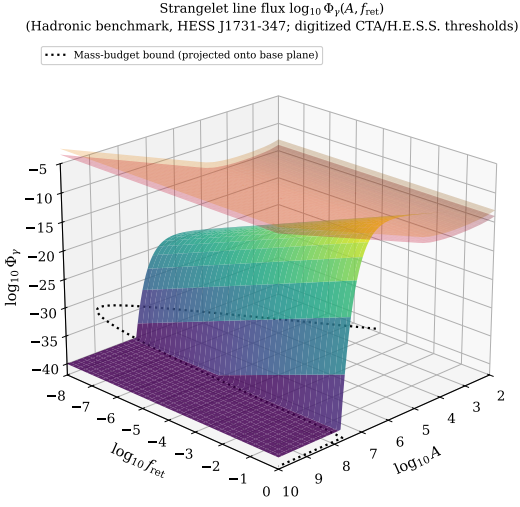

What the 3D view adds

- The line flux depends on both A and $f_{\rm ret}$; a single 2D slice at fixed A hides the A-dependence.
- The red plane is the CTA threshold 10^{-13} ph cm^{-2} s^{-1}.
- The dotted black curve on the base plane is the mass-budget bound: it defines the region where a real source can actually supply the required SQM.

Takeaway

The intersection of the CTA-sensitive region and the mass-budget-allowed region is the only region where a self-consistent detection is possible. It is very small — this is the central open problem.

Backup: 3D (M, R, Λ) space for the three structural hypotheses

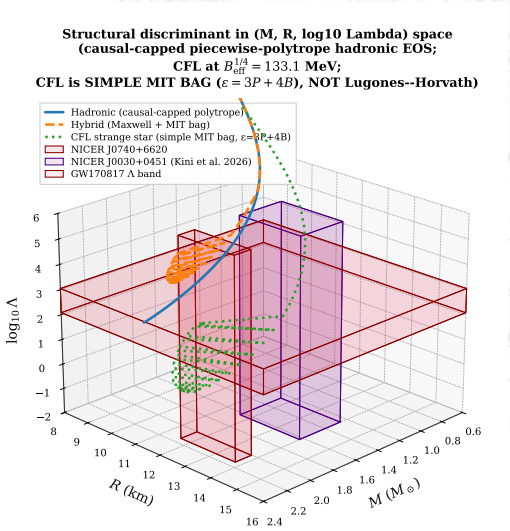

What the 3D view adds

- Each EOS is a 1D curve in (M, R, Λ) space, parametrised by central density.
- The three families overlap in M and R but differ in the slope of the $\Lambda(M)$ projection.
- Grey curves on the base planes show the 2D projections that appear in the main talk.

Structural discriminant

The two-family scenario (NS + strange stars) is the only hypothesis that naturally populates both the low-Λ and high-Λ branches. A single-event measurement of $\tilde{\Lambda}$ cannot establish this; population-level statistics are required.

CFL curve drawn at $B_{\rm eff}^{1/4} = 133.1$ MeV, NICER boxes at the unified values.

Backup: 3D direct-detection landscape

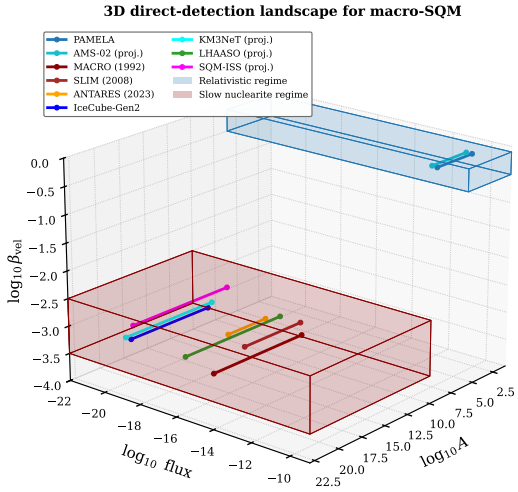

What the 3D view adds

- The third axis is the velocity band $\beta_{\rm vel} = v/c$, which is the physical discriminant between relativistic strangelets (PAMELA, AMS-02) and slow nuclearites (MACRO, SLIM, ANTARES, IceCube-Gen2, KM3NeT, LHAASO, SQM-ISS).
- The grey translucent plane separates the two regimes.
- A single 2D (A, flux) plot would superimpose the two regimes and give the misleading impression that they form one exclusion curve.

Key point

PAMELA and MACRO constraints cannot be combined into a single exclusion curve; the 3D view makes this geometrically explicit.

Backup: 3D neutrino mean free path for hadronic, 2SC, and CFL

The 3D surfaces are computed from the same proxy opacity used in the main-talk MFP frame; they are *not* the output of a full Boltzmann or matrix-kinetic transport solver. Temperature dependence is schematic; phase-space blocking is a smooth tanh proxy; the CFL branch is $\exp(\Delta_{\mathrm{CFL}}/T)$ multiplying the 2SC-like opacity.

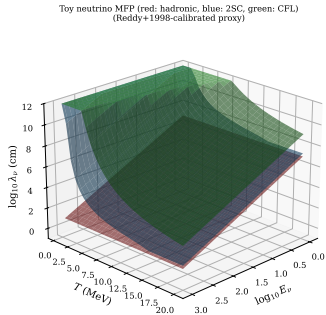

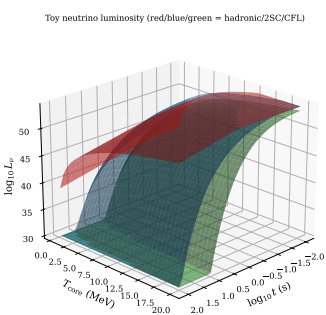

What would be required for a quantitative prediction

- A specified phase-dependent weak-interaction kernel (species, couplings, degeneracy factors).
- A merged 2SC / CFL thermodynamic potential and the corresponding collective-mode spectrum.
- Neutrino degeneracy, μ-flavour distinction, and lepton-fraction evolution.
- A coupled Boltzmann transport solver.

What the 3D view adds

- λ_ν depends on both E_ν and T; a 1D slice at fixed T (as in the main talk) hides the temperature dependence.
- The surfaces illustrate the qualitative trend of the proxy model, not a quantitative prediction.

Caveat

The present figure should be used only to motivate the qualitative question of phase-dependent neutrino opacity. It does *not* predict a measurable merger-neutrino imprint.

Astrophysical Observations: NICER, GW, Kilonova

- T. Salmi et al., *The Radius of the High-mass Pulsar PSR J0740+6620 with 3.6 yr of NICER Data*, Astrophys. J. **974**, 294 (2024).
- A. J. Dittmann et al., *A More Precise Measurement of the Radius of PSR J0740+6620 Using Updated NICER Data*, Astrophys. J. **974**, 295 (2024).
- D. Choudhury et al., *A NICER View of the Nearest and Brightest Millisecond Pulsar: PSR J0437-4715*, ApJL **971**, L20 (2024).
- M. C. Miller et al., *The Radius of PSR J0437-4715 from NICER Data*, Astrophys. J. Lett. **1000**, L48 (2026).
- Y. Kini et al., *A NICER View of PSR J0030+0451: Updated Constraints from 6 yr of NICER Observations*, Astrophys. J. **1005**, 201 (2026).
- N. Rutherford et al., *Constraining the Dense Matter Equation of State with New NICER Mass-Radius Measurements and New Chiral Effective Field Theory Inputs*, Astrophys. J. Lett. **971**, L19 (2024).
- S. Vinciguerra et al., *An Updated Mass–Radius Analysis of the 2017–2018 NICER Data Set of PSR J0030+0451*, Astrophys. J. **961**, 62 (2024).
- B. P. Abbott et al. (LIGO/Virgo), *GW170817: Observation of Gravitational Waves from a Binary Neutron Star Inspiral*, Phys. Rev. Lett. **119**, 161101 (2017).
- B. P. Abbott et al. (LIGO/Virgo), *Properties of the Binary Neutron Star Merger GW170817*, Phys. Rev. X **9**, 011001 (2019).

Astrophysical Observations: NICER, GW, Kilonova

- E. R. Most et al., *New Constraints on Radii and Tidal Deformabilities of Neutron Stars from GW170817*, Phys. Rev. Lett. **120**, 261103 (2018).
- M. Breschi et al., *AT2017gfo: Bayesian Inference and Model Selection of Multi-component Kilonovae and Constraints on the Neutron Star Equation of State*, Mon. Not. Roy. Astron. Soc. **505**, 1661 (2021).
- M. Nicholl et al., *Tight Multimessenger Constraints on the Neutron Star Equation of State from GW170817 and a Forward Model for Kilonova Light-curve Synthesis*, Mon. Not. Roy. Astron. Soc. **505**, 3016 (2021).
- M. W. Coughlin et al., *Multimessenger Bayesian Parameter Inference of a Binary Neutron Star Merger*, Mon. Not. Roy. Astron. Soc. Lett. **489**, L91 (2019).
- J. Sedaghat et al., *Constraint on the Equation of State of Strange Quark Star: Perturbative QCD Along with a Density-Dependent Bag Constant*, Annals Phys. **472**, 169864 (2025), arXiv:2411.12048.
- R. Nandi and P. Char, *Hybrid Stars in the Light of GW170817*, Astrophys. J. **857**, 12 (2018).
- R. Nandi and S. Pal, *Finding Quark Content of Neutron Stars in Light of GW170817*, Eur. Phys. J. Spec. Top. **230**, 551 (2021).
- J.-E. Christian et al., *Comprehensive analysis of constructing hybrid stars with a renormalization group-consistent Nambu-Jona-Lasinio model*, Astron. Astrophys. **701**, A145 (2025).
- D. Blaschke et al., *Was GW170817 a Canonical Neutron Star Merger? Bayesian Analysis with a Third Family of Compact Stars*, Universe **6**, 81 (2020).

Astrophysical Observations: NICER, GW, Kilonova

- S. Blacker and A. Bauswein, *Comprehensive Survey of Hybrid Equations of State in Neutron Star Mergers and Constraints on the Hadron-Quark Phase Transition*, Phys. Rev. D **112**, 123041 (2025).
- A. Bauswein et al., *Identifying a First-Order Phase Transition in Neutron-Star Mergers through Gravitational Waves*, Phys. Rev. Lett. **122**, 061102 (2019).
- E. R. Most et al., *Signatures of Quark-Hadron Phase Transitions in General-Relativistic Neutron-Star Mergers*, Phys. Rev. Lett. **122**, 061101 (2019).
- M. G. Alford, S. Han, and M. Prakash, *Generic Conditions for Stable Hybrid Stars*, Phys. Rev. D **88**, 083013 (2013).
- S. Traversi et al., *Speed of Sound in Dense Matter and Two Families of Compact Stars*, Astron. Astrophys. **660**, A62 (2022).
- S. Yang et al., *Confronting Strange Stars with Compact-Star Observations and New Physics*, Universe **9**, 202 (2023).
- N. Khosravi Largani et al., *Universal Relations for Rapidly Rotating Cold and Hot Hybrid Stars*, Mon. Not. Roy. Astron. Soc. **515**, 3539 (2022).
- L. R. Weih, M. Hanauske, and L. Rezzolla, *Postmerger Gravitational-Wave Signatures of Phase Transitions in Binary Mergers*, Phys. Rev. Lett. **124**, 171103 (2020).

Astrophysical Observations: NICER, GW, Kilonova

- A. K. Saha, T. Malik, and R. Mallick, *Are NICER and GW170817 Constraints Suggesting a Compactified Scenario for Neutron Stars?*, Astrophys. J. **1005**, 206 (2026).
- D. Zhou et al., *Reexamining Constraints on Neutron Star Properties from Perturbative QCD*, Phys. Rev. C **111**, 015810 (2025).
- D. Curin et al., *Hybrid Stars with Color Superconducting Cores in an Extended FCM Model*, Universe **7**, 370 (2021).
- B. P. Abbott et al., *GW170817: Measurements of Neutron Star Radii and Equation of State*, Phys. Rev. Lett. **121**, 161101 (2018).
- W.-J. Xie et al., *Bayesian Constraints on Quark Stars from Multimessenger Observations*, Phys. Rev. D **114**, 023016 (2026).
- S. Shirke et al., *Constraining the Equation of State of Hybrid Stars Using Recent Information from Multidisciplinary Physics*, Astrophys. J. **944**, 7 (2023).
- M. C. Miller et al., *The Radius of the Neutron Star PSR J0614–3329 from NICER Data*, arXiv:2609.00965 (2026).
- L. Brandes and W. Weise, *Implications of Latest NICER Data for the Neutron Star Equation of State*, Phys. Rev. D **111**, 034005 (2025).

Astrophysical Observations: NICER, GW, Kilonova

- L. Mauviard et al., *A NICER View of the 1.4 $M_\odot$ Edge-on Pulsar PSR J0614-3329*, Astrophys. J. **995**, 60 (2025).
- C. Huang, *Model-independent Determination of the Tidal Deformability of a 1.4$M_\odot$ Neutron Star from Gravitational-wave Measurements*, Astrophys. J. **985**, 216 (2025).
- S. Borsányi et al., *Lattice QCD constraints on the critical point from an improved precision equation of state*, Phys. Rev. D **112**, L111505 (2025).
- K. Chatziioannou et al., *Neutron Stars and the Dense Matter Equation of State*, Rev. Mod. Phys. **97**, 045007 (2025).

Color Superconductivity: 2SC, CFL, Cooper Pairing

- H. Gholami et al., *Astrophysical Constraints on Color-Superconducting Phases in Compact Stars within the RG-consistent NJL Model*, Phys. Rev. D **111**, 103034 (2025).
- C. Gartlein, O. Ivanytskyi, V. Sagun, and L. Lopes, *Color-Superconducting Quarkyonic Matter*, Phys. Rev. D **113**, 034017 (2026).
- M. G. Alford, K. Rajagopal, and F. Wilczek, *QCD at Finite Baryon Density: Nucleon Droplets and Color Superconductivity*, Phys. Lett. B **422**, 247 (1998).
- M. G. Alford, K. Rajagopal, and F. Wilczek, *Color-Flavor Locking and Chiral Symmetry Breaking in High Density QCD*, Nucl. Phys. B **537**, 443 (1999).
- K. Rajagopal and F. Wilczek, *The Condensed Matter Physics of QCD*, in *At the Frontier of Particle Physics*, arXiv:hep-ph/0011333 (2000).
- M. G. Alford, A. Schmitt, K. Rajagopal, and T. Schäfer, *Color Superconductivity in Dense Quark Matter*, Rev. Mod. Phys. **80**, 1455 (2008).
- A. Kurkela, P. Romatschke, and A. Vuorinen, *Cold Quark Matter*, Phys. Rev. D **81**, 105021 (2010).
- A. Kurkela, K. Rajagopal, and R. Steinhorst, *Astrophysical Equation-of-State Constraints on the Color-Superconducting Gap*, Phys. Rev. Lett. **132**, 262701 (2024).
- A. Kurkela, K. Rajagopal, and R. Steinhorst, *Updated Astrophysical Equation-of-State Constraints on the Color-Superconducting Gap*, arXiv:2508.20763 (2025).

Color Superconductivity: 2SC, CFL, Cooper Pairing

- S.-P. Tang, Y.-J. Huang, and Y.-Z. Fan, *Neutron Star Observations Challenge a Large Colour-Superconducting Gap in Dense Quark Matter*, arXiv:2606.03707 (2026).
- T. Noda et al., *Cooling of Hybrid Stars with a $2SC + \langle dd \rangle$ Phase*, Prog. Theor. Exp. Phys. **2026**, 083E01 (2026).
- D. Blaschke and J. Berdermann, *Neutrinos in Dense Quark Matter and Cooling of Compact Stars*, arXiv:0912.3075 (revised 2024).
- M. G. Alford, A. Harutyunyan, A. Sedrakian, and S. Tsiopelas, *Bulk Viscosity of Two-Color Superconducting Quark Matter in Neutron Star Mergers*, Phys. Rev. D **110**, L061303 (2024).
- M. G. Alford, A. Harutyunyan, A. Sedrakian, and S. Tsiopelas, *Bulk Viscosity of Two-Flavor Color Superconducting Quark Matter in Neutron Star Mergers*, Front. Astron. Space Sci. **12**, 1648066 (2025).
- M. G. Alford, L. Brodie, M. Buballa, H. Gholami, A. Haber, and M. Hofmann, *Neutrino Absorption in Two-Flavor Color-Superconducting Quark Matter*, Phys. Rev. C (accepted 2026), arXiv:2509.04240.
- Y. Fujimoto, K. Fukushima, and W. Weise, *Continuity from Neutron Matter to Two-Flavor Quark Matter with ${}^3P_2$ Superfluidity*, Phys. Rev. D **101**, 094009 (2020).
- M. Prakapenia, C.-J. Xia, and G. Vereshchagin, *Pair Luminosity and Cooling of Newborn Strange Star: Color-Flavor-Locked and Two-Flavor Color Superconducting Quarks*, Phys. Rev. D (accepted 2026), arXiv:2607.25766.

Color Superconductivity: 2SC, CFL, Cooper Pairing

- A. W. Steiner, S. Reddy, and M. Prakash, *Color-Neutral Superconducting Quark Matter*, Phys. Rev. D **66**, 094007 (2002).
- A. Geißel, T. Gorda, and J. Braun, *Color Superconductivity under Neutron-Star Conditions at Next-to-Leading Order*, Phys. Rev. Lett. **135**, 211901 (2025).
- M. Buballa, *NJL-Model Analysis of Chiral Symmetry Restoration and Color Superconductivity*, Phys. Rep. **407**, 205 (2005).
- G. Cao, *Extended Nambu-Jona-Lasinio Model for Quark and Nuclear Matters*, Phys. Lett. B **860**, 139140 (2025).
- F. Köpp et al., *Repulsive Vector Couplings and Massive Strange Stars*, Astron. Nachr. **346**, e20240119 (2025).
- M. B. Pinto, *Equation of state for strange quark matter: Linking the Nambu–Jona-Lasinio model to perturbative QCD*, Phys. Rev. C **107**, 045807 (2023).
- M. Imam et al., *Massive Cold Hybrid Stars in a Modified Polyakov–Nambu–Jona-Lasinio Model*, Phys. Rev. D **114**, 083016 (2026).
- M. Albino et al., *A Bayesian Inference of Hybrid Stars with Large Quark Cores*, Phys. Rev. D **113**, 083019 (2026), arXiv:2511.02653.
- X. Geng, K. Huang, H. Shen, L. Li, and J. Hu, *Crossover Equation of State Constrained by Astronomical Observations and pQCD*, arXiv:2604.08841 (2026).

Color Superconductivity: 2SC, CFL, Cooper Pairing

- T. M. da Silva et al., *Bayesian Study of Quark Models in View of Recent Astrophysical Constraints*, Phys. Rev. D **109**, 043054 (2024).
- D. Blaschke, S. Hanu, and G. Liebing, *Neutron Stars with Crossover to Color Superconducting Quark Matter*, Phys. Rev. C **105**, 035804 (2022).
- I. A. Shovkovy, *Two Lectures on Color Superconductivity*, arXiv:nucl-th/0410091 (2005).
- S. B. Rüster et al., *The Phase Diagram of Neutral Quark Matter: Self-Consistent Treatment of Quark Masses*, Phys. Rev. D **72**, 034004 (2005).
- M. G. Alford and A. Schmitt, *Bulk Viscosity in 2SC Quark Matter*, J. Phys. G **34**, 67 (2007).
- M. Anglani et al., *Crystalline Color Superconductors*, Rev. Mod. Phys. **86**, 509 (2014).
- C. Knippel and A. Sedrakian, *Gravitational Radiation from Crystalline Color-Superconducting Hybrid Stars*, Phys. Rev. D **79**, 083007 (2009).

Strangelets and Strange Quark Matter

- A. R. Bodmer, *Collapsed Nuclei*, Phys. Rev. D **4**, 1601 (1971).
- E. Witten, *Cosmic Separation of Phases*, Phys. Rev. D **30**, 272 (1984).
- E. Farhi and R. L. Jaffe, *Strange Matter*, Phys. Rev. D **30**, 2379 (1984).
- C. Alcock and E. Farhi, *Evaporation of Strange Matter in the Early Universe*, Phys. Rev. D **32**, 1273 (1985).
- J. Madsen, H. Heiselberg, and K. Riisager, *Does Strange Matter Evaporate in the Early Universe?*, Phys. Rev. D **34**, 2947 (1986).
- F. Weber, *Strange Quark Matter and Compact Stars*, Prog. Part. Nucl. Phys. **54**, 193 (2005).
- H.-S. You et al., *Strangelets at Finite Temperature: Nucleon Emission Rates, Interface, and Shell Effects*, Phys. Rev. D **109**, 034003 (2024).
- F. Di Clemente, A. Drago, and G. Pagliara, *Strange Dwarfs: A Review on the (In)stability*, Universe **10**, 322 (2024).
- F. Chen, C. J. Xia, and G. X. Peng, *Strangelets at Finite Temperature in a Baryon Density-Dependent Quark Mass Model*, Phys. Rev. D **105**, 014011 (2022).
- S.-H. Yang and F. Weber, *XTE J1814-338 as a Strange Star Admixed with Bosonic Dark Matter*, Chin. Phys. Lett. **43**, 021102 (2026).
- J. Madsen, *Intermediate Mass Strangelets Are Positively Charged*, Phys. Rev. Lett. **85**, 4687 (2000).

Strangelets and Strange Quark Matter

- J. Madsen, *Strangelet Propagation and Cosmic Ray Flux*, Phys. Rev. D **71**, 014026 (2005).
- J. Madsen, *Universal Charge-Radius Relation for Subatomic and Astrophysical Compact Objects*, Phys. Rev. Lett. **100**, 151102 (2008).
- J. Madsen, *Colour-Flavour Locked Strangelets and Their Detection*, J. Phys. G **28**, 1737 (2002).
- J. Madsen, *Strangelets, Nuclearites, Q-balls — A Brief Overview*, J. Phys. G **32**, S41 (2006).
- J. Madsen, *Color-Flavor Locked Strangelets and Their Detection*, arXiv:hep-ph/0112153 (2001).
- S. Biswas et al., *Multifragmentation Model for Astrophysical Strangelets*, Phys. Lett. B **715**, 30 (2012).
- M. Guerrini, G. Pagliara, L. Passarella, and A. Drago, *Coexistence of Strange Quark Stars and Neutron Stars: Metastability and Nucleation in Proto-Neutron Stars*, arXiv:2610.00699 (2026).
- M. Guerrini et al., *Role of Thermal Fluctuations in Nucleation of Three-Flavor Quark Matter*, Universe **11**, 258 (2025).
- C. Greiner, P. Koch, and H. Stöcker, *Separation of Strangeness from Anti-strangeness in the Phase Transition from Quark to Hadron Matter*, Phys. Rev. Lett. **58**, 1825 (1987).
- A. Kent, *A Critical Look at Catastrophe Risk Assessments*, Risk Anal. **24**, 157–168 (2004).
- R. L. Jaffe et al., *Review of Speculative "Disaster Scenarios" at RHIC*, Rev. Mod. Phys. **72**, 1125 (2000).

Strangelets and Strange Quark Matter

- J. J. Zapata Campos and R. Negreiros, *Substellar Strange Quark Matter Objects: Predicting a New Class of Highly Compact Candidates*, Astrophys. J. **1008**, 39 (2026).
- N. Bucciantini et al., *Formation and Evaporation of Strangelets during the Merger of Two Compact Stars*, Phys. Rev. D **106**, 103032 (2022).
- E. S. Fraga, A. da Mata, and M. Pitsinigkos, *Strange Quark Matter from a Baryonic Approach*, Phys. Rev. D **106**, 074018 (2022).
- S. Cecchini et al., *Results of the Search for Strange Quark Matter and Q-balls with the SLIM Experiment*, Eur. Phys. J. C **57**, 525 (2008).
- O. Adriani et al. (PAMELA Collaboration), *New Upper Limit on Strange Quark Matter Abundance in Cosmic Rays with the PAMELA Space Experiment*, Phys. Rev. Lett. **115**, 111101 (2015).
- S. Ahlen et al., *Search for Nuclearites Using the MACRO Detector*, Phys. Rev. Lett. **69**, 1860 (1992).
- A. Albert et al. (ANTARES Collaboration), *Limits on the Nuclearite Flux Using the ANTARES Neutrino Telescope*, JCAP **2023**, 012 (2023).
- E864 Collaboration, *Search for Strange Quark Matter Produced in Relativistic Heavy-Ion Collisions*, Phys. Rev. C **63**, 054903 (2001).
- K. Borer et al., *Strangelet Search in S-W Collisions at 200A GeV/c*, Phys. Rev. Lett. **72**, 1415 (1994).

Strangelets and Strange Quark Matter

- G. Appelquist et al., *Strangelet Search in Pb-Pb Interactions at 158 GeV/c per Nucleon*, Phys. Rev. Lett. **76**, 3907 (1996).
- A. L. S. Angelis and A. D. Panagiotou, *CASTOR: A Dedicated Detector for the Detection of Centauros and Strangelets at the LHC*, J. Phys. G **23**, 2069 (1997).
- A. H. Tang (STAR Collaboration), *Strangelet Search at RHIC*, J. Phys. G **31**, S1187 (2005).
- J. Ellis et al., *Review of the Safety of LHC Collisions*, J. Phys. G **35**, 115004 (2008).
- S. Kasuya, M. Kawasaki, and T. T. Yanagida, *IceCube Potential for Detecting Q-ball Dark Matter in Gauge Mediation*, Prog. Theor. Exp. Phys. **2015**, 053B02 (2015).
- G. Lugones, *From quark drops to quark stars*, Eur. Phys. J. A **52**, 53 (2016).
- H.-S. You et al., *Compact Dwarfs Made of Light-Quark Nuggets*, Phys. Rev. D **110**, 054041 (2024).

Neutrino Physics, Cooling, and Transport

- D. Page et al., *Rapid Cooling of the Neutron Star in Cassiopeia A Triggered by Neutron Superfluidity in Dense Matter*, Phys. Rev. Lett. **106**, 081101 (2011).
- P. S. Shternin et al., *Cooling Neutron Star in the Cassiopeia A Supernova Remnant: Evidence for Superfluidity*, Mon. Not. Roy. Astron. Soc. **412**, L108 (2011).
- D. Page et al., *Minimal Cooling of Neutron Stars: A New Paradigm*, Astrophys. J. Suppl. **155**, 623 (2004).
- M. E. Gusakov et al., *Minimal Models of Cooling Neutron Stars with Accreted Envelopes*, Astron. Astrophys. **423**, 1063 (2004).
- P. S. Shternin, D. G. Yakovlev, and D. Page, *Model-Independent Constraints on Superfluidity from the Cooling Neutron Star in Cassiopeia A*, Mon. Not. Roy. Astron. Soc. **506**, 709 (2021).
- P. S. Shternin et al., *Constraints on Neutron Star Superfluidity from the Cooling Neutron Star in Cassiopeia A Using All Chandra ACIS-S Observations*, Mon. Not. Roy. Astron. Soc. **518**, 2775 (2023).
- O. Komoltsev, *Perturbative QCD Reveals the Softening of Matter in the Cores of Massive Neutron Stars*, arXiv:2506.06465 (2025).
- L. B. Leinson, *Neutrino Emission from Triplet Pairing of Neutrons in Neutron Stars*, Phys. Rev. C **81**, 025501 (2010).
- E. E. Kolomeitsev and D. N. Voskresensky, *Neutral Weak Currents in Nucleon Superfluid Fermi Liquids: Larkin-Migdal and Leggett Approaches*, Phys. Rev. C **81**, 065801 (2010).

Neutrino Physics, Cooling, and Transport

- B. P. Abbott et al. (LIGO/Virgo), *Estimating the Contribution of Dynamical Ejecta in the Kilonova Associated with GW170817*, Astrophys. J. Lett. **850**, L39 (2017).
- Super-Kamiokande Collaboration, *Search for Neutrinos in Super-Kamiokande Associated with the GW170817 Neutron-Star Merger*, Astrophys. J. Lett. **857**, L4 (2018).
- ANTARES, IceCube, and Pierre Auger Collaborations, *Search for High-Energy Neutrinos from Binary Neutron Star Merger GW170817*, Astrophys. J. Lett. **850**, L35 (2017).
- Baikal-GVD Collaboration, *Search for High-Energy Neutrinos from GW170817 with Baikal-GVD*, JETP Lett. **108**, 787 (2018).
- V. Brdar et al., *Prospects for Neutrino Observation and Mass Measurement from Binary Neutron Star Mergers*, Phys. Rev. D **113**, 123017 (2026).
- K. Kyutoku and K. Kashiyama, *Detectability of Thermal Neutrinos from Binary-Neutron-Star Mergers and Implication to Neutrino Physics*, Phys. Rev. D **97**, 103001 (2018).
- M. Mukhopadhyay, S. S. Kimura, and B. D. Metzger, *High-Energy Neutrino Signatures from Pulsar Remnants of Binary Neutron-Star Mergers*, Astrophys. J. **987**, 218 (2025).
- M. Chabanov and L. Rezzolla, *Impact of Bulk Viscosity on the Post-Merger Gravitational-Wave Signal from Merging Neutron Stars*, Phys. Rev. Lett. **134**, 071402 (2025).

Neutrino Physics, Cooling, and Transport

- Y. Qiu, D. Radice, S. Richers, and C. Bhattacharyya, *Neutrino Flavor Transformation in Binary Neutron Star Mergers*, Phys. Rev. Lett. **135**, 091401 (2025).
- F. Foucart et al., *General Relativistic Simulations of Collapsing Binary Neutron Star Mergers with Monte Carlo Neutrino Transport*, Phys. Rev. D **107**, 103055 (2023).
- A. C. Semposki et al., *From Chiral Effective Field Theory to Perturbative QCD: A Bayesian Model Mixing Approach to Symmetric Nuclear Matter*, Phys. Rev. C **111**, 035804 (2025).
- S. Rossoni, D. Boncioli, and G. Sigl, *Investigating Binary-Neutron-Star Mergers as Production Sites of High-Energy Neutrinos*, JCAP **2025**, 009 (2025).
- G. Guo, Y.-Z. Qian, and M.-R. Wu, *Binary Neutron Star Mergers as Potential Sources for Ultra-High-Energy Cosmic Rays and High-Energy Neutrinos*, Phys. Rev. D **112**, 063022 (2025).
- JUNO Collaboration, *JUNO Physics and Detector*, Prog. Part. Nucl. Phys. **123**, 103927 (2022).
- JUNO Collaboration, *The Design and Technology Development of the JUNO Central Detector*, Eur. Phys. J. Plus **139**, 1128 (2024).
- JUNO Collaboration, *Initial Performance Results of the JUNO Detector*, Chin. Phys. C **50**, 043001 (2026).
- D. Radice and S. Bernuzzi, *Ab-Initio General-Relativistic Neutrino-Radiation Hydrodynamics Simulations of Long-Lived Neutron Star Merger Remnants to Neutrino Cooling Timescales*, Astrophys. J. **959**, 46 (2023).

Neutrino Physics, Cooling, and Transport

- F. Foucart et al., *Robustness of Neutron Star Merger Simulations to Changes in Neutrino Transport and Neutrino-Matter Interactions*, Phys. Rev. D **110**, 083028 (2024).
- Y. Yang et al., *Far-from-Equilibrium Bulk-Viscous Transport Coefficients in Neutron Star Mergers*, Phys. Rev. C **109**, 015805 (2024).
- J. M. Espino et al., *Impact of Moment-Based, Energy-Integrated Neutrino Transport on Microphysics and Ejecta in Binary Neutron Star Mergers*, Phys. Rev. D **109**, 103027 (2024).
- E. R. Most et al., *Emergence of Microphysical Bulk Viscosity in Binary Neutron Star Postmerger Dynamics*, Astrophys. J. Lett. **967**, L14 (2024).
- D. Page et al., *Neutrino Emission from Cooper Pairs and Minimal Cooling of Neutron Stars*, The Astrophysical Journal, **707**, No. 2, 1131 (2009).
- D. G. Yakovlev et al., *Neutrino Emission from Neutron Stars*, Phys. Rep. **354**, 1 (2001).
- P. S. Shternin and D. G. Yakovlev, *Self-similarity relations for cooling superfluid neutron stars*, Mon. Not. Roy. Astron. Soc. **446**, 3621 (2015).
- A. Y. Potekhin, M. E. Gusakov, and A. I. Chugunov, *Thermal evolution of neutron stars in soft X-ray transients with thermodynamically consistent models of the accreted crust*, Mon. Not. Roy. Astron. Soc. **522**, 4830 (2023).
- A. I. Chugunov and N. A. Shchechilin, *Crucial role of neutron diffusion in the crust of accreting neutron stars*, Mon. Not. Roy. Astron. Soc. **495**, L32 (2020).

- M. E. Gusakov and A. I. Chugunov, *Thermodynamically Consistent Equation of State for an Accreted Neutron Star Crust*, Phys. Rev. Lett. **124**, 191101 (2020).

Heavy-Ion Collisions and Terrestrial Constraints

- STAR Collaboration, *Strangeness Production in $\sqrt{s_{NN}} = 3$ GeV Au+Au Collisions at RHIC*, JHEP **10**, 139 (2024).
- H. Li, *Strange Hadron Production at High Baryon Density*, arXiv:2501.07089 (2025).
- L. Liu et al., *Elliptic and Triangular Flow of (Multi-)Strange Hadrons and ϕ Mesons in BES-II Energies at STAR*, arXiv:2208.14604 (2022).
- CBM Collaboration, *Performance of the Prototype Silicon Tracking System of the CBM Experiment Tested with Heavy-Ion Beams at SIS18*, arXiv:2505.20517 (2025).
- MUSES Collaboration, *Theoretical and Experimental Constraints for the Equation of State of Dense and Hot Matter*, Living Rev. Relativ. **27**, 3 (2024).
- P. Danielewicz, R. Lacey, and W. G. Lynch, *Determination of the Equation of State of Dense Matter*, Science **298**, 1592 (2002).
- M. Oertel et al., *Equations of State for Supernovae and Compact Stars*, Rev. Mod. Phys. **89**, 015007 (2017).
- H. Shen, H. Toki, K. Oyamatsu, and K. Sumiyoshi, *Relativistic Equation of State for Core-Collapse Supernova Simulations*, Astrophys. J. Suppl. **197**, 20 (2011).
- HADES Collaboration, *Directed, Elliptic, and Higher Order Flow Harmonics of Protons, Deuterons, and Tritons in Au+Au Collisions at $\sqrt{s_{NN}} = 2.4$ GeV*, Phys. Rev. Lett. **125**, 262301 (2020).

Heavy-Ion Collisions and Terrestrial Constraints

- J. Steinheimer et al., *Simultaneous Description of High Density QCD Matter in Heavy Ion Collisions and Neutron Star Observations*, Phys. Lett. B **867**, 139605 (2025).
- M. O. Kuttan et al., *QCD Equation of State of Dense Nuclear Matter from a Bayesian Analysis of Heavy-Ion Collision Data*, Phys. Rev. Lett. **131**, 202303 (2023).
- STAR Collaboration, *Elliptic and Quadrangular Flow of Protons in the High Baryon Density Region*, arXiv:2411.06196 (2024).
- N. Mallick, S. Prasad, A. N. Mishra, R. Sahoo, and G. G. Barnaföldi, *Deep Learning Predicted Elliptic Flow of Identified Particles in Heavy-Ion Collisions*, Phys. Rev. D **107**, 094001 (2023).
- STAR Collaboration, *Elliptic Flow of Heavy-Flavor Decay Electrons in Au+Au Collisions at* $\sqrt{s_{NN}} = 27$ *and 54.4 GeV*, Phys. Lett. B **844**, 138071 (2023).
- ALICE Collaboration, *Anisotropic Flow and Flow Fluctuations of Identified Hadrons in Pb–Pb Collisions at* $\sqrt{s_{NN}} = 5.02$ *TeV*, JHEP **05**, 243 (2023).
- C. Y. Tsang, M. B. Tsang, W. G. Lynch, R. Kumar, and C. J. Horowitz, *Determination of the Equation of State from Nuclear Experiments and Neutron Star Observations*, Nature Astronomy **8**, 328 (2024).
- Y. Zhang, M. Liu, C.-J. Xia, Z. Li, and S. K. Biswal, *Constraints on Symmetry Energy and Its Associated Parameters from Nuclei to Neutron Stars*, Phys. Rev. C **101**, 034303 (2020).

Heavy-Ion Collisions and Terrestrial Constraints

- P. Parfenov, A. Taranenko, I. Selyuzhenkov, and P. Senger, *Performance Studies of Anisotropic Flow with MPD at NICA*, arXiv:1901.03125 (2019).
- D. Colella for the ALICE Collaboration, *Strangeness Production in p-Pb and Pb-Pb Collisions with ALICE at the LHC*, arXiv:1609.06900 (2016).
- ALICE Collaboration, *Strangeness Production in Light-Ion Collisions with ALICE at the LHC*, arXiv:2608.02874 (2026).
- S. Pucillo for the ALICE Collaboration, *Recent Results on Strangeness Enhancement in Small Collision Systems with ALICE*, arXiv:2504.02527 (2025).

Neutron Star Mergers and Multimessenger Astronomy

- L. Baiotti and L. Rezzolla, *Binary neutron star mergers: a review of Einstein's richest laboratory*, Rep. Prog. Phys. **80**, 096901 (2017).
- A. Perego et al., *Thermodynamics conditions of matter in neutron star merger*, Eur. Phys. J. A **55**, 124 (2019).
- W.-Z. Qiumu, M.-H. Chen, Q.-H. Chen, and E.-W. Liang, *Kilonova Emission from Neutron Star Mergers with Different Equations of State*, RAA **25**, 035013 (2025).
- K. A. Lund, R. Somasundaram, G. C. McLaughlin, J. M. Miller, M. R. Mumpower, and I. Tews, *Kilonova Emissions from Neutron Star Merger Remnants: Implications for the Nuclear Equation of State*, arXiv:2408.07686 (2024).
- N. Vieira et al., *Spectroscopic r-Process Abundance Retrieval for Kilonovae. I.*, Astrophys. J. **944**, 123 (2023).
- C. Collins, L. Shingles, and V. Vijayan, *Kilonova Simulations: Connecting Observations with the Underlying Physics*, Phil. Trans. R. Soc. A **383**, 20240119 (2025).
- F. Grippa, A. Prakash, D. Logoteta, D. Radice, and I. Bombaci, *General Relativistic Hydrodynamic Simulations of Binary Strange-Star Mergers*, Phys. Rev. D **111**, 083009 (2025).
- R. Abbott et al. (LIGO/Virgo/KAGRA), *GWTC-3: Compact Binary Coalescences Observed by LIGO and Virgo during the Second Part of the Third Observing Run*, Phys. Rev. X **13**, 041039 (2023).
- M. Colombo et al., *Multi-messenger Observations in the Einstein Telescope Era: Binary Neutron Star and Black Hole–Neutron Star Mergers*, Astron. Astrophys. **704**, A260 (2025).

Neutron Star Mergers and Multimessenger Astronomy

- K. Hayashi, K. Kiuchi, K. Kyutoku, Y. Sekiguchi, and M. Shibata, *Jet from Binary Neutron Star Merger with Prompt Black Hole Formation*, Phys. Rev. Lett. **134**, 211407 (2025).
- F. Lecce, A. Lella, G. Lucente, V. Vijayan, A. Bauswein, M. Giannotti, and A. Mirizzi, *Probing Axionlike Particles with Multimessenger Observations of Neutron Star Mergers*, Phys. Rev. D **112**, 023001 (2025).
- P. T. H. Pang, T. Dietrich, M. W. Coughlin, M. Bulla, I. Tews, et al., *An updated nuclear-physics and multi-messenger astrophysics framework for binary neutron star mergers*, Nature Communications **14**, 8352 (2023).
- L. Rezzolla, E. R. Most, and L. R. Weih, *Using Gravitational-wave Observations and Quasi-universal Relations to Constrain the Maximum Mass of Neutron Stars*, Astrophys. J. Lett. **852**, L25 (2018).
- B. Margalit and B. D. Metzger, *Constraining the Maximum Mass of Neutron Stars from Multi-messenger Observations of GW170817*, Astrophys. J. Lett. **850**, L19 (2017).
- D. Radice et al., *GW170817: Joint Constraint on the Neutron Star Equation of State from Multimessenger Observations*, Astrophys. J. Lett. **852**, L29 (2018).
- V. Villa-Ortega, A. Lorenzo-Medina, J. Calderón Bustillo, M. Ruiz, D. Guerra, P. Cerdá-Durán, and J. A. Font, *Self-Consistent Treatment of Thermal Effects in Neutron-Star Postmerger Remnants: Observational Implications for Third-Generation Gravitational-Wave Detectors*, Phys. Rev. D **111**, 103030 (2025).
- T. Hinderer, *Tidal Love Numbers of Neutron Stars*, Astrophys. J. **677**, 1216 (2008).

Neutron Star Mergers and Multimessenger Astronomy

- M. Ferreira, R. C. Pereira, and C. Providência, *Hybrid Stars with Large Strange Quark Cores Constrained by GW170817*, Phys. Rev. D **103**, 123020 (2021).
- M. Miravet-Tenés, D. Guerra, M. Ruiz, P. Cerdá-Durán, and J. A. Font, *Identifying Thermal Effects in Neutron Star Merger Remnants with Model-Agnostic Waveform Reconstructions and Third-Generation Detectors*, Phys. Rev. D **111**, 043006 (2025).

Bayesian Analysis and EOS Inference

- E. Annala et al., *Evidence for Quark-Matter Cores in Massive Neutron Stars*, Nature Physics **16**, 907 (2020).
- P. Landry, R. Essick, and K. Chatziioannou, *Nonparametric constraints on neutron star matter with existing and upcoming gravitational wave and pulsar observations*, Phys. Rev. D **101**, 123007 (2020).
- S. A. Imam and N. K. Patra, *Bayesian Analysis of the Neutron Star Equation of State and Model Comparison: Insights from PSR J0437-4715, PSR J0614-3329, and Other Multi-Physics Data*, Phys. Rev. D **112**, 103018 (2025), arXiv:2509.07109.
- C. A. Raithel, F. Özel, and D. Psaltis, *From Neutron Star Observables to the Equation of State. II. Bayesian Inference of Equation of State Pressures*, ApJ **844**, 156 (2017).
- F. J. Fattoyev et al., *Neutron skins and neutron stars in the multimessenger era*, Phys. Rev. Lett. **120**, 172702 (2018).
- A. Ayriyan et al., *Bayesian analysis of multimessenger M-R data with interpolated hybrid EoS*, Eur. Phys. J. A **57**, 318 (2021).
- P. Landry and R. Essick, *Nonparametric Inference of Neutron Star Equation of State from Gravitational Wave Observations*, Phys. Rev. D **99**, 084049 (2019).
- R. Essick, P. Landry, and D. E. Holz, *Nonparametric inference of neutron star composition, equation of state, and maximum mass with GW170817*, Phys. Rev. D **101**, 063007 (2020).

Bayesian Analysis and EOS Inference

- C. Huang and S. Sourav, *Constraining First-Order Phase Transition inside Neutron Stars with Application of Bayesian Techniques on PSR J0437-4715 NICER Data*, Astrophys. J. **983**, 17 (2025).
- R. Kashyap et al., *Optimizing Bayesian Model Selection for Equation of State of Cold Neutron Stars*, Phys. Rev. D **113**, 063019 (2026).
- F. Köpp, C. H. Lenzi, C. V. Flores, and D. P. Menezes, *A Bayesian Approach Study of Hybrid Neutron Stars*, Phys. Rev. D **114**, 043009 (2026).
- X. Grundler and B.-A. Li, *Bayesian Constraints on the Neutron Star Equation of State with a Smooth Hadron-Quark Crossover*, Phys. Rev. D **113**, 103012 (2026).
- W.-J. Xie and B.-A. Li, *Bayesian Inference of the Dense-Matter Equation of State Encapsulating a First-Order Hadron-Quark Phase Transition from Observables of Canonical Neutron Stars*, Phys. Rev. C **103**, 035802 (2021).
- M. Imam and R. N. Patra, *Bayesian Analysis of the Neutron Star Equation of State and Model Comparison: Insights from PSR J0437-4715, PSR J0614+3329, and Other Multiphysics Data*, Phys. Rev. D **112**, 103018 (2025).
- Z. Miao et al., *Bayesian Inference of Strange Star Equation of State Using the GW170817 and GW190425 Data*, Astrophys. J. Lett. **917**, L22 (2021).

Bayesian Analysis and EOS Inference

- S. Podder, S. Pal, D. Sen, and G. Chaudhuri, *Constraints on Density Dependent MIT Bag Model Parameters for Quark and Hybrid Stars*, Nucl. Phys. A **1040**, 122763 (2023).
- M. Ju, P. Chu, X. Wu, and H. Liu, *HESS J1731-347 is Likely a Quark Star Based on the Density-Dependent vMIT Bag Model*, arXiv:2404.14775 (2024).
- M. C. A. Lobo and D. P. Menezes, *The Vector MIT Bag Model under the Light of New Data*, arXiv:2305.11740 (2023).
- S.-P. Wang, Z.-J. Ma, J.-F. Xu, and Z.-Y. Lu, *Constraints on the Equation of State of Quark Stars from Compact Star Observations*, Particles **7**, 64 (2024).
- A. Ayriyan et al., *Bayesian Inference Favors Quark Matter in Neutron Star Interiors*, Phys. Rev. D **113**, 114045 (2026).

Kibble-Zurek Mechanism and Superfluidity

- P. Bagchi et al., *Detecting Superfluid Transition in the Pulsar Core*, Mon. Not. Roy. Astron. Soc. **532**, 2934 (2024).
- M. Eto, Y. Hirono, M. Nitta, and S. Yasui, *Vortices and Other Topological Solitons in Dense Quark Matter*, Zentralblatt MATH (2014).
- A. B. Migdal, *Superfluidity and the Moments of Inertia of Nuclei*, Nucl. Phys. **13**, 655 (1959).
- V. L. Ginzburg and D. A. Kirzhnits, *On the Superfluidity of Neutron Stars*, Zh. Eksp. Teor. Fiz. **47**, 2006 (1964) [Sov. Phys. JETP **20**, 1346 (1965)].
- W. Ketterle and N. J. van Druten, *Evaporative Cooling of Trapped Atoms*, Adv. At. Mol. Opt. Phys. **37**, 181 (1996).
- T. W. B. Kibble, *Topology of Cosmic Domains and Strings*, J. Phys. A **9**, 1387 (1976).
- W. H. Zurek, *Cosmological Experiments in Superfluid Helium?*, Nature **317**, 505 (1985).
- G. Lamporesi et al., *Spontaneous Creation of Kibble-Zurek Solitons in a Bose-Einstein Condensate*, Nature Physics **9**, 656 (2013).
- J. A. Sauls, *Generation of Quantum Turbulence by Neutrino Cooling in Neutron Stars*, Phys. Rev. D **114**, 043031 (2026), arXiv:2605.22768.
- K. Lee et al., *Universal Kibble–Zurek Scaling in an Atomic Fermi Superfluid*, Nature Phys. **20**, 1570 (2024).

Bulk Viscosity and Transport

- S. Blacker et al., *Exploring Thermal Effects of the Hadron-Quark Matter Transition*, Phys. Rev. D **108**, 063032 (2023).
- J. L. Hernández, *Bulk-viscous Dissipation in Strange Quark Stars and Mergers*, DOI 10.1016/j.jspc.2026.100323 (2026).
- M. Chabanov and L. Rezzolla, *Numerical Modeling of Bulk Viscosity in Neutron Stars*, Phys. Rev. D **111**, 044074 (2025).
- N. Celora et al., *Formulating Bulk Viscosity for Neutron Star Simulations*, Phys. Rev. D **105**, 103016 (2022).
- S. P. Harris and C. J. Horowitz, *Bulk Viscosity from Neutron Decays to Dark Baryons in Neutron Star Matter*, arXiv:2509.25838 (2025).

Theoretical Foundations: QCD Phase Diagram, NJL, MIT Bag

- A. Chodos et al., *A New Extended Model of Hadrons*, Phys. Rev. D **9**, 3471 (1974).
- M. Albino, T. Malik, M. Ferreira, and C. Providência, *Hybrid Star Properties with the NJL and Mean Field Approximation of QCD Models: A Bayesian Approach*, Phys. Rev. D **110**, 083037 (2024).
- C. Ratti, S. Roessner, M. A. Thaler, and W. Weise, *Thermodynamics of the PNJL Model*, arXiv:hep-ph/0609218 (2006).
- K. Zhao and J. M. Lattimer, *Quarkyonic Matter Equation of State in Beta-Equilibrium*, Phys. Rev. D **102**, 023021 (2020).
- J. O. Andersen, W. R. Naylor, and A. Tranberg, *Phase Diagram of QCD in a Magnetic Field: A Review*, Rev. Mod. Phys. **88**, 025001 (2016), arXiv:1411.7176.
- H. Liu, X.-M. Zhang, and P.-C. Chu, *Properties of Quark-Matter Cores in Massive Hybrid Stars*, Phys. Rev. D **107**, 094032 (2023).
- T. Gorda et al., *Equation of State of Cold Quark Matter to $O(\alpha_s^3 \ln \alpha_s)$*, Phys. Rev. Lett. **131**, 181902 (2023).
- A. Mitra et al., *Hybrid Stars in a Relativistic Quark Model*, Phys. Rev. C **105**, 045802 (2022).
- S. Pal and G. Chaudhuri, *Medium Effects in the MIT Bag Model for Quark Matter: Self-Consistent Thermodynamical Treatment*, Phys. Rev. D **108**, 103028 (2023).
- W.-L. Yuan and B. Gao, *The Stability of Color-Flavor-Locked Quark Matter and Massive CFL Quark Stars*, arXiv:2605.19657 (2026).

Theoretical Foundations: QCD Phase Diagram, NJL, MIT Bag

- J. O. Andersen, M. Linares, and M. P. Nødtvedt, *Massive Hybrid Stars within the Extended Three-Flavor Quark-Meson Diquark Model*, arXiv:2605.05816 (2026).
- C. Zhang, J. M. Z. Pretel, and R. Xu, *Self-Bound Hybrid Stars with Strong Phase Transitions Can Relieve Major Compact Star Observation Tensions*, arXiv:2507.01371 (2025).
- J. V. Zastrow, J. P. Pereira, R. C. R. de Lima, and J. E. Horvath, *Constraints on QCD-based Equation of State of Quark Stars from Neutron Star Maximum Mass, Radius, and Tidal Deformability Observations*, arXiv:2504.08926 (2025).
- Y.-J. Huang, L. Baiotti, T. Kojo, K. Takami, H. Sotani, H. Togashi, T. Hatsuda, S. Nagataki, and Y.-Z. Fan, *Merger and Postmerger of Binary Neutron Stars with a Quark-Hadron Crossover Equation of State*, Phys. Rev. Lett. **129**, 181101 (2022).
- M. Shahrbaf, S. Antić, A. Ayriyan, D. Blaschke, and A. G. Grunfeld, *Constraining Free Parameters of a Color Superconducting Nonlocal Nambu-Jona-Lasinio Model Using Bayesian Analysis of Neutron Stars Mass and Radius*, Phys. Rev. D **104**, 083016 (2021).
- E.-P. Zhou, X. Zhou, and A. Li, *Constraints on Interquark Interaction Parameters with GW170817 in a Binary Strange Star Scenario*, Phys. Rev. D **97**, 083007 (2018).
- S. Bhattacharyya, I. Bombaci, D. Logoteta, and A. V. Thampan, *Fast Spinning Strange Stars: Possible Ways to Constrain Interacting Quark Matter Parameters*, Mon. Not. Roy. Astron. Soc. **457**, 3101 (2016).

Theoretical Foundations: QCD Phase Diagram, NJL, MIT Bag

- J. Sedaghat, G. H. Bordbar, M. Haghighat, and S. M. Zebarjad, *Two-Fluid CFL Strange Quark Stars with Scalar Dark Matter*, arXiv:2607.05972 (2026).
- N. Priyobarta, S. K. Maurya, K. N. Singh, and B. Mishra, *Dark Matter Admixed Quark Stars: A Relativistic Two-Fluid Approach*, arXiv:2608.16064 (2026).
- S.-H. Yang and C.-M. Pi, *Color-Flavor Locked Strange Stars Admixed with Mirror Dark Matter*, JCAP **2024**, 052 (2024).
- J. Lugones and A. G. Grunfeld, *Scaling and Universality in Strange Quark Stars*, Phys. Rev. D **111**, 123027 (2025).

Strange Star Candidates and Compact Objects

- V. Doroshenko et al., *A strangely light neutron star within a supernova remnant*, Nature Astronomy **6**, 1444 (2022).
- V. Sagun et al., *What Is the Nature of the HESS J1731-347 Compact Object?*, Astrophys. J. **958**, 49 (2023).
- S. Shirke, R. Maiti, and D. Chatterjee, *PSR J0614-3329: A NICER Case for Strange Quark Stars*, arXiv:2508.02652 (2025).
- M. C. Miller et al., *The Radius of PSR J0740+6620 from NICER and XMM-Newton Data*, Astrophys. J. Lett. **918**, L28 (2021).
- F. Di Clemente et al., *Strange Quark Matter as Dark Matter: 40 yr Later, a Reappraisal*, Mon. Not. Roy. Astron. Soc. **537**, 1056 (2025).
- C. Zhang, *Probing Up-Down Quark Matter via Gravitational Waves*, Phys. Rev. D **101**, 043003 (2020).

Kaon Condensation and Competing Exotic Phases

- Z. Sharifi et al., *Binary Neutron Star Mergers within Kaon Condensation: GW170817*, Phys. Scr. **96**, 125311 (2021).
- C. Adam, A. G. Martín-Caro, M. Huidobro, A. Wereszczynski, and R. Vázquez, *Kaon Condensation in Skyrmion Matter and Compact Stars*, arXiv:2212.00385 (2022).
- K. Kim, H. K. Lee, and M. Rho, *Dense Stellar Matter with Strange Quark Matter Driven by Kaon Condensation*, arXiv:1102.5167 (2011).
- P. Senger, *Heavy-Ion Collisions at FAIR-NICA Energies*, Particles **4**, 201 (2021).
- D. Almaalol, M. Hippert, J. Noronha-Hostler, J. Noronha, E. Speranza, et al., *Continuation of the BES Physics Program with CBM at FAIR*, arXiv:2209.05009 (2022).
- N. K. Glendenning and J. Schaffner-Bielich, *Kaon Condensation and Dynamical Nucleons in Neutron Stars*, Phys. Rev. Lett. **81**, 4564 (1998).
- M. Muto, *Properties of a Kaon-Condensed Phase in Hyperon-Mixed Matter with Three-Baryon Forces*, Phys. Rev. C **111**, 045802 (2025).
- M. Veselský, P. S. Koliogiannis, V. Petousis, J. Leja, and Ch. C. Moustakidis, *How the HESS J1731-347 Object Could Be Explained Using K^- Condensation*, Phys. Lett. B **860**, 139185 (2025).

Instrumentation and Detector Papers

- M. Bianchi et al., *Search for Strange Quark Matter and Nuclearites on Board the International Space Station (SQM-ISS)*, Sensors **24**, 5090 (2024).
- M. Mukhopadhyay, *Prospects for Gravitational Wave Triggered High Energy Neutrino Searches*, PoS **444**, 1586 (2024).
- M. Mukhopadhyay, S. S. Kimura, and K. Murase, *Gravitational Wave Triggered Searches for High-Energy Neutrinos from BNS Mergers*, Phys. Rev. D **109**, 043053 (2024).
- M. Mukhopadhyay, S. S. Kimura, and B. D. Metzger, *High-Energy Neutrino Signatures from Pulsar Remnants of Binary Neutron-Star Mergers: Coincident Detection Prospects with Gravitational Waves*, arXiv:2407.04767 (2024).
- M. Teklishyn for the CBM Collaboration, *Detectors and Electronics for the CBM Experiment at FAIR*, Journal of Subatomic Particles and Cosmology **4**, 100250 (2025).
- M. Di Giovanni, *Einstein Telescope and Cosmic Explorer*, arXiv:2505.11033 (2025).

References for Comprehensive Strange Star/Quark Star Audit

- M. Ju, P. Chu, X. Wu, and H. Liu, *Hess J1731-347 is likely a quark star based on the density-dependent vMIT bag model*, Eur. Phys. J. C **85**, 40 (2025).
- S.-H. Yang, C.-M. Pi, X.-P. Zheng, and F. Weber, *Confronting strange stars with compact-star observations and new physics*, arXiv:2304.09614 (2023).
- Z. Cao et al., *GW190814: Circumstantial evidence for up-down quark star*, Phys. Rev. D **106**, 083007 (2022).
- I. Bombaci et al., *Was GW190814 a black hole–strange quark star system?*, Phys. Rev. Lett. **126**, 162702 (2021).
- P.-C. Chu, H. Liu, H.-M. Liu, M. Ju, X.-H. Wu, Y. Zhou, and X.-H. Li, *Quark star matter within an extended quasiparticle model*, Eur. Phys. J. C **85**, 466 (2025).
- H. Shahinyan, T. Sargsyan, and A. Babajanyan, *Maximal mass strange quark stars based on the modified MIT model with variable vacuum pressure*, Nucl. Phys. B **1014**, 116956 (2025).

Reviews and General References

- M. G. Alford, *Color-Superconducting Quark Matter*, Annu. Rev. Nucl. Part. Sci. **51**, 131 (2001).
- O. Lourenço, C. H. Lenzi, M. Dutra, E. J. Ferrer, V. de la Incera, L. Paulucci, and J. E. Horvath, *Tidal Deformability of Strange Stars and the GW170817 Event*, Phys. Rev. D **103**, 103010 (2021).
- Y. Zhou, C. Zhang, J. Zhao, K. Kiuchi, S. Fujibayashi, and E. Zhou, *Constraints of the Maximum Mass of Quark Stars Based on Post-merger Evolutions*, arXiv:2407.08544 (2024).
- B.-J. Cai, B.-A. Li, and Y.-G. Ma, *Neutron Star Equation of State with Nucleon Short-Range Correlations: A Concise Review and Open Issues*, arXiv:2512.23455 (2025).
- C. R. Das, *Finding Strangelets in Cosmic Rays from HESS J1731-347 Using CTA*, arXiv:2507.12817 (2025).
- C. R. Das, *Strangelet Searches from Neutron Stars, Binary Mergers, and Gamma-Ray Bursts with Current and Future Observatories*, arXiv:2511.19799 (2025).
- P. L. Espino, P. Hammond, D. Radice, S. Bernuzzi, R. Gamba, F. Zappa, L. F. L. Micchi, and A. Perego, *Neutrino Trapping and Out-of-Equilibrium Effects in Binary Neutron-Star Merger Remnants*, Phys. Rev. Lett. **132**, 211001 (2024).
- F. Iacovelli, M. Mancarella, C. Mondal, A. Puecher, T. Dietrich, F. Gulminelli, M. Maggiore, and M. Oertel, *Nuclear Physics Constraints from Binary Neutron Star Mergers in the Einstein Telescope Era*, Phys. Rev. D **108**, 122006 (2023).
- M. Di Giovanni, *Einstein Telescope and Cosmic Explorer*, arXiv:2505.11033 (2025).

Reviews and General References

- B. Daszuta et al., *Binary Neutron Star Merger Simulations with Neutrino Transport Using gr-athena++*, Phys. Rev. D **114**, 044062 (2026).
- Y. Fujimoto and S. Reddy, *Bounds on the Equation of State from QCD Inequalities and Lattice QCD*, Phys. Rev. D **109**, 014020 (2024).

Thank you very much!

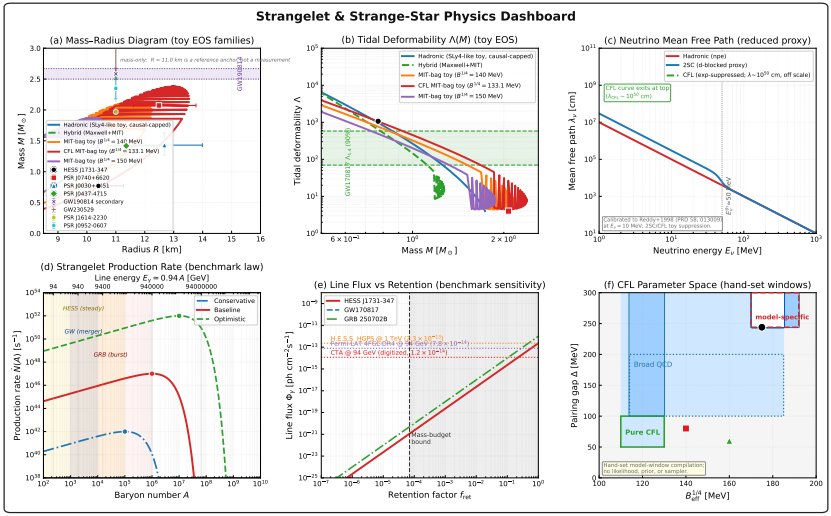

Numerical integration: TOV equations (all M-R curves); TOV + Hinderer Love-number ODE (all $\Lambda(M)$ curves).
EOS inputs: toy families (piecewise polytrope, Maxwell+MIT hybrid, massless MIT bag).
Neutrino panel: calibrated reduced proxy. Not data-inferred constraints.

Acknowledgments and Contact

Acknowledgments

- The Bogoliubov Laboratory of Theoretical Physics (BLTP), Joint Institute for Nuclear Research (JINR), Dubna, Moscow Region, Russia.
- The organizers of the Next Frontiers in Magnetic Monopole Searches workshop at IHEP, CAS, Beijing, China.
- The H.E.S.S., MAGIC, Fermi-LAT, and CTA collaborations for making their public data and instrument-response functions available.

Contact

- Email: `das@theor.jinr.ru`

- Journal: C.R. Das, Phys. Atom. Nuclei **88**, 1142-1148 (2025), *arXiv:2507.12817*.
- Python codes available on request.

Backup: Three Recent Strangelet Papers I

1. Finding Strangelets in Cosmic Rays from HESS J1731-347 (C. R. Das, 2025)

- **Approach:** Phenomenological framework linking 2SC $\rightarrow$ CFL transition in a strange quark star to observable γ-ray lines via strangelet–anti-strangelet annihilation.
- **Key result:** Predicts benchmark line fluxes for HESS J1731-347 and evaluates CTA sensitivity. The Baseline scenario lies at the projected CTA threshold; the Optimistic scenario is disfavoured by H.E.S.S.-like limits.
- **Novelty:** First end-to-end pipeline connecting QCD-motivated production, retention, and γ-ray line searches for this specific source.
- **Citation:** C. R. Das, arXiv:2507.12817 (2025); Phys. Atom. Nuclei **88**, 1142 (2025).

Backup: Three Recent Strangelet Papers II

2. Substellar Strange Quark Matter Objects (Zapata Campos & Negreiros, 2026)

- **Approach:** Bayesian exploration of the MIT bag model for finite-size strangelets with $A \leq 100$, including surface and curvature terms.
- **Key result:** Self-gravitating SQM objects are confined to the substellar regime ($M \sim 10^{-6}$–$10^{-2}\, M_{\odot}$, $R \sim 10^{2}$–10^{3} km). Predicts a new class of highly compact substellar objects, distinct from brown dwarfs and exoplanets.
- **Novelty:** Identifies a density gap that could be tested by future microlensing surveys.
- **Citation:** J. J. Zapata Campos and R. Negreiros, ApJ (2026).

Backup: Three Recent Strangelet Papers III

3. Strange Quark Matter as Dark Matter: 40 yr Later (Di Clemente et al., 2025)

- **Approach:** Reappraisal of strangelet production in the Early Universe, incorporating an instability in the hadronic phase and colour-superconducting gaps.
- **Key result:** Strangelets can survive with masses $\lesssim 10^{17}$ g. This mass range is distinct from primordial black holes, providing a way to distinguish the two dark-matter candidates.
- **Novelty:** Demonstrates that strangelets remain a viable dark-matter candidate despite earlier lattice-QCD constraints.
- **Citation:** F. Di Clemente et al., MNRAS **537**, 1056 (2025).